AUTONOMOUS FULL-TIME LIDAR MEASUREMENTS OF POLAR STRATOSPHERIC CLOUDS AT THE SOUTH POLE

A

THESIS

Presented to the Faculty

of the University of Alaska Fairbanks

in Partial Fulfillment of the Requirements

for the Degree of

DOCTOR OF PHILOSOPHY

By

James R. Campbell, B.S., M.S.

Fairbanks, Alaska

December 2006

INFORMATION TO USERS

The quality of this reproduction is dependent upon the quality of the copy submitted. Broken or indistinct print, colored or poor quality illustrations and photographs, print bleed-through, substandard margins, and improper alignment can adversely affect reproduction.

In the unlikely event that the author did not send a complete manuscript and there are missing pages, these will be noted. Also, if unauthorized copyright material had to be removed, a note will indicate the deletion.

ProQuest Information and Learning Company
300 North Zeeb Road
P.O. Box 1346
Ann Arbor, MI 48106-1346

AUTONOMOUS FULL-TIME LIDAR MEASUREMENTS OF POLAR STRATOSPHERIC CLOUDS AT THE SOUTH POLE

By

James R. Campbell

RECOMMENDED:

Catherine J. Cahill

Nicole Mölders

Glen E. Shaw

Advisory Committee Chair

Nicole Mölders

Chair, Atmospheric Sciences Program

APPROVED:

Dean, College of Natural Science and Mathematics

Susan M. Henrichs

Dean of the Graduate School

December 15, 2006

Date

Abstract

Polar stratospheric clouds (PSC) are an artifact of extremely low temperatures in the lower-stratosphere caused by a lack of sunlight during winter. Their presence induces increased concentrations of chlorine and bromine radicals that drive catalytic ozone destruction upon the return of sunlight in spring. An eye-safe micropulse lidar (MPL; 0.523 μm) was installed at the Scott-Amundsen South Pole Station, Antarctica in December 1999 to collect continuous long-term measurements of polar clouds. A four-year data subset for analyzing PSC is derived from measurements for austral winters 2000 and 2003 - 2005. A statistical algorithm based on MPL signal uncertainties is designed to retrieve PSC boundary heights, attenuated scattering ratios and demonstrate instrument performance for low signal-to-noise measurements. The MPL measurements consist mostly of Type II PSC (i.e., ice). The likelihood for Type I measurements are described for specific conditions. Seasonal PSC macrophysical properties are examined relative to thermodynamic and chemical characteristics. The potential for dehumidification and denitrification of the lower Antarctic stratosphere is examined by comparing PSC observations to theoretical predictions for cloud based on common scenarios for water vapor and nitric acid concentrations. Conceptual models for seasonal PSC occurrence, denitrification and dehumidification and ozone loss are described. A linear relationship is established between total integrated PSC scattering and ozone loss, with high correlation. Polar vortex dynamics are investigated in relation to PSC occurrence, including synoptic-scale geopotential height anomalies, isentropic airmass

trajectories and local-scale gravity waves. Moisture overrunning, from quasi-adiabatic cooling and transport along isentropic boundaries, is considered a primary mechanism for PSC occurrence. Middle and late-season PSC are found to be the result of mixing of moist air from the outer edges of the vortex that cools upon reaching South Pole. Gravity waves are considered to be only a secondary influence on PSC nucleation and growth.

Table of Contents

Page

Signature Page i

Title Page ii

Abstract iii

Table of Contents v

List of Figures viii

List of Tables xi

List of Appendices xii

Acknowledgments xiii

Chapter 1 Introduction 1

1.1 Stratospheric Ozone and Natural Loss Cycles 3

1.2 The Austral Polar Vortex 7

1.3 Polar Stratospheric Clouds and Lower-Stratospheric Denitrification 12

1.4 Halogen-based Catalytic Ozone Loss and the Antarctic Ozone Hole 24

Chapter 2 Micropulse Lidar Measurements at South Pole Station 1999-2005: Instruments, A PSC Data Subset, Particulate Layer Detection Algorithm and Processed Datasets 33

2.1 The South Pole MPL Project 37

2.2 MPL Normalized Relative Backscatter and Uncertainty Analysis 39

2.3 South Pole MPL PSC Data Subset 41

2.4 Statistical Algorithm for Particulate Layer Detection in MPL Data 48

2.5 Lidar Scattering Ratios 62

2.6 Algorithm Results for PSC Data Subset 67

2.7 Algorithm Sensitivity 72

2.8 Image Aliasing 77

Chapter 3 South Pole 2000, 2003-2005: Ozone, Thermodynamic and PSC Seasonal Properties and the Correlation between Ozone Loss and PSC Occurrence 79

3.1 Lower-Stratospheric Ozone Partial Pressures at the South Pole 82

3.2 Lower-Stratospheric Temperatures, and Nitric Acid Condensation-Point and Water Vapor Frost-Point Thermal Depressions 86

3.3 Temporally and Spatially Smoothed PSC Observations 98

3.4 Composite Summary Images 109

3.5 Correlations between PSC Occurrence and the Depth of Seasonal Ozone Loss 120

Chapter 4 Antarctic Polar Vortex Dynamics 2000, 2003-2005: Geopotential Height Anomalies, Transport and South Pole Gravity Wave Characteristics 126

4.1 High-Latitude Southern Hemispheric Winter/Spring Geopotential Height Anomalies 127

4.2 Transport Patterns and Thermodynamic Development of Air Observed at the South Pole 135

4.3 Gravity Wave Characteristics at the South Pole 147

Chapter 5 Conclusions 157

References 166

Appendices 186

List of Figures

Page

Figure 1.1: Polar stereographic map of Antarctica 8

Figure 1.2: Annual mean temperatures at the South Pole 10

Figure 1.3: Annual mean virtual potential temperatures at the South Pole 11

Figure 1.4: Condensation and frost point temperatures for NAT and ice 14

Figure 1.5: Comparison of saturation vapor pressure parameterizations 15

Figure 1.6: Model for Type I PSC formation 18

Figure 1.7: OMI composite ozone concentrations 24

Figure 1.8: Annual maximum austral ozone hole area 25

Figure 2.1: Optical design for the micropulse lidar 34

Figure 2.2: The South Pole MPL 36

Figure 2.3: The South Pole MPL operational timeline 38

Figure 2.4: Monthly subset data breakdown 42

Figure 2.5: MPL NRB and fractional uncertainties from 2000, 2003-2005 43-46

Figure 2.6: NRB fractional uncertainties from 10 June 2003 52

Figure 2.7: Algorithm diagnostic statistics 56

Figure 2.8: Processed algorithm signal retrievals 59

Figure 2.9: Algorithm particulate layer signal smoothing 64

Figure 2.10: Annual profiles for scattering ratio and minimum threshold 68-71

Figure 2.11: Algorithm tuning for SNR threshold 73

Figure 2.12: Algorithm tuning for clear threshold 74

Figure 2.13: Image aliasing for variable time-iteration output 76

Figure 3.1: Annual South Pole ozone profiles 80-81

Figure 3.2: Yearly winter/spring temperature profiles 87-88

Figure 3.3: NAT and ice saturation temperature depressions 90-93

Figure 3.4: Saturation concentrations of water vapor over ice 96-97

Figure 3.5: Smoothed annual attenuated scattering ratio profiles 99-100

Figure 3.6: Smoothed annual approximate attenuated backscatter profiles .. 101-102

Figure 3.7: Optical depth retrievals from raw algorithm output 103

Figure 3.8: Annual composite summary images 110-111

Figure 3.9: Lower-stratospheric fall-trajectories for spherical particles 112

Figure 3.10: Onset dates for NAT and ice saturation in 2003-2005 117

Figure 3.11: Correlation between total smoothed backscatter and DU days 121

Figure 3.12: Correlation between total raw backscatter and DU days 124

Figure 4.1: Annual normalized geopotential height anomalies 127-128

Figure 4.2: Annual geopotential height anomalies and PSC structure 129-130

Figure 4.3: Daily five-day back-trajectories for 2000 133

Figure 4.4: Six-hour temperature changes along trajectories in 2000 134

Figure 4.5: Daily five-day back-trajectories for 2003 136

Figure 4.6: Six-hour temperature changes along trajectories in 2003 137

Figure 4.7: Daily five-day back-trajectories for 2004 138

Figure 4.8: Six-hour temperature changes along trajectories in 2004 139

Figure 4.9: Daily five-day back-trajectories for 2005 140

Figure 4.10: Six-hour temperature changes along trajectories in 2005 141

Figure 4.11: Gravity wave energy densities 151-152, 154

Figure B.1: Rayleigh, transitional and Mie scattering domains 189

Figure B.2: UIUC lidar attenuated scattering ratios from 8 July 2000 190

Figure B.3: MPL algorithm output at base resolution from 8 July 2000 191

Figure B.4: MPL algorithm output at 0.02 and full-day resolutions 192

Figure B.5: Thermal profiles at the South Pole for 0000 UTC 8 July 2000 193

List of Tables

Page

Table 1.1: The Chapman ozone reactions 4

Table 1.2: Natural ozone loss cycles 6

Table 1.3: Seven distinct classes of PSC 21

Table 1.4: Spherical particle fall-velocities in lower-stratosphere 22

Table 1.5: The industrial chlorofluorocarbons 27

Table 1.6: Catalytic ozone destruction cycles of chlorine 28

Table 1.7: Catalytic ozone destruction cycles of chlorine/bromine 31

Table 2.1: Algorithm output statistics for PSC Data Subset 66

Table 3.1: Statistics from South Pole ozonesonde processing 83

Table 3.2: Statistical analysis of smoothed processed datasets 105

Table 4.1: Five-day back-trajectory statistics 144

Table 4.2: Six-hour cooling rate statistics for June 145

Table 4.3: Six-hour cooling rate statistics for July 146

Table 4.4: Six-hour cooling rate statistics for August 147

List of Appendices

Page

Appendix A: Two-Dimensional Hanning Function for Data Smoothing 186

Appendix B: Lidar Intercomparison to Investigate the Sensitivity of Micropulse Lidar Polar Stratospheric Cloud Detection and Algorithm Retrievals at the South Pole 188

Acknowledgments

To my Advisor, Dr. Kenneth Sassen, thank you for fourteen years of goodwill and encouragement. To my committee members, Drs. Glenn Shaw, Nicole Mölders, Cathy Cahill and Richard Collins, thank you for your suggestions and patience. In particular to Glenn, thank you for sharing your enthusiasm for thermodynamics. It inspired so much of this research, and will no doubt have a great influence on future work. To Dr. Uma Bhatt, thank you for the conversations that helped motivate the statistical framework for the particulate layer algorithm. To Dr. Xinzhao Chu and Wentao Huang at the University of Colorado, Boulder, thank you for your insights and assistance in coordinating the lidar comparisons in Appendix B.

I am forever indebted to my colleagues at the Goddard Space Flight Center who have provided me with so many opportunities and learning experiences over the past ten years. To Drs. Ellsworth Welton, James Spinhirne, Matthew McGill and Si-Chee Tsay, I am very grateful for all that you have done for me. To Dennis Hlavka, William Hart and Steve Palm, thank you for your friendship, wisdom, and for sharing so much of your IDL processing and imaging code/tricks, a great deal of which can be seen in action among the forthcoming pages. To Stan Scott, a truly unsung hero, thank you for all of your time in the laboratory teaching me the basics of optics and how they applied to the micropulse lidar. I cannot emphasize enough how much you taught me, and how much perspective and confidence I gained from our time working together. To Timothy Berkoff, thank you for your continuing work to preserve and advance the technology.

Finally, to Charissa Ledbetter for seventeen years of love and support, thank you honey, I love you. And to Linda Albert, thank you for helping us accomplish and maintain something I thought would never be possible, and that has become a source of enormous joy and pride. The folks above taught me the principles and helped me acquire the skills that led to this crazy mess. You both kept me sane and happy over the last three years while this work was completed.

This research was supported by grants from the National Science Foundation (NSF ATM-0296190) and the Measurement and Signature Intelligence program (MASINT; IRS 92-6000147).

CHAPTER 1

INTRODUCTION

This thesis examines continuous measurements of polar stratospheric clouds (PSC) at the Scott-Amundsen South Pole Station (~ 90.0° S) from May to September 2000 and May to October 2003-2005. The data were collected with an eye-safe micropulse lidar (MPL; *Spinhirne*, 1993). Macrophysical cloud properties are derived using a statistical algorithm based on the photon-counting technique of the MPL avalanche photo-diode detector. These data are examined in conjunction with atmospheric thermodynamic parameters and chemical concentrations measured from balloonsondes. Scenarios for denitrification, a proxy for atmospheric conditioning and partitioning of reactive chlorine and bromine species, are investigated. The result is a composite analysis of PSC occurrence and ozone destruction through the polar night and into spring. Airmass back-trajectories and climatological flow patterns are also examined to gain an understanding of transport and the thermodynamic evolution of air transported to South Pole. These data are examined relative to geopotential height anomalies measured from 60° - 90° S to correlate any notable influence of austral polar vortex dynamics on PSC incidence. For a layer where air has previously been identified as denitrified and/or dehumidified, subsequent PSC presence serves as a passive tracer for nitric acid and water vapor.

Situated near the core of the polar vortex the South Pole represents a unique and significant observing point for studying PSC. What occurs at or near South Pole is not

necessarily indicative of what occurs over points, say, near the edges of the polar vortex, where sufficiently cold temperatures are not as persistent and gravity wave influence is potentially more important toward the nucleation and growth of PSC (e.g., *Gobbi et al.*, 1998). Furthermore, meridional mixing of air across the vortex is more significant at the edges from baroclinic disturbances and planetary-scale wave breaking. It is both necessary and beneficial to characterize PSC properties from South Pole for it represents one end of a longitudinal cross-section of the vortex upon which PSC macrophysical and microphysical processes likely vary. The primary research objectives, therefore, are to understand how PSC occurrence evolves temporally and spatially during the polar night, and whether or not PSC presence at South Pole is positively correlated with the magnitude of the austral ozone hole. Another objective is to understand to what degree polar vortex dynamics influence PSC occurrence. However, before answering these questions it is necessary to both develop an algorithm to retrieve the PSC signal from the low-powered MPL backscatter profile, as well as characterize the signal with respect to noise so as to demonstrate that instrument performance is satisfactory to these tasks.

The remainder of this chapter is a review of the literature describing stratospheric ozone, natural and halogen-based catalytic ozone loss cycles, austral polar vortex dynamics, polar stratospheric clouds, previous PSC research and the Antarctic ozone hole. The second chapter is a summary of the MPL instrument, South Pole MPL datasets, a statistical algorithm for deriving significant scattering layer heights from low signal-to-noise MPL data and the results from a four-year data subset (2000, 2003-2005). The third chapter is a description of seasonal ozone, thermodynamic and PSC

macrophysical properties correlated with algorithm output, and an investigation into the correlation of PSC occurrence and seasonal ozone loss. The fourth chapter describes results from the examination of polar vortex dynamics, including isentropic back-trajectory analyses, geopotential height anomalies and gravity wave energies during the subset years. Conclusions are presented in the fifth chapter. Appendix A is a description of a data-smoothing filter used at multiple stages in this research. Appendix B is a case-study of MPL PSC observations compared to measurements made with a co-located high-power mesospheric lidar at South Pole in 2000. Doing so serves to further characterize the sensitivity of the MPL relative to PSC detection.

1.1 Stratospheric Ozone and Natural Loss Cycles

In the global radiation budget ozone regulates the atmospheric transmission of solar ultraviolet radiation and, therefore, that which is incident at the surface of the earth (e.g., *Cornu*, 1879; *Hartley*, 1880) a recent summary on stratospheric ozone is given by *Solomon*, 1999). Ozone absorption of high-energy photons induces electronic transitions to elevated potential and vibrational energy states around the molecule that warms the ambient environment (e.g., *Liou*, 2002). The strongest ozone absorption bands are centered at the 0.255 μm wavelength, with weaker ones extending between 0.300 and 0.360 μm and even further into the visible part of the electromagnetic spectrum. Photons absorbed with an appropriate measure of energy however, can lead to unstable excited states, thereby inducing either dissociation or ionization (e.g., *Liou*, 2002). Peak ozone concentrations vary between 15.0 and 25.0 km as a function of latitude and season with

Table 1.1 The Chapman ozone reactions.
Chemical reactions described by *Chapman* (1930), updated by *Solomon* (1999), to describe stratospheric ozone formation and destruction for an oxygen-only scenario.

$$O_2 + h\nu \rightarrow 2O \quad (\lambda < 0.240\ \mu m) \quad \textbf{(R1)}$$
$$O + O_2 + M \rightarrow O_3 + M \quad \textbf{(R2)}$$
$$O_3 + h\nu \rightarrow O_2 + O(^1D) \quad (\lambda < 0.320\ \mu m) \quad \textbf{(R3)}$$
$$O(^1D) + M \rightarrow O + M \quad \textbf{(R4)}$$
$$O_3 + h\nu \rightarrow O_2 + O \quad (\lambda < 0.320\ \mu m) \quad \textbf{(R5)}$$
$$O + O + M \rightarrow O_2 + M \quad \textbf{(R6)}$$
$$O + O_3 \rightarrow 2O_2 \quad \textbf{(R7)}$$

exponential decreases above and below (*Wayne*, 1991). Ozone absorption is responsible for the inverted thermal structure of the stratosphere (e.g., *Andrews et al.*, 1987). Indirectly, the ozone layer protects terrestrial organisms by limiting damaging ultraviolet radiation reaching the planet surface (e.g., *van der Leun et al.*, 1989; *van der Leun and de Gruijl*, 1993).

Chapman (1930) first conceptualized the existence of an elevated ozone layer based on the photochemistry of molecular oxygen. Later Director of the Geophysical Institute at this university, the work and initiative of Dr. Chapman inspired many generations of scientists within the very halls that this thesis was prepared, and began the study of upper-atmospheric aeronomy. Little was known at that time about the vertical distribution of ozone, except that there were large amounts of total ozone present in the atmosphere, and that it was likely concentrated at an elevated height. Furthermore, little was known about the ultraviolet spectrum and the parameters influencing the formation and dissociation of O, O_2 and O_3 (*Akasofu et al.*, 1967). *Chapman* (1930) reconciled all

known facts concerning atmospheric ozone using photochemical theory. His model, revised in the review by *Solomon* (1999) is shown in Table 1.1. Photolysis of molecular oxygen drives ozone formation. This same process also destroys it. Reaction R5 represents the net reaction of R3 and R4. Reactions R1, R6 and R7 are relatively slow such that steady-state equilibrium is governed by R2 and R5. However, the slower reactions ultimately govern ozone concentrations through the production and loss of atomic oxygen and subsequent loss of O and O_3 combined. This discovery was fundamental for predicting the vertical distribution of atmospheric ozone with high accuracy, but over-estimated their concentrations (e.g., *Jacob*, 1999).

It was later found that catalytic ozone loss could occur naturally through reaction with hydrogen oxide and nitrogen oxide radicals (*Bates and Nicolet*, 1950; *Hampson*, 1964; *Crutzen*, 1970, 1971; *Johnston*, 1971). The term "catalytic" describes a series of reactions whereby the molecule that destroys another is reformed and capable of reinitializing the cycle. These reactions, including formation and termination steps (through the water and nitric acid molecules, respectively) are shown in Table 1.2. In the stratosphere, oxidation of water vapor molecules yields the hydroxyl radical OH (R8). This molecule may then react with ozone to form the hydroperoxy radical HO_2 (R9), which may further react with another ozone molecule to reproduce OH (R10). Termination occurs when the two radicals react to reform water vapor and a molecular oxygen molecule (R11). The net effect of this cycle is

$$2O_3 \rightarrow 3O_2 \qquad \textbf{(R15)}$$

Table 1.2 Natural ozone loss cycles.
Initiation, propagation and termination reactions for catalytic ozone destruction by hydrogen oxide through water vapor (R8-R11) and nitrogen oxide radicals (R12-R14), after *Bates and Nicolet* (1950), *Hampson* (1964), *Crutzen* (1970; 1971) and *Johnston* (1971).

$$H_2O + O(^1D) \rightarrow 2OH \quad \textbf{(R8)}$$

$$OH + O_3 \rightarrow HO_2 + O_2 \quad \textbf{(R9)}$$

$$HO_2 + O_3 \rightarrow OH + 2O_2 \quad \textbf{(R10)}$$

$$OH + HO_2 \rightarrow H_2O + O_2 \quad \textbf{(R11)}$$

$$NO + O_3 \rightarrow NO_2 + O_2 \quad \textbf{(R12)}$$

$$NO_2 + O \rightarrow NO + O_2 \quad \textbf{(R13)}$$

$$NO_2 + OH + M \rightarrow HNO_3 + M \quad \textbf{(R14)}$$

Water vapor in the stratosphere occurs through mixing with the troposphere or oxidation of methane, the latter being subject to fluctuations from human input.

Nitric oxide is produced naturally in the atmosphere from the oxidation of N_2O. Anthropogenic modification of NO concentrations in the lower stratosphere occurs through oxidation of molecular nitrogen at high temperatures in aircraft exhaust plumes. In the upper stratosphere, perturbations of NO concentrations are also possible from solar photon events (*Heath et al.*, 1977). NO reacts rapidly with O_3 to form NO_2 (R12). Subsequent reaction of this product with atomic oxygen reforms the NO molecule and perpetuates the cycle (R13). Termination occurs when NO_2 reacts with OH to form nitric acid, a stable species considered a reservoir for reactive nitrogen compounds (R14). The net sum of this cycle is equal to R7. Following improved measurements of kinetic reaction rates (*Ko and Sze*, 1983) hydrogen and nitrogen-based loss mechanisms and their

perturbations combined with the *Chapman* (1930) theory produced an accurate model of the steady-state stratospheric ozone budget (*McElroy and Salawitch*, 1989).

1.2 The Austral Polar Vortex

The atmosphere surrounding Antarctica may be referred to as the "South Polar atmospheric cap", which is defined by the bounds of the planet surface, the top of the atmosphere and an imaginary zenith-reaching wall anchored at 70° S latitude (Fig. 1.1; *King and Turner*, 1997). This region experiences net radiative cooling throughout the year (*Masuda*, 1990) and top-of-the-atmosphere (TOA) solar irradiance is zero over portions of this area between April and August. *Nakamura and Oort* (1988) estimate the TOA net radiative flux over the cap to approach – 150 W/m^2 during autumn and early winter. To balance this loss during this period energy is transported from mid-latitudes via the mean meridional atmospheric circulation. Lower-stratospheric infrared cooling by ozone during polar night is significant such that the thermal inversion normally associated with heights above the tropopause level is eroded. Meridional temperature gradients form around 60.0° S with peak values occurring near 25.0 km above mean sea level (MSL). Compensating mid-latitude transport and the Coriolis force create cyclonic convergence at these heights over the austral pole (e.g., *King and Turner*, 1997). The result is a strong jet stream and persistent circumpolar vortex. The analogous boreal feature is otherwise disrupted by planetary waves and mixing initiated by more complex surface topography in the northern hemisphere (Newman et al., 2001).

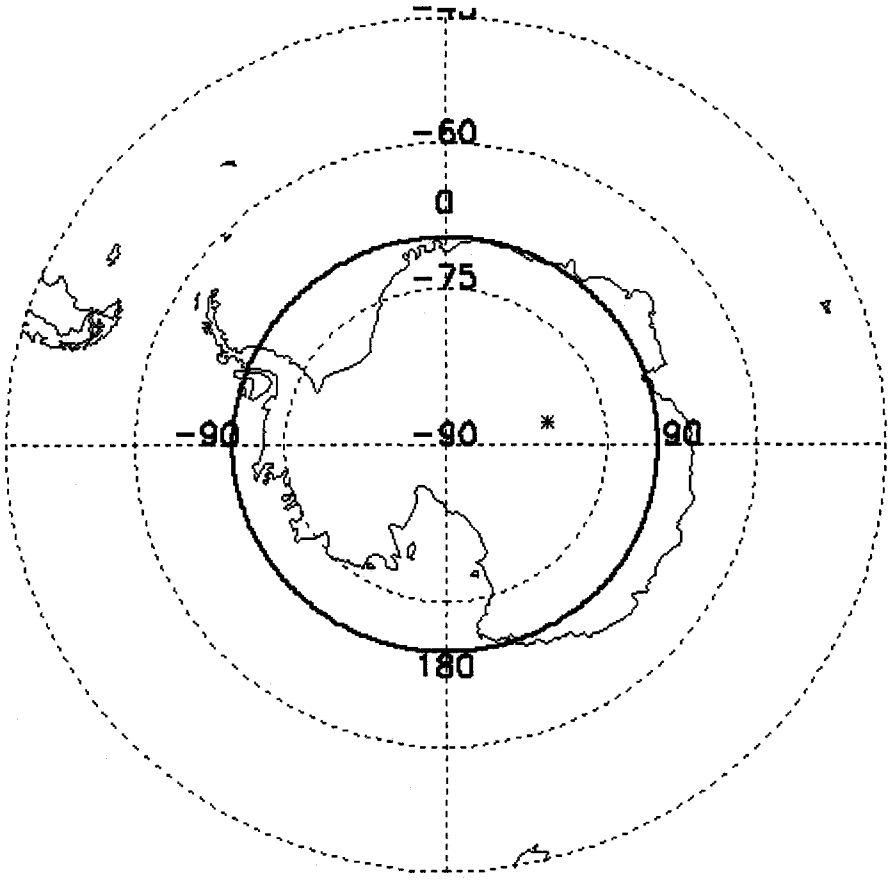

Figure 1.1 Polar stereographic map of Antarctica.
Southern hemispheric map south of 45° S, including Antarctic continent and outline around 70° S denoting South Polar cap (see text). An asterisk denotes the approximate location of the maximum altitude above sea level of the continental plateau.

The vortex expanse frequently fills the area of the South Polar cap, though it is by no means a static entity. Rossby waves, baroclinic disturbances and low-level cyclogenesis produce distortion visible along the vortex edges. During the polar night these disturbances and vertical eddy transport act to shed cyclonic vorticity from the upper-level core to enable low-level outflow and increase meridional heat transport (e.g., *James*,

1989; *Egger*, 1992; *Juckes et al.*, 1994). Radiative cooling and subsidence induce concurrent katabatic flow in the lower troposphere driving anticyclonic outflow off the continental shelf. The two features are coupled such that cyclonic spin-up at upper-levels constricts low-level outflow (*Simmonds and Law*, 1995). The vortex reflection at low-levels is therefore centered not directly over South Pole but over the maximum height of the Antarctic continental plateau (denoted by the asterisk in Fig. 1.1). Climatologically, the austral vortex exists year round (e.g., *Renwick*, 2004), however its ability to inhibit significant mixing of lower-latitude air is strongest from April, lasting sometimes into December (e.g., *Fleming et al.*, 1988).

Upper-atmospheric data at South Pole is limited. Daily sounding launches rely on balloons made of fragile materials (most commonly Mylar) unable to withstand extreme winter temperatures. As a result balloons frequently burst before sampling to heights of 30.0 km MSL (a common burst height in the summer months). However, at an irregular frequency, highest during late winter and spring, plastic (i.e., expensive) balloons are used to launch advanced ozone sampling radiosonde packages that ensure measurements to these altitudes.

Shown in Fig. 1.2 are averaged temperatures calculated from episodic ozonesonde datasets collected from 2000 – 2005 from 10.0 – 25.0 km MSL (a) and from daily balloonsonde measurements collected from August 1998 through December 2005 from 3.0 – 12.0 km MSL (b). Only balloons reaching 25.0 km MSL were used in the former sample, while only those reaching 12.0 km MSL were used for the latter. To include as many data points as possible for each height region, the differing databases were

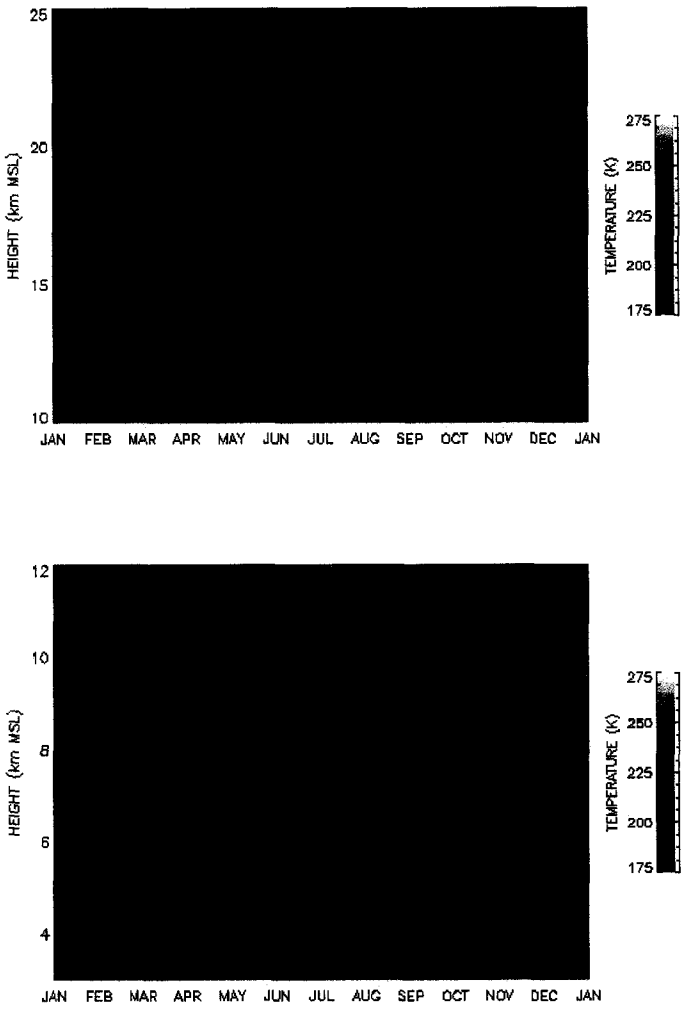

Figure 1.2 Annual mean temperatures at the South Pole.
Mean temperatures measured from South Pole Station for 2000 – 2005 from 10.0 – 25.0 km MSL (a) and for August 1998 – December 2005 from 3.0 – 12.0 km MSL (b).

examined. A traditional tropopause is visible near 10.0 km MSL through early March. It then disappears during polar night (Fig. 1.2b) and reforms in December. An inverted stratospheric thermal profile disappears between April and November (Fig. 1.2a). A deep

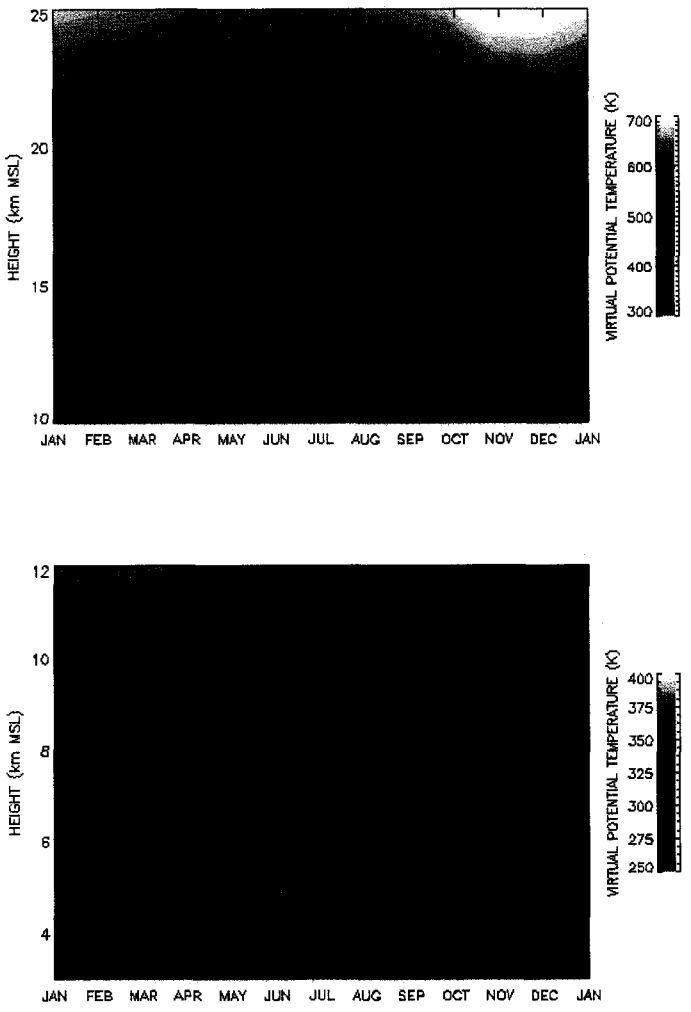

Figure 1.3 Annual mean virtual potential temperatures at the South Pole. Mean virtual potential temperatures measured from South Pole Station for 2000 – 2005 from 10.0 – 25.0 km MSL (a) and for August 1998 – December 2005 from 3.0 – 12.0 km MSL (b).

layer of persistent cold air is instead observed with a core (approx. 180 K) centered near 20.0 km MSL in late July and early August. Thermal inversions are intermittently present during the polar night at the tropopause but they are shallow and rarely more than

a few degrees. A strong planetary boundary layer inversion occurs between April and September in response to surface cooling. Shown in Fig 1.3 are mean virtual potential temperature (VPT) profiles for 10.0 – 25.0 km MSL (a) and for 3.0 – 12.0 km MSL (b), derived in a manner similar to above. Isentropic transport in the vortex produces rising/cooling air approaching the pole. During winter VPT surfaces reach maximum heights in response to infrared cooling, though these peaks are offset with respect to height with higher altitudes exhibiting them earlier than those near the surface. The loss of sunlight is apparent in both figures during April and March with a reoccurrence of solar insolation evident from August.

1.3 Polar Stratospheric Clouds and Lower-Stratospheric Denitrification

PSC have long been observed from both hemispheres (*Stanford and Davis*, 1974). However, the fortitude of the austral polar vortex inhibits rapid mixing of warm mid-latitude air and enhances radiational cooling relative to the northern hemisphere (e.g., *Waugh and Randal*, 1999). The condensation and frost point temperatures for background concentrations of nitric acid and water vapor are repeatedly surpassed for long periods, whereas this occurs only episodically over the boreal pole. Summaries of the physical processes, theories and observations of PSC research have been reported by *Toon et al.* (1989), *Turco et al.* (1989), *Solomon* (1999) and *Toon et al.* (2000).

McCormick et al. (1982) and *Steele et al.* (1983) first reported the extent of PSC occurrence using satellite occultation data over Antarctica. The initial report of significant ozone loss occurring over the southern pole came from *Farman et al.* (1985).

A subsequent report came from *Solomon et al.* (1986). The latter paper showed that gas-phase chemistry could not be used to reconcile observed losses. Given the ubiquitous nature of PSC, *Prather et al.* (1984), *Crutzen and Arnold* (1986), *McElroy et al.* (1986b) and *Solomon et al.* (1986) proposed models for heterogeneous chemistry involving PSC particle surfaces as a method for activating chlorine and bromine capable of photochemical catalytic ozone destruction. *Toon et al.* (1986) and *Crutzen and Arnold* (1986) calculated that condensation of HNO_3 and HCl would be possible in the winter polar stratosphere. Based on *McCormick et al.* (1982) and *Hamill and McMaster* (1984) *Toon et al.* (1986) characterized downward motions of air in PSC and aerosol scavenging effects. They postulated that sedimentation of cloud particles may remove nitric acid from the stratosphere, which would enhance reactive halogen-bearing chemical mechanisms. These pioneering papers (P. J. Crutzen would eventually share the Nobel Prize for Chemistry in 1995 for work in ozone-loss chemistry) established the link between ozone loss and PSC occurrence.

Junge (1961), *Junge and Manson* (1961) and *Junge et al.* (1961) described measurements of the non-volcanic background aerosol of the stratosphere and identified the prevalence of deliquesced sulfate particles. The presence of water ice in PSC composition was recognized early on (*Stanford*, 1973; *McCormick et al.*, 1982). Following earlier work on nacreous clouds (*Hallett and Lewis*, 1967) it was initially believed that PSC particle growth occurred through sulfate particle deliquescence and freezing (*Steele et al.*, 1983; *Hamill and McMaster*, 1984). This hypothesis proved inconsistent with satellite measurements of solar extinction and particle fall velocity rates

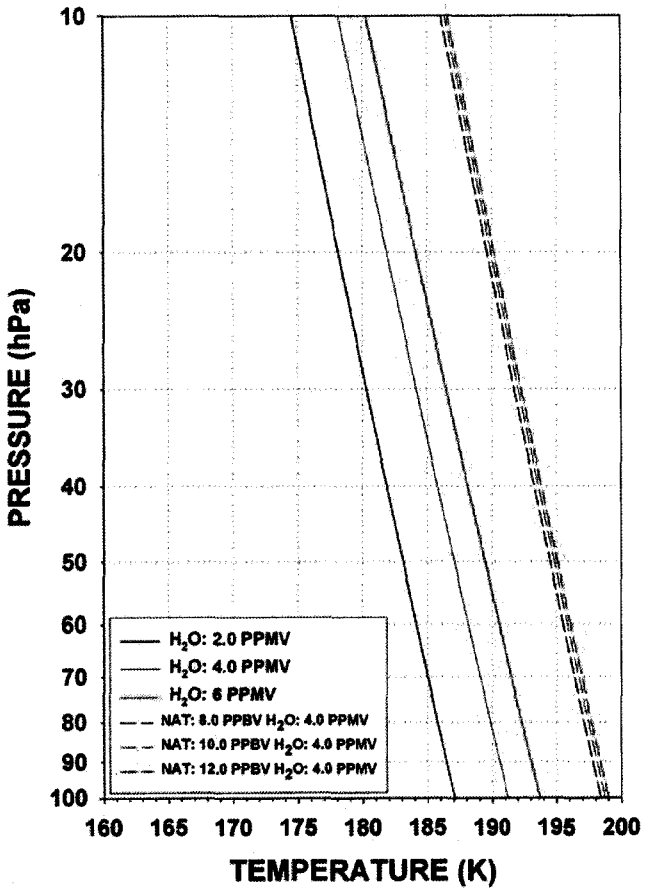

Figure 1.4 Condensation and frost point temperatures for NAT and ice. Condensation and frost point temperatures as a function of pressure for nitric acid trihydrate and ice, respectively, for given HNO_3 and water vapor concentrations (see insert).

(*Hamill et al.*, 1986; *Toon et al.*, 1986). *Toon et al.* (1986) reconciled these observations using condensed nitric acid as the predominant particle composition.

McElroy et al. (1986a), *Toon et al.* (1986) and *Crutzen and Arnold* (1986) suggested that solutions of HNO_3 and HCl would condense at slightly warmer temperatures than water ice at stratospheric temperatures and pressures. The latter two papers further

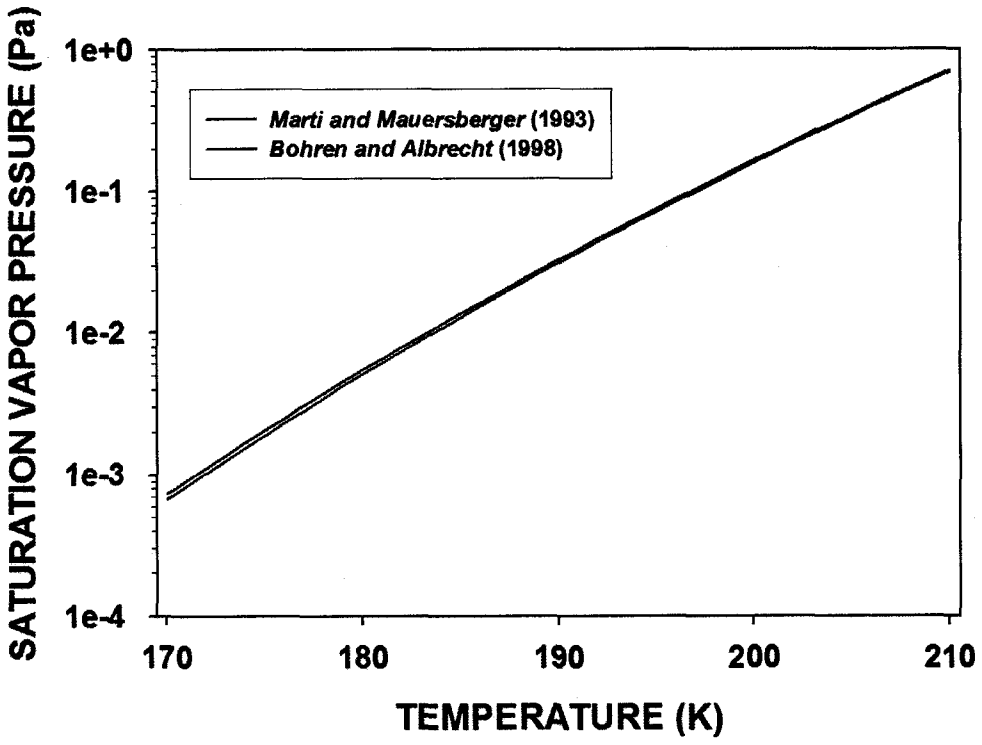

Figure 1.5 Comparison of saturation vapor pressure parameterizations. Comparison of saturation vapor pressures as a function of temperature derived from *Marti and Mauersberger* (1993) and *Bohren and Albrecht* (1998).

proposed saturation vapor pressure curves for solid solutions of H_2O and HNO_3 near the stoichiometric trihydrate (nitric acid trihydrate; NAT). *McElroy et al.* (1986a) and *Hamill et al.* (1988) reported a variable solubility for each molecule and therefore a variable absolute composition to the stoichiometric trihydrate leading to a range of stratospheric pressures over which it is stable. From laboratory measurements, *Hanson and Mauersberger* (1988) showed that NAT is expected to form in the stratosphere nearly 7 K above the ice frost point. Their data are shown in Fig. 1.4 for 8.0, 10.0 and 12.0 parts per billion by volume (ppbv) HNO_3 and 4.0 parts per million by volume

(ppmv) of water vapor. The ice frost point is also shown using a relationship derived by *Bohren and Albrecht* (1998) for 2.0, 4.0 and 6.0 ppmv water vapor.

Marti and Mauersberger (1993) derived an empirical equation for calculating the saturation vapor pressure over ice. The *Bohren and Albrecht* (1998) relationship was chosen for this research as it is a solution to the Clausius-Clapeyron equation, albeit one assuming that the enthalpy of sublimation changes as a linear function of temperature. The two relationships are compared in Fig. 1.5 between 170 and 210 K. They diverge as an inverse function of temperature, but never differ by more than 0.5 K for this region. Ultimately, homogeneous freezing of liquid water in solution droplets is constrained relative to the ice frost-point as a function of water activity, which is in turn a function of the partial-pressure of water vapor over the solution droplet relative to that of pure ice (e.g., *Koop et al.*, 2000). For qualitative discussion the small difference is not important.

Kent et al. (1986) reported ground-based linear lidar depolarization measurements (defined as the ratio of signal measured in the orthogonal polarization plane to that of the transmitted parallel plane; e.g., *Sassen*, 1991) from the Arctic. Linear depolarization measurements unambiguously separate spherical (i.e., mostly liquid) from non-spherical particles (i.e., ice) and are sensitive to the exact shape of irregular particles. They reported layers of near-zero depolarization in weakly scattering PSC supporting the likelihood for a solution droplet composition. From strongly scattering layers they reported significant depolarization. *Iwasaka* (1986a, b) and *Iwasaka et al.* (1985) reported similar depolarization measurements made from the Japanese Syowa Station (69.0° S, 39.6° E) along the northeast Antarctic coast. *Poole and McCormick* (1988)

correlated airborne lidar backscatter measurements with temperature to discriminate between stages for NAT and ice particle growth.

From the 1987 Airborne Antarctic Ozone Expedition (AAOE) filter measurements (*Gandrud et al.*, 1989), species concentration sampling (*Fahey et al.*, 1989), particle counting (*Ferry et al.*, 1989) and infrared spectra collected from low optical depth clouds (*Kinne et al.*, 1989) indicated the presence of condensed sub-micron HNO_3 particles at temperatures below 200 K. *Arnold et al.* (1989) reported evidence of nitric acid condensation from balloon and rocket sampling in the Arctic. *Ferry et al.* (1989) and *Wilson et al.* (1989) directly confirmed the presence of ice crystals on the order of a few microns diameter in lenticular PSC observed near the frost point temperature. *Toon et al.* (1989) proposed that PSC be divided into three classifications, denoting those composed of concentrated nitric acid formed at temperatures above the ice front point (Type I), and optically thin (Type II) and thick (Type III) water ice. Type I PSC were divided in two sub-categories to discriminate between relatively large ($r > 1.0$ μm) frozen particles (Type Ia) and small ($r \sim 0.5$ μm) liquid droplets (Type Ib) as a function of lidar depolarization measurements (*Browell et al.*, 1990; *Toon et al.*, 1990).

Conceptual models for PSC growth and composition at this stage proved incomplete. Airborne in-situ and balloon measurements in the Arctic showed that high HNO_3 supersaturations were common with respect to NAT, and that ratio values up to 10 were required before increases in particle numbers and volume were detected (e.g., *Dye et al.*, 1990; 1992; *Hofmann et al.*, 1990; *Hofmann and Deshler*, 1991; *Kawa et al.*, 1992). *Dye et al.* (1992) measured the growth of liquid-phase sulfate particles outside of cloud to

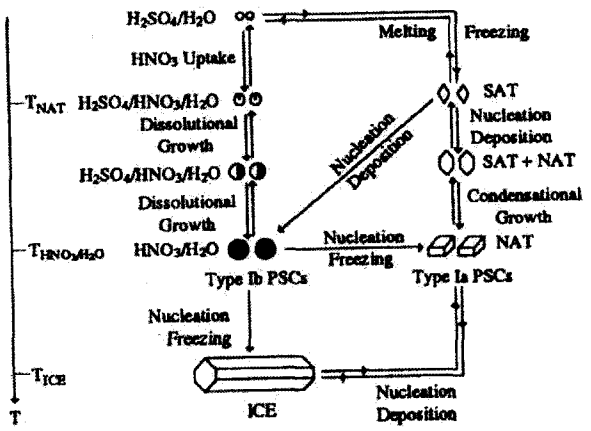

Figure 1.6 Model for Type I PSC formation.
After *Tabazadeh et al.* (1994), a model for PSC Type I PSC formation. Temperature decreases from top to bottom along the vertical axis (left). Approximate temperatures for the condensation/frost points for NAT (195-197 K), HNO_3 (191-193 K) and ice (188-190 K) are used. Arrows pointing upward indicate evaporation.

temperatures well below that of saturation with respect to NAT. Ternary solution mixtures of H_2SO_4-HNO_3-H_2O had been hypothesized as an intermediate PSC growth stage (*Crutzen et al.*, 1988). Laboratory measurements of large HNO_3 uptake in ternary solutions were reported by *Zhang et al.* (1993). Model analyses by *Carslaw et al.* (1994), *Drdla et al.* (1994) and *Tabazadeh et al.* (1994) showed that many of these inconsistencies could be reconciled by assuming the presence of ternary solution droplets. A reexamination of AAOE data showed that particle infrared spectra were more likely that of ternary solution droplets than nitric acid hydrates (*Toon and Tolbert*, 1995). Laboratory measurements showed that ternary solution droplets do not readily freeze, though *Crutzen et al.* (1988) suggested that a requirement for solid NAT growth was a frozen embryonic sulfate particle. *Turco et al.* (1989) described the heterogeneous

nucleation of frozen sulfate particles and subsequent vapor deposition growth of NAT as a means for Type Ia PSC growth. Measurements reported by *Larsen et al.* (1995; 1996) confirmed their occurrence.

A model for PSC growth described by *Tabazadeh et al.* (1994) is shown in Fig. 1.6. They suggested two pathways to PSC growth for Type I particles, each being a function of the phase of the embryonic sulfate particle. Ternary solutions and dissolutional growth are described along the liquid-phase path, whereas deposition and condensational growth represent stages of solid-phase particle growth from the thermodynamically stable phase of H_2SO_4, sulfuric acid tetrahydrate (SAT; *Gable et al.*, 1950), into NAT. Type II PSC nucleation would occur after continued cooling of either variety of Type I particle. Although subsequent laboratory and field measurements provided evidence that from the saturation of solution droplets with respect to ice required to overcome nucleation barriers the corresponding nucleating temperature would be depressed relative to the frost point on the order of a 2-3 K (*Carslaw et al.*, 1998a; *Koop et al.*, 2000). Measurements of SAT formation, HNO_3 uptake in the melting phase and subsequent refreezing under laboratory conditions were described by *Iraci et al.* (1998). *Marti and Mauersberger* (1993) showed that if vapor containing stratospheric molar ratios of HNO_3 to H_2O are cooled to near 192 K a hydrate or solution with high H_2O to HNO_3 ratios form. *Tabazadeh et al.* (1994) suggested the formation of such solutions on sulfate ice particles as an alternate means for Type Ib nucleation aside from condensational growth, and that such processes would be highly selective resulting in a relatively low concentration of large particles.

A third sub-classification was proposed by *Tabazadeh et al.* (1996; Type Ic) to describe small nonspherical particles consisting of metastable HNO_3/H_2O solid phases (*Fox et al.*, 1995; *Tabazadeh and Toon*, 1996) that are not described in Fig 1.6 and were thought likely to be the first solid phase Type I particle that forms upon cooling. From Upper Atmospheric Research Satellite (UARS) measurements *Massie et al.* (1997) and *Santee et al.* (1998) indicated that early season PSC properties were more consistent with the appearance of ternary solutions followed by formation of the metastable nitric acid dehydrate (NAD) rather than NAT, as predicted by *Worsnop et al.* (1993) and *Fox et al.* (1995). *MacKenzie et al.* (1995), *Drdla et al.* (1994) and observations by *Murphy et al.* (1998) described trace impurities (i.e., meteoric residue, organics and soot) in stratospheric particles that may influence freezing. Following ground-based lidar observations from South Pole Station reported by *Collins et al.* (1993), *Gobbi et al.*, (1998) grouped backscatter ratios (defined as the ratio between measured backscatter and that attributed to the molecular component of the background atmosphere), depolarization and volume concentration measurements collected with a 0.532 μm lidar at McMurdo Station, Antarctica (77.8° S, 166.7° E) into seven categories for phase and composition. The first two parameters are shown in Table 1.3. Their data further supported the presence of metastable hydrate solids such as NAD as opposed to NAT. Their constraints on backscatter ratio will be referred to in future chapters. Nucleation rate constants and freezing mechanisms for NAD and NAT described by *Bertram and Sloan* (1998a, b) showed NAD nucleation to be favorable at stratospheric conditions, whereas the freezing of NAT through homogeneous nucleation was unlikely.

Table 1.3 Seven distinct classes of PSC.
After *Gobbi et al.* (1998), seven classes of PSC particles, as measured by lidar from McMurdo Station, Antarctica during winter 1995. R refers to the backscatter ratio at 0.532 μm, and D the linear depolarization ratio. MSP denotes metastable phases associated with nitric acid condensate referred to in the text.

Class	R_{min}	R_{max}	D_{min} %	D_{max} %	Phase Dominating
0	1.0	1.2	0	2	Liquid sulfate background
1	1.0	1.2	2	20	Liquid and frozen sulfates
2	1.2	...	2	...	Mixed phase ternary solutions+HNO_3-MSP/NAT
3	1.2	...	...	2	Ternary solutions
4	1.2	...	2	...	Solid phase NAT/ HNO_3-MSP
5	1.2	...	2	...	Mixed phase ice and ternary solutions
6	1.2	...	2	...	Ice

The role of denitrification in ozone loss is well-known. However, the process is a complex function of PSC nucleation and growth mechanisms (e.g., *Solomon*, 1990; *Toon et al.*, 1990). Sedimenting PSC particles may irreversibly remove HNO_3 (the principal reactive stratospheric nitrogen-based species, of which NO, NO_2, N_2O_5 and $ClONO_2$ are also important) and water from the nucleating regions. Denitrification suppresses the stable partitioning of reactive chlorine and bromine molecules, as illustrated by Reaction R14 (Table 1.2), which is the termination step in the example of catalytic ozone destruction by nitrogen and hydrogen oxides. It is still not understood what conditions favor the growth of a few large particles at the expense of, or in spite of large numbers of smaller ones, what the primary composition is of such particles, or how these conditions vary over the polar night with respect to geographic location and air mass trajectory and

Table 1.4 Spherical particle fall-velocities in lower-stratosphere.
From *Kasten* (1968), falling velocities (m sec^{-1}) of spherical particles of given radii and mass density 1.0 gm cm^{-3} in the 1962 U. S. Standard Atmosphere at 15.0, 20.0 and 25.0 km MSL.

Height MSL (km)	0.01 μm	0.10 μm	1.00 μm	10.00 μm
15.0	1.07×10^{-6}	1.16×10^{-5}	2.35×10^{-4}	1.61×10^{-2}
20.0	2.33×10^{-6}	2.42×10^{-5}	3.49×10^{-4}	1.70×10^{-2}
25.0	5.06×10^{-6}	5.15×10^{-5}	6.10×10^{-4}	1.87×10^{-2}

thermodynamic history. In Table 1.4 are fall-velocities for spherical particles of given radius and a mass density of 1.0 gm cm^{-3} in a standard atmosphere at 15.0, 20.0 and 25.0 km MSL based on the Stokes friction law modified by the Cunningham-Millikan correction (*Kasten*, 1968). Values vary over four orders of magnitude, with those at 10.0 μm exceeding 1.0 km day^{-1}.

Denitrification is not a required process for catalytic ozone destruction, but instead enhances it. Heterogeneous chlorine activation may occur on PSC surfaces in the presence of sunlight irregardless of denitrification (*Portmann et al.*, 1996; *Chipperfield and Pyle*, 1998). Supporting evidence for denitrification, however, is abundant from over both poles (e.g., *Gobbi et al*, 1991; *Solomon,* 1999; *Waibel et al.*, 1999; *Kondo et al.*, 2000), though denitrification and dehydration may occur regionally exclusive of one another depending on temperature and the dominant PSC growth mechanism of the air mass (e.g., *Fahey et al.*, 1990). Measurements from the Antarctic indicate that denitrification occurs before dehydration (*Tabazadeh et al,* 2000; *Santee et al.*, 1995). Recent reports of Antarctic denitrification and dehydration have come from Microwave

Limb Sounding (*Santee et al.*, 2005; *Waters et al.*, 2006) measurements made aboard the Earth Observing System Aura satellite (*Schoeberl et al.*, 2004).

Ongoing research into PSC composition, nucleating and growth mechanisms over the past ten years has focused on characterizing denitrification (*Tabazadeh et al.*, 2001). *Fahey et al.* (2001) reported a previously unknown class of large nitric acid-containing particles with diameters of 10.0 to 20.0 μm that would sediment and denitrify. They were unable to address the nucleation process responsible, but were able to model their growth and eventual fall using NAT. However, *Knopf et al.* (2002) argued that homogeneous nucleation rates derived from in-situ measurements in the Arctic for NAD and NAT from ternary solution and hydrate aerosols are insufficient to explain PSC number densities of large nitric acid particles required for denitrification.

Tabazadeh et al. (2000; 2001) showed that continued stratospheric cooling in the Arctic (*Ramaswammy et al.*, 2001) of 4.0 K would trigger widespread denitrification that could enhance future ozone loss there by up to 30%. *Tabazadeh et al.* (2001) also theorized the existence of a "polar belt" for conditions optimized to NAD growth relative to NA, and particle sedimentation as a function of nucleation rates versus temperature and thermal history. However, their study considers only the airmass that reaches the optimal NAD nucleation temperatures without further cooling. This scenario does not take into account the case where trajectories continue to cool beyond the ice frost point, similar to what is observed near South Pole from June through August. Nor do they consider the impact these embryonic species may have on ice nucleation and sedimentation of water mass (e.g., *Pruppacher and Klett*, 1997).

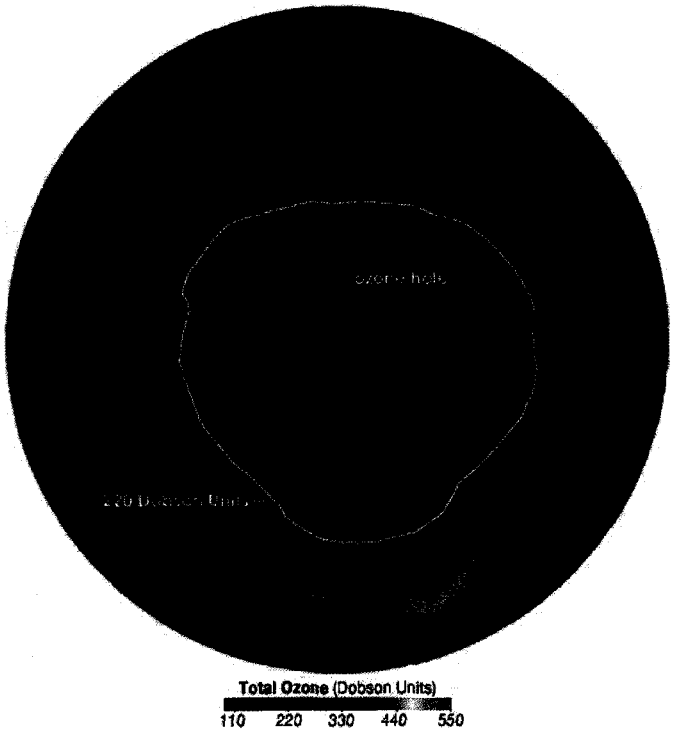

Figure 1.7 OMI composite ozone concentrations.
Example of ozone Monitoring Instrument measurements of total ozone over the austral pole in Dobson units (DU). The ozone hole is considered present for the airmass containing less than 220 DU, denoted in the figure by the white contour.

1.4 Halogen-based Catalytic Ozone Loss and the Antarctic Ozone Hole

Well before the discovery of the ozone hole, models for stratospheric ozone destruction involving halogenated (i.e., chlorine and bromine) aliphatic hydrocarbons (halocarbons) were proposed (e.g., *Stolarski and Cicerone*, 1974; *Wofsy et al.*, 1975). Anthropogenic halocarbons accumulate in the troposphere, where they are relatively inert, and gradually migrate into the stratosphere. There reactive sub-species are activated both photochemically, and heterogeneously on PSC particle surfaces where

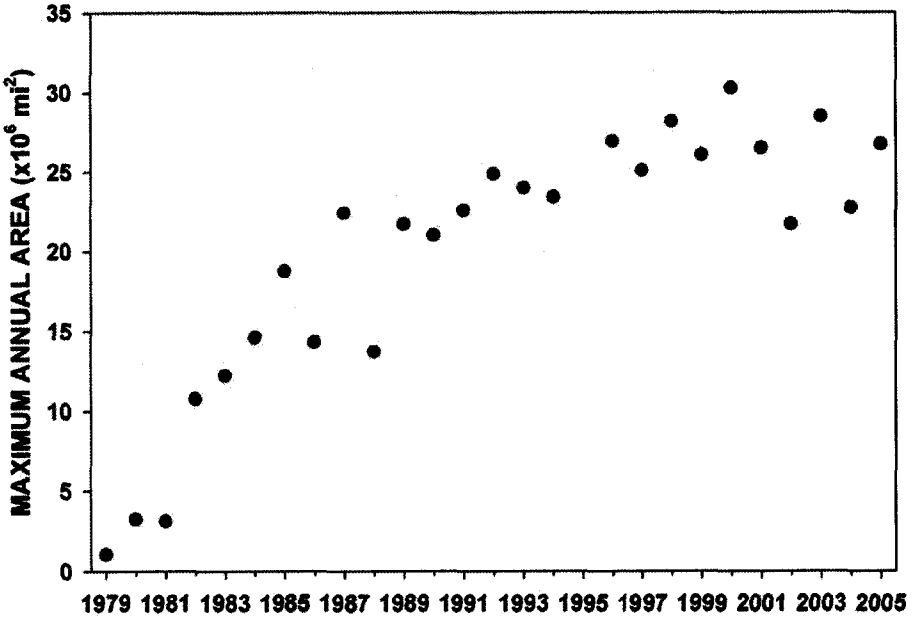

Figure 1.8 Annual maximum austral ozone hole area.
Annual maximum austral ozone hole area (km^2) from 1979-1995 determined from satellite measurements of ozone concentration for a Dobson Unit threshold of 220 DU.

they may then react with ozone. *Solomon* (1999) provides an extensive summary of measurements of stratospheric ozone loss, the relevant chemical processes and a history of relevant research.

The ozone hole was first confirmed by *Farman et al.* (1985) from comparing spectrometer measurements of ozone at two British research stations along the Antarctic coastline during 1980-1984 to historical records. *Stolarski et al.* (1986) then described the spatial extent of abnormally low ozone concentrations over the austral pole in terms of Dobson units (1 DU = 10^{-3} atm cm) from satellite spectrometer measurements. The feature first forms in August, peaks from late September to early October, and dissipates most typically in December. An example of Ozone Monitoring Instrument (OMI; *Levelt*

et al., 2006) data depicting the ozone hole is shown in Fig. 1.7[1], where the outer boundary of the ozone hole is designated by the 220 DU contour. In this example the hole is seen to cover nearly the entire Antarctic continent. In Fig. 1.8 are annual values for the maximum area for the Antarctic ozone hole calculated from satellite measurements[2]. These values increase rapidly in the middle 1980s, reaching just under 25.0 million km^2 by 1992. In recent years the values have varied about this approximate number. The maximum area value reached just over 30.0 million km^2 in 2000. Relatively low values, nearing 20.0 million km^2 were observed in 2002 and 2004. In 2002, anomalous stratospheric warming induced by unusually large Rossby wave activity occurred, and the ozone hole split into two vortices in September (*Hoppel et al.*, 2003). Each season will be discussed more in depth in future chapters.

Activating reactive chlorine and bromine-based molecules from PSC surfaces begins as a function of the uptake of their inert gas-phase species. Heterogeneous conversion is then a function of the composition and phase of PSC combined with ambient temperature, pressure and water vapor abundance (*Tolbert et al.*, 1988; *Ravishankara and Hanson*, 1996; *Carslaw and Peter*, 1997, *Carslaw et al.*, 1997a, *Carslaw et al.*, 1997b). The process is most efficient with ice surfaces. The primary heterogeneous reaction for chlorine is

$$HCl + ClONO_2 \rightarrow Cl_2 + HNO_3 \qquad \textbf{(R16)}$$

[1] Data posted at http://ozonewatch.gsfc.nasa.gov; P. A Newman, NASA/Goddard Space Flight Center, Responsible Official.
[2] Data posted at http://www.theozonehole.com as calculated by R. McPeters, NASA/Goddard Space Flight Center.

Table 1.5 The industrial chlorofluorocarbons.
Industrial chlorofluorocarbons found in the atmosphere, designated by technical classification, name, molecular composition, residence time (years) and contribution to total atmospheric chlorine, after *Prather and Watson.* (1990).

Class	Name	Molecule	Res. Time (yr)	Atmos. %
CFC-11	Trichlorotrifluoromethane	CCl_3F	60	22
CFC-12	Dichlorodifluoromethane	CCl_2F_2	120	25
CFC-113	Trichlorotrifluoroethane	$C_2Cl_3F_3$	90	3
CFC-114	Dichlorotetrafluoroethane	$C_2Cl_2F_4$	200	< 1
CFC-115	Chloropentafluoroethane	C_2ClF_5	400	< 1

For bromine both

$$BrONO_2 + HCl \rightarrow BrCl + HNO_3 \quad \textbf{(R17)}$$

$$BrONO_2 + H_2O \rightarrow HOBr + HNO_3 \quad \textbf{(R18)}$$

are important (*Peter*, 1997). Photolysis readily breaks both the BrCl and HoBr molecular bonds into their atomic components. R17 requires high solubility of HCl, found for temperatures less than 200 K. R18 is efficient at all temperatures. Heterogeneous processes are mostly efficient over all types of PSC at temperatures below ~ 198 K near 20 km. Water ice has been measured to be highly reactive (*Jet Propulsion Laboratory*, 1997). For liquid solutions the efficiency of the reaction is a function of the water mole fraction and inversely a function of sulfuric acid concentration (e.g., *Hanson et al.*, 1994),

Table 1.6 Catalytic ozone destruction cycles of chlorine.
Examples for catalytic ozone destruction cycles involving chlorine (R19-R20 and R19-R23 sequentially), after *Stolarski and Cicerone* (1974) and *Molina and Molina* (1987).

$$Cl + O_3 \rightarrow ClO + O_2 \quad \textbf{(R19)}$$

$$ClO + O \rightarrow Cl + O_2 \quad \textbf{(R20)}$$

$$Cl + O_3 \rightarrow ClO + O_2 \quad \textbf{(R19)}$$

$$Cl + O_3 \rightarrow ClO + O_2 \quad \textbf{(R19)}$$

$$ClO + ClO + M \rightarrow Cl_2O_2 + M \quad \textbf{(R21)}$$

$$Cl_2O_2 + hv \rightarrow Cl + ClO_2 \quad \textbf{(R22)}$$

$$ClO_2 + M \rightarrow Cl + O_2 + M \quad \textbf{(R23)}$$

though they are more effective than Type Ia and c PSC at temperatures below 195 K (*Ravishankara and Hanson*, 1996).

Anthropogenic chlorofluorocarbons (CFCs; originally named chlorofluoromethanes in the literature, since their formation comes from the substitution of chlorine and fluorine for the hydrogen atoms found in methane, CH_4) were predicted as primary sources for stratospheric chlorine due to a widespread abundance and long atmospheric residence times (*Crutzen*, 1974; *Lovelock*, 1974; *Molina and Rowland*, 1974; *Rowland and Molina*, 1975). CFC-related ozone destruction was predicted to exceed the natural sinks discussed earlier for many decades beginning from the middle to late 1980s (*Cicerone et al.*, 1974). CFCs were developed as non-toxic and non-flammable gases for industrial use in refrigerators. Their acknowledged role in ozone destruction and the subsequent identification of the Antarctic ozone hole (*Farman et al.*, 1985; *Solomon et al.*, 1986) led to the 1987 Montreal Protocol agreed to by 27 nations to reduce production levels by 50% before the year 2000 (*United Nations Environmental Programme*, 1987).

The Copenhagen Amendment, agreed upon in 1992, limited production even further (*United Nations Environmental Programme*, 2001). By the beginning of 1996 their production had practically ceased, though their release into the atmosphere continues from the delay between production and actual emission (e.g., *Prather and Watson*, 1990). Growth rates in CFC concentrations were observed to be flattening out by the middle 1990s in response (*Elkins et al.*, 1993). Alternative gases were developed to replace CFCs, including hydrochlorofluorocarbons (HCFCs) and hydrofluorocarbons (HFCs; *Prather and Watson*, 1990). While their production still yields atmospheric chlorine, molecular residence times are approximately an order of magnitude less than CFCs. Ironically, both compound groups contribute significantly to greenhouse warming (e.g., *Prather and Wilson.*, 1990). The Copenhagen Amendment calls for total redundancy of these gases by the year 2030. A list of the most important CFCs, including their name, composition, residence time and contribution to total atmospheric chlorine is given in Table 1.5.

Total lower-stratospheric chlorine concentrations in the early 1990's were measured to be approximately 3.0 ppbv, of which only about 20% could be attributed to natural sources (e.g., *Schauffler et al.*, 1993). A century previous the total value was 0.6 ppbv, and only 2.0 ppbv in the late 1970s when the ozone hole was first found to be present (*Farman et al.*, 1985). Two examples for chlorine-based catalytic ozone loss cycles are listed sequentially in Table 1.6. The first and most basic case (R19-R20) shows a chlorine atom reacting with an ozone molecule to yield ClO and oxygen. The ClO molecule then reacts with atomic oxygen (as seen produced through photolysis from R1

and R5, among other potential mechanisms) to release the chlorine atom. The sum of these reactions is R7. In the second example two ozone molecules are destroyed via R19 producing two ClO molecules. These then combine to yield Cl_2O_2 (R21). Subsequent reactions (R22-R23), one involving photolysis, release the two bound chlorine atoms. The sum of this cycle is R15. The amount of Cl and ClO available to participate in such chains depends on the partitioning of chlorine in reactive states versus neutral ones (e.g., *Solomon*, 1999). Elevated ClO concentrations in the ozone hole region have been measured and modeled (*De Zafra et al*, 1987, 1989; *Anderson et al.*, 1989; *Jones et al.*, 1989) as a result of chlorine release from reservoir gases. Peak values on the order of 1.0 ppbv have been measured near 20.0 km MSL. Important neutralizing reactions for chlorine are

$$Cl + CH_4 + \rightarrow HCl + CH_3 \qquad \textbf{(R24)}$$

$$HO_2 + ClO \rightarrow HOCl + O_2 \qquad \textbf{(R25)}$$

$$ClO + NO_2 + M \rightarrow ClONO_2 + M \qquad \textbf{(R26)}$$

$$OH + NO_2 + M \rightarrow HNO_3 + M \qquad \textbf{(R27)}$$

where HCl and $ClONO_2$ are primary reservoir species (e.g., *Stolarski and Cicerone*, 1974; *Rowland et al.*, 1976).

Though found in lower concentrations, bromine is more efficient than chlorine when catalytically destroying ozone. Total concentrations were measured in the early 1990s to be approximately 0.2 ppbv (*Prather and Watson*, 1990). Neutralizing reactions common

Table 1.7 Catalytic ozone destruction cycles of chlorine/bromine.
A model for chlorine-bromine catalytic destruction of ozone, after *McElroy et al.* (1986b).

$$Cl + O_3 \rightarrow ClO + O_2 \quad \textbf{(R28)}$$

$$Br + O_3 \rightarrow BrO + O_2 \quad \textbf{(R29)}$$

$$BrO + ClO \rightarrow Br + ClO_2 \quad \textbf{(R30)}$$

$$ClO_2 + M \rightarrow Cl + O_2 + M \quad \textbf{(R31)}$$

for chlorine are not as efficient for bromine, resulting in longer catalytic chains. For example, R22 neutralizes chlorine atoms through reaction with methane. However, the corollary reaction involving bromine is endothermic (*Wofsy et al.*, 1975). Still, the relative catalytic efficiency between the two species is ultimately dependent on the amount of reactive chlorine available due to chemical coupling between them (*Pyle et al.*, 1992). A model for the chlorine-bromine catalytic cycle based on *McElroy et al.* (1986b) describing this interrelation is shown in Table 1.7. In this cycle, bromine oxide reacts with chlorine oxide to reform the radical bromine atom. However, this reaction rate is dependent upon those for R17 and R20, among others. The net sum of this cycle is equal to R15, or two ozone molecules for three oxygen ones. A higher fraction of bromine species exist in reactive forms (*Peter*, 1997). The key reservoir reactions for bromine are

$$BrO + NO_2 + M \rightarrow BrONO_2 + M \quad \textbf{(R32)}$$

$$BrO + NO_2 \rightarrow HOBr + O_2 \quad \textbf{(R33)}$$

However, as was the case for the example of heterogeneous activation of bromine, $BrONO_2$ and HOBr are easily photolyzed, leaving most commonly a reactive molecule (i.e., Br or BrO) rather than a neutral one. From R26, R27, R32 and R33, reaction with NO_2 yielded stable reservoir species. This highlights the significance of denitrified air in enhancing catalytic ozone loss for these reactions cannot readily occur to stop the cycles. Studies of the 1987 Antarctic ozone hole produced estimates that as much as 30% of total depletion could be attributed to bromine (*Anderson et al.*, 1989; *Ko et al.*, 1989) with the remainder due to chlorine.

CHAPTER 2

MICROPULSE LIDAR MEASUREMENTS AT SOUTH POLE STATION 1999-2005: INSTRUMENTS, A PSC DATA SUBSET, PARTICULATE LAYER DETECTION ALGORITHM AND PROCESSED DATASETS

Micropulse Lidar (MPL) was developed in 1992 at the National Aeronautics and Space Administration (NASA) Goddard Space Flight Center (GSFC; *Spinhirne*, 1993) as a by-product of research into space-borne and eye-safe lidar techniques. MPL represented a then newly-emerging generation of lidar instruments made possible by advances in solid-state diode-pumped lasers and the introduction of high-efficiency quantum noise-limited photon-counting devices. Traditional lidars are typically large systems bound to laboratories or crafted into robust mobile containers (e.g., *Sassen*, 1991). Practicality, costs and a maintenance-intensive nature have limited widespread lidar usage (e.g., *Sassen*, 1995). The technique has more traditionally been applied to episodic measurement campaigns with focused research initiative. In developing what would become the Geoscience Laser Altimeter System (GLAS; *Spinhirne et al.*, 2005), launched aboard the NASA Earth Observing System (EOS) Ice, Cloud and land Elevation Satellite (ICESat) in January 2003, a practical instrument design was needed that was flight-sensible and unaffected by common safety considerations associated with laser sources. Eye-safety enabled autonomous and full-time instrument operation, and in turn created the potential for data accumulation consistent with long-term climate study.

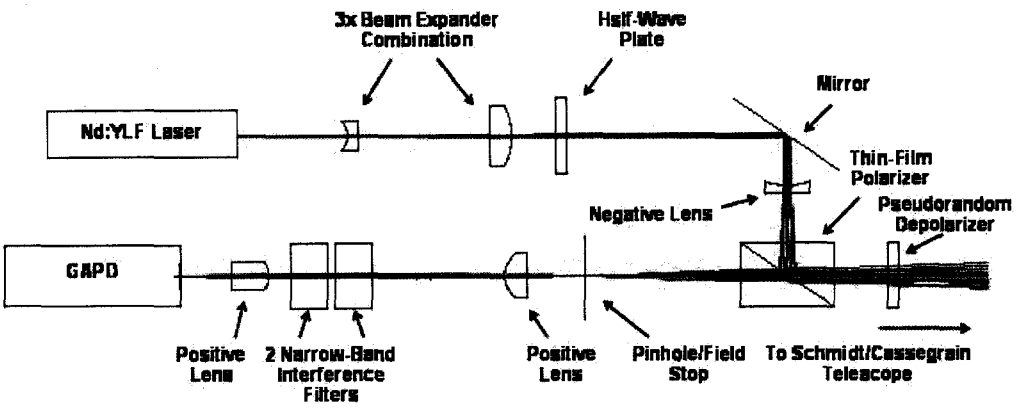

Figure 2.1 Optical design for the micropulse lidar.

MPL instruments detect nearly all significant tropospheric and lower-stratospheric cloud and aerosol, to the limit of signal attenuation, through pulse summation and geometric signal compression (*Spinhirne et al.*, 1995). An example of the MPL optical design is shown in Fig. 2.1. Although multiple versions of the optical layout of the instrument exist (*Campbell et al.*, 2002) this design is most relevant. The MPL features a linearly polarized, low-energy and high-repetition Nd:YLF source (2500 Hz; 0.523 μm). Dual optical paths separate incoming and outgoing energy propagation. Along the outgoing path a source pulse is expanded, rotated to the orthogonal polarization plane and turned by a mirror to a negative lens whose focal point is aligned to that of the telescope just upstream. A thin-film polarizer acts as the junction between the outgoing laser and incoming path. The pulse is turned by this piece toward a pseudorandom depolarizer and then expanded through the 0.20 m Schmidt-Cassegrain transmitter/receiver (transceiver) telescope. Outgoing pulse energies are between 5 and 10 μj, which is less than 40% of the quoted 25 μj ANSI eye-safety limit for a 0.20 m aperture source at 2500 Hz.

Received energy incident upon the telescope first passes through the pseudorandom depolarizer. Along the incoming path the thin-film polarizer rejects energy in the orthogonal polarization state and redirects it back toward the laser. The remaining energy passes through the polarizer and is focused to a 200 μm pinhole. The pinhole acts as a field-stop. Combined with the focal length of the telescope (2.0 m) this yields a field-of-view of approximately 100 μrad. A positive lens collimates the light focused at the pinhole. It then passes through two narrow interference filters (approx. 1.2-Å combined spectral width). Combined these filters and the narrow field-of-view limit the effects of background light and the ambiguities of multiple scattering (e.g., *Eloranta*, 1998). A final positive lens focuses the light to a solid-state Geiger mode avalanche photo-diode with a 100 μm active area diameter. Quantum efficiencies approach 70% with 20 MHz maximum signal acquisition rate. Detector saturation is rare. Instruments have been demonstrated to run without major mechanical failure for as long as three years. Modifications to the laser diode controller and fiber-coupling of the detector improve performance by making on-site repair more practical.

The MPL Network (MPLNET; http://mplnet.gsfc.nasa.gov) is a federated group of MPL instruments deployed worldwide in support of basic science and the EOS program (*Welton et al.*, 2001). MPLNET is coordinated at GSFC in cooperation with the Aerosol Robotic Network (AERONET; *Holben et al.*, 1998) and project sites feature a co-located CIMEL Electronique Sun-photometer. MPLNET serves as a central repository for long-term MPL datasets of aerosol and cloud observations. Algorithms have been created that process raw data into quantitative cloud and aerosol products, such as layer heights,

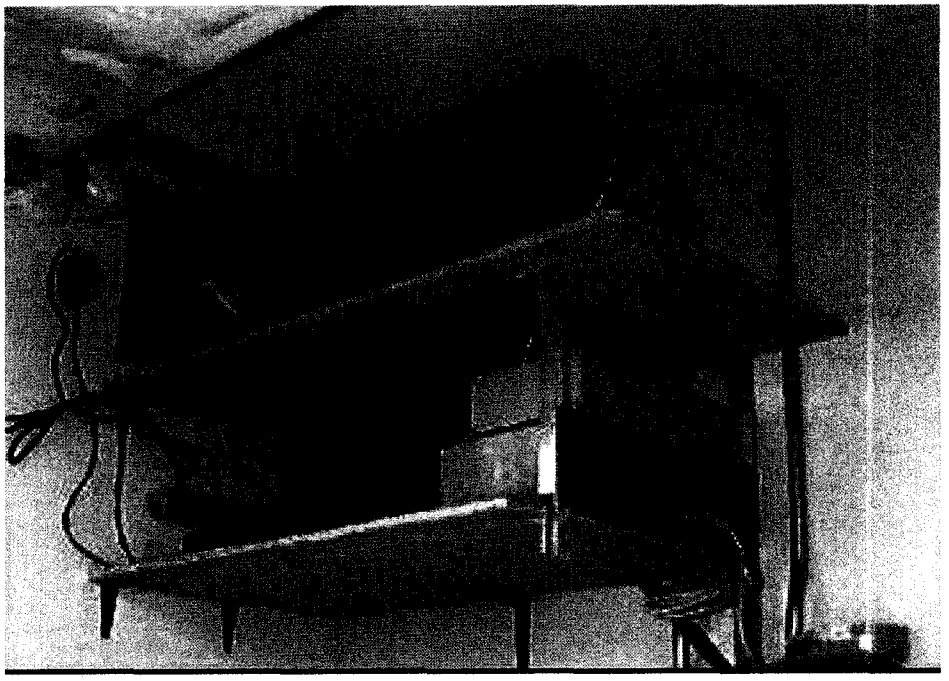

Figure 2.2 The South Pole MPL.
The transceiver is on the top shelf pointed at the 90° turning mirror. The laptop computer, laser power supply and scalar control unit are on bottom shelf.

optical depths and backscatter and extinction cross-section profiles. MPLNET results have contributed to studies of dust, biomass burning, marine and continental aerosol properties, aerosol transport processes, polar clouds and blowing snow. Datasets are also used in validation studies for NASA satellites including GLAS, Multi-angle Imaging Spectral Radiometer (MISR) and Total Ozone Mapping Interferometer (MISR). Agreements are in place with many governmental organizations. This includes the National Oceanic and Atmospheric Administration (NOAA) Earth Surface Research Laboratory (ESRL) that operates an MPL at its Atmospheric Research Observatory (ARO) at the Scott-Amundsen South Pole Station (90.00° S; 2.835 km MSL).

2.1 The South Pole MPL Project

An MPL was first deployed to the NOAA ARO facility in December 1999. This instrument is shown in Fig 2.2. The transceiver/optics unit is seen resting upon the upper shelf. The laser diode and data-acquisition controllers are mounted along the right side of the bottom shelf. A Microsoft Windows-based personal computer (PC) maintaining the MPL and all internet communications (i.e., data transfer) is seen on the right side of the bottom shelf. The combined package volume is less than 1.0 m^3. Due to logistics at South Pole, the instrument was installed pointing horizontally toward a support wall. A window was built into the wall with a mounted scanning 90° turning-mirror. The transceiver is aligned at 45° relative to the mirror. The PC operates the scanning apparatus. Three MPL instruments have been operated at South Pole through December 2005. An instrument timeline with data collection periods is shown in Fig 2.3. Significant data gaps ($\geq$ 10 days) are displayed. The MPL51 experienced a detector failure in September 2000. A compromise to the scanner assembly occurred in winter 2001 ending the deployment of MPL65. MPL70 was installed in spring 2001 and was first to feature a fiber-coupled detector assembly. After a laser diode failed in winter 2002 a reset team was dispatched to modify the diode controller so as to allow for onsite diode replacements. This instrument remains in operation.

Data from South Pole are recorded and processed at 60 s temporal and 0.030 km vertical resolution. Processed data is available via download from the MPLNET website. An input file determines the viewing-angle of the scanner over the course of a full day. This angle is recorded in a log-file and later integrated into processed files. Null values

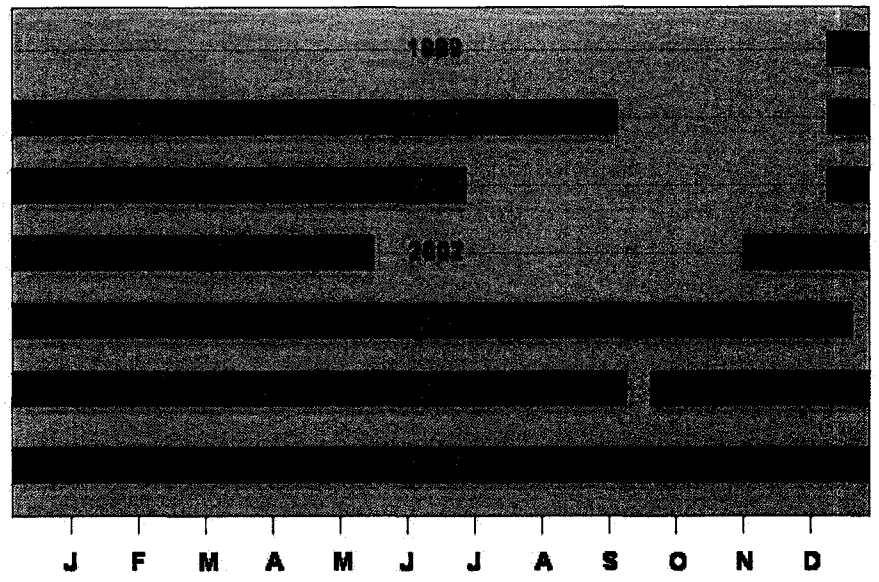

Figure 2.3 The South Pole MPL operational timeline.
Instrument numbers are listed on the right, corresponding with the year of their initial deployment.

are used for "shots" during which the scanner was moving during the sampling period so as to be rejected for analysis. While the scanner position most commonly is set to zenith nadir "tips" occur multiple times daily to relieve snow accumulation from the exterior window face. These scans take no more than three minutes. Low-angle scans along the horizon are conducted daily to collect data that aid instrument calibrations, measure blowing-snow layer depths (*Mahesh et al.*, 2003) and accommodate slant-path retrievals for cloud extinction cross-section profiles (*Spinhirne et al.*, 1980). These scans occur near the end of the day beginning from fractional day 0.87. They have last variable times, though never longer than 0.05 fractional days. From early 2002 ± 5.0° scans about zenith were conducted to study changes in the backscatter cross-section from horizontally-aligned ice crystals (*Sassen*, 1991).

2.2 MPL Normalized Relative Backscatter and Uncertainty Analysis

Processed MPLNET data files contain a normalized relative backscatter product (NRB; *Campbell et al.*, 2002). Their algorithm describes processing photon count-rates to uncalibrated attenuated backscatter after accounting for instrument calibration terms. Based on the lidar equation, they describe raw MPL count rates in the form

$$n(r') = \frac{\frac{\left(O_c(r')CE\beta(r')T(r')^2\right)}{r'^2} + n_b + n_{ap}(r', E)}{D[n(r')]} \tag{2.1}$$

where n is photo-electron counts per second at range r', O_c is the optical overlap correction as a function of range (the result of field-of-view conflicts in the transceiver system), C represents a dimensional calibration constant, E is the laser-transmitted pulse energy, β is the backscatter cross section from all types of atmospheric scattering, T is atmospheric transmittance, n_b is background contribution of ambient light, n_{ap} is the contribution from afterpulse (cross-talk caused by the laser pulse, of which it is also a function of), and D is the detector photon-coincidence 'deadtime' factor as a function of raw count rate. Range is written in Eq. (2.1) in an intermediate initial form, r', to account for the sum of two offsets (Δr_o) such that

$$r = r' - \Delta r_o \tag{2.2}$$

where r is the true range. One portion of this offset results from the software recording-range being the temporal distance to the end of a sampling bin. A subtraction equal to half of the spatial resolution centers the range relative to the bin width. The second portion of the offset accounts for a timing inaccuracy between the laser pulse and the scalar trigger that starts detector sampling. For each of the South Pole instruments the trigger occurs before the laser fires. The correction is approximately two range bins, or 0.060 km (400 ns). NRB is derived by accounting for Eq. (2.2) in Eq. (2.1), moving the correction terms to the left side, and solving for attenuated backscatter cross-section ($\beta(r)T^2(r)$) times the calibration constant (C).

$$\frac{\left[\left[n(r) * D[n(r)]\right] - n_{ap}(r,E) - n_b\right] r^2}{O_c(r)E} = C\beta(r)T(r)^2 \qquad \textbf{(2.3)}$$

The units for NRB are (photoelectrons·km^2)/(μsec·μj). The NRB algorithm, correction terms, and calibration techniques are described by *Campbell et al.* (2002).

Welton and Campbell (2002) describe the algorithm for uncertainty analysis of Eq. (2.3). Knowledge of the uncertainty in NRB helps to characterize the level of noise relative to signal strength in the MPL profile. NRB uncertainties will be used to derive particulate layer boundaries from South Pole data below. Using Poisson statistics they rewrite Eq. (2.3) as

$$\delta NRB(r) = NRB(r)\sqrt{\frac{[\delta P(r)]^2 + [\delta n_b]^2 + [\delta n_{ap}(r,E)]^2}{[P(r) - n_b - n_{ap}(r,E)]^2} + \left[\frac{\delta E}{E}\right]^2 + \left[\frac{\delta O_c(r)}{O_c(r)}\right]^2} \quad \textbf{(2.4)}$$

where

$$\delta P(r) = \sqrt{\frac{[n(r) * D[n(r)]]}{N}} \quad \textbf{(2.5)}$$

and

$$\eta(r) = \frac{\delta NRB(r)}{NRB(r)} \quad \textbf{(2.6)}$$

In Eq. 2.5 N refers to the total number of laser pulses per shot. For South Pole NRB files 60-s resolution represents the summation of 150,000 pulses at 2500 Hz. Uncertainty in the deadtime correction is not considered as its magnitude is not significant at count-rates commonly measured with the MPL. In Eq. (2.6) η(r) is the fractional uncertainty in NRB as a function of range. The inverse of η(r) is the signal-to-noise ratio (SNR).

2.3 South Pole MPL PSC Data Subset

As discussed in Chapter 1, PSC are common in the southern hemisphere between May and September. From Fig. 1.3a the coldest temperatures in the lower-stratosphere occur between May and early October. These six months serve as the period of focus in

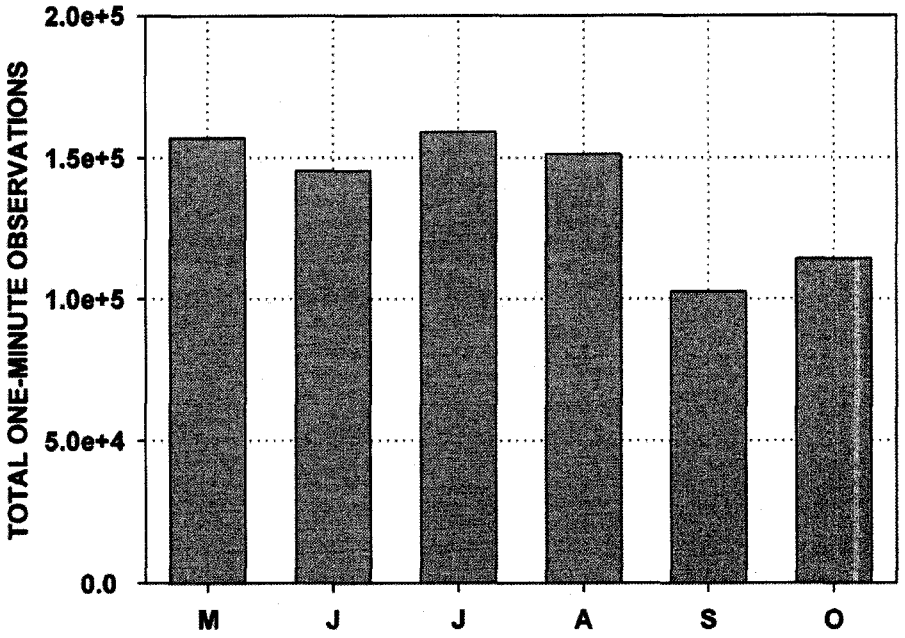

Figure 2.4 Monthly subset data breakdown.
Total one-minute observations for South Pole MPL PSC Data Subset by month for May – October.

this study. From Fig 2.3 there are three years where MPL data are available for this entire period: 2003, 2004 and 2005. In 2000 data were collected through 2 September. Though truncated much of that PSC season is captured and the data were included in this study. Data from 2001 and 2002 were eliminated from lack of data. Approximately 830,000 one-minute shots are included in the subset. Figure 2.4 is a breakdown of these observations by month. Low totals from September and October represent missing data from 2001 and 2004 (Fig. 2.3).

Figures 2.5a-d are concatenated images of MPL NRB (top) and NRB fractional uncertainty (bottom) from South Pole between May and October for 2000, 2003, 2004 and 2005, respectively. The images were constructed using 1009 vertical lines for the

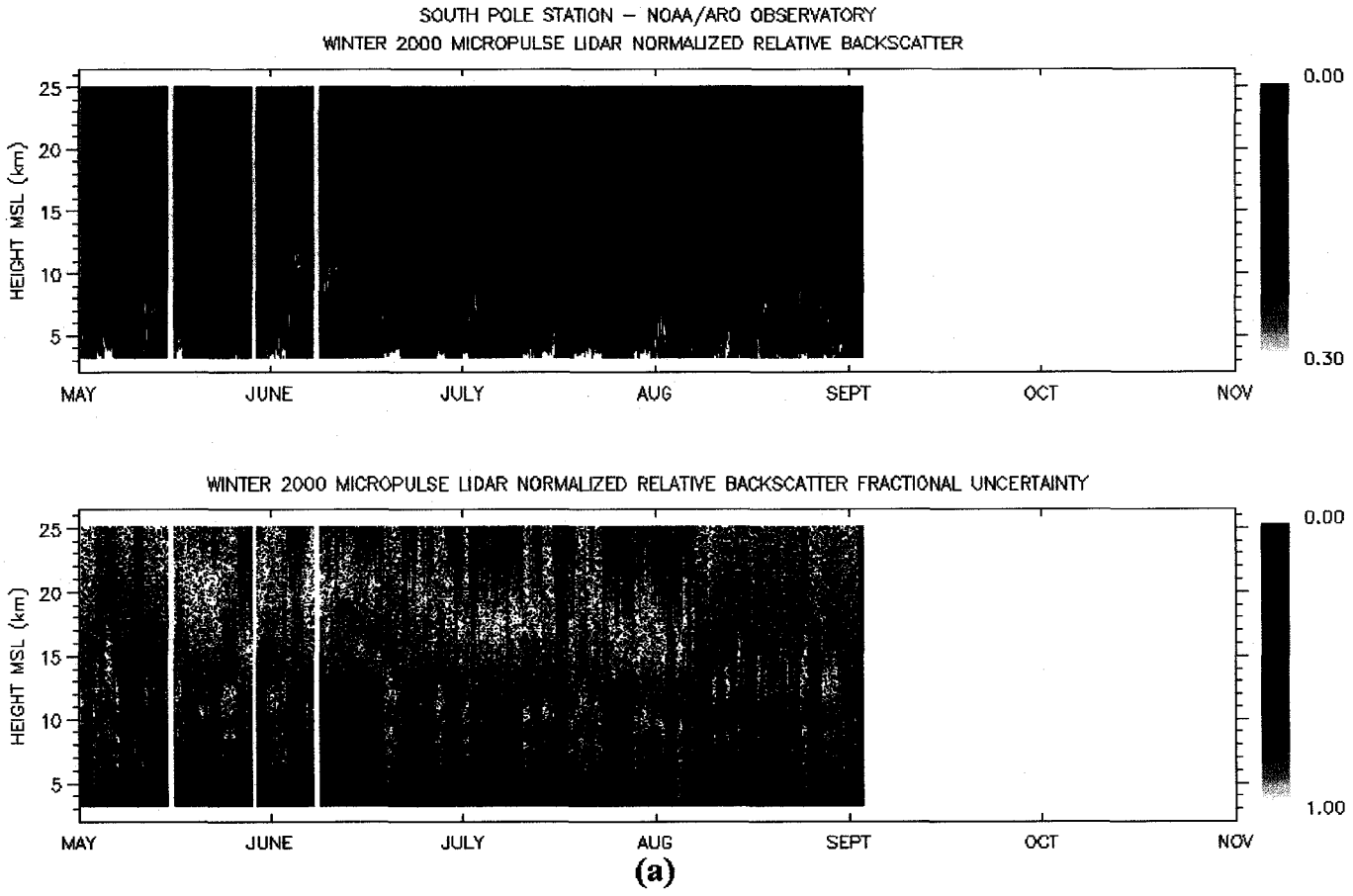

Figure 2.5 MPL NRB and fractional uncertainties from 2000, 2003-2005.
South Pole MPL normalized relative backscatter (top; photoelectrons·km^2/μsec·μj) and fractional percent uncertainty (bottom) for May – October 2000 from 2.8 – 25.0 km MSL (a).

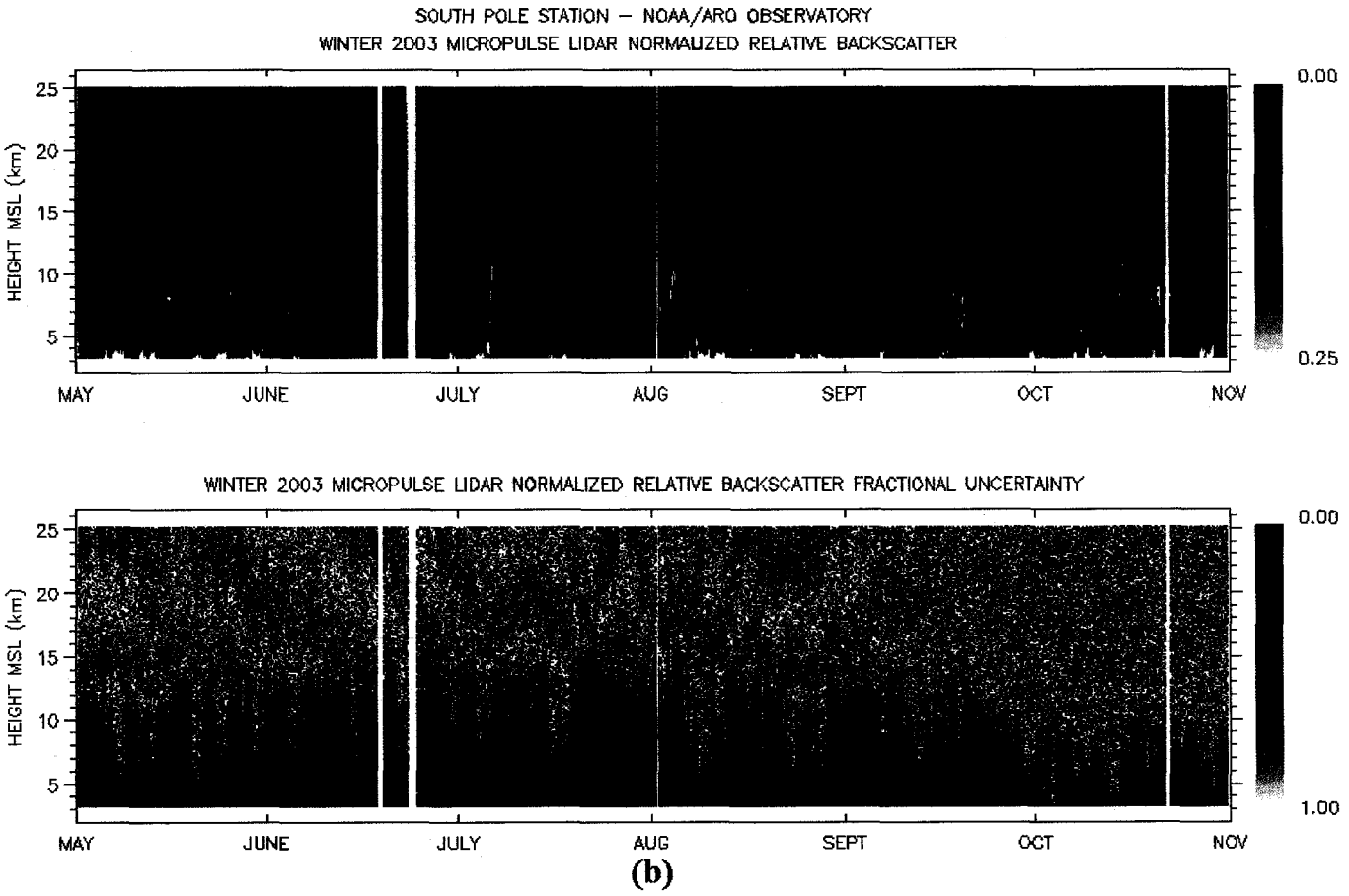

Figure 2.5 (cont.) MPL NRB and fractional uncertainties from 2000, 2003-2005.
South Pole MPL normalized relative backscatter (top; photoelectrons·km^2/μsec·μj) and fractional percent uncertainty (bottom) for May – October 2003 from 2.8 – 25.0 km MSL (b).

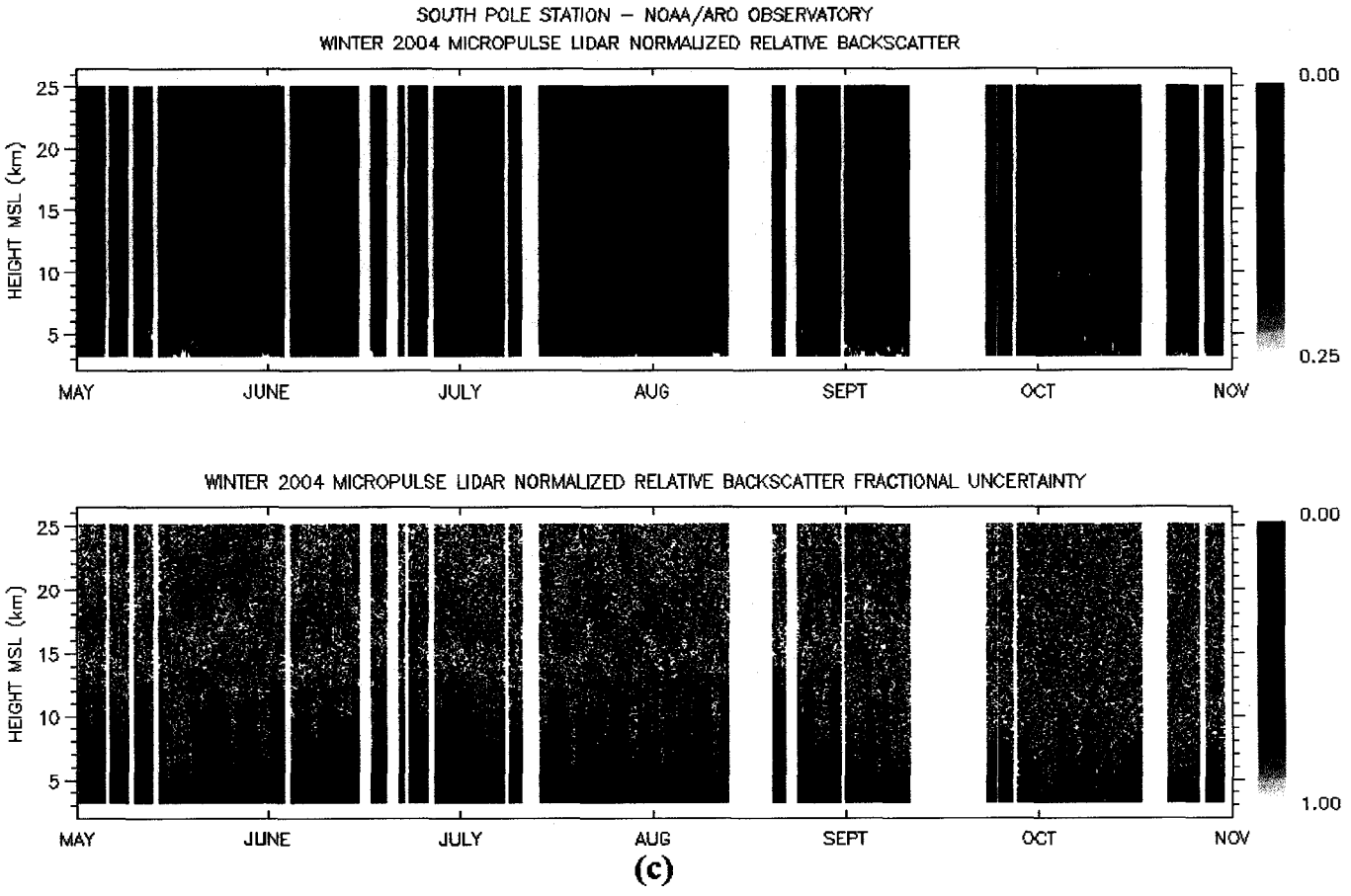

Figure 2.5 (cont.) MPL NRB and fractional uncertainties from 2000, 2003-2005.
South Pole MPL normalized relative backscatter (top; photoelectrons·km^2/μsec·μj) and fractional percent uncertainty (bottom) for May – October 2004 from 2.8 – 25.0 km MSL (c).

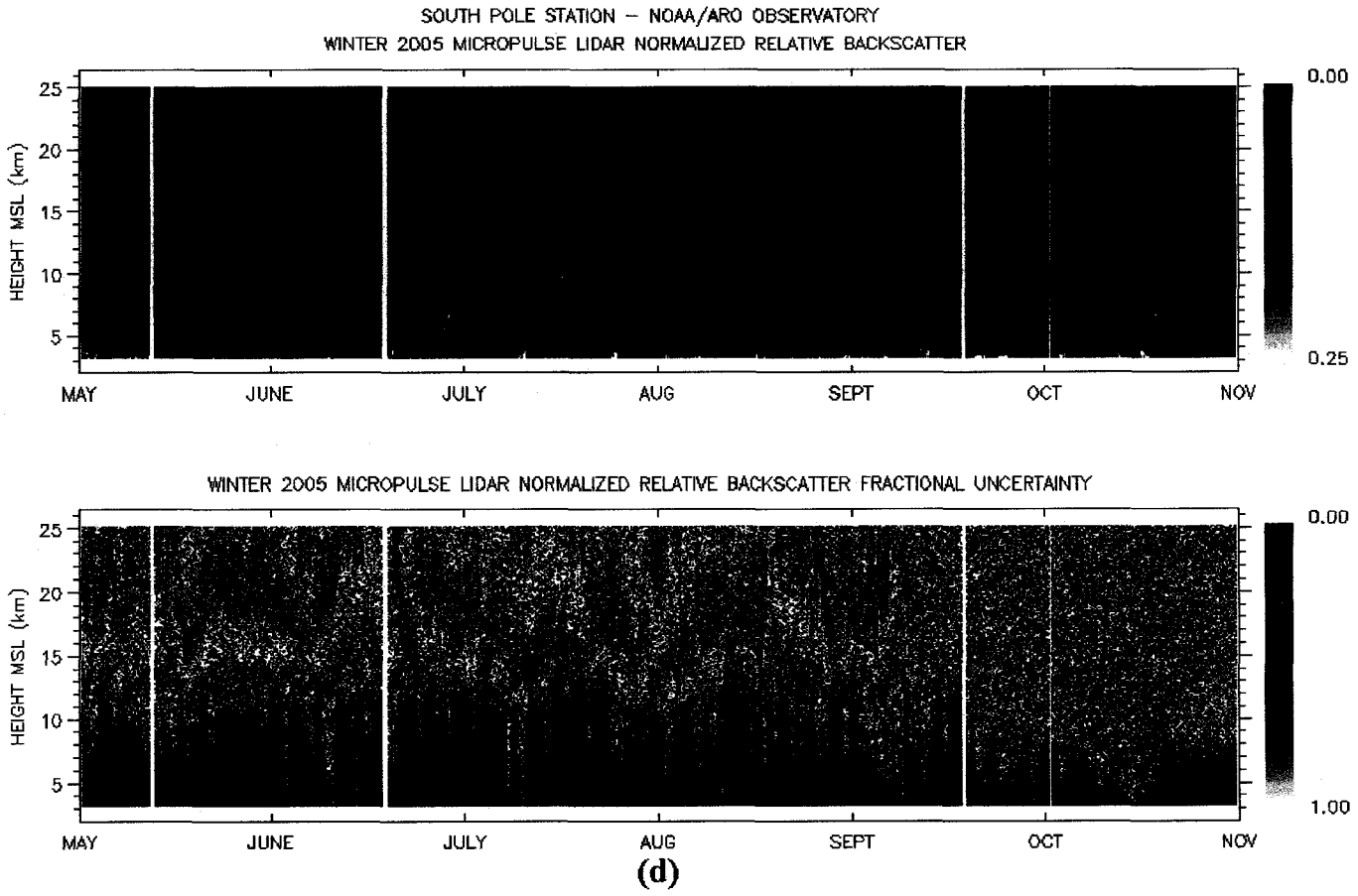

Figure 2.5 (cont.) MPL NRB and fractional uncertainties from 2000, 2003-2005.
South Pole MPL normalized relative backscatter (top; photoelectrons·km^2/μsec·μj) and fractional percent uncertainty (bottom) for May – October 2005 from 2.8 – 25.0 km MSL (d).

184 days of data each season. Data gaps are represented by blank color-fills. Data averaging has been done to fit this resolution. Image aliasing is discussed further below. In Eq. (2.3), afterpulse and overlap corrections are significant in the first 0.30 km of every profile and difficult to calibrate (*Campbell et al.*, 2002). Data in this range are ignored and the instrument is considered blind. Data are first displayed working from the instrument upward near 3.20 km MSL. For NRB data higher values reflect higher measured signal. For NRB fractional uncertainty higher values reflect greater relative uncertainty and lower SNR. The scales are reversed. The MPL exhibits acceptable performance (i.e., SNR $\geq$ 10) at one-minute resolution under clear-sky conditions up to approximately 12.0 km MSL during polar darkness. This drops to near 8.0 km MSL with the onset of sunlight from late September. At one-minute resolution NRB SNR is never higher than approximately 50.0 in the South Pole datasets. SNR should approach 1000.0 in the boundary layer under such conditions. However, from Eq. (2.4) the uncertainty in the overlap function varies between two and seven percent and this value is a limiting factor.

Tropospheric clouds frequently occur over the Antarctic plateau during winter. However, most are optically transmissive. Total attenuation of the MPL pulse is uncommon. Those few cases where attenuation occurs can be seen where values of NRB fractional uncertainty approach 1.0 at heights well below the clear-sky threshold height discussed previously ($\leq$ 12.0 km MSL). Blowing snow likely contributes to cases of strong surface signal. A recent study of blowing snow at South Pole using the MPL

slant-angle data shows that these layers regularly approach 1.0 km above ground-level (AGL; *Mahesh et al.*, 2003). PSC are evident above 10 km in the NRB data of each profile. The signal returns from these clouds are weak and difficult to discriminate. It is necessary to construct an algorithm capable of deriving PSC cloud heights in the presence of appreciable noise.

2.4 Statistical Algorithm for Particulate Layer Detection in MPL Data

Lidar cloud-detection algorithms are difficult to devleop. What is a fairly straight-forward task for the trained eye is a difficult one for automated processing code. The trained eye benefits from an understanding of the nature of hydrometeors, aerosols and molecules residing in the lower atmosphere. Clouds are bright, have distinct edges, are not relatively persistent temporally (i.e., lifetimes on the order of hours) and are commonly well-detached from the ground. Compared with clouds aerosols exhibit lower emissivities, lower relative scattering cross-sections, can be very persistent temporally, and are most commonly found near the surface. Molecules in turn have very low scattering cross-sections and act as the background from which particulate layers are distinguished. Despite obvious caveats (e.g., clouds are frequently embedded in aerosol layers and vice-versa) a trained observer encounters little difficulty dissecting data plots to record significant layer heights and basic macrophysical properties of the vertical profile. Yet the logic and decision-making skills of the trained observer fail to translate easily to the banal structures of computer programs.

Currently there is no uniform cloud algorithm that can be applied to lidar measurements without limitation. This is because there is no binary solution to analyzing signal returns for layer boundaries. The trained eye responds to discontinuities, dissimilarities and persistence. Although algorithms can be built to consider these factors, it would be impossible to properly weigh (or code) their significance for every conceivable scenario of cloud and aerosol presence. Thresholds bridge these gaps. Minimum standards for signal strength, and temporal and spatial depth give algorithms the logical parameters necessary to minimize the number of factors that influence their decisions. Thresholds are inevitable and compulsory for lidar cloud algorithms and they require fine-tuning to insure accuracy and relevance. What may be an applicable threshold in one climate regime may not be the same in another. For example, a minimum scattering cross-section used to differentiate between cloud and aerosol layers may be different in the tropics versus the high-latitudes. Similarly, minimum spatial thresholds relative to cloud thickness may be used to distinguish signal from noise. Yet noise may be a more significant factor for retrieving tropical cirrus clouds at heights near 20.0 km MSL versus ice layers at high-latitudes near 10.0 km MSL.

Threshold tuning is only one complication when considering algorithm portability between instruments. Lidars operate at wavelengths in and near the visible light spectrum (approx. 0.1 - 1.0 μm). Hydrometeors and most aerosols can be treated as Mie scatterers where particle sizes are on the order of or greater than the source wavelength. With diameters on the order of nanometers molecules can be treated as Rayleigh scatterers, where the source wavelength is much larger. This is opportune and a key

advantage of the lidar technique. With wavelengths on the order of millimeters or greater radars do not exhibit reliable sensitivity to aerosols and small cloud particles as they may scatter in the Rayleigh domain and be confused for molecular scattering. Rayleigh scattering cross-sections vary as the inverse of the fourth-power of the wavelength (e.g., *Bohren and Huffman*, 1998). Lidar cloud algorithms benefit from molecular response as greater clear-air signal provides for greater differentiation from particulate boundaries. Algorithms may be tuned to maximize the efficiency of this response and be subject to varying effects as a function of wavelength.

The MPLNET project is a unique testbed for algorithm development, as it represents the first widespread global deployment of a common instrument and source wavelength. Cloud algorithms for MPL instruments have been designed previously (*Campbell et al.*, 1998; *Clothiaux et al.*, 1998; *Mahesh et al.*, 2005). But their portability between instruments and varying climate regimes has not been demonstrated without threshold tuning. This is neither practical nor desirable for use in a network. The goal here is to develop an algorithm independent of subjective thresholding. Objective thresholds are developed such that the signal is analyzed for particulate scattering layers with statistical significance. With a single-channel instrument cloud and aerosol scattering cannot be unambiguously discriminated. Measurements of linear depolarization of laser backscatter are useful in this regard (*Sassen*, 1991). For the MPL optical layout, use of the random depolarizer piece between the thin-film polarizer and telescope inhibits addition of a second channel necessary to discriminate the two energy planes. This work is specifically referred to as a particular layer search algorithm. Since PSC detection is the

goal for this work, and aerosol scattering is not typically present at PSC heights at South Pole, the algorithm defaults to being a cloud algorithm.

SNR performance at one-minute resolution is not sufficient at PSC heights for analysis due to noise saturation above 10.0 km AGL (Figs 2.5a-d). Longer averages improve SNR performance. However, instrument performance can vary adversely over relatively short time-periods from thermal effects (*Campbell et al.*, 2000), while clouds and blowing snow can bias signal profiles from averages that are too long. To include as much data as possible for analysis, while producing meaningful profiles with high SNR, one-minute shots are grouped into 0.01 fractional day averages for all shots where the scanner angle pointed to the zenith. Based on *Bevington* (1969), that is,

$$NRB_{\chi}(r) = \frac{\sum_{t=\chi}^{t=\chi+0.01} NRB(r,t)}{N} \tag{2.7}$$

and

$$\delta NRB_{\chi}(r) = \frac{\sqrt{\sum_{t=\chi}^{t=\chi+0.01} \left(\delta NRB(r,t)\right)^2}}{N} \tag{2.8}$$

where χ is the beginning of the sampling period in fractional day and N is the number of one-minute shots in the average. NRB fractional uncertainty from 10 June 2003 using

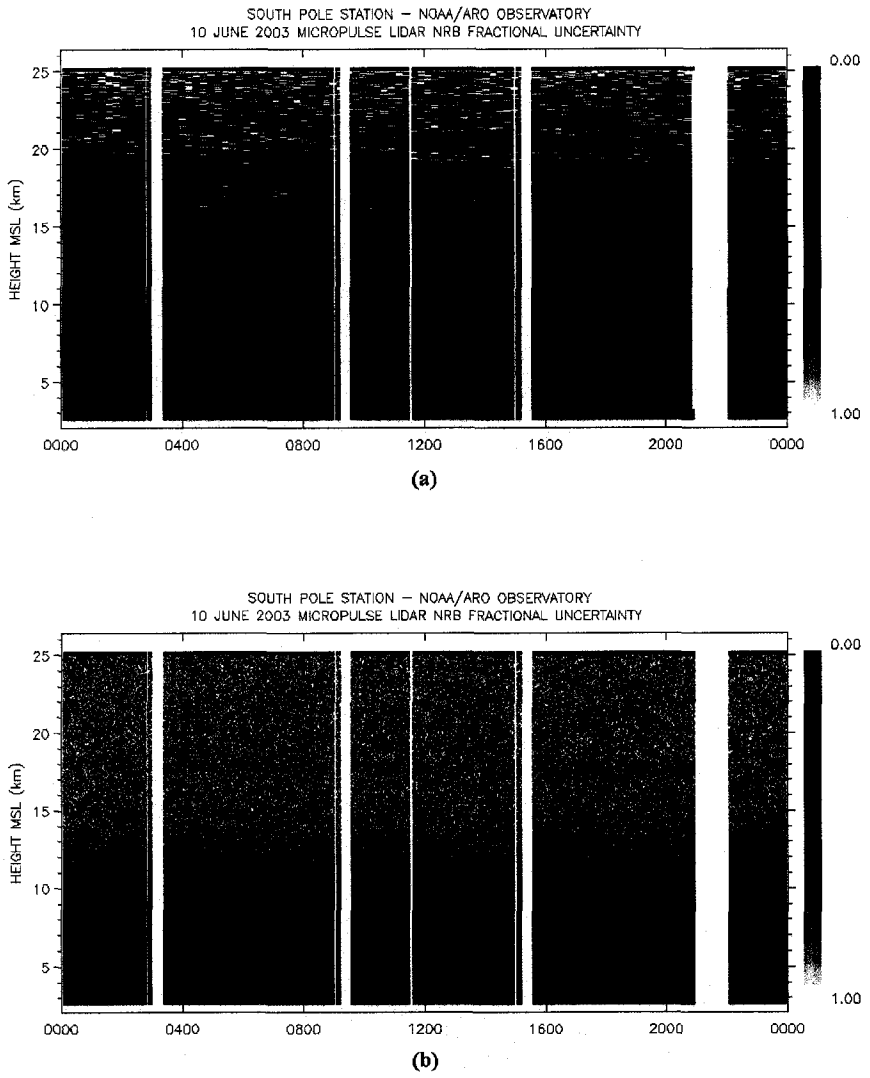

Figure 2.6 NRB fractional uncertainties from 10 June 2003.
MPL NRB fractional percent uncertainties at South Pole from 10 June 2003 for one-minute average profiles (a) and 0.01 fractional day averaged profiles (b).

one-minute averaging is shown in Fig. 2.6a. Following Eq. (2.6), fractional uncertainties for 0.01 fractional day averages from this day are shown in Fig. 2.6b. Two PSC layers become more clearly visible. Fractional uncertainties for the layer centered near 18.0 km

MSL are below 10%. Note that the discontinuity just above 8.0 km MSL reflects the effect of uncertainties for the overlap correction that apply to the signal below this range.

After averaging is complete the profile is normalized to a molecular scattering profile and the result is used to search for regions of clear-sky scatter nearest the instrument to solve for C in Eq. (2.3). A layer-boundary search then works vertically from the height where C is solved. It is useful to find clear-sky as near the instrument as possible to increase the depth of the profile searched. At South Pole, it is advantageous that optically thick aerosols are frequently lacking near the surface. At mid-latitudes aerosols are regularly observed from as high as 5.0 km AGL. As mentioned, blowing snow and diamond dust particles are common to near 1.0 km AGL at South Pole. MPL calibrations affecting the near-field signal profile have been made at South Pole in irregular intervals allowing for drift to occur over time. After many integrations and testing it was determined that 3.0 km AGL is the stable minimum height to begin the clear-air search so as to eliminate any such influences. Note that from this point forward when referring to data and results the height coordinate is reported with respect to MSL. However, for discussion relating specifically to the algorithm AGL range is used in consideration of the r^2 effect in Eq. (2.3) that directly affects signal uncertainties and bin relevance.

A molecular scattering profile was developed from a standard atmosphere table for air density during the Antarctic winter. The averaged NRB profile (Eq. (2.8)) can be normalized by this standard profile as

$$C^*(r) = \frac{C(\beta_m + \beta_p){T_m}^2{T_p}^2}{\beta_m(r){T_m}^2(r)} \approx \frac{NRB_\chi(r)}{\beta_m(r){T_m}^2(r)} \tag{2.9}$$

and the uncertainty for this, again based on *Bevington* (1969), is then

$$\delta C^*(r) = C^*(r)\sqrt{\left[\frac{\delta NRB_\chi(r)}{NRB_\chi(r)}\right]^2 + \left[\frac{\delta\beta_m}{\beta_m}\right]^2 + 2\left[\frac{\delta T_m}{T_m}\right]^2} \tag{2.10}$$

The uncertainty in the molecular scattering terms in Eq. (2.9) is unknown and set to a combined 5% for Eq. (2.10). Note that C^* is not C from Eq. (2.3), thought the two values are equal in the case of no particulate transmission between the instrument and r. This is an intermediate step and the two values should not be confused. Also note that the χ notation is dropped from this step forward such that the following equations involving NRB refer to the averaged profile.

Beginning from 3.0 km AGL a clear-air slot is determined by finding the range bin nearest the ground that satisfies the following threshold

$$\left(C^*(r:r_s) \pm \delta C^*(r:r_s)\right) \underset{\leq}{\geq} \left(C^*(r) \mp \delta C^*(r)\right) \tag{2.11}$$

where

$$r_s = r + \left(\left[\frac{\varepsilon^2}{\left(\frac{C^*(r)}{\delta C^*(r)} \right)^2} \right] * \Delta r \right) \tag{2.12}$$

Equation (2.11) requires that C^* and its uncertainty for those range bins between r and r_s (specified by Eq. (2.12)) fall within that of $C^*(r)$ and its uncertainty. Equation (2.12) determines the number of range bins so as to ensure statistical significance relative to a reference value ε, with Δr being the range resolution. These equations assume vertical inhomogeneity in any particulate scattering structure present relative to that of molecular scatter. The value inside the bracket is always rounded up such that the minimum value for N is 1. This is derived based on Eq. (2.8) where for a given NRB(r) and δNRB(r)

$$\delta NRB(r) = \frac{\sqrt{N(\delta NRB(r))^2}}{N} \tag{2.13}$$

and N = 1. The value N for the hypothetical case $\eta = 1/\varepsilon$ is

$$\left(\frac{NRB(r)}{\varepsilon} \right)^2 = \frac{N(\delta NRB(r))^2}{N^2} \tag{2.14}$$

and

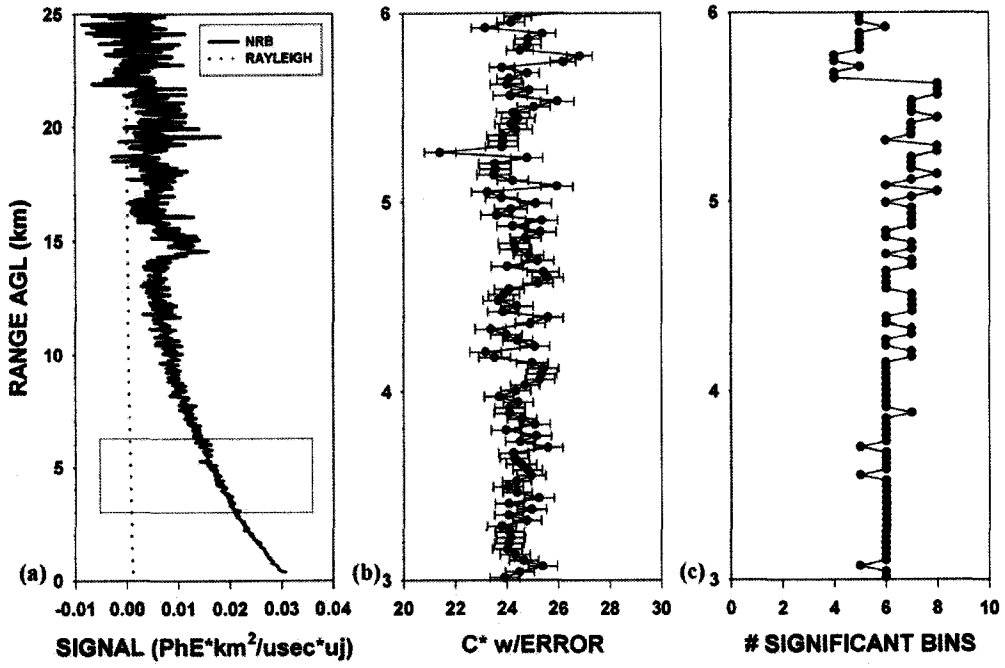

Figure 2.7 Algorithm diagnostic statistics.
MPL NRB averaged profile for 0.01 fractional days beginning 0.55 10 June 2003 versus attenuated Rayleigh profile between 0.30 and 25.0 km AGL (a), C^* with error bars between 3.0 and 6.0 km AGL (Eqs. (2.9) and (2.10)) and the number of significant bins required by Eq. (2.12) for searching out clear-air regions in Eq. (2.11). The regions shown in (b) and (c) are outlined by a box in (a).

$$N = \frac{\varepsilon^2}{\left(\frac{NRB(r)}{\delta NRB(r)}\right)^2} \tag{2.15}$$

Choosing $\varepsilon = 100.0$ ensures a significant number of bins so as to have agreement in Eq. (2.11) to within 1%. This methodology is accurate when δNRB(r) does not change significantly over the range r to r_s. That is, in Eq. (2.14), δNRB(r) is considered constant over the range N, whereas in reality it is not. For practical purposes any deviation is

negligible. The assumption of vertical particulate inhomogeneity is vital. Any such scattering present in the profile must not exhibit vertical structure similar to molecular scattering within the uncertainties over the number of significant bins required by Eq. (2.12). Otherwise, a false positive may occur. In the absence of aerosol loading at South Pole, this is a reliable assumption.

An example is shown in Fig. 2.7 for the 0.01 fractional day period beginning 0.55 10 June 2003. The averaged NRB profile is shown in Fig 2.7a versus the molecular scattering profile. It is evident that between the ground and 15.0 km AGL no significant particulate scattering was measured. Normalization of the profile using Eq. (2.9) is shown in Fig 2.7b for the range 3.0 to 6.0 km AGL with error bars derived using Eq. (2.10). The number of bins required to satisfy Eq. (2.11) within this range is shown in Fig 2.7c. The drop in this value near 6.0 km AGL is an artifact of the overlap correction noted previously. In this case Eq. (2.10) was first satisfied by the bin centered at 3.04 km AGL using six bins vertically for significance. A final normalization value (C_f^*) and its uncertainty are derived by averaging these six bins using applicable forms of Eqs. (2.7) and (2.8). The NRB profile is then renormalized using C_f^* to derive a final value termed pseudo-attenuated backscatter (PAB),

$$PAB(r) = \frac{NRB(r)}{C_f^*} \tag{2.16}$$

where

$$\delta PAB(r) = PAB(r)\sqrt{\left[\frac{\delta NRB_{\chi}(r)}{NRB_{\chi}(r)}\right]^2 + \left[\frac{\delta C_f^*}{C_f^*}\right]^2} \tag{2.17}$$

Attenuated backscatter refers back to Eq. (2.3) and the term $\beta(r)T^2(r)$ that would be achieved by dividing through by the system calibration constant (C). As noted earlier C_f^* is defined as

$$C_f^*(r) = CT_P^2(r) \tag{2.18}$$

PAB denotes the ambiguity between C_f^* and C from a lack of knowledge for T_p^2 that may be less than 1 for any scattering present below 3.0 km AGL.

A threshold for particulate boundary detection is now possible by modifying Eq. (2.17) under the assumption of a clear-sky. That is, the molecular scattering profile is substituted for NRB. This intermediate value is then added to the molecular scattering cross-section to form an outer error bar relative to PAB. Therefore, uncertainties for PAB are superimposed onto the hypothetical clear-sky profile. The threshold (α) is then

$$\alpha(r) = \left(\beta_m(r)T_m^2(r)\right) + \left[\left(\beta_m(r)T_m^2(r)\right)\sqrt{\left[\frac{\delta NRB_{\gamma}(r)}{\left(\beta_m(r)T_m^2(r)\right)C_f^*}\right]^2 + \left[\frac{\delta C_f^*}{C_f^*}\right]^2}\right] \tag{2.19}$$

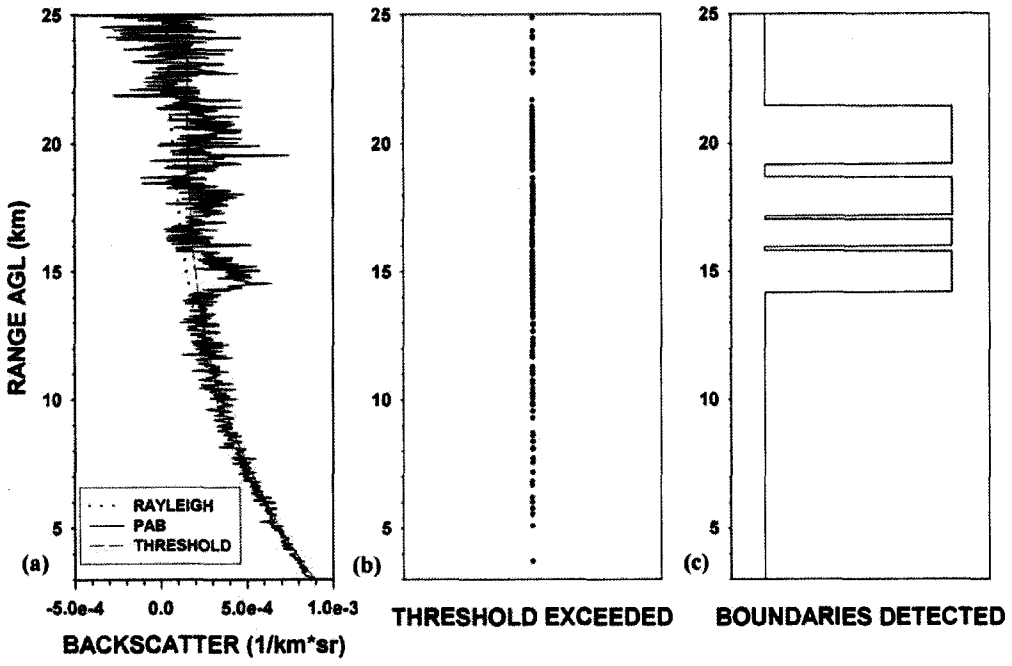

Figure 2.8 Processed algorithm signal retrievals.
MPL PAB averaged profile for 0.01 fractional days beginning 0.55 10 June 2003 versus an attenuated Rayleigh profile and the particulate layer threshold from 3.0 – 25.0 km AGL (a), points where the threshold was exceeded (b) and where particulate layers were detected (c).

As an initial screen range bins are considered as possibly containing particulate scattering when

$$PAB(r) - \delta PAB(r) > \alpha(r) \qquad (r \geq r_b) \tag{2.20}$$

where r_b corresponds to the lower range bin height from which C_f^* was derived. The algorithm is only valid for those data above this height. This threshold requires that the lower bound of any PAB value be greater than the threshold such that there is no

ambiguity between what may be considered cloud and clear-sky. An example is shown in Fig 2.8a, where PAB is shown for the aforementioned case on 10 June 2003 versus the molecular scattering profile and particulate threshold. Error bars are not shown here for image clarity. Of the 733 range bins between r_b and 25.0 km AGL 232 of them satisfied Eq. (2.20), and these are shown in Fig 2.8b.

Based on Eqs. (2.6), (2.7) and (2.8) each bin satisfying Eq. (2.20) is independently analyzed for potential as a lower particulate boundary. Working vertically from a subject bin (r_1) running averages for PAB and δPAB are tabulated. A lower boundary is considered to be found when

$$\frac{\sum_{r=r_1}^{r=r_N}\left(PAB(r)\right)}{\sqrt{\sum_{r=r_1}^{r=r_N}\left(\delta PAB(r)\right)^2}} \geq \varepsilon \qquad \textbf{(2.21)}$$

providing Eq. (2.20) is satisfied for each bin included in the running averages. Bins within the range r_1 and r_N that do not satisfy Eq. (2.20) are ignored in Eq. (2.21). However, a bin r_1 is eliminated from consideration in the event that

$$\frac{\sum_{r=r_1}^{r=r_N}\left(PAB(r)^*\right)}{\sqrt{\sum_{r=r_1}^{r=r_N}\left(\delta PAB(r)^*\right)^2}} \geq \kappa \qquad \textbf{(2.22)}$$

for any consecutive bins encountered before reaching r_N that do not satisfy Eq. (2.20) (denoted by the asterisk). This is used to signify clear-sky slots. One-bin "gaps" are not considered important, similar to the logic in finding clear-sky calibration slots. κ is set to 10.0, an order of magnitude less than ε. This is due to the lower SNR inherent for clear-sky with increasing range from the instrument. When a layer base is found the search continues vertically from r_N to find the corresponding layer top. Either of two criteria may be met for this to occur. Equation (2.22) may be satisfied to signify a clear-sky slot and thus a layer top. Also the running averages for Eq. (2.21) are continued. If the value drops below ε a layer top height is considered to be found. Algorithm layer boundaries for the case on 10 June 2003 are shown in Fig. 2.8c.

The algorithm is predicated on three conjectures and includes three objective signal thresholds (ε is used twice for convenience though the values are independent of one another). First, persistence in the normalization value with range relative to the molecular profile is considered clear-sky. This is a vital element for the algorithm. Second, scattering signal from one bin is not relevant to be considered either that of particulate or clear-sky on its own, and instead must be considered relative to an adjacent bin. Finally, the scattering ratio value must exceed the statistical threshold outside of its uncertainty to be differentiated from clear-sky. Either of the thresholds may be altered with some quantitative consequence, which may be then used to interpret the results. This will be examined further in Section 2.7.

A weakness in the algorithm logic is that analysis of returned signal below r_b for particulate layer search is not possible. As will be discussed, some understanding of the

scattering properties of any particulate layers present is required. Implementation of this algorithm would require subjective thresholds to handle these regions of the profile. This would not be true, however, for nadir-pointing instruments, such as on an aircraft or satellite platform. The scenario for PSC detection at South Pole is analogous to the nadir-pointing instrument in the case for no particulate scattering in the range nearest the MPL. Then the profile must only be normalized to a molecular profile and the layer boundary search then follows. For nadir-viewing instruments this is also most commonly the case, given the lack of significant scattering targets in their near-range. Application of this algorithm would be well-suited to such datasets.

2.5 Lidar Scattering Ratios

From *Measures* (1984) the lidar scattering ratio ($\beta_r(r)$) is defined as

$$\beta_r(r) = \frac{\left(\beta_p(r) + \beta_m(r)\right)}{\beta_m(r)} \tag{2.23}$$

Gobbi et al. (1998) and *Toon et al.* (2000) correlate scattering ratios and linear depolarization measurements (Table 1.3) as a means for distinguishing PSC types. The single-channel MPL records no information on the polarization state of the returned signal. However, their results can be used qualitatively as a reference for analyzing scattering ratio values derived from the PSC Data Subset.

For the PAB profile in Fig. 2.8a (above r_b) Eq. (2.23) must be modified. Between r_b and the base height of the first incident particulate layer (r_{p1}) the equation is valid and equal to unity. Above that initial range, an attenuated lidar scattering ratio follows Eq. (2.23) as

$$\beta_{r^*}(r) = \frac{\left(\beta_p(r) + \beta_m(r)\right)T_p^2(r)T_m^2(r)}{\beta_m(r)T_m^2(r)} \qquad (r \geq r_{p1}) \qquad \textbf{(2.24)}$$

Eq. (2.24) is only solved for bins within cloud layers identified by the algorithm. All other regions are set to 1.0. The molecular transmission terms cancel each other. As evidenced in Fig. 2.8, some bins fall below the required threshold within the boundaries of a cloud. After solving Eq. (2.24) for a given profile, those values corresponding to such bins are smoothed over using a one-dimensional form of the Hanning window (Appendix A; also referred to as the "Von Hann" window) with no temporal coordinate and 0.150 km spatial half-width. From Eqs. (2.19) and (2.20), a minimum detectable scattering ratio can be defined as

$$\beta_{r\min}(r) = \frac{\left(\alpha(r) + \delta PAB(r)\right)}{\beta_m(r)T_m^2(r)} \qquad \textbf{(2.25)}$$

An example for Eq. (2.25) is shown in Fig. 2.9 for the case from 10 June 2003. The signal threshold and attenuated molecular scattering profile are shown in Fig. 2.9a, the minimum detectable scattering ratio and smoothed attenuated scattering profile in Fig. 2.9b and the unsmoothed scattering ratio profile in Fig. 2.9c. For this case at 0.01

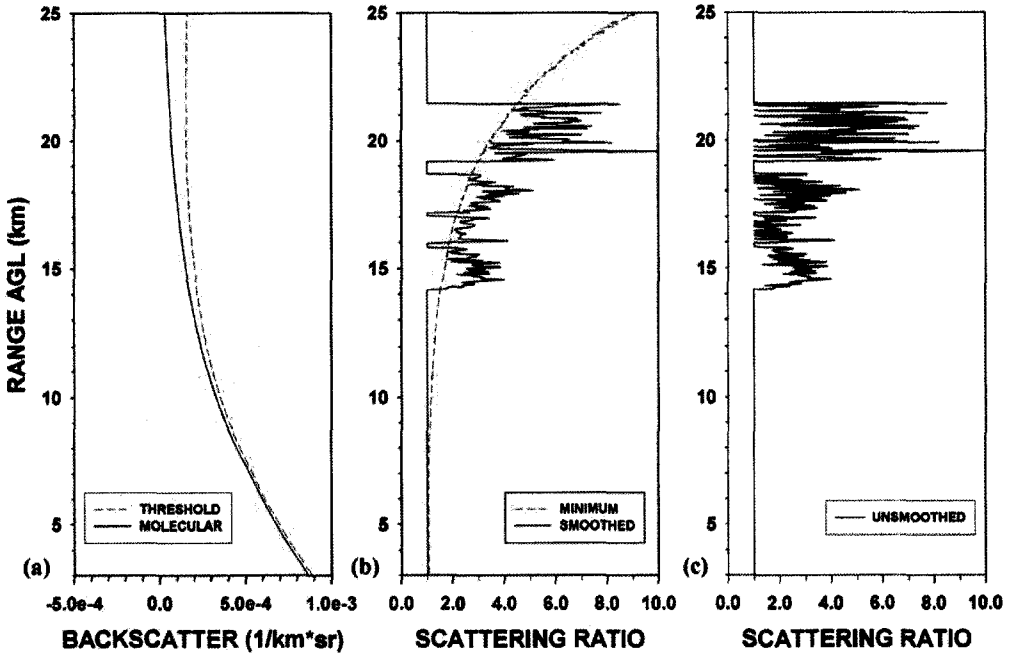

Figure 2.9 Algorithm particulate layer signal smoothing.
For the 0.01 fractional days profile beginning 0.55 10 June 2003 the particulate layer threshold (red) from 3.0 – 25.0 km AGL versus attenuated molecular scattering (solid; a), the minimum detectable scattering ratio (red) versus the smoothed attenuated scattering ratio (solid; b) and the unsmoothed attenuated scattering ratio (c).

fractional day resolution the MPL is sensitive to particulate layers with a scattering ratio under 2.0 up to near 16.0 km AGL and approaching 10.0 near 25.0 km AGL.

To calculate a corrected lidar scattering ratio (Eq. (2.23)) above r_{pl} some value must be prescribed for the particulate extinction-to-backscatter ratio ($S_p(r)$) for those bins where particulate scattering is deemed present. The particulate extinction-to-backscatter ratio is defined as the ratio between particulate extinction (σ) and backscatter cross-sections by *Measures* (1984) as

$$S_p(r) = \frac{\sigma_p(r)}{\beta_p(r)} \tag{2.26}$$

At r_{pl}, $\beta_p(r_{pl})$ can be solved using Eq. (2.19) for the known value of $\beta_m(r_{pl})$. The extinction cross-section is then solved as

$$\sigma(r_{pl}) = S_r \beta_p(r_{pl}) \tag{2.27}$$

Under the condition that

$$T_p^2(r_{pl} + \Delta r) = e^{-2\int_{r_b}^{r_{pl}} \sigma(r)dr} \tag{2.28}$$

Eq. (2.23) at height $r_{pl}+\Delta r$ is solved as

$$\beta_r(r + \Delta r) = \frac{\beta_{r^*}(r + \Delta r)}{T_p(r + \Delta r)} \qquad (r > r_{pl}) \tag{2.29}$$

Solving Eqs. (2.26) to (2.29) is then repeated working upward through the rest of the profile.

PSC frequently exist as liquid aerosols (*Toon et al.*, 1989). In processing the South Pole PSC Data Subset the extinction-to-backscatter ratio could vary widely for

Table 2.1 Algorithm output statistics for PSC Data Subset.
Sum and percentage values for total and missing data points are relative to possible total of 18400 data points between 1 May and 31 October. Values for blocked, cloudy and clear points are relative to the total available points in the first column.

	TOTAL	MISSING	BLOCKED	CLOUDY	CLEAR
2000	11688 (63.5%)	6712 (36.4%)	2965 (25.4%)	7464 (63.9%)	1259 (10.8%)
2003	17061 (92.7%)	1339 (7.3%)	4026 (23.6%)	9880 (57.9%)	3155 (18.5%)
2004	13424 (73.0%)	4976 (27.0%)	5274 (39.3%)	5184 (38.6%)	2966 (22.1%)
2005	16024 (87.1%)	2376 (12.9%)	7308 (45.6%)	5810 (36.3%)	2906 (18.1%)
TOTALS	58197 (79.1%)	15403 (20.9%)	19573 (33.6%)	28338 (48.7%)	10286 (17.7%)

backscatter measured from ice versus ternary solution droplets (*Sassen*, 1978). Any attempt to adjust for particulate transmission using $S_r(r)$ would introduce great uncertainty to an already noisy process. For this reason only the attenuated lidar scattering ratio is calculated. Furthermore, no effort is made to adjust the threshold in Eq. (2.19) for boundary detection as a function of particulate transmission present above r_b. Note also that the minimum detectable scattering ratio (Eq. (2.25)) is derived under the scenario that particulate transmission above r_b is zero. When particulate scattering is present Eq. (2.25) is only valid up to the range bin corresponding to the initial particulate layer base. An attenuated minimum value is not derived due to the same reluctance to correct for $S_r(r)$. However, in the presence of particulate scattering it can be shown that Eq. (2.25) is simply the minimum detectable corrected scattering ratio. The parameter has relevance under most conditions for qualitative analysis.

2.6 Algorithm Results for PSC Data Subset

Table 2.1 displays algorithm output from the PSC Data Subset. Data were analyzed by the algorithm from 3.0 – 25.0 km AGL (approximately 5.8 – 27.8 km MSL). The first two columns indicate the number of available and missing data points (i.e., 0.01 fractional day averages). The percentages listed are based on a possible 184 days between 1 May and 31 October each year and 73,600 points over the four-year dataset. The final three columns include the number of uncalibrated (i.e., blocked), cloudy and clear points for each year and their totals. These percentages are relative to the number of available points from the first column. Points where the scanner was positioned off-zenith are shown in the missing column. It is possible that uncalibrated points were cloudy points, and that the reason the algorithm failed for these profiles was from attenuation of the pulse by clouds below the 3.0 km AGL algorithm base level. Nearly 90% of the possible data were available from 2003 and 2005. However, low clouds were present ~ 50% of the time during 2005 that limited performance. Only one-quarter of the data were affected as such in 2003. In total, clear-sky conditions above 3.0 km AGL (~ 5.8 km MSL) were observed at South Pole approximately 20% of the time. Cloudy conditions were detected nearly 50% of the time.

From Eqs. (2.24) and (2.25) attenuated scattering ratio values (top) and minimum detectable scattering ratio values (bottom) are shown for the PSC Data Subset in Fig. 2.10 for 2000 (a), 2003 (b), 2004 (c) and 2005 (d). The data are shown now between 3.0 and 28.0 km MSL. Similar to Figs. 2.5a-d missing data are left blank. New gaps indicate

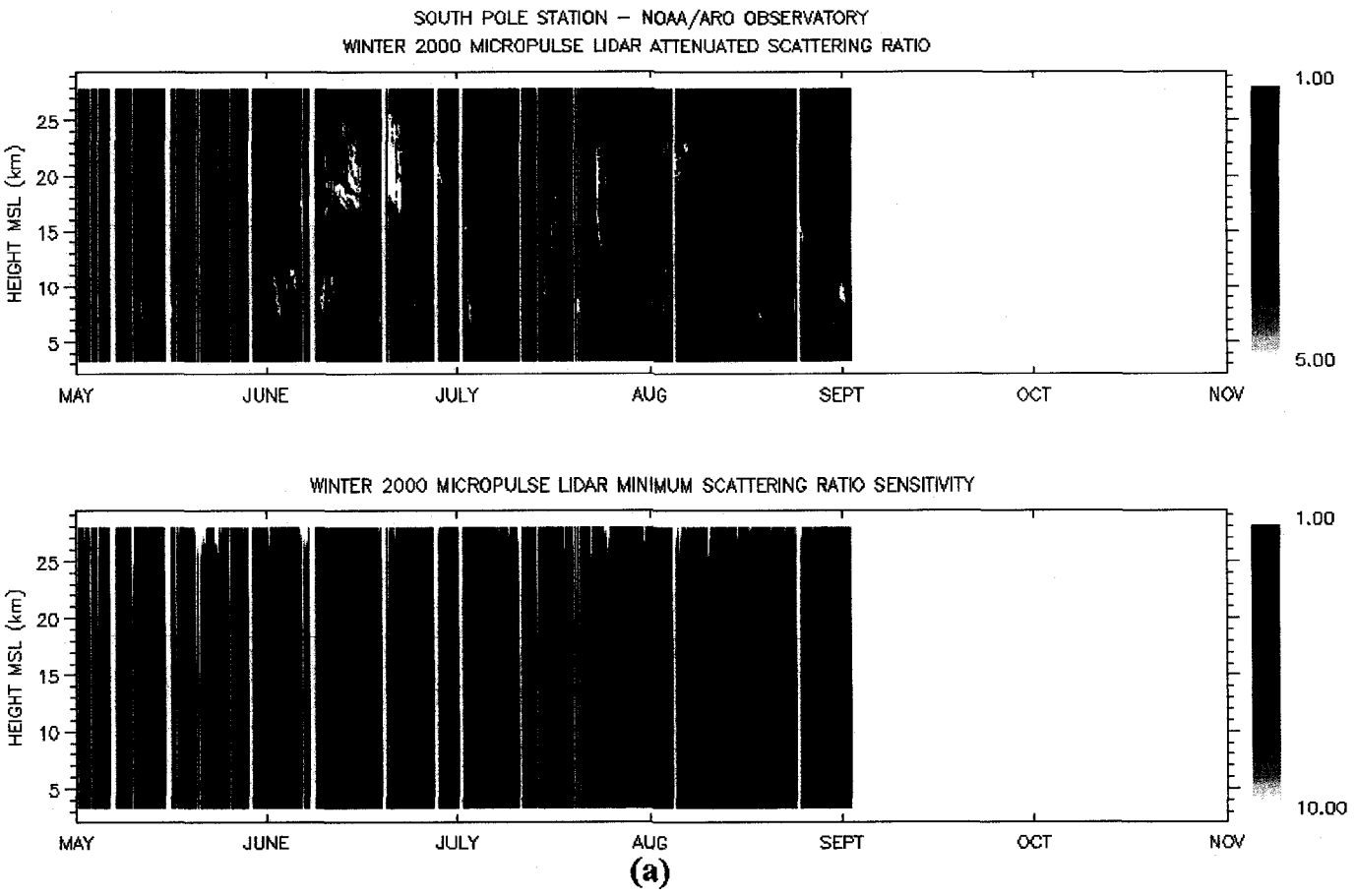

Figure 2.10 Annual profiles for scattering ratio and minimum threshold.
Algorithm scattering ratios (top) and minimum detectable scattering ratios (bottom) for PSC Data Subset for May – October 2000 from 2.8 – 28.0 km MSL (a).

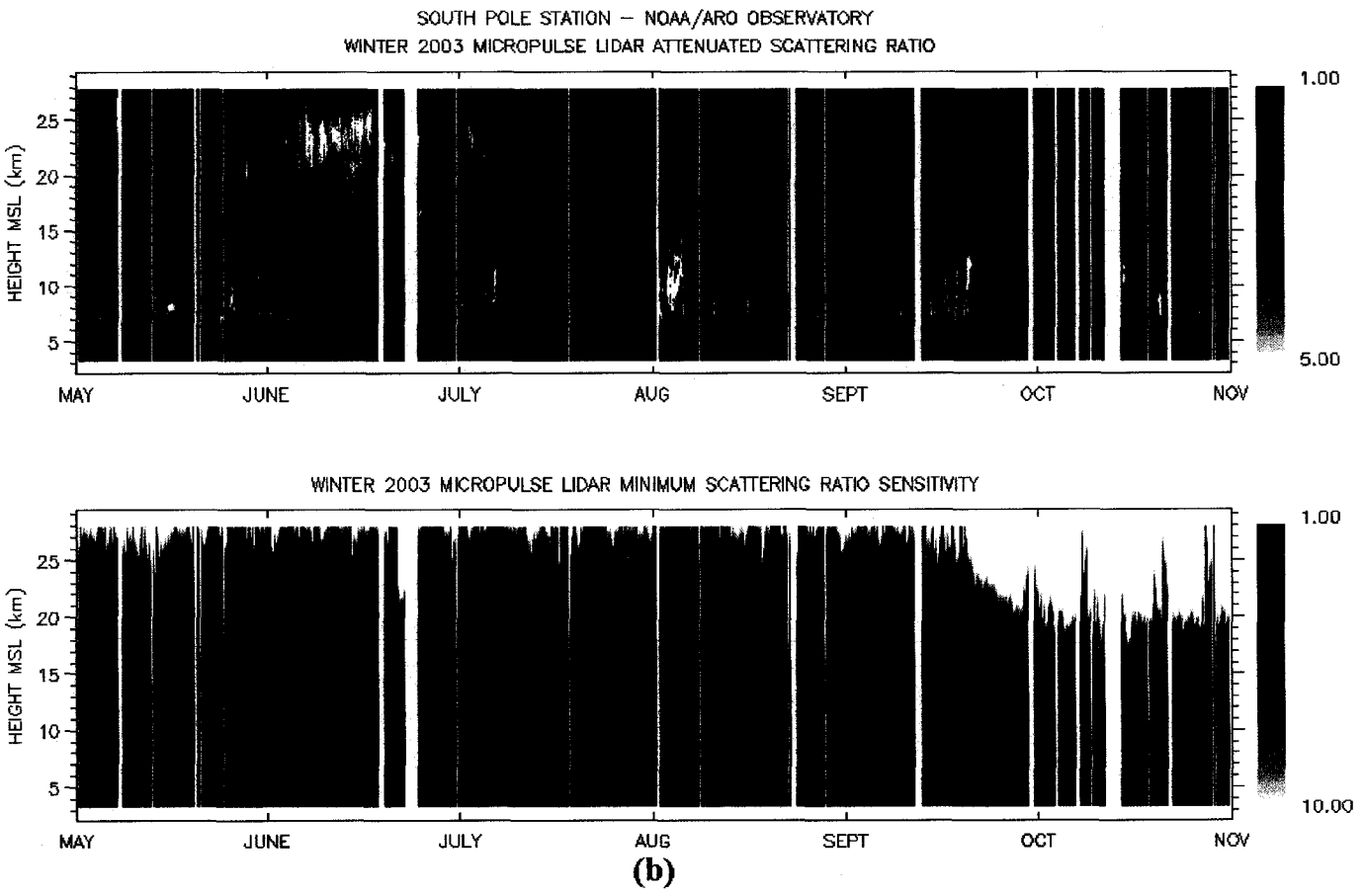

Figure 2.10 (cont.) Annual profiles for scattering ratio and minimum threshold.
Algorithm scattering ratios (top) and minimum detectable scattering ratios (bottom) for PSC Data Subset for May – October 2003 from 2.8 – 28.0 km MSL (b).

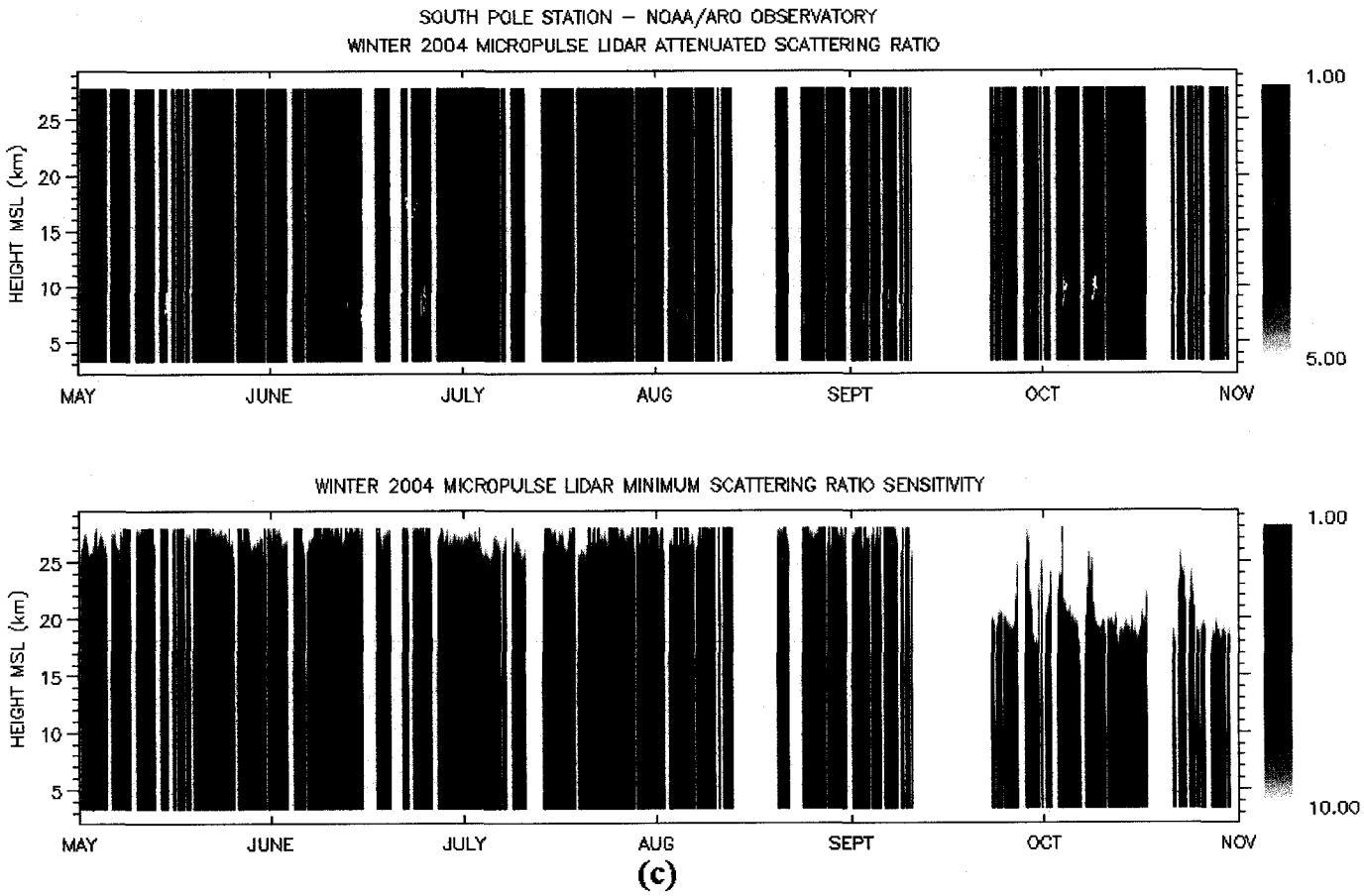

Figure 2.10 (cont.) Annual profiles for scattering ratio and minimum threshold.
Algorithm scattering ratios (top) and minimum detectable scattering ratios (bottom) for PSC Data Subset for May – October 2004 from 2.8 – 28.0 km MSL (c).

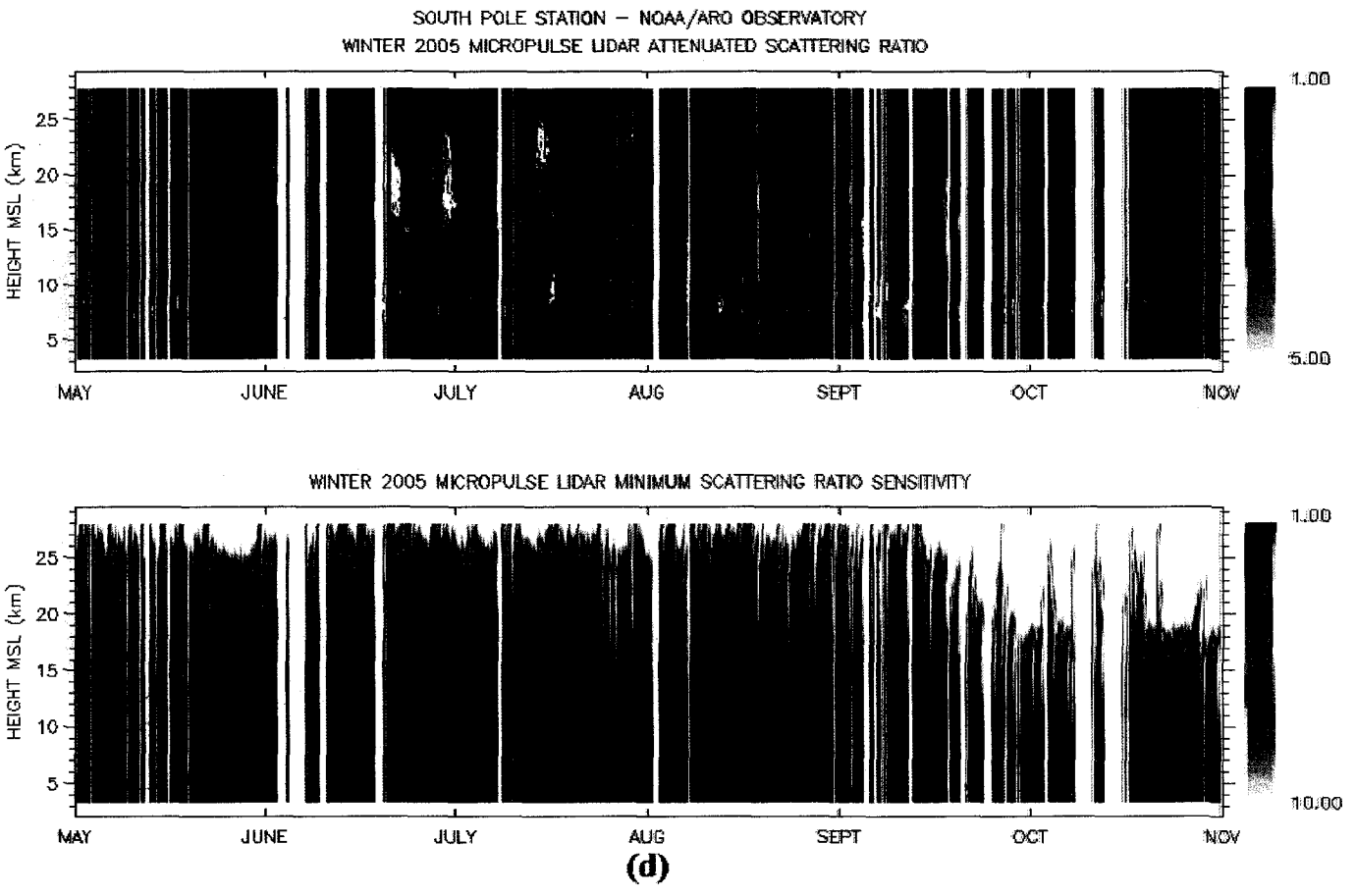

Figure 2.10 (cont.) Annual profiles for scattering ratio and minimum threshold.
Algorithm scattering ratios (top) and minimum detectable scattering ratios (bottom) for PSC Data Subset for May – October 2005 from 2.8 – 28.0 km MSL (d).

uncalibrated points where Eq. (2.16) is not solved. Instrument performance was best in 2000, where minimum detectable scattering ratios approaching 10.0 are not as common as in subsequent years. Accordingly, algorithm performance is best during this year. Poor instrument calibrations are to blame for the numerous false positives observed near 20.0 km MSL in early May 2003. Data from 2004 is most affected by missing and uncalibrated points. This year was least cloudy (i.e., above 3.0 km MSL), particularly at PSC heights. Much of the missing and uncalibrated data points from 2005 come in May and October. Overall algorithm performance is good, though where the minimum detectable scattering ratio rapidly increases above 20.0 km MSL the upper edges of the PSC appear fuzzy in 2003 and 2005. It is worth recalling that these are composite images. While it appears that the tops of such clouds rarely exhibit high attenuated scattering ratios, smoothing has occurred.

2.7 Algorithm Sensitivity

Tuning the SNR (ε in Eq. (2.21)) and clear (κ in Eq. (2.22)) algorithm thresholds to improve performance is tantamount to focusing a lens to an image. It is not possible to derive exact parameters for these thresholds. However, they may be optimized. To test the sensitivity of the threshold values, tests were performed where both parameters were varied to compare algorithm output, diagnose any biases and better interpret the final results. Data from the 2003 season were used as input. The SNR threshold influences the detection of cloud base for the algorithm. Two tests were run with SNR varied from 200.0 to 50.0, or a factor two greater than and less than the implemented value of 100.0.

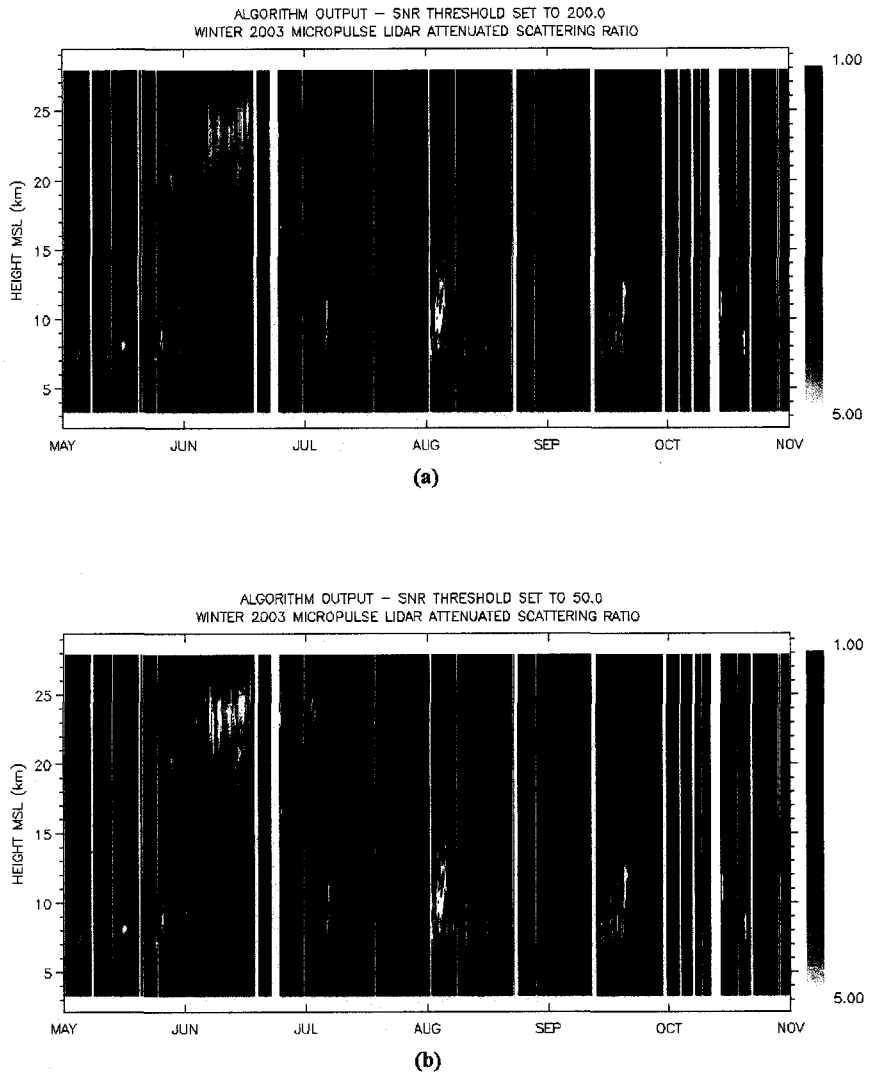

Figure 2.11 Algorithm tuning for SNR threshold.
Algorithm results for May – October 2003 for SNR threshold set to 200.0 (a) and 50.0 (b) with clear threshold set at 10.0.

For these runs the clear threshold was maintained at 10.0. The results are shown in Figs. 2.11a and b respectively. They may be compared directly with the upper panel of Fig. 2.10b. An SNR threshold value of 200.0 results in fewer cloud layers detected. This is

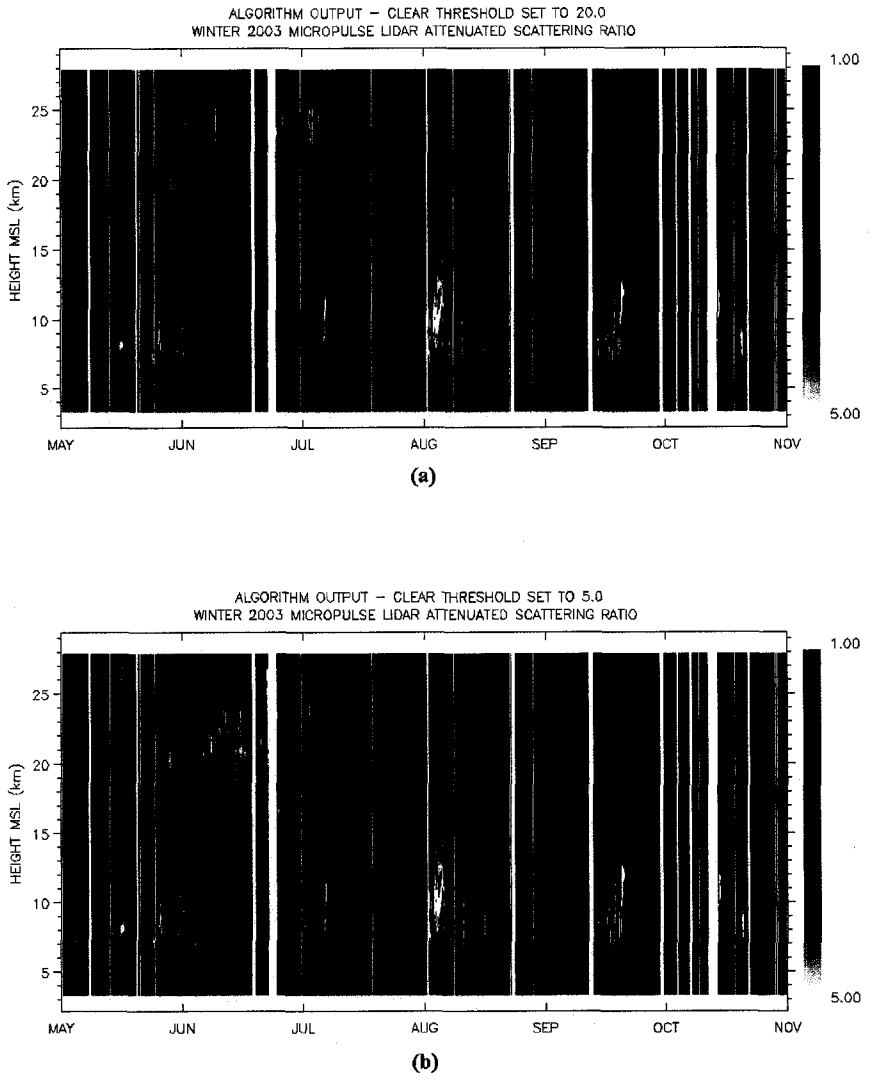

Figure 2.12 Algorithm tuning for clear threshold.
Algorithm results for May – October 2003 for clear threshold set to 20.0 (a) and 5.0 (b) with SNR threshold set at 100.0.

consistent with Eq. (2.21) given that a greater number of bins satisfying Eq. (2.20) must be present before the conditions of Eq. (2.22) are met and a cloud base search ceased. This effect is most apparent for low scattering ratio cases through the column (best

observed by comparing Figs. 2.11a and b for the thin cloud layers observed from mid-August to mid-September between 10.0 and 15.0 km MSL) and at upper-levels where SNR is at a minimum (best seen from the PSC complex observed in June centered near 20.0 km MSL). This scenario produces a high bias in scattering ratio values calculated over the entire season. However, at 50.0 (Fig. 2.11b) the profile exhibits a greater influence from noise. This is most apparent during May near the top of the profile where numerous false positives were calculated.

The clear threshold affects the detection of cloud base, but has a more significant influence on the detection of cloud top. Two tests were run with the clear threshold varied from 20.0 to 5.0, similar to the previous case a factor of two greater than and less than the chosen value of 10.0. The SNR threshold was maintained at 100.0 during these runs. These data are shown in Figs. 2.12a and b respectively. A clear threshold value of 20.0 results has two effects. First, more cloud layers are detected overall since Eq. (2.22) is not satisfied as readily during cloud base search that would stop it. This leads to a low bias in scattering ratio values derived over the entire season. Second, and more noticeably from Fig. 2.12a, the threshold is not as easily surpassed in the low SNR regions at upper levels. Frequently, no cloud top height is found for cloud detected at these heights and the algorithm defaults the value to the top of the profile at 27.8 km MSL. Lowering the clear threshold to 5.0 produces an opposite effect. Fewer cloud layers are found overall since Eq. 2.22 is satisfied more easily during the cloud base search. The leads to a high bias in scattering ratio values derived over the entire season since only clouds exhibiting high SNR are found. Cloud top heights are found at lower

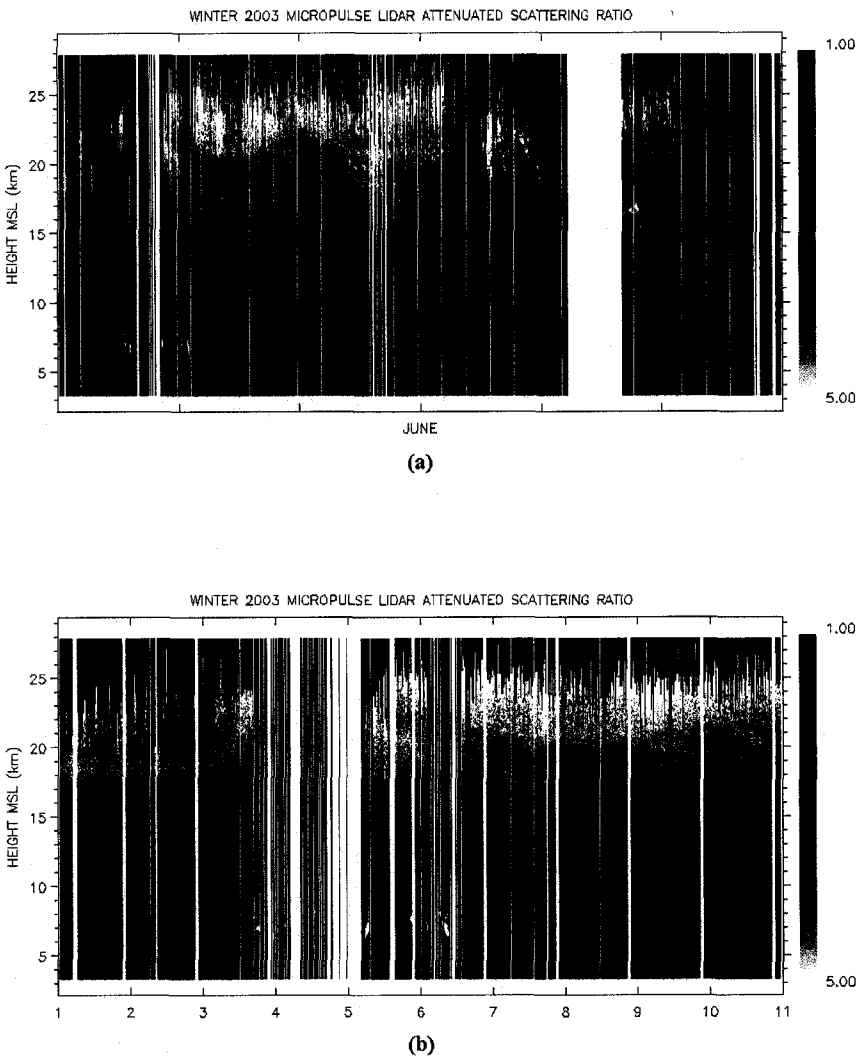

Figure 2.13 Image aliasing for variable time-iteration output.
Algorithm results from 2003 data subset for June (a) and 1-10 June (b).

heights relative to values of 10.0 and 20.0. Again, this is consistent from Eq. (2.22) being satisfied more easily with the lower standard.

2.8 Image Aliasing

Imaging software was used to generate many of the images shown from this research. Most depict the concatenation of many days of data into one plot. This lowers the resolution of the images. For example, the seasonal images in Figs. 2.5 and 2.10 respectively represent the concatenation of 18,400 profiles (184 days versus 100 profiles per day) into 1009 vertical imaging lines, a number unique to the source program code used. For this example a ten-fold decrease in temporal resolution results. The vertical (i.e., spatial) resolution is unchanged. However, the software employs routines that implement additional smoothing along both axes when displaying the concatenated array.

To examine the effects of aliasing, in Figs. 2.13a and b are scattering ratios derived from algorithm output during June 2003 and 1-10 June 2003. The full season is depicted in the top panel of Fig. 2.10b. Figure 2.13a consists of 3000 data points, representing the thirty days from that month. This results in a three-fold decrease in the temporal resolution of this image. Figure 2.13b consists of 1000 available data points. Therefore, there is no change of temporal resolution for this image. The 10-day image (Fig. 2.13b) depicts a greater concentration of saturated scattering ratio values ($\geq$ 5.0; see color bar) relative to both the 30-day (Fig. 2.13a) and seasonal images (Fig. 2.10b). Cloud structure is less apparent as the length of the plot is increased. Centered at 20.0 km MSL from 9-10 June in the 10-day image is a shallow hole in the PSC layer. This hole is not apparent in the longer plots, though the hole at the same height from 7-8 June appears in the 30-day image. PSC fallstreaks are visible intermittently from the 30-day image. However, in the seasonal image only the streaks that occurred at the end of the month are clearly

distinguishable. Visible data gaps (i.e., missing data and uncalibrated profiles) disappear with increasing image duration. When concatenating the data, a minimum of 20% of the possible data points for a given imaging line were required for it to be plotted. Otherwise, the line appears as blank, or white. Only the most significant gaps appear in the longer duration images. From a positive standpoint, however, the effects of noise are minimized with increasing image duration. At 10-day resolution cloud top height levels are inconsistent. This may be attributed to noise. However, the effect may be real as a result either of instrument performance and the SNR profile for the given shot, or from attenuation effects. Both of these factors may influence the threshold in Eq. 2.19. These inconsistencies are gradually smoothed out as the length of the image increases.

CHAPTER 3

SOUTH POLE 2000, 2003-2005: OZONE, THERMODYNAMIC AND PSC SEASONAL PROPERTIES AND THE CORRELATION BETWEEN OZONE LOSS AND PSC OCCURENCE

In this chapter, ozone partial pressures, thermodynamic measurements and modeled cloud-saturation scenarios are described and correlated with PSC macrophysical properties for 2000 and 2003-2005. The result is a series of composite summary images that depict the seasonal evolution of PSC presence, thermal structure and ozone loss. More specifically, thermal depressions relative to the NAT condensation point and ice frost point for constrained nitric acid and water vapor concentrations were calculated from available radiosonde datasets. Periods of denitrification and dehumidification may be inferred from negative correlations between PSC presence and extended periods of NAT or ice saturation that would indicate conditions favorable to the occurrence of clouds. The primary research objectives proposed in the introductory chapter are addressed here. That is, the data are examined to establish whether a correlation exists between PSC occurrence evolve and ozone loss.

In reaching this point, the previous chapter dealt with characterizing the performance of the MPL for detecting PSC. From previous measurements for all types of PSC and their embryonic sub-species, the lower range of lidar scattering ratio measurements at 0.532 and 0.589 μm approaches unity (*Collins et al.*, 1993; *Gobbi et al.*, 1998). The

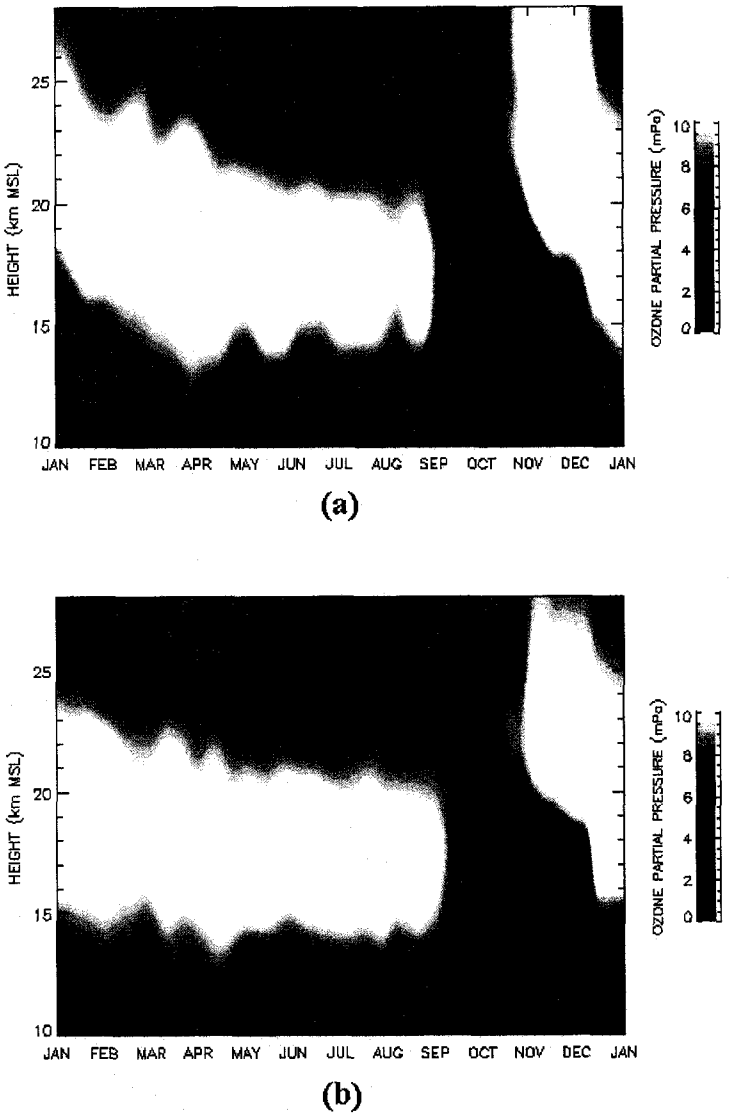

Figure 3.1 Annual South Pole ozone profiles.
Annual profiles of ozone partial pressure (mPa) from 10.0 – 28.0 km MSL at the South Pole for 2000 (a) and 2003 (b).

sensitivity of the MPL instrument as a function of scattering ratio was demonstrated (e.g., Fig. 2.9). At 0.01 fractional day resolution, the minimum detectable MPL scattering ratio for the designed algorithm typically exceeds 2.0 just above 15.0 km MSL. The

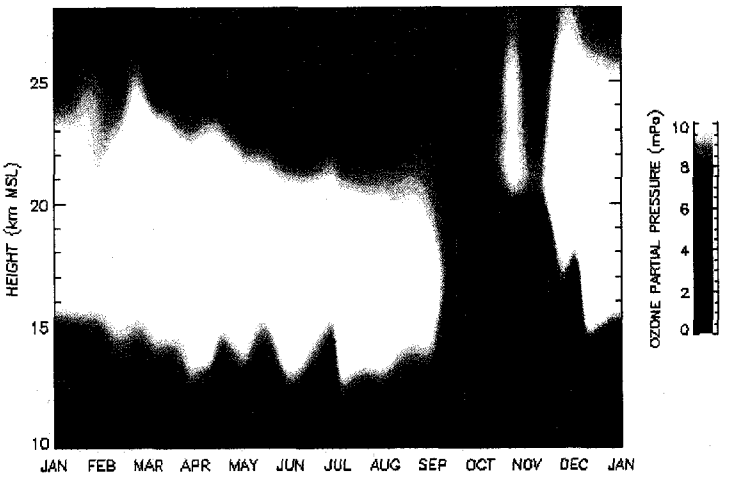

(c)

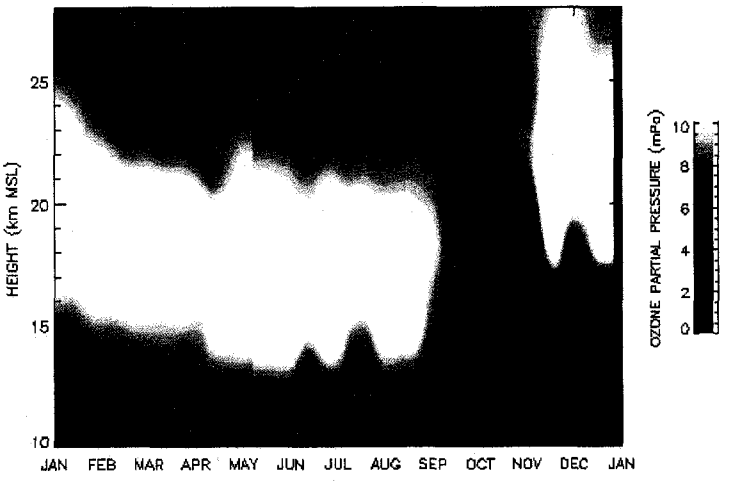

(d)

Figure 3.1 (cont.) Annual South Pole ozone profiles.
Annual profiles of ozone partial pressure (mPa) from 10.0 – 28.0 km MSL at South Pole for 2004 (c) and 2005 (d).

instrument is not sensitive to all PSC, and is clearly not detecting all optically thin clouds. Yet, it is not possible to accurately estimate the extent of PSC occurrence that goes undetected. In the process of describing seasonal climate and chemical properties at

South Pole over the four-year sample here some observations can be made about the likely nature of the clouds being detected by the MPL. Additionally, Appendix B is a case-study comparing MPL retrievals to PSC measurements from a high-power 0.372/0.374 μm Fe-Boltzmann lidar instrument operated episodically by the University of Illinois at South Pole during 2000. The primary objective of this chapter is to investigate any correlation present between PSC occurrence, as measured by an MPL, and ozone loss. Furthermore, if present, those caveats inherent to the instrument and measurements must be established and recommendations made to redesign the experiment to make the future datasets more robust. The comparison in Appendix B provides further context from which to consider the results described in this chapter.

3.1 Lower-Stratospheric Ozone Partial Pressures at the South Pole

Lower-stratospheric ozone partial pressures (mPa) recorded from ozonesonde launches at South Pole station are shown for 2000 and 2003-2005 in Figs. 3.1a-d, respectively, from 10.0 – 28.0 km MSL. Individual sounding files were first interpolated to 0.250 km resolution starting from 3.0 km MSL using a one-dimensional form of the Hanning function (Appendix A) at 0.500 km spatial half-width. The data were then smoothed temporally to produce composite arrays at 1-day and 0.050 km resolution, again using the Hanning function at 14-day and 2.0 km temporal and spatial half-widths.

Table 3.1 displays statistics corresponding to the data shown in Fig. 3.1. Only those ozonesondes reaching 25.0 km MSL were used to construct the images. The total number of qualifying sondes for each year is listed, followed by the total number of days

Table 3.1 Statistics from South Pole ozonesonde processing.
Corresponding to Figs. 3.1a-d the number of ozonesonde files used to construct each annual image, the number of days where < 220 DU was observed from the surface corresponding to the ozone hole overhead and the number of 0.050 km bins corresponding to the given ozone partial pressure constraints South Pole.

Year	# Files	Ozone Hole Days		# Bins
2000	57	72	$\leq$ 4.0 mPa	12917
			$\leq$ 2.0 mPa	6518
			$\leq$ 1.0 mPa	3524
2003	73	63	$\leq$ 4.0 mPa	11338
			$\leq$ 2.0 mPa	6152
			$\leq$ 1.0 mPa	2734
2004	54	71	$\leq$ 4.0 mPa	8045
			$\leq$ 2.0 mPa	2519
			$\leq$ 1.0 mPa	654
2005	57	69	$\leq$ 4.0 mPa	11803
			$\leq$ 2.0 mPa	4044
			$\leq$ 1.0 mPa	1597

each year where less than 220 DU (i.e., the ozone hole being over the site) were derived from the 3.0 km MSL observation. Furthermore, the two-dimensional arrays (time vs. height) were integrated according to three partial pressure constraints to calculate total numbers of 0.050 km bins exhibiting less than or equal to 4.0, 2.0 and 1.0 mPa, respectively. The numbers of days with the ozone hole overhead, as well as yearly aerial maximums for the ozone hole, reported in Fig. 1.8, offer no reference to the depth of the ozone loss. In fact, the duration of the ozone hole is approximately seventy days each

year despite wide disparity in the aerial maximum values. The data detailed in Table 3.1 more appropriately represent this aspect of seasonal losses.

Ozone loss during 2000 (Fig. 3.1a), both at South Pole and over the region, was the most severe of the four-year sample. Losses at South Pole were first observed in early September from 11.0 to 25.0 km MSL. In only one other year (2005) early season losses were observed at this height. Minimum partial pressures were measured in early October just above 17.0 km MSL. The low concentrations were mostly replenished by mid-December. From Fig. 1.8, the mean value for the maximum annual area of the ozone hole from 1996 – 2005 was 2.63 x 10^7 km^2, with a standard deviation of 0.258 x 10^7 km^2. The maximum value during 2000 was 3.031 x 10^7 km^2 in early September, which exceeded the standard deviation and is the largest measurement in the sample. The peak occurred just as losses were first being observed at South Pole, showing the photochemical dependence of ozone loss and suggesting that the hole formed from the outer edges of the polar vortex inward returning with solar irradiance as a function of latitude. Peak stratospheric chlorine concentrations were predicted to occur before 2000 (*Montzka et al.*, 1996; *World Meteorological Organization*, 1998). However, the combination of consistent bromine emissions (*Montzka et al.*, 1999) and cooling stratospheric temperatures (*Ramaswammy et al.*, 2001) are factors that may have offset the period for maximum ozone depletion (e.g., *Shindell et al.*, 1998). Record stratospheric ozone minima were measured at McMurdo Station during the spring of 2000 and 2001 (*Kröger et al.*, 2003). From Table 3.1, maximum occurrences were recorded for all three ozone partial pressure constraints.

Ozone loss during 2003 (Fig. 3.1b) was above average compared to the ten-year mean, and second highest among those in this four-year sample. In 2002, a significant Antarctic stratospheric warming occurred in spring, and the maximum ozone hole area that season was the lowest since 1990 (*Hoppel et al.*, 2003). Unfortunately, the MPL failed in June due to laser failure. Losses in 2003 were first observed in early September from 11.0 to 23.0 km MSL. Minimum concentrations were observed in mid-October near 16.0 km MSL, and the hole had recovered by mid-December. The maximum annual area was observed in late September at 2.85 x 10^7 km^2. This value ranks second from the ten-year sample (Fig. 1.8). However, from Table 3.1, the year ranks third among the four-year sample for number of bins exhibiting less than 4.0 mPa partial pressure. For bins exhibiting less than 2.0 mPa the 2003 season ranks a close second to 2000. For bins exhibiting less than 1.0 mPa the year ranks a clear second, but at roughly 75% of the 2000 total. Sub-220 DU measurements at 3.0 km MSL lasted only 63 days in 2003, or 90% of the average value for other sample years.

Ozone loss during 2004 (Fig. 3.1c) was the lowest of the four years in the data sample. Initial losses were measured in early September from 12.0 to 23.0 km MSL. Minimum ozone partial pressures were sampled in early October, just above 16.0 km MSL. These losses were mostly replenished by mid-November, the earliest of any sample year. The maximum area for the 2004 ozone hole occurred in late September, measured at 2.27 x 10^7 km^2. This is the second-lowest value recorded since 1990. Nearly 2.5 times more bins exhibiting less than 1.0 mPa partial pressure were observed from the next closest year (2005) relative to 2004 (Table 3.1).

Measurements from 2005 (Fig. 3.1d) indicate an average year for ozone loss relative to the ten-year average (Fig. 1.8). Beginning from early September losses were measured from 13.0 – 25.0 km MSL. Minimum concentrations were recorded in late September near 18.0 km MSL and then again in early October below 17.0 km MSL. Unlike previous years in the four-year sample, however, full recoveries were observed by mid-December. Ozone-poor air was detected near 15.0 km MSL through the end of the year. The maximum area of the 2005 ozone hole was measured at 2.68 x 10^7 km^2 in early September, which is just above the ten-year average. This is similar to 2000, where the aerial maximum coincided with the beginning of significant losses being measured at South Pole. As noted, the second highest number of bins exhibiting less than 4.0 mPa partial pressure were observed in 2005 (Table 3.1). However, the year ranks a clear third for bins exhibiting less than 2.0 and 1.0 mPa ozone partial pressure.

3.2 Lower-Stratospheric Temperatures, and Nitric Acid Condensation-Point and Water Vapor Frost-Point Thermal Depressions

Temperatures derived from daily balloonsonde launches at South Pole station are shown for May through October 2000 and 2003-2005 in Figs. 3.2a-d, respectively, from 10.0 – 28.0 km MSL. This dataset is separate from the ozonesonde archive. However, similar to those data, individual sondes were first interpolated to 0.250 km resolution beginning from 3.0 km MSL using a one-dimensional form of the Hanning function (Appendix A) at 0.500 km spatial half-width. The data were then smoothed temporally to produce composite images at 1-day and 0.050 km resolution using the Hanning function

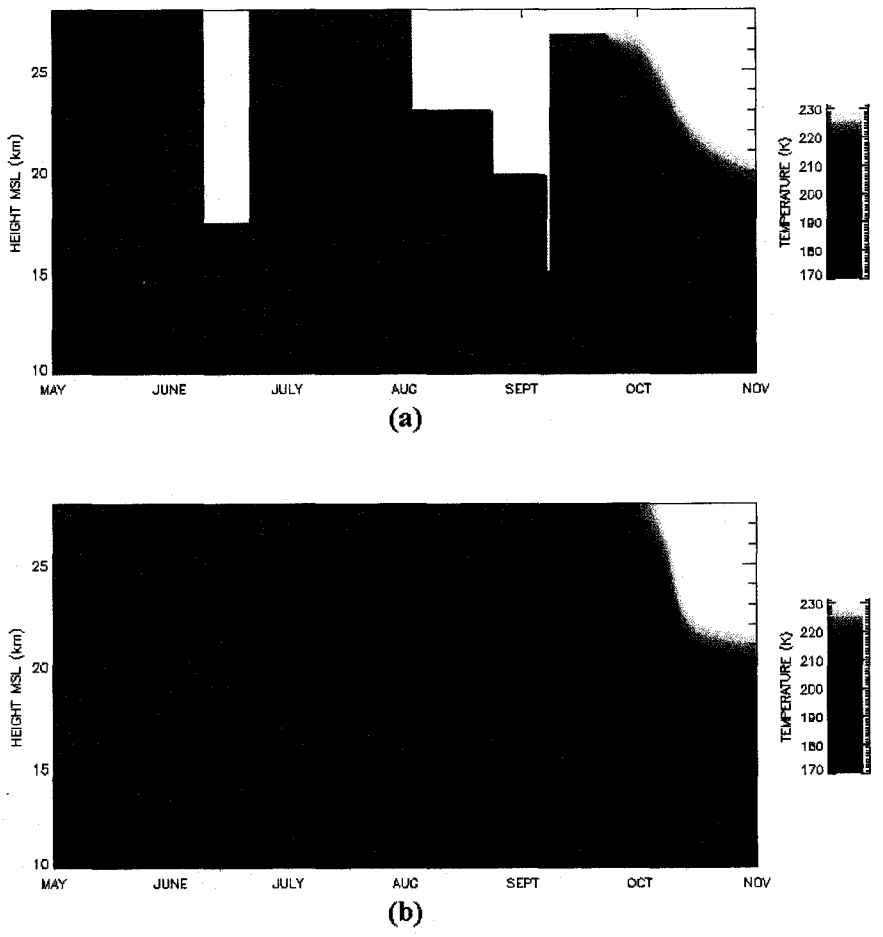

Figure 3.2 Yearly winter/spring temperature profiles.
Profiles of temperature (K) from 10.0 – 28.0 km MSL at South Pole for May – October 2000 (a) and 2003 (b). Data gaps are denoted by abrupt white gaps, and are not to be confused with saturation of the color bar.

at 14-day and 2.0 km temporal and spatial half-widths. Unlike the ozonesonde dataset gaps in the daily balloonsonde were present, despite only requiring launches reaching a minimum height of 18.0 km MSL to be included in the sample. It was decided not to supplement the latter archive with those of the former to fill these gaps at the risk of inhomogeneities that could bias the sample as a result of sensor differences (e.g., *Gaffen*

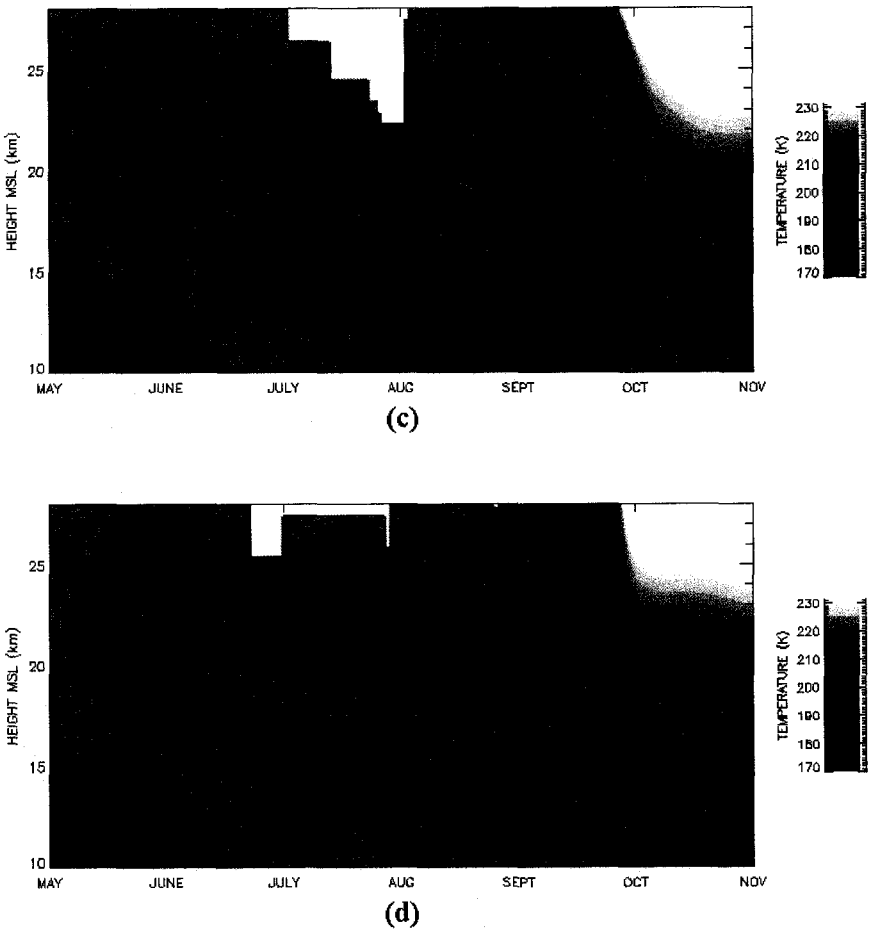

Figure 3.2 (cont.) Yearly winter/spring temperature profiles. Profiles of temperature (K) from 10.0 – 28.0 km MSL at South Pole for May – October 2004 (c) and 2005 (d). Data gaps are denoted by abrupt white gaps, and are not to be confused with saturation of the color bar.

et al., 2000). This dilemma further highlights the deficiencies in operational radiosonde launches from the on-site NOAA meteorological office during polar night. Major gaps in the smoothed datasets occurred in 2000, with minor gaps present at upper-levels in July 2004 and 2005. No gaps are present in the smoothed 2003 data.

From these smoothed temperature datasets thermal, depressions relative to the condensation point for NAT (*Hanson and Mauersberger*, 1988) and the frost point for ice (*Bohren and Albrecht*, 1998; see Fig 1.4 and accompanying text) were derived for three hypothetical concentrations of nitric acid and water vapor, respectively. For NAT, 12.0, 10.0 and 8.0 ppbv HNO_3, given 4.0 ppmv water vapor concentration, were used, based on historical measurements and a desire for reasonable upper and lower bounds of lower stratospheric background concentrations in an unperturbed (i.e., not denitrified) environment (e.g., *Gille et al.*, 1993). For ice, 6.0, 4.0 and 2.0 ppmv were chosen from similar concerns (*Rosen et al.*, 1993). These data are shown in Fig. 3.3 from 10.0 to 28.0 km MSL, where NAT depressions are shown in Figs. 3.3a, c, e and g and ice depressions are shown in Figs. 3.3b, d, f and h for each successive year, respectively. Data gaps present from the previous series of images in Fig. 3.2 are also present here. A second thermodynamic inversion of the smoothed temperature datasets is shown in Fig. 3.4. These figures are natural logarithmic profiles of saturation water vapor concentrations with respect to ice from 10.0 to 28.0 km MSL for each year, respectively.

These calculations are with respect to the saturation vapor pressure over both pure NAT and ice. Therefore, they are only rough approximations to reality, where ternary solution droplets or Type I PSC hydrates act as cloud particle embryos. Discussing homogeneous nucleation of ice, *Koop et al.* (2000) postulated that nucleation rates in aqueous solutions are independent of the nature of the solute and instead a function solely upon water activity. A recent review by *Cantrell and Heymsfield* (2005) discusses the practicality of the *Koop et al.* (2000) model. Actual saturation temperatures for Type I

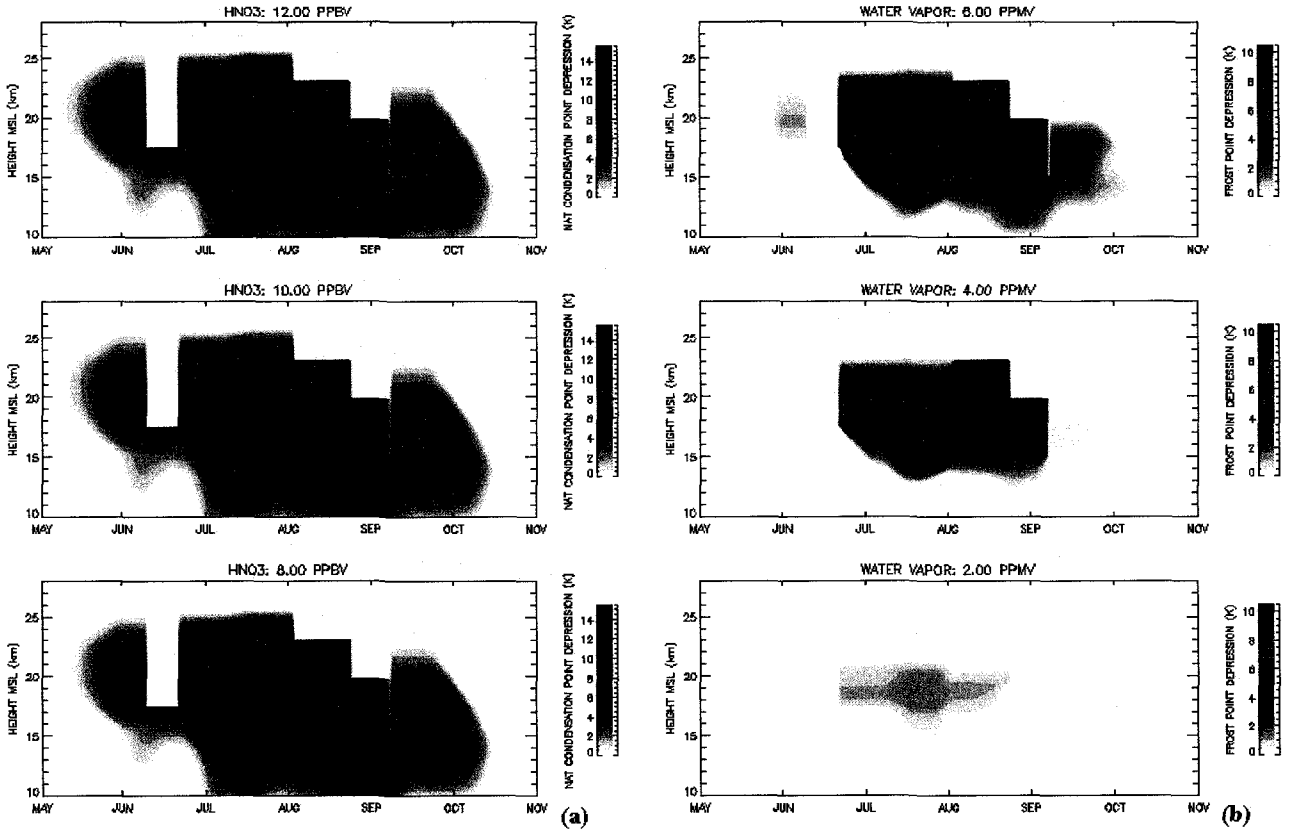

Figure 3.3 NAT and ice saturation temperature depressions.
Nitric acid condensation-point thermal depressions for 12.00 (top), 10.00 (middle) and 8.00 ppbv (bottom) and 4.00 ppmv water vapor (a), and water vapor frost point thermal depressions for 6.00 (top), 4.00 (middle) and 2.00 ppmv (bottom; b) for May - October 2000. Missing data are denoted by abrupt white gaps, and are not to be confused with zero values of the color bar.

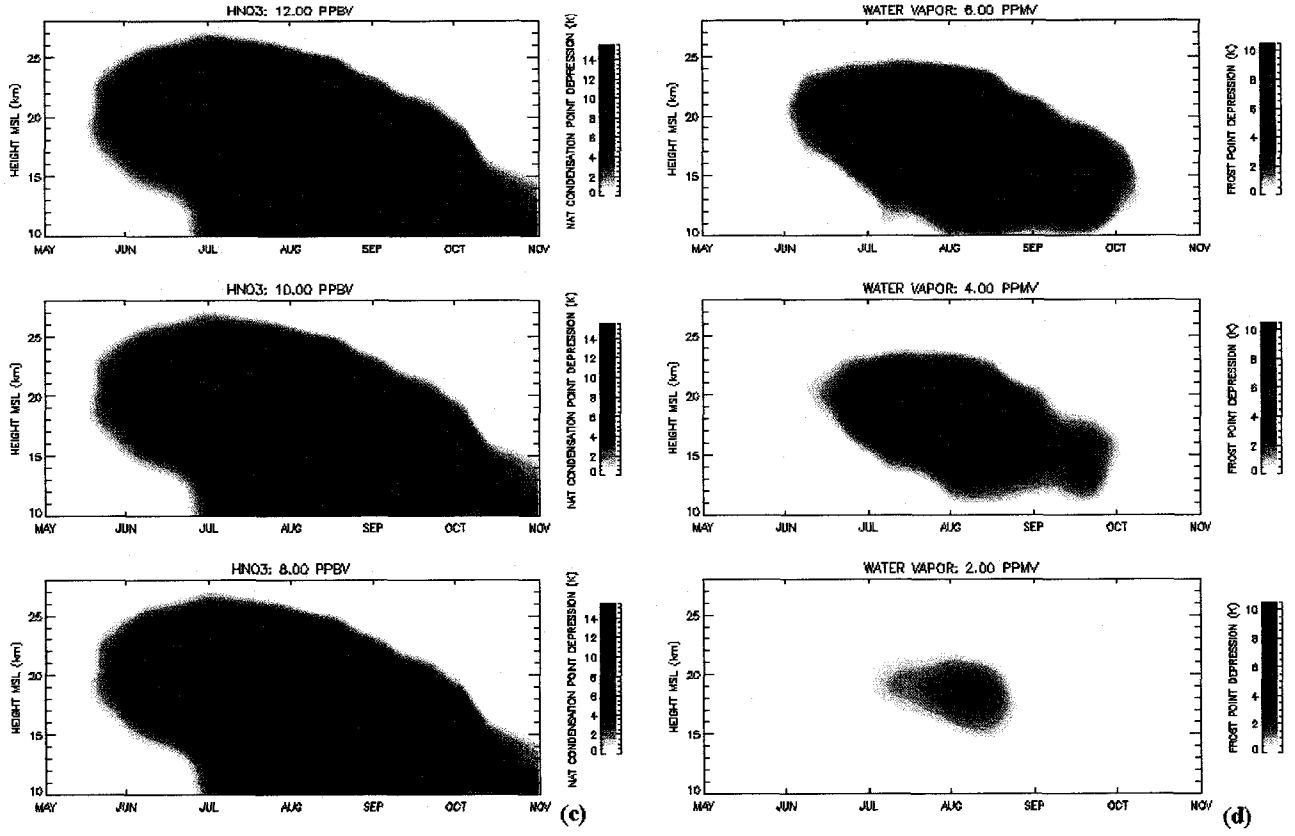

Figure 3.3 (cont.) NAT and ice saturation temperature depressions.
Nitric acid condensation-point thermal depressions for 12.00 (top), 10.00 (middle) and 8.00 ppbv (bottom) and 4.00 ppmv water vapor (c), and water vapor frost point thermal depressions for 6.00 (top), 4.00 (middle) and 2.00 ppmv (bottom; d) for May - October 2003. Missing data are denoted by abrupt white gaps, and are not to be confused with zero values of the color bar.

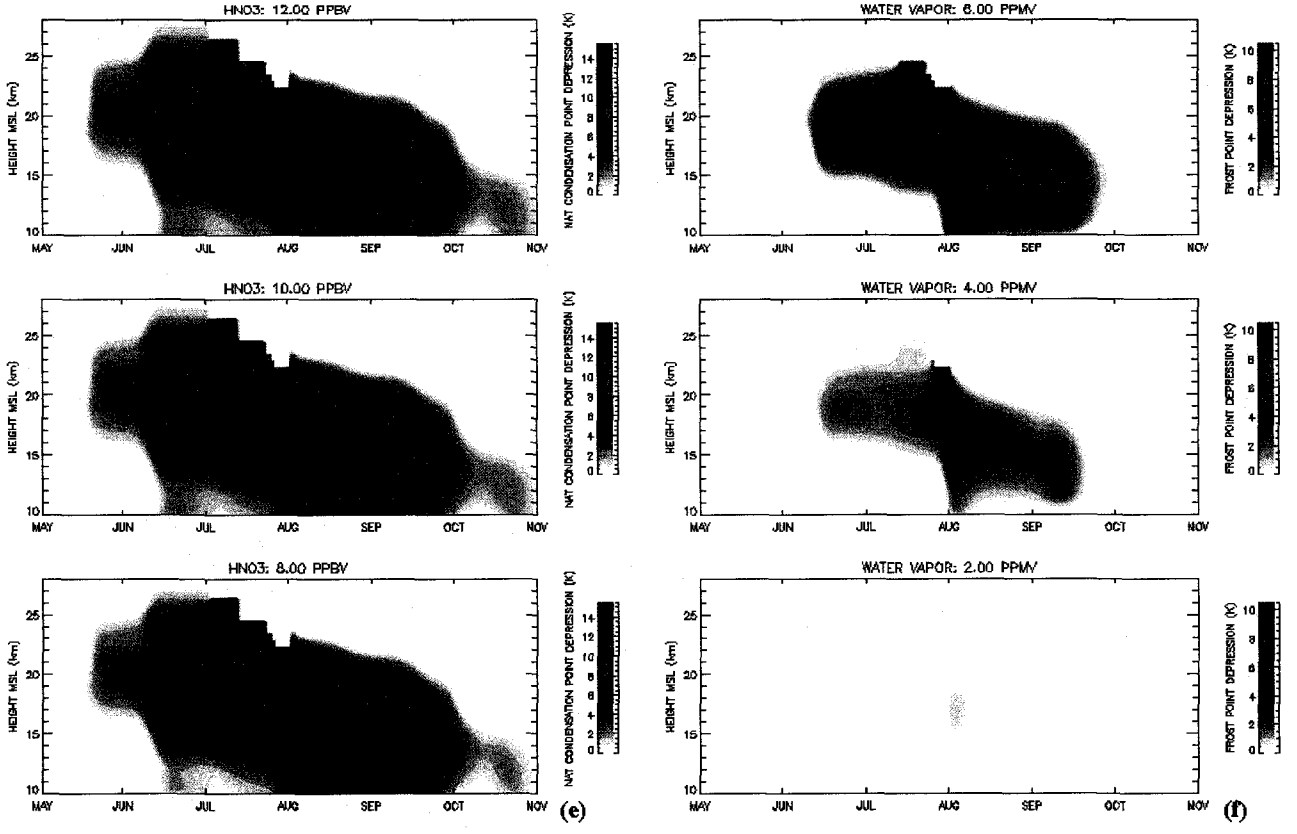

Figure 3.3 (cont.) NAT and ice saturation temperature depressions.
Nitric acid condensation-point thermal depressions for 12.00 (top), 10.00 (middle) and 8.00 ppbv (bottom) and 4.00 ppmv water vapor (e), and water vapor frost point thermal depressions for 6.00 (top), 4.00 (middle) and 2.00 ppmv (bottom; f) for May - October 2004. Missing data are denoted by abrupt white gaps, and are not to be confused with zero values of the color bar.

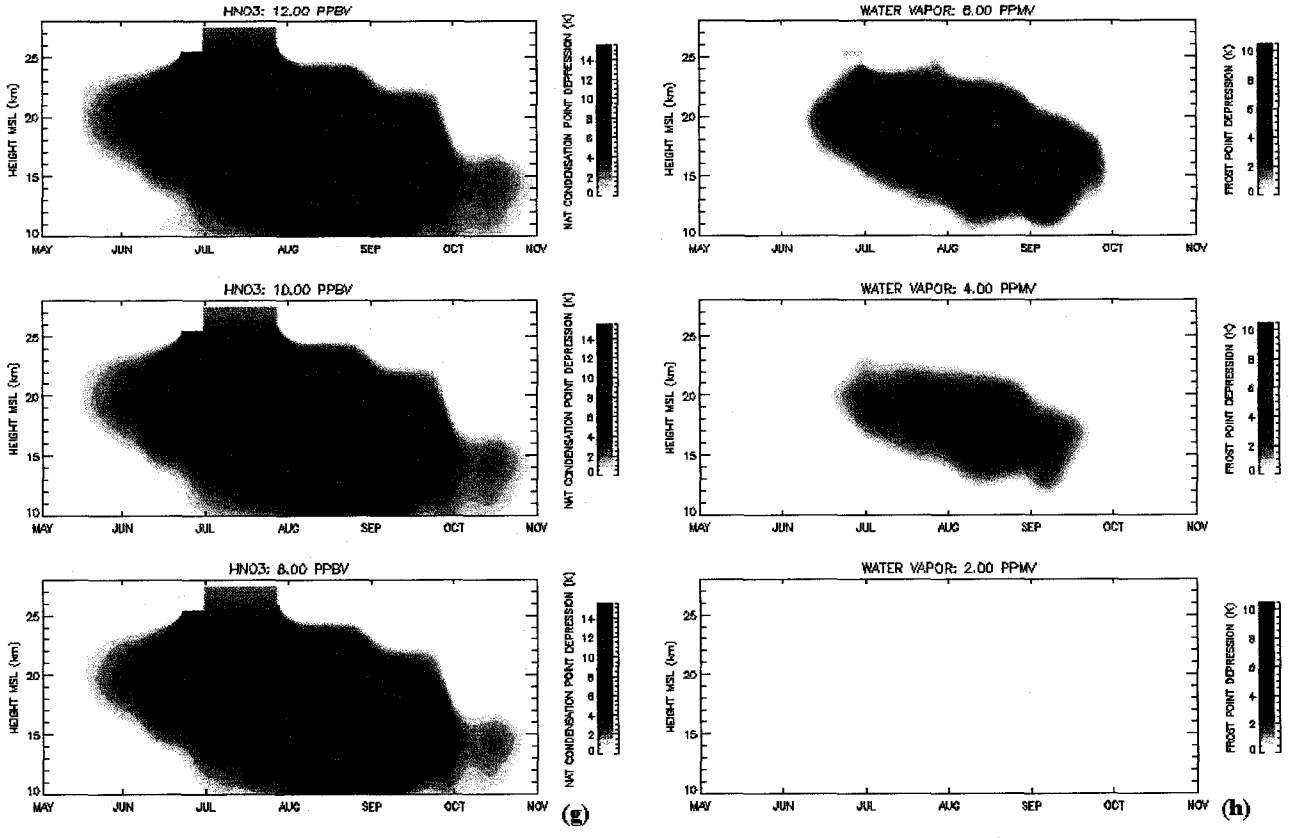

Figure 3.3 (cont.) NAT and ice saturation temperature depressions.
Nitric acid condensation-point thermal depressions for 12.00 (top), 10.00 (middle) and 8.00 ppbv (bottom) and 4.00 ppmv water vapor (g), and water vapor frost point thermal depressions for 6.00 (top), 4.00 (middle) and 2.00 ppmv (bottom; h) for May - October 2005. Missing data are denoted by abrupt white gaps, and are not to be confused with zero values of the color bar.

and II PSC will occur at lower values, likely on the order of 1 to 2 K. Therefore, these data are only approximate proxies for actual saturation scenarios, and are presented solely for qualitative analysis.

Consistent with climatological mean profiles shown in Fig. 1.3, temperatures in the lower stratosphere measured in 2000 and 2003-2005 decreased at South Pole through August (Figs. 3.2a-d). The coldest air observed each season, as a function of height, occurred at progressively lower levels beginning from May near 25.0, down through 15.0 km MSL. Temperatures dropped below 200 K at nearly every level displayed at some point during each season. The coldest air occurred during the 2000 and 2003 seasons (Figs. 3.2a and b), with the coldest temperatures overall being measured in latter season. During that year, a persistent layer of near-180 K air was detected just above 20.0 km MSL from late July into early August. Temperature minimums from other sample years also were detected near this same height, though not to this magnitude and at varying times. In 2000 the minimum temperature occurred in mid-July, in early August during 2004 (Fig 3.2c), and mid-August in 2005 (Fig 3.2d).

The 2004 and 2005 seasons were warmer relative to 2000 and 2003. Warming at the end of each season was measured to unfold from the middle-stratosphere downward. The timing of these events varied. Measurements from 2004 indicate that warming began in early August near 28.0 km MSL, and temperatures above 200 K were measured at 20.0 km MSL by early October. During the other seasons warming at 28.0 km MSL was observed to begin in early September. However, 200 K measurements at 20.0 km MSL

did not occur in 2000 and 2005 until mid-October, whereas in 2003 this occurred in early October.

With only minor discrepancies temperatures during the four-year sample were sufficiently cold to support Type I PSC for persistent periods over most of the lower stratosphere (Figs. 3.3a, c, e and g). It was shown in Fig 1.4 that the condensation temperature for NAT does not vary much at low temperatures and with HNO_3 concentrations. This is reflected in these figures as condensation-point depressions depict NAT-saturated air at each of the sample concentrations over most of the season at nearly all levels. The onset of these conditions occurred in mid-May in each of the four years, centered near 20.0 km MSL. The layer expanded to between 10.0 and 25.0 km MSL by the end of June. In 2000 (Fig 3.3a), the layer was capped at 25.0 km MSL. In other years the depth of the layer exceeded this height. Thermal depressions greater than 10 K were calculated from each season. Data from the two coldest years, 2000 and 2003 (Fig 3.3c), indicate persistent 10 K depressions in relatively deep layers. During 2004 (Fig 3.3e) and 2005 (Fig 3.3g) the 10 K threshold was exceeded only for brief periods in relatively shallow layers. NAT-saturation was calculated in 2003-2005 to have persisted through October, albeit at low levels. Warming nearing the tropopause was measured in 2000, and saturated air was not calculated past early October. Near 20.0 km MSL each year, warming caused saturated conditions to cease at the end of September.

Relative to NAT the ice frost-point temperature varies more with nominal background water vapor concentrations (Fig. 1.4). The magnitude of winter cooling, directly a function of the strength of the polar vortex (discussed in Chapter 4), determines

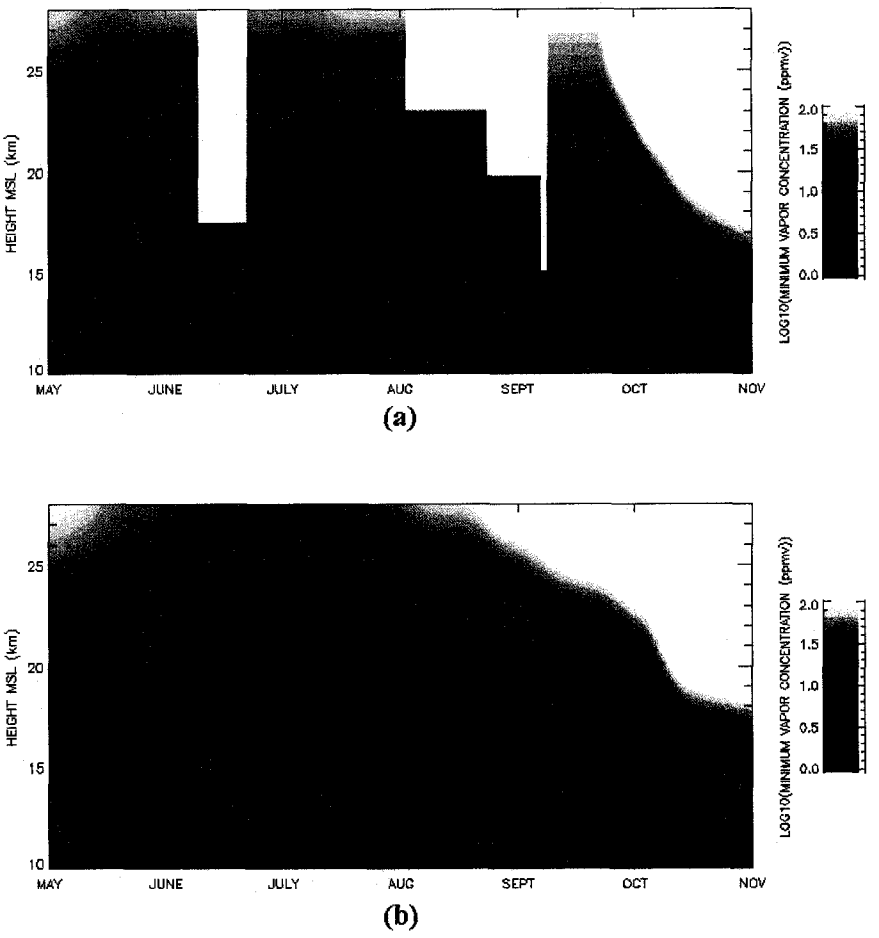

Figure 3.4 Saturation concentrations of water vapor over ice.
Profiles of water vapor saturation concentrations with respect to ice ($\log_{10}$(ppmv)) from 10.0 – 28.0 km MSL at South Pole for May - October 2000 (a) and 2003 (b). Data gaps are denoted by white gaps, and are not to be confused with saturation of the color bar.

the temporal and spatial extent to which ice saturation is possible. At 6.0 ppmv water vapor sub-saturated air was calculated over much of the lower stratosphere each season beginning from early June centered near 20.0 km MSL (Figs. 3.3b, d, f and h). These conditions persisted through September, though at progressively lower heights. Depressions approaching 10 K were common from this concentration. At the lower

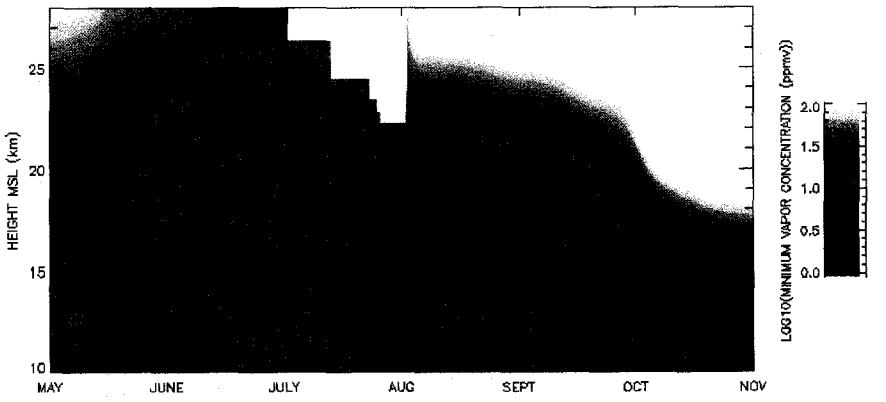

(c)

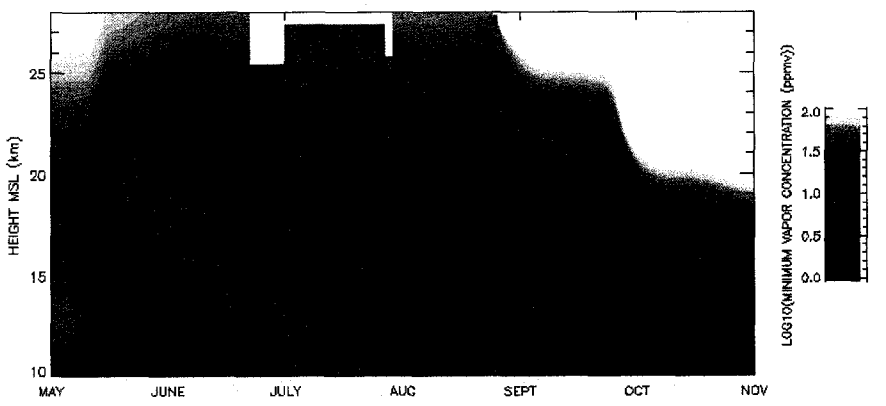

(d)

Figure 3.4 (cont.) Saturation concentrations of water vapor over ice. Profiles of water vapor saturation concentrations with respect to ice ($\log_{10}$(ppmv)) from 10.0 – 28.0 km MSL at South Pole for May - October 2004 (c) and 2005 (d). Data gaps are denoted by white gaps, and are not to be confused with saturation of the color bar.

water vapor concentrations, however, differences in the four years become more apparent. In 2000 (Fig. 3.3b), depressions were calculated from 12.5 to near 24.0 km MSL at 4.0 ppmv from mid-June through early September. In 2003 (Fig. 3.3d), such values persisted within the same range through early October. At 2.0 ppmv saturation was derived from a 3.0 km layer centered near 19.0 km MSL each season, coinciding

with the coldest air from each year. In the warmer years, 2004 (Fig. 3.3f) and 2005 (Fig. 3.3h), relatively low depressions were calculated between 12.5 and 20.0 km MSL at 4.0 ppmv from mid-June to mid-September. At 2.0 ppmv, minimal depressions were calculated from either year.

These data can also be viewed in the form of the saturation vapor concentration with respect to ice (Figs. 3.4a-d). Either method is simply a proxy for temperature. The likelihood for ice nucleation and growth in PSC at South Pole can be limited by the extent of seasonal cooling and the availability of water vapor. These calculations are not necessarily truth, but instead reasonable estimates for where Type I and II PSC should be observed based on previous measurements, assuming no major perturbations. The lack of high spatial and temporal resolution measurements of water vapor and other chemical compounds in and around South Pole is an issue that needs to be resolved during polar night. Satellite techniques and measurements are improving, but limitations exist, as discussed in Chapter 1. Depolarization lidar measurements would be very beneficial to differentiating between ice, near-spherical hydrate particles and solution droplets.

3.3 Temporally and Spatially Smoothed PSC Observations

Algorithm results for attenuated scattering ratio (ASR) corresponding to the data shown in Fig. 2.10 are reintroduced in Fig. 3.5a, having been smoothed to 0.5 day and 0.250 km resolution using the Hanning function at 5.0 day and 0.750 km temporal and spatial half-widths. These settings were chosen to balance the need for smoothing gaps resulting from missing data, or attenuation-limiting effects, without blurring PSC

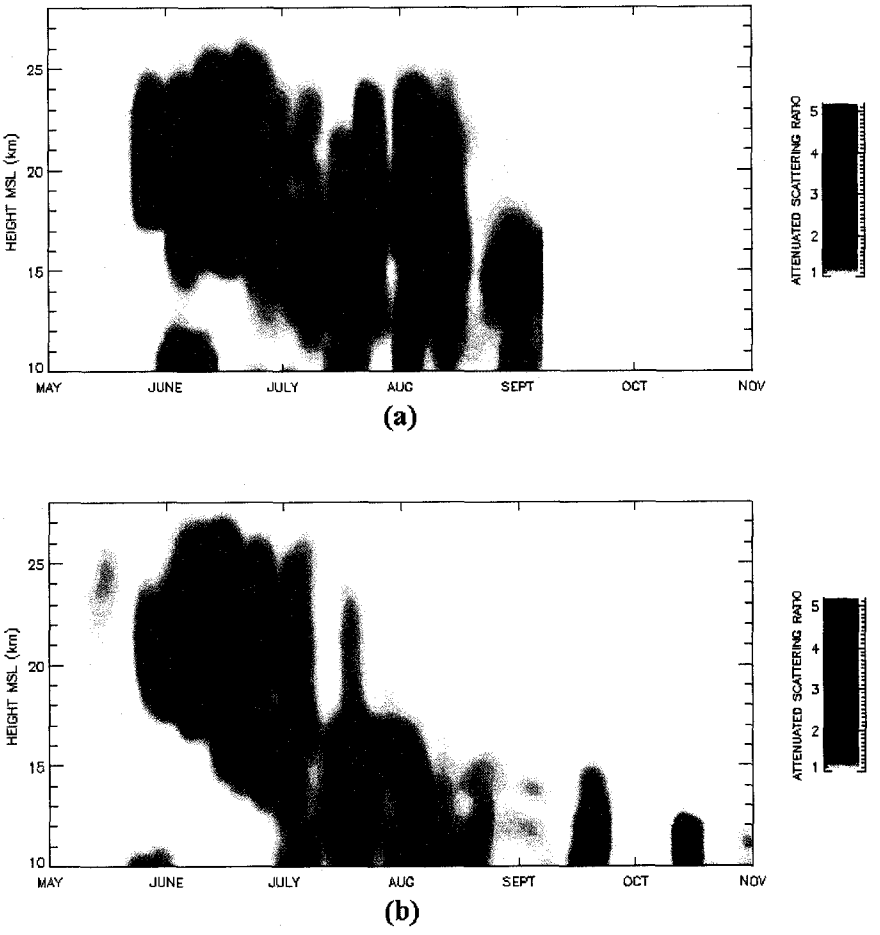

Figure 3.5 Smoothed annual attenuated scattering ratio profiles. Corresponding to Figs. 2.10a-d, smoothed profiles of attenuated scattering ratio from 10.0 – 28.0 km MSL at South Pole for May - October 2000 (a) and 2003 (b). Data from 2000 are only through early September.

episodes too severely. The data are shown from 10.0 to 28.0 km MSL. In Fig. 3.6 the ASR data are converted to an approximate attenuated backscatter cross-section based on Eq. (2.24). The data are only shown for values exceeding 1.0×10^{-5} $km^{-1} \cdot sr^{-1}$, an approximate lower limit based on *Gobbi et al.* (1998). Equation (2.24) may be written as

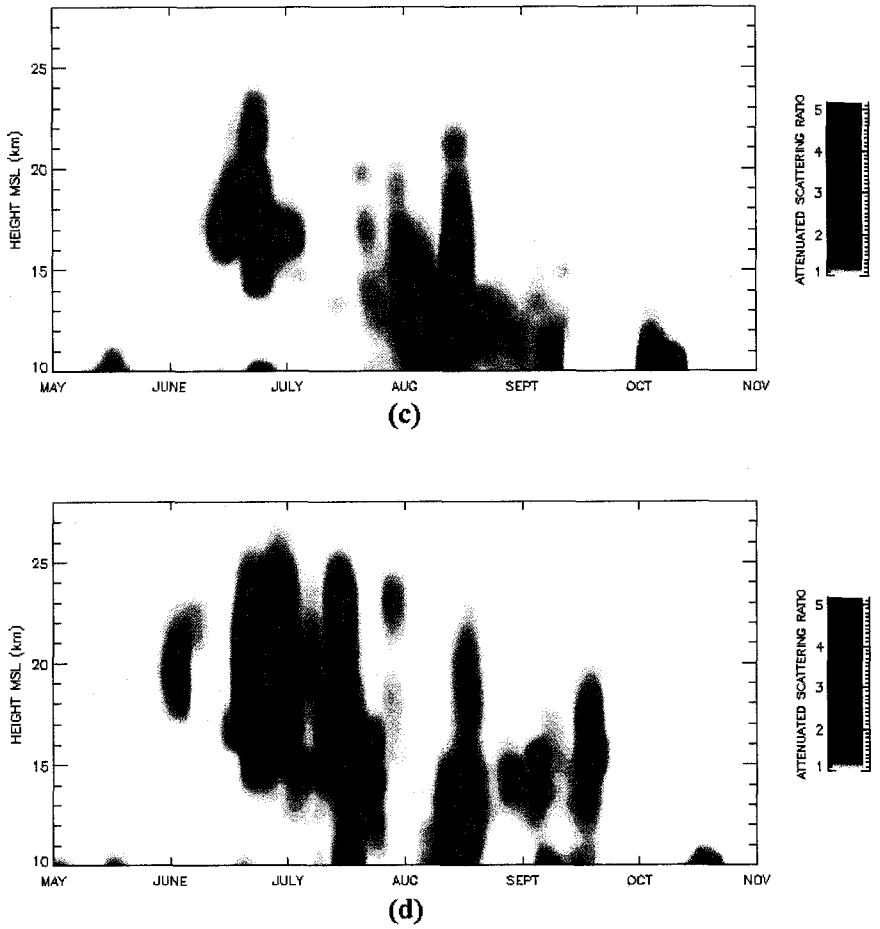

Figure 3.5 (cont.) Smoothed annual attenuated scattering ratio profiles. Corresponding to Figs. 2.10a-d, smoothed profiles of attenuated scattering ratio from 10.0 – 28.0 km MSL at South Pole for May - October 2004 (c) and 2005 (d).

$$\beta_r(r) = \left(\frac{\beta_p(r)}{\beta_m(r)} + 1\right) T_p^2(r) \tag{3.1}$$

After subtracting for unity and multiplying by the molecular backscatter cross-section, Eq. (3.1) becomes

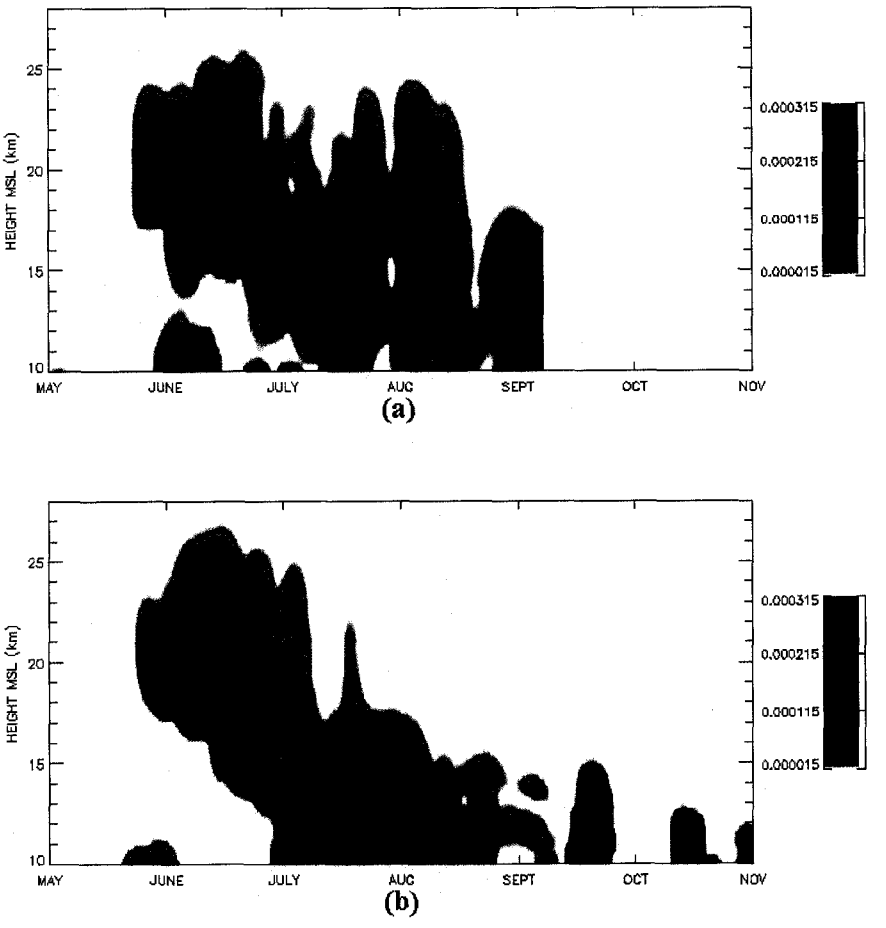

Figure 3.6 Smoothed annual approximate attenuated backscatter profiles. Following Fig. 3.5, smoothed profiles of approximate attenuated backscatter cross-section (> 1.5×10^{-5} $km^{-1} \cdot sr^{-1}$) from 10.0 – 28.0 km MSL at South Pole for 2000 (a) and 2003 (b).

$$\beta_p(r) = \left(\frac{\beta_{r^*}(r)}{T_p^2(r)} - 1 \right) \beta_m(r) \tag{3.2}$$

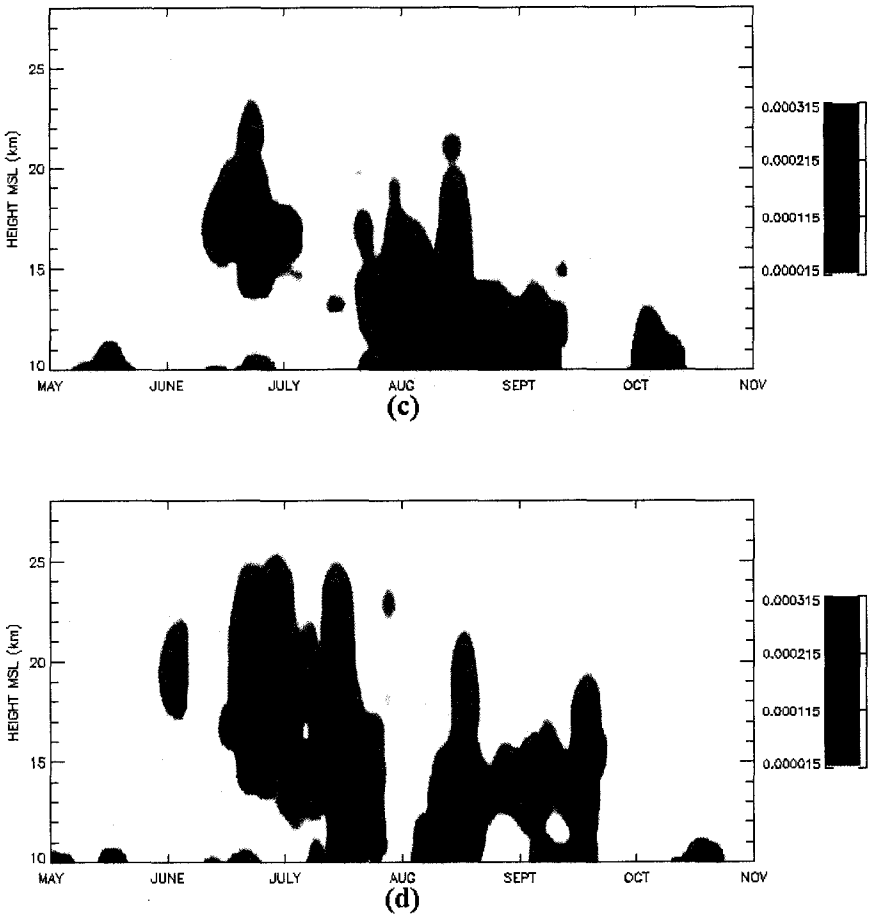

Figure 3.6 (cont.) Smoothed annual approx. attenuated backscatter profiles. Following Fig. 3.5, smoothed profiles of approximate attenuated backscatter cross-section (> 1.5×10^{-5} $km^{-1} \cdot sr^{-1}$) from 10.0 – 28.0 km MSL at South Pole for 2004 (c) and 2005 (d).

For the case where particulate attenuation is small, which is common for PSC and other polar clouds (e.g., *Collins et al.*, 1993; *Gobbi et al.*, 1998), the transmission term in the denominator approaches 1.0 and this equation reduces to

$$\beta_p(r) = \left(\beta_{r^*}(r) - 1\right)\beta_m(r) \tag{3.3}$$

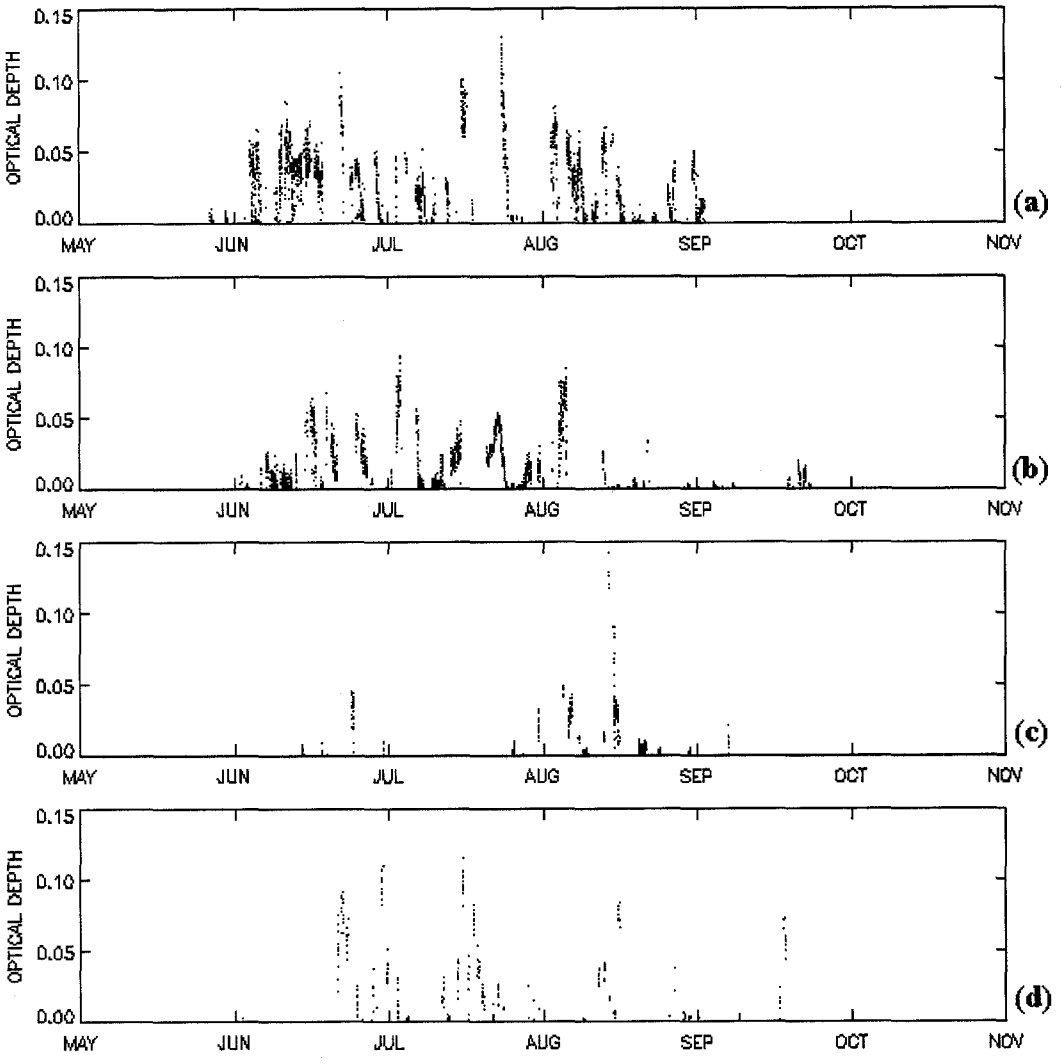

Figure 3.7 Optical depth retrievals from raw algorithm output. Optical depths (0.523 μm) derived from unsmoothed algorithm profiles (Fig. 2.10) for May – November 2000 (a), 2003 (b), 2004 (c) and 2005 (d).

or the attenuated backscatter cross-section. However, this assumption is not always appropriate. In Fig. 3.7, optical depths derived based on raw algorithm profiles (Fig. 2.10) for each year are shown. They were calculated from signal measured between 12.0

and 24.0 km MSL, using an extinction-to-backscatter ratio of 25.0 (typical of tropospheric ice particles; e.g., *Ansmann et al.*, 1992) for a minimum backscatter cross-section of 1.0×10^{-5}, as described above. Derived values frequently exceed 0.03, the approximate threshold separating visual and sub-visual clouds (*Sassen and Cho*, 1992). At this value, from Eq. (2.28) two-way transmission at cloud top is approximately 0.94. Therefore, with many cases, signal attenuation is approaching and exceeding five percent. This limits both the sensitivity to optically thin clouds at upper-levels, and violates the assumption leading to Eq. (3.3). For this discussion, the retrieved backscatter cross-section is referred to as the approximate attenuated backscatter (AAB).

Table 3.2 is a summary of PSC occurrence statistics from these smoothed datasets. From 12.0 – 24.0 km MSL those bins where AAB exceeds 1.0×10^{-5} km^{-1} sr^{-1} are summed, followed by the corresponding total integrated ASR and AAB values. Similar values are also shown for three height intervals (20.0 – 24.0, 16.0 – 20.0 and 12.0 – 16.0 km MSL). The threshold value of was chosen based on the order of magnitude corresponding to the lower end of similar PSC backscatter measurements from a 0.532 μm lidar at McMurdo Station, Antarctica (*Gobbi et al.*, 1998). This value also serves to limit the inclusion of what can be considered 'noisy' bins into the data sample developed from smoothing. Limiting the sample tops to 24.0 km MSL was done to coincide with the typical maximum height of ozone loss that occurred during these four years (Fig. 3.1).

In data from the four-year sample, the most PSC bins, highest integrated ASR, and highest integrated AAB were derived from 2000 data (Fig. 3.5a; Fig. 3.6a). Interestingly, data from that season are only available through early September. From the integrated

Table 3.2 Statistical analysis of smoothed processed datasets.
From Figs. 3.5 and 3.6, the number of 0.250 km bins at 0.5 day resolution measuring a smoothed attenuated scattering ratio greater than 1.2 from 12.0 to 24.0 km MSL and the corresponding integrated backscatter ratio and backscatter cross-section, followed by those same values for three specific height intervals.

Year	# Bins	$\Sigma\frac{\beta_p T_p^2}{\beta_m}$	$\Sigma\beta_p T_p^2$	Range	# Bins	$\Sigma\frac{\beta_p T_p^2}{\beta_m}$	$\Sigma\beta_p T_p^2$
2000	8477	14913.43	0.99	20.0 – 24.0 km	2567	4850.28	0.20
				16.0 – 20.0 km	3029	6002.43	0.47
				12.0 – 16.0 km	2881	4060.72	0.33
2003	6382	10947.17	0.70	20.0 – 24.0 km	1649	3806.95	0.18
				16.0 – 20.0 km	1904	3304.61	0.22
				12.0 – 16.0 km	2829	3835.60	0.30
2004	3709	5263.11	0.33	20.0 – 24.0 km	343	450.36	0.01
				16.0 – 20.0 km	1386	2212.25	0.14
				12.0 – 16.0 km	1980	2600.50	0.18
2005	6186	9669.44	0.59	20.0 – 24.0 km	1377	2430.56	0.09
				16.0 – 20.0 km	2177	3593.28	0.24
				12.0 – 16.0 km	2692	3645.60	0.27

ASR analysis, values in 2000 exceeded the next closest year, 2003, by nearly fifty percent. However, ASR is a weighted value dependent upon the molecular scattering cross-section, which decreases with height. At 12.0 km MSL the molecular scattering cross-section is approximately 4.0×10^{-4} $km^{-1} \cdot sr^{-1}$, whereas at 24.0 km MSL the value is roughly 2.5 times less. AAB is, instead, an absolute value. Using this parameter, the integrated value in 2000 exceeded the next closest year, 2003, by only about twenty-five percent. In comparing Figs. 3.5 and 3.6, ASR is more appropriate for delineating all PSC

layers, including those that are optically thin. AAB varies commonly by an order of magnitude, and is, therefore, more sensitive to optically thick episodes. It is best used as a proxy for more dense clouds.

The onset of persistent PSC in 2000 occurred in late May from 18.0 to near 25.0 km MSL (Fig 3.5a). By mid-June the layer was over 10.0 km deep, and present from 15.0 to near 26.0 km MSL. Seasonal peaks in ASR were observed near 18.0 km MSL during the latter half of that month. AAB peaks corresponded to these same events (Fig. 3.6a). Perhaps not coincidentally, the integrated ASR and AAB maximums were derived from the 16.0 to 20.0 km MSL interval in this year (Table 3.2). From July through August PSC occurrence was episodic. Clouds were observed to near 25.0 km MSL through mid-August, and to near 18.0 km MSL through the end of the observing period.

The 2003 season was second highest for PSC occurrence (Table 3.2). Cloud structure, as observed from mid-May to the end of June, evolved comparably to 2000 (Figs. 3.5b and 3.6b). PSC were first observed near 20.0 km MSL, though the lower boundary of their presence reached 15.0 km MSL a few weeks later than having occurred in 2000. Seasonal peaks in ASR and AAB were observed near 24.0 km MSL in the first half of June. This was nearly 5.0 km higher and approximately one week earlier than in 2000. An additional AAB peak were observed in mid-June near 17.0 km MSL, followed by strong lower-level peaks intermittently seen the rest of the season, and likely due to upper-tropospheric events. PSC occurrence ceased above 17.0 km MSL beginning in early July, except for a brief episode in the middle of the month seen from ASR data. The distribution of cloud was consistent over each of the three height ranges described in

Table 3.2. Overall occurrence was approximately 10% higher than the next closest year, 2005, and integrated ASR was roughly 20% higher. Integrated AAB, however, was nearly 50% higher than 2005. This indicates that optically thicker clouds and greater ice content were observed in 2003 relative to 2005, which correlates with colder temperatures occurring in that year.

PSC occurrence during the 2004 season was the lowest of the four- year sample by a wide margin. The number of PSC bins measured was roughly half of the values measured in 2003 and 2005 (Table 3.2). Total integrated ASR was less than that. Although the number of bins sampled was low at each of the three height intervals, the lack of measurements in the 20.0 to 24.0 km MSL interval deviated most from other years. The onset of PSC occurrence did not begin in late May, but rather in mid-June (Figs. 3.5c and 3.6c). The initial pulse of clouds was not persistent compared to other years, and only a brief period of relatively high ASR and AAB was detected near 17.0 km MSL in the second half of the month. Few episodes were detected from July forward, though a strong pulse in mid-August produced measurable ASR and AAB near and above 20.0 km MSL.

The 2005 season began in a manner consistent with measurements from 2000 and 2003. Clouds were first observed centered at 20.0 km MSL in late May (Figs. 3.5d and 3.6d). They then abruptly ceased. Instrument performance from 2-7 June was poor, the result of a failing laser diode that would soon be replaced. Data gaps, from both poor SNR and low-level cloud attenuation, occurred during the ten first days of June (Fig. 2.10d). Still, nominal instrument performance was restored by 11 June, clear skies were

apparent near the surface, and no PSC was measured. Clouds would not return for another week, when the seasonal maximum of ASR was detected at 20.0 km MSL and a corresponding AAB maximum was measured near 17.0 km MSL. Clouds detected during the remainder of the season occurred in limited episodes. They were measured above 20.0 km MSL through mid-August, and to near 20.0 km MSL in mid-September. This season ranks third among the four-year sample for total PSC, integrated ASR and integrated AAB for both the sum totals and at each of the three height intervals.

The ASR and AAB data are consistent with previous measurements reported from lidar studies at the South Pole. *Fiocco et al.* (1991, 1992) and *Fuà et al.* (1992) report 0.532 μm measurements of PSC layers made episodically during winter 1988. *Fiocco et al.* (1992) describe continuous layers frequently greater than 5.0 km in depth up to 21.0 km MSL, with attenuated backscatter ratios regularly approaching 4.0 and backscattering cross-sections commonly on the order of 1.0×10^{-4} $km^{-1} \cdot sr^{-1}$. *Cacciani et al.* (1997a; 0.532 μm) and *Collins et al.* (1993; 0.589 μm) report similar characteristics in episodic measurements made during winter 1990, just before the Mt. Pinatubo eruption. *Collins et al.* (1993), in particular, report diffuse PSC, with ASR just above 1.0, near and above 15.0 km MSL as late as October. *Rosen et al.* (1993) report measurements from a series of balloon-borne dual-wavelength backscattersondes (akin to the lidar technique, though in-situ) that, though limited, are also consistent in cloud structure evolution versus temperature during winter 1991. *Cacciani et al.* (1997b) report measurements made post-Pinatubo during the winters of 1992 and 1993. These MPL data are also consistent with measurements from coastal Antarctic sites, including from Syowa Station (*Iwasaka et al.*,

1985; *Iwasaka*, 1986a, b), Dumont d'Urville (66.4° S, 140.0° E; *Stefanutti et al.*, 1991; *Santacesaria et al.*, 2001) and McMurdo Station (*Gobbi et al.*, 1998).

3.4 Composite Summary Images

Data from the preceding sections, including ozone concentrations, thermal depressions relative to NAT/ice saturation and ASR, are overlaid and redisplayed here in a series of composite summary images from 5.0 to 28.0 km MSL for May to December each year (Figs. 3.8a-d). Beneath each image is the corresponding time-series of smoothed 3.0 km MSL DU measurements for column ozone concentration from ozonesonde measurements. A dashed line is shown representing 220 DU, where the ozone hole is considered overhead. Ozone partial pressures are plotted for 4.0, 2.0 and 1.0 mPa. Positive thermal depressions are displayed for temperatures relative to the NAT condensation point only at 10.0 ppbv HNO_3 given 4.0 ppmv water vapor and relative to the ice frost-point at 6.0, 4.0 and 2.0 ppmv water vapor. As proxies for temperature, the thermal depressions plotted versus ASR effectively mirror temperature versus cloud boundary displays generated from episodic South Pole lidar measurements in winter 1990 by both *Collins et al.* (1993) and *Cacciani et al.*, (1997a).

PSC occurrence was highest during the two colder years of the sample, 2000 and 2003 (Figs. 3.8a and b). Yet, more cloud was observed and ozone loss more severe in 2000, rather than 2003 where colder air was observed. During both years PSC were first observed in late-May. Clouds appeared after the onset of NAT-saturated air derived at 10.0 ppbv HNO_3/4.0 ppmv water vapor concentrations, but before saturation with respect

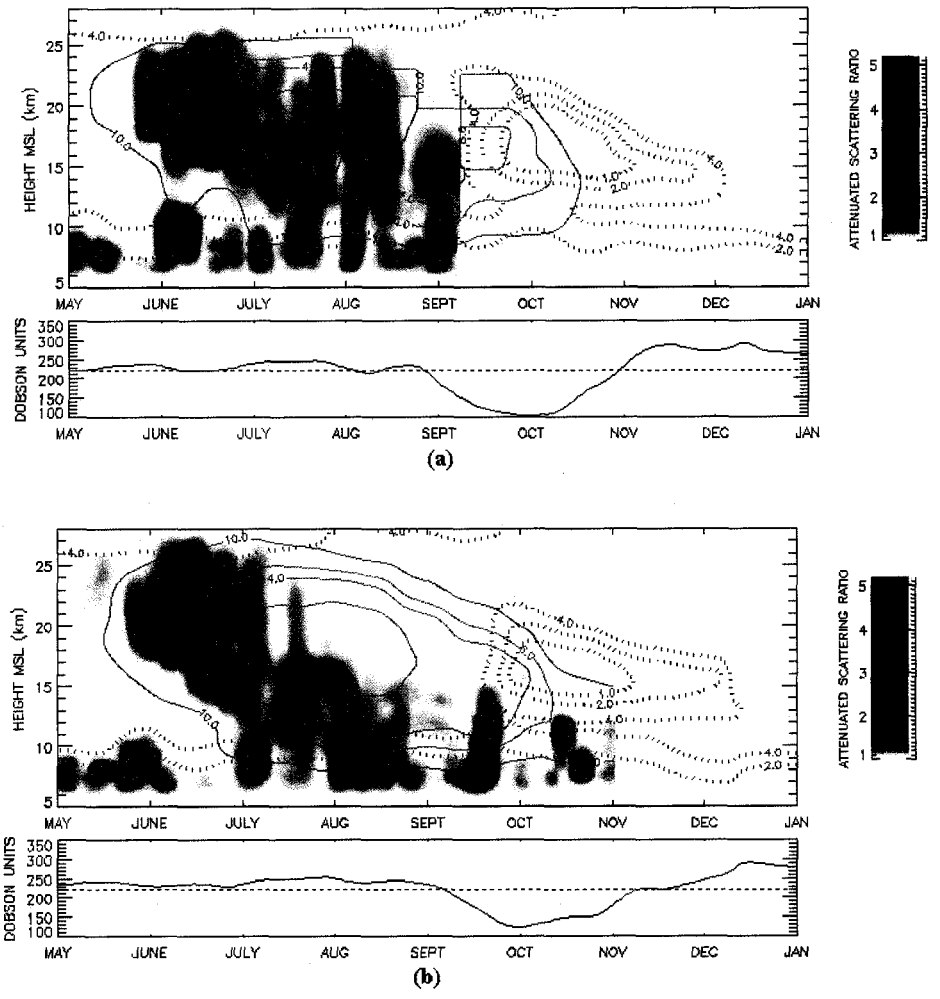

Figure 3.8 Annual composite summary images.
Composite summaries of the data from Figs. 3.1, 3.3 and 3.5 for May to December 2000 (a) and 2003 (b), including positive NAT condensation-point depressions for 10.0 ppbv HNO_3/4.0 ppmv H_2O (green), positive ice frost-point depressions for 6.0, 4.0 and 2.0 ppmv water vapor (red) and ozone partial pressures less than 4.0, 2.0 and 1.0 mPa (blue dashed). 3.0 km MSL Dobson Unit measurements are shown in lower graph, with the dotted line representing 220 DU.

to ice at 6.0 ppmv water vapor. As temperatures cooled through June, conditions more favorable to ice saturation gradually evolved and higher ASR were observed. The 2003

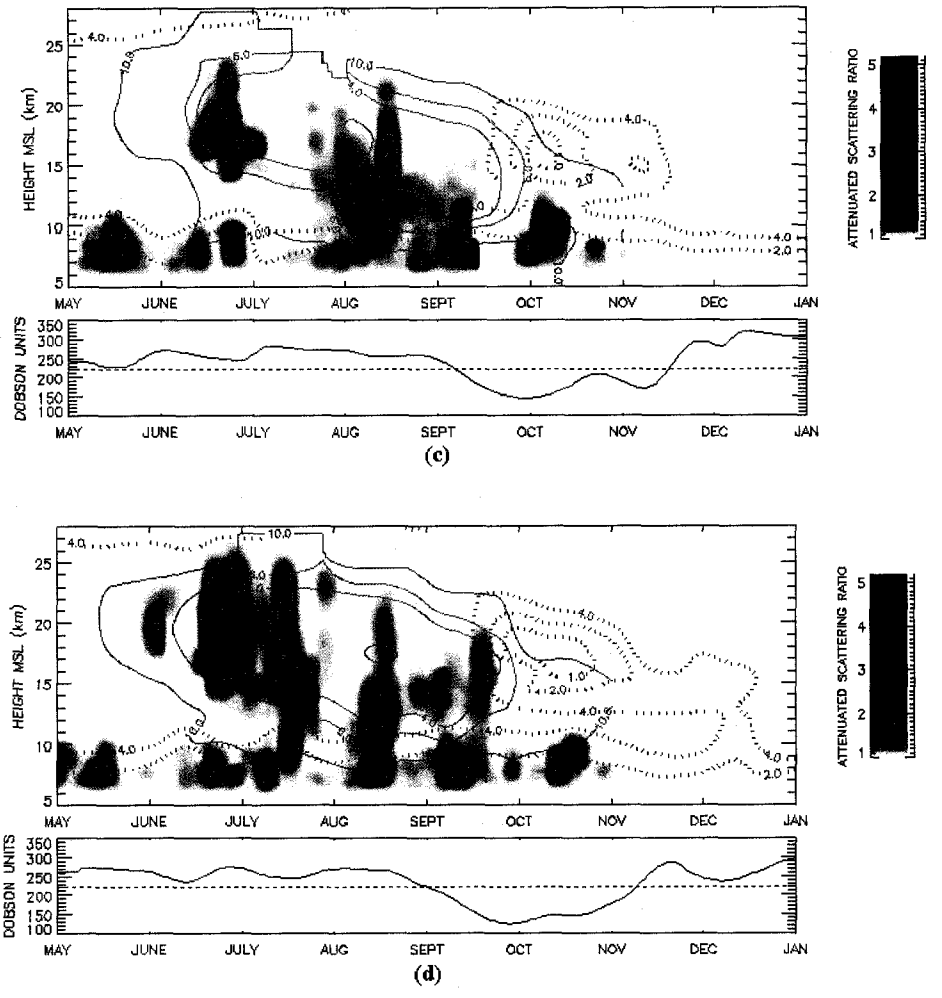

Figure 3.8 (cont.) Annual composite summary images.
Composite summaries of the data from Figs. 3.1, 3.3 and 3.5 for May to December 2004 (c) and 2005 (d), including positive NAT condensation-point depressions for 10.0 ppbv HNO_3/4.0 ppmv H_2O (green), positive ice frost-point depressions for 6.0, 4.0 and 2.0 ppmv water vapor (red) and ozone partial pressures less than 4.0, 2.0 and 1.0 mPa (blue dashed). 3.0 km MSL Dobson Unit measurements are shown in lower graph, with the dotted line representing 220 DU.

ASR maximum occurred just after the onset of ice saturation at 6.0 ppmv water vapor.

The upper limit to cloud observations in both years closely matches the 10.0 ppbv/4.0

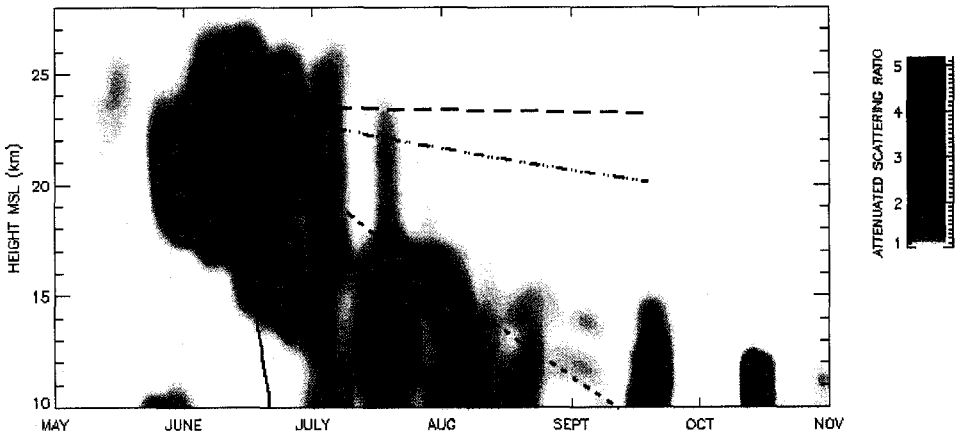

Figure 3.9 Lower-stratospheric fall-trajectories for spherical particles. Fall-trajectories for spherical particles of mass density 1.0 gm/cm^3 based on *Kasten* (1968) at 10.0 μm (solid), 3.0 μm (short dash) 1.0 μm (dash/dot) and 0.1 μm (long dash) radius superimposed on attenuated scattering ratio data from 2003 (Fig. 3.5b).

ppmv NAT isopleth, whereas the lower extent of cloud presence follows that for saturation with respect to ice. The possibility for gravity wave enhancement is more likely at upper levels given a higher wave potential energy component inherent in the thermal inversions occurring there (discussed further in Chapter 4). Evaporation is likely occurring at lower levels below cloud base, and thus in the region between the ice and NAT-saturated isopleths.

Type I PSC are likely present in these measurements under certain conditions (discussed further in Chapter 4 and in Appendix B). If so, they would need to be present in sufficiently high particle concentrations so as to generate sufficient volume scattering cross-sections to exceed minimum threshold at 0.01 fractional day resolution. Otherwise, most PSC observed with the MPL fall within the bounds of ice-saturated air masses. It is

possible that anomalously high water vapor concentrations are present in these summaries (e.g., *Rosenlof et al.*, 2001). However, it can be roughly approximated that the instrument is detecting Type II PSC, particularly at heights exceeding 15.0 km MSL where the sensitivity of the algorithm with respect to ASR decreases rapidly with height and air is mostly ice-saturated.

Rather than an immediate removal of nitrogen and water vapor, most commonly inferred from conceptual descriptions of denitrification and dehumidification, these data indicate a gradual repartitioning within the lower stratosphere over time. The migration of nitrogen and water vapor downward through nucleation, growth, sedimentation and evaporation, particularly in clouds originating from heights exceeding 20.0 km MSL, may influence PSC occurrence and growth later in the season as temperatures at lower levels gradually become more favorable. This would enhance the surface area available to heterogeneous reactions, and eventually influence the magnitude of catalytic ozone loss in spring, which is at a maximum at these heights. In Fig. 3.9 are 100-day fall-trajectories superimposed on data from Fig. 3.5b for spherical particles (1.0 gm/cm^3 mass density) of 10.0, 3.0, 1.0 and 0.1 μm radius (*Kasten*, 1968), assuming no evaporation, corresponding to the ASR maximum near 23.0 km MSL in June 2003. Accordingly, particles with diameters approaching 20.0 μm fall at a rate of approximately 1.0 km day^{-1}. Near 1.0 μm diameter, the falling velocity varies through the lower-stratosphere from between a kilometer every twenty-five to sixty days. Sub-micron sized particles do not fall appreciably. Multiple number concentration modes in particle size distributions within these ranges have been measured in PSC (e.g., *Dye et al.*, 1992; *Toon et al.*, 2000),

and sub-micron particles capable of a persistent presence are consistent with measurements of diffuse PSC above 20.0 km in lidar measurements from as late as August (*Collins et al.*, 1993), and below this height through October (*Fiocco et al.*, 1992) at the South Pole. There is the possibility that particles with diameters between 2.0 and 6.0 μm formed during May and June at upper levels fall at a rate consistent with the rate of cooling (also negatively sloped versus height through August, e.g., Fig. 3.2b) so as to maintain thermal equilibrium. Since these calculations do not consider evaporation or airmass trajectories, this cannot be said definitively.

In May and June 2003, high ASR and AAB were measured above 20.0 km MSL. These levels do not coincide with levels where appreciable ozone loss was detected later in the year. In 2000, maximum ASR values were measured at heights corresponding with maximum ozone loss. Greater ozone losses were measured in that year than 2003. These data alone cannot be used to say one way or another whether or not these findings are coincidental or not.

Data from 2000 and 2003 during July and August depict two scenarios having occurred. In 2000, PSC occurrence was episodic, but persistent. Clouds were observed mostly within the bounds of air favorable to ice saturation, and NAT at lower levels, at standard background concentrations. During 2003, however, PSC were not observed, despite similar, if not colder conditions. Given the abundance of clouds detected early in 2003, denitrification and dehumidification were likely major factors for air in and around South Pole influencing cloud formation during that year. That is, barring some unknown

recycling of vortex air, whereby anomalously low nitrogen and water vapor concentrations were introduced.

Similar amounts of PSC were detected early in 2000 compared to 2003, but denitrification and dehumidification would not appear to have been anywhere near as significant that season, at least through August. Three explanations are plausible. First, more mixing occurred within the polar vortex during 2000 without significant intra-vortex influence. If adiabatic lifting and cooling along isentropic trajectories approaching South Pole is the dominant mechanism inducing PSC observed there (e.g., *Palm et al.*, 2005) then over the course of three months, in a highly mixed vortex, the area immediately surrounding the Pole may act to induce PSC in a manner similar to an orographic cap cloud. In this scenario, air within the vortex would gradually mix toward South Pole, and PSC there would generally be seen as persistent. Denitrification and dehumidification would be widespread, but occur more gradually. Gravity waves and baroclinic disturbances would still remain important processes in PSC nucleation, but be confined more to along the edges of the vortex. For a particularly strong vortex mixing would not be as great. Temperatures near the Pole would be colder, but in the absence of a significant mixing of air from nearer the vortex edges over time denitrification and dehumidification would occur more rapidly, and in a more confined area. A second explanation would be a meridional weakening of gradients along the vortex edges such that mixing across this boundary is replenishing nitrogen and water vapor concentrations at heights already denitrified and dehumidified from previous PSC events. This is not necessarily consistent with measurements in 2000, since such mixing would also increase

meridional heat transport, and that year was a relatively cold one for this sample. A final explanation would be a compromise somewhere between these two scenarios. This discussion is continued in Chapter 4, following a review of vortex dynamics, their potential influence on PSC at South Pole and trajectory analysis.

It is possible that it the data from 2000 are biased with respect to the other years. As noted previously, data collected with the instrument that season exhibited higher SNR. The particulate layer algorithm may have been more sensitive to low optical-depth PSC as a result. Episodes of high attenuated scattering ratio, however, were measured in late July and early August that are not evident in 2003 data. If biases were to be found, more likely ASR values just above minimum ASR thresholds would be expected. Instead, these appear to be legitimate PSC episodes, with clouds exhibiting appreciable backscatter cross-sections.

During the two warmer seasons of the four-year sample, 2004 and 2005 (Figs. 3.8c and d), springtime ozone losses and PSC occurrence were lower than the previous seasons. The maximum ozone hole area during 2004 was second-lowest since 1991. PSC during the year were scarce. Losses during 2005 were average compared to the ten-year mean, and PSC occurrence was moderate compared to other years. The onset of PSC during 2004 coincided with that of ice-saturation at 6.0 ppmv water vapor concentration, with the seasonal ASR and AAB peak occurring in late June at 17.0 km MSL. Save for episodes in late July and early August clouds were not observed during the remainder of the year, despite conditions favorable to saturation of both NAT and ice at standard background concentrations.

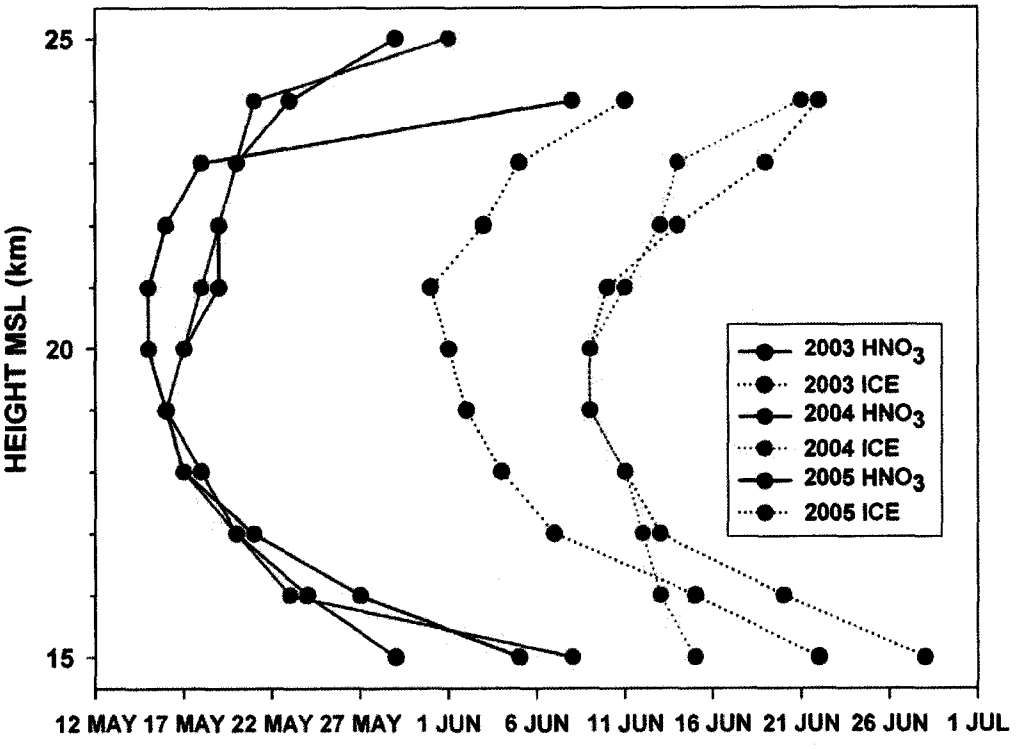

Figure 3.10 Onset dates for NAT and ice saturation in 2003-2005.
Onset dates for the presence of saturated air with respect to nitric acid trihydrate (solid) and ice (dashed) for 10.0 ppbv nitric acid/4.0 ppmv vapor water vapor and 6.0 ppmv water vapor in 1.0 km intervals from 10.0 – 25.0 km MSL at South Pole for 2003 (black), 2004 (red) and 2005 (black).

The 2005 season commenced similar to 2000 and 2003, with PSC occurring before saturation with respect to ice. However, as discussed above, the clouds vanished, only returning in late June and continuing through mid-July. The seasonal ASR maximum was derived in mid-June just above 20.0 km MSL. Brief episodes occurred in mid-August and mid-September with cloud above 15.0 km MSL. The tops of clouds observed from both of the years are capped by saturation isopleths with respect to ice at 6.0 ppmv

water vapor, except in late June 2005 where tops briefly exceed this threshold. The extent of gravity wave influence here is examined in Chapter 4. Similar to 2000 and 2003 the lower extent of PSC follow the 6.0 ppmv ice isopleth closely indicating evaporation below these levels.

One notable aspect of 2004 and 2005 measurements relates to the hypothesis of *Tabazadeh et al.* (2001). From model calculations, incorporating growth rates for solid NAD and NAT particles as a function of temperature, they describe a polar "freezing belt" corresponding to temperatures between 190 and 192 K. Within this range NAD nucleates at a rate an order of magnitude higher than that of NAT. Large NAD particles more efficiently denitrify nucleating levels, as particle sizes grow to between 1.0 and 10.0 μm in diameter. The nucleation of a few ternary solution droplets into this more stable hydrate allows for differential growth mechanisms to dominate and produce a small population of relatively large particles (*Salawitch, et al.*, 1989, *Toon et al*, 1990; *Tabazadeh et al.*, 2001). They conclude that presence of this "belt" within the polar vortex could amplify denitrification and ozone loss.

In Fig. 3.10, onset dates from 2003, 2004 and 2005 are plotted at 1.0 km resolution from 15.0 to 25.0 km MSL for air saturated with respect to NAT at 10.0 ppbv HNO_3/4.0 ppmv water vapor and ice at 6.0 ppmv water vapor (2000 data is not shown from lacking data). From the *Tabazadeh et al.* (2001) model, the 190 – 192 K "belt" (at 50 mPa; ~ 20.0 km MSL) occurs sometime between these two profiles each year. In all three years, NAT saturation occurs on almost exactly the same days at most heights, and the onset of ≤ 192 K temperatures occurs on the same day each year (22 May; not shown). Ice

saturation, however, occurs roughly ten days earlier during 2003 (and 2000 from 20.0 km MSL below; not shown) than 2004 and 2005. Temperatures less than 190 K are first measured on 27 May (2003), 30 May (2004) and 1 June (2005). So, the "freezing belt" is present over South Pole for a few days longer during the latter years, yet ozone losses are lower in those seasons.

These data put into question the role of NAD growth and sedimentation in the PSC/ozone relationship at South Pole. Denitrification involving hydrate particles is most typically not as efficient as that of ice. The process is a function of particle size, vapor uptake and sedimentation speeds (e.g., *Kasten*, 1968; *Fahey et al.*, 1989; *Hoffman et al.*, 1990). It is plausible that NAD growth and sedimentation may occur at the expense of ice nucleation, growth and associated heterogeneous surface chemistry, and therefore could have a relatively negative influence on catalytic ozone loss in regions of the vortex where persistent cold temperatures are more likely to occur. Satellite measurements of HNO_3 and water vapor made from MLS in mid-June 2005 (not shown) show total loss of the former near 18.0 km MSL south of 80.0° S, whereas water vapor concentrations were approximately 4.5 ppmv. These measurements precede the PSC episode detected at South Pole in the latter half of the month (Fig. 3.8d). Of course, this is just one four-week window during a three month season. Mixing within the vortex and the depth of cooling through August likely have just as much of an effect on PSC occurrence, denitrification and the depth of ozone loss measured in spring. Still, these data, and their correlation with ozone loss (examined in the next section), indicate that the "freezing belt" hypothesis requires further examination to reconcile what influence it has at South

Pole. Approaching the edges of the vortex where persistent cold temperatures are lacking, there is no reason to doubt a stronger role in these processes.

3.5 Correlations between PSC Occurrence and the Depth of Seasonal Ozone Loss

Data from Fig. 3.8 and Table 3.2 are discussed in tandem here to determine whether or not a correlation exists between MPL PSC presence and the extent of springtime ozone loss. From Figs. 3.8a-d, negative daily DU departures from the ozone hole threshold (220 DU) are calculated (i.e., analogous to a "degree day"; *Geer*, 1996) and integrated to produce an value representative of both temporal extent and the depth of low ozone column concentrations (henceforth referred to as "DU days"). These values are 4872.52, 3787.52, 3012.56 and 4138.62 for 2000 and 2003 – 2005, respectively. By this calculation, greater ozone losses were experienced during the 2005 season than 2003. It was shown in Table 3.1, however, that the 2003 season was approximately 10% shorter than the other three years. The maximum area of the ozone hole that year was larger than in 2005 (Fig. 1.8). Recoveries in November 2003 occurred much faster than average (Fig. 3.8b). Representing PSC presence in this comparison are the total (12.0 – 24.0 km MSL) and range-resolved integrated AAB from Table 3.2. The data are compared in Fig. 3.11 for total AAB (a) and that derived from each of the three height intervals (b).

Total integrated AAB and DU days are linearly correlated to a high confidence (R^2 = 0.88). The relationship is not congruent. That is, the linear regression function crosses zero along the DU day axis well above that for AAB, suggesting that ozone loss would occur in the absence of PSC. Similarly high correlations are derived for the 12.0 – 16.0

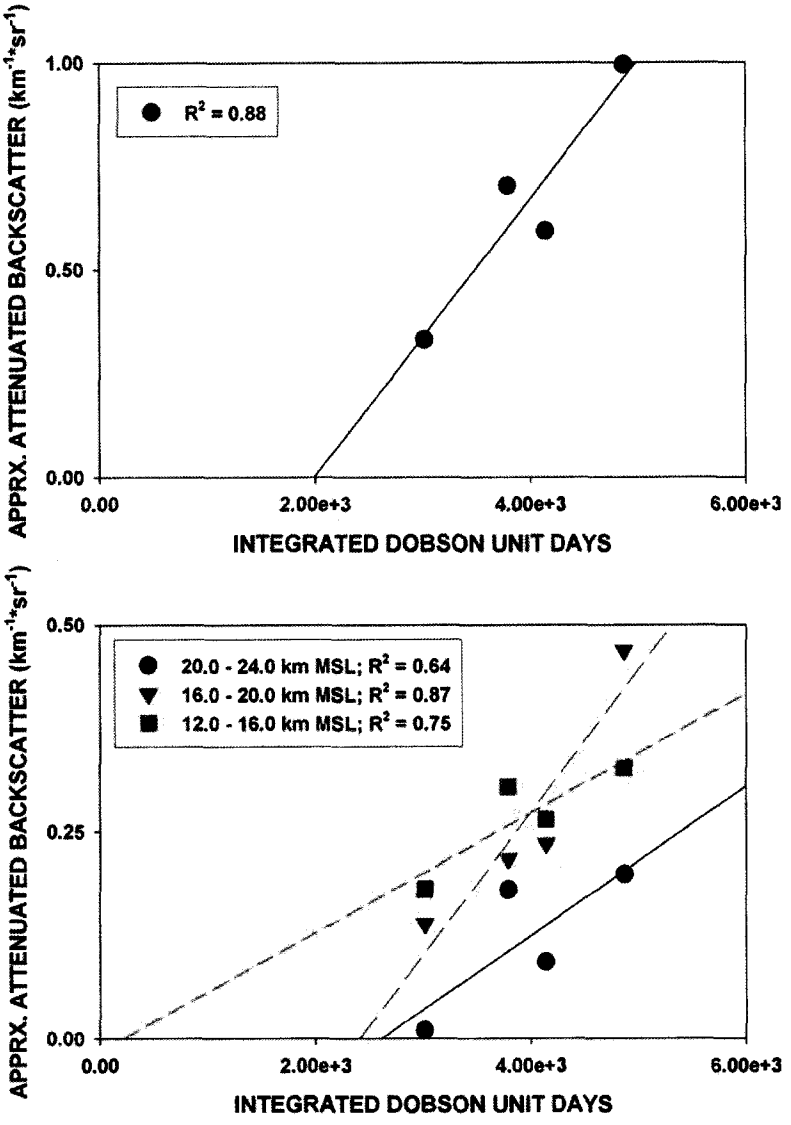

Figure 3.11 Correlation between total smoothed backscatter and DU days. From Table 3.2 and Fig. 3.7, linear regression fits and R^2 confidence values for total integrated Dobson Unit days versus total integrated scattering ratio from 12.0 – 24.0 km MSL (bin^{-1}) (a) and versus the total integrated approximate attenuated scattering ratio ($km^{-1} \cdot sr^{-1}$) for 20.0 – 24.0 , 16.0 – 20.0 and 12.0 – 16.0 km MSL (b; see legend).

and 16.0 – 20.0 km MSL intervals. The lowest correlation was derived for the relationship representing 20.0 – 24.0 km MSL. As discussed above, the MPL is most

likely detecting Type II PSC, particularly at upper-levels where particulate layer algorithm sensitivity decreases. The likeliest explanation for the failure to derive a congruent relationship between total AAB and DU days is the lack of embryonic solution droplet and Type I PSC observations in this sample. An increase of AAB from increased instrument sensitivity would increase values in the weaker PSC years relative to the stronger ones. Since Type II clouds nucleate from sub-detection species there is some finite component of AAB occurring at the expense of scattering from the smaller particles. If instrument performance were optimal, and all AAB measured, in years where more Type II were detected less Type I would be present since they are ultimately activated and scavenged to yield ice particles. This would shift the curve towards the origin.

A nearly congruent relationship is seen for the 12.0 – 16.0 km MSL interval (Fig. 3.11b). For these lower heights, where instrument and algorithm sensitivity is more amenable to Type I detection, the regression function is oriented more toward the origin and the correlation confidence remains high (R^2 = 0.75). As height increases, the two successive functions shift away from that point (this would be clearer if not for the otherwise outlying 2003 data point in the 20.0 – 24.0 km MSL region that biases the regression line to the left). Relative ozone losses are greatest between 12.0 and 20.0 km MSL. Therefore, the correlation between AAB and DU days should be highest at these levels compared to that from the 20.0 – 24.0 km MSL region. Still, the primary conclusion to be taken from these data is that there is a demonstrable correlation between

the MPL PSC observations, even if they are skewed toward Type II measurements, and ozone loss over Antarctica.

These findings are consistent with model calculations made by *Rex et al.* (2004) and *Douglass et al.* (2006), albeit for the Arctic, and using PSC volume rather than AAB and modeled ozone losses rather than DU days. Cloud volumes were estimated using model reanalysis temperatures and NAT condensation and ice frost-points for unperturbed background concentrations of HNO_3 and water vapor. They do not consider the effects of denitrification or dehumidification, though their effects in the Arctic are typically localized and not widespread (e.g., *Fahey et al.*, 1990). *Rex et al.* (2004) do not find a congruent relation between ozone loss and cloud volume, despite a cloud proxy that represents both types of PSC. Their relationship mirrors Fig. 3.11a, as their function crosses the axis for ozone-loss well above the origin. *Douglass et al.* (2006) use a chemistry-based model that constrains ozone loss based on both PSC presence and chlorine and bromine loading. They find a more congruent relationship.

In Fig. 3.12, the raw data from Fig. 2.10, converted to AAB, are plotted versus integrated DU days. The purpose is to compare and contrast the effects of data smoothing on the results presented in this chapter. Recall that smoothing was done in two places. First, gaps within cloud base and top boundaries dropping below the minimum signal threshold were smoothed with the Hanning window. Second, the data were then smoothed temporally and spatially to produce the data mostly used in this chapter. Gaps exist in the MPL datasets, either from missing data, or from episodes of persistent low cloudiness that inhibited calibration using the algorithm. In the case of

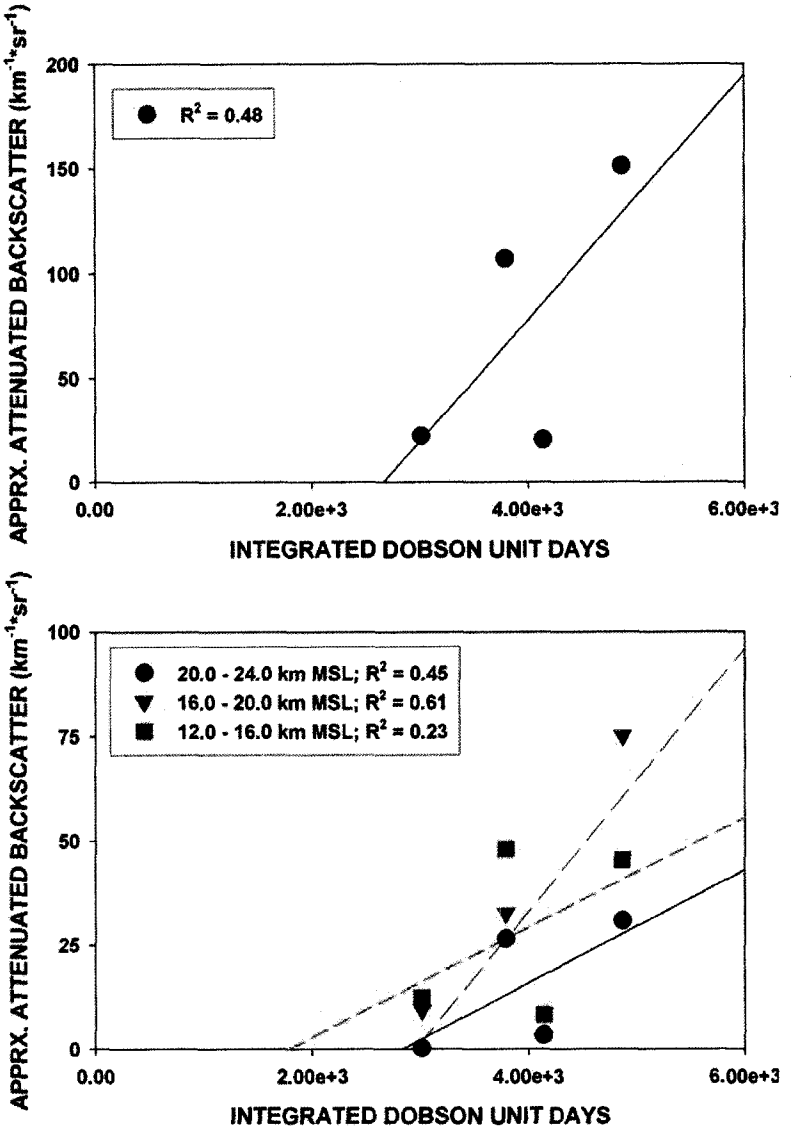

Figure 3.12 Correlation between total raw backscatter and DU days.
Using unsmoothed data from Fig. 2.10, linear regression fits and R^2 confidence values for integrated Dobson Unit days versus integrated scattering ratio from 12.0 – 24.0 km MSL (bin^{-1}) (a) and versus the total integrated approximate attenuated scattering ratio ($km^{-1} \cdot sr^{-1}$) for

missing data, a comparison of this nature becomes difficult to do since the goal is to compare total PSC (using some form of absolute measurement like AAB) to total ozone loss. The second smoothing step was designed to address this problem. Comparison

between Figs. 3.11 and 3.12 suggest that this changed the data appreciably. Correlation over the sum totals is reasonable, but not exceedingly high ($R^2 = 0.48$). Surprisingly, the 12.0 – 16.0 km MSL interval yields the lowest correlation of the three intervals ($R^2 = 0.23$), and is lower than for the smoothed data. Correlation values from the other two intervals are lower ($R^2 = 0.45$, 0.61, respectively), though not as egregiously. Notably, it turns out that the 2005 dataset included many gaps caused by missed calibrations, and the sum totals for ASR and AAB derived from the raw data that year are below those of even 2004. This is not immediately apparent from comparing Figs. 2.10c and d. Aliasing is occurring in Fig. 2.10d, and thereby enhancing the amount of cloud apparent in the image relative to that in Fig. 2.10c. This result may be improved after reprocessing with a lower resolution setting for the algorithm (Appendix B), since smoothing has apparently had a more than cursory influence. Viewed either way, the conclusion that a linear correlation between PSC, as measured with an MPL, and ozone loss remains consistent. However, the smoothed datasets reflect some measure of data massaging that, though not by any means artificial, have a qualified meaning.

CHAPTER 4

ANTARCTIC POLAR VORTEX DYNAMICS 2000, 2003 – 2005: GEOPOTENTIAL HEIGHT ANOMALIES, TRANSPORT AND SOUTH POLE GRAVITY WAVE CHARACTERISTICS

In the previous chapter, relationships between South Pole PSC occurrence, thermodynamic structure and chemical properties were examined. It was concluded that for clouds detectable with an MPL there exists, with reasonable confidence, a linear relationship between seasonal PSC occurrence and ozone loss. Furthermore, PSC structure was consistently bounded by the coldest temperatures that occur each winter in the lower-stratosphere over the South Pole. The depth of winter cooling is a function of the dynamic intensity of the austral polar vortex. This chapter investigates dynamic mechanisms relating to the vortex that may influence PSC observed at the South Pole. First, synoptic-scale properties are examined. Geopotential height anomalies averaged along the 60° S – 90° S longitudinal band are correlated with the South Pole MPL PSC observations from 2000 and 2003-2005. Five-day back-trajectories are shown to investigate transport within the vortex as a function of height, and determine the rate of cooling for air approaching the Antarctic plateau. Finally, local-scale dynamics are investigated. Gravity wave energy densities are shown from each season, having been derived from South Pole radiosonde measurements. These data are correlated with PSC occurrence to determine periods where they may have held any notable influence.

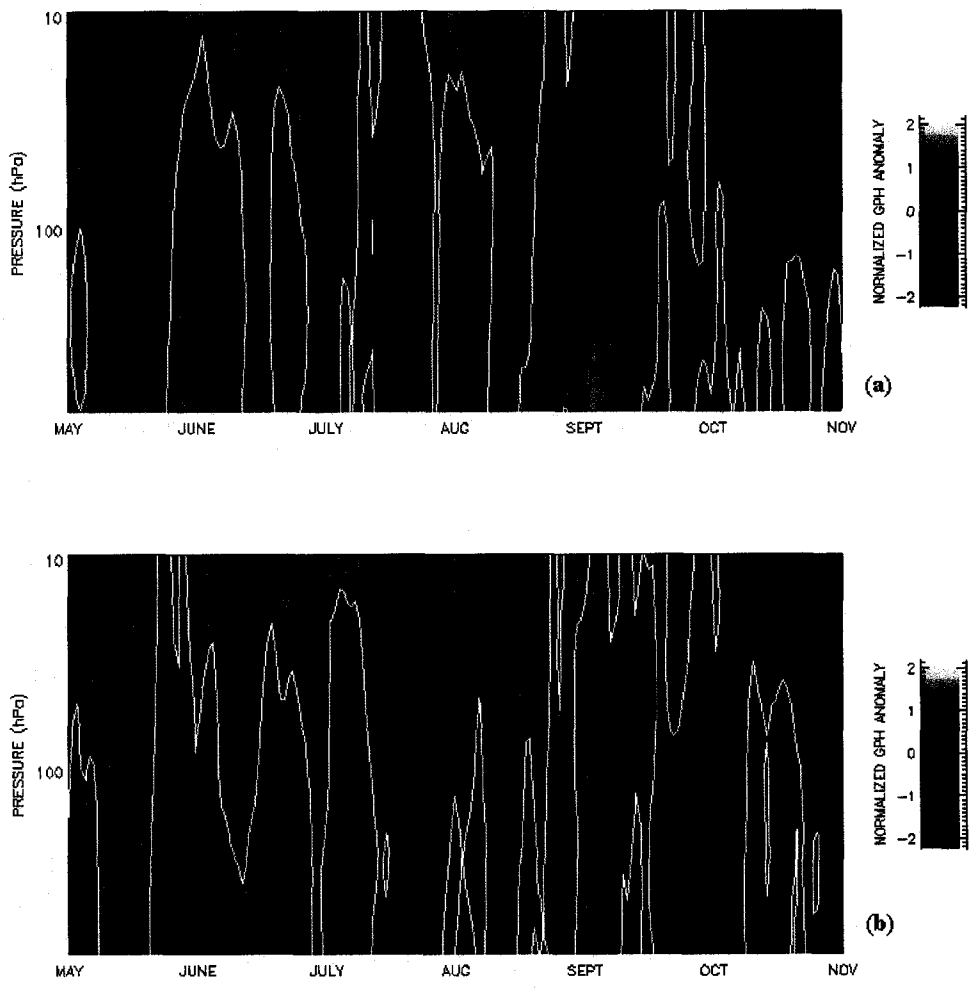

Figure 4.1 Annual normalized geopotential height anomalies. Averaged normalized geopotential height anomalies between 60.0° and 90.0° S from 700.0 – 10.0 mPa for May – November 2000 (a) and 2003 (b). The white line represents the 0.0 isopleth.

4.1 High-Latitude Southern Hemispheric Winter/Spring Geopotential Height Anomalies

Figure 4.1 displays averaged normalized geopotential height anomalies (GHA) for 60.0° S – 90.0° S from 700 – 10 hPa for May – October 2000 (a) and 2003 – 2005 (b-d).

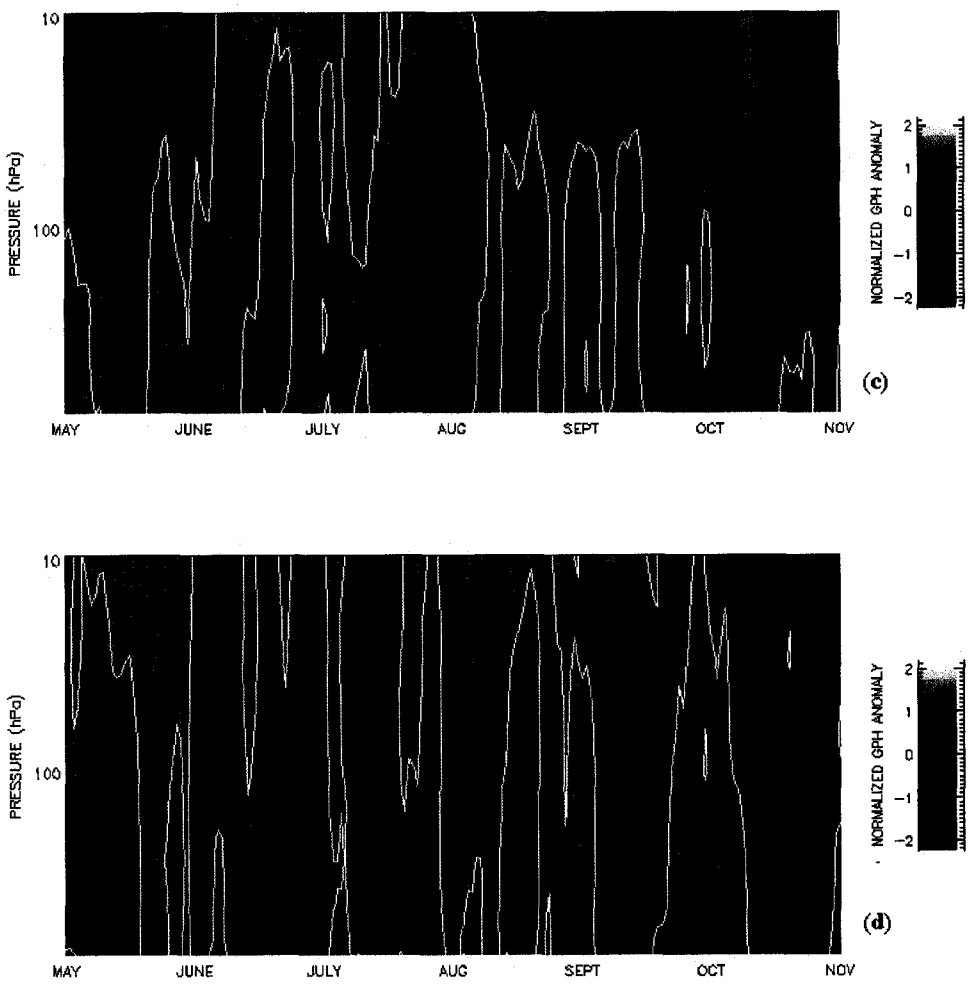

Figure 4.1 (cont.) Annual normalized geopotential height anomalies. Averaged normalized geopotential height anomalies between 60.0° and 90.0° S from 700.0 – 10.0 mPa for May – November 2004 (c) and 2005 (d). The white line represents the 0.0 isopleth.

They were derived from data retrieved from the NOAA ESRL Reanalysis Project archives of National Center for Environmental Prediction (NCEP) model reanalysis data[1]

[1] Accessible via NOAA/ESRL Reanalysis Project Website, http://www.cdc.noaa.gov/cdc/reanalysis/

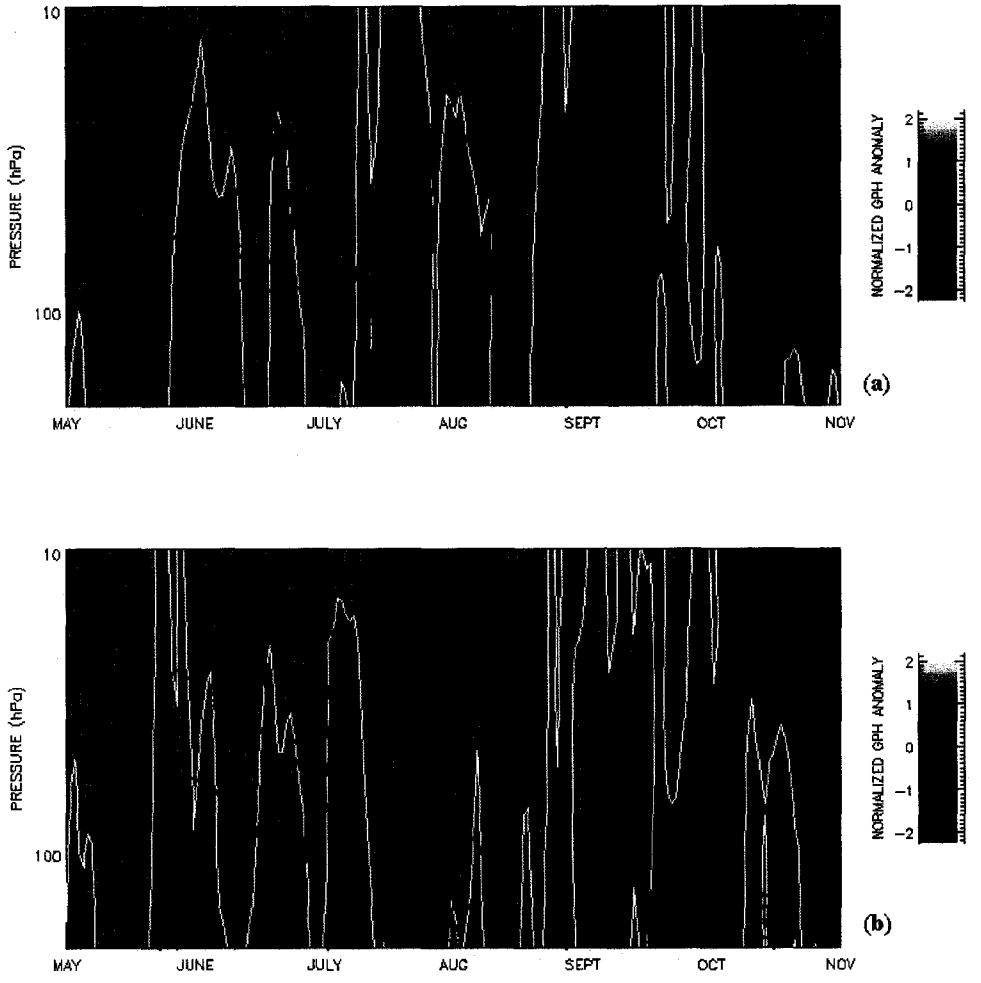

Figure 4.2 Annual geopotential height anomalies and PSC structure. Averaged normalized geopotential height anomalies between 60.0° and 90.0° S from 200.0 – 10.0 mPa with attenuated scattering ratios (Fig. 3.5) superimposed at 1.5 and 3.0 isopleths for May – November 2000 (a) and 2003 (b). The white line represents the 0.0 isopleth.

(*Kalnay et al.*, 1996; *Kistler et al.*, 2001). A 22-year climatology of daily geopotential heights and their standard deviations at 2.5° latitudinal resolution was derived for 1979 – 2000 at seventeen height levels, ranging from 1000.0 to 10.0 mPa between 60° S and 90°

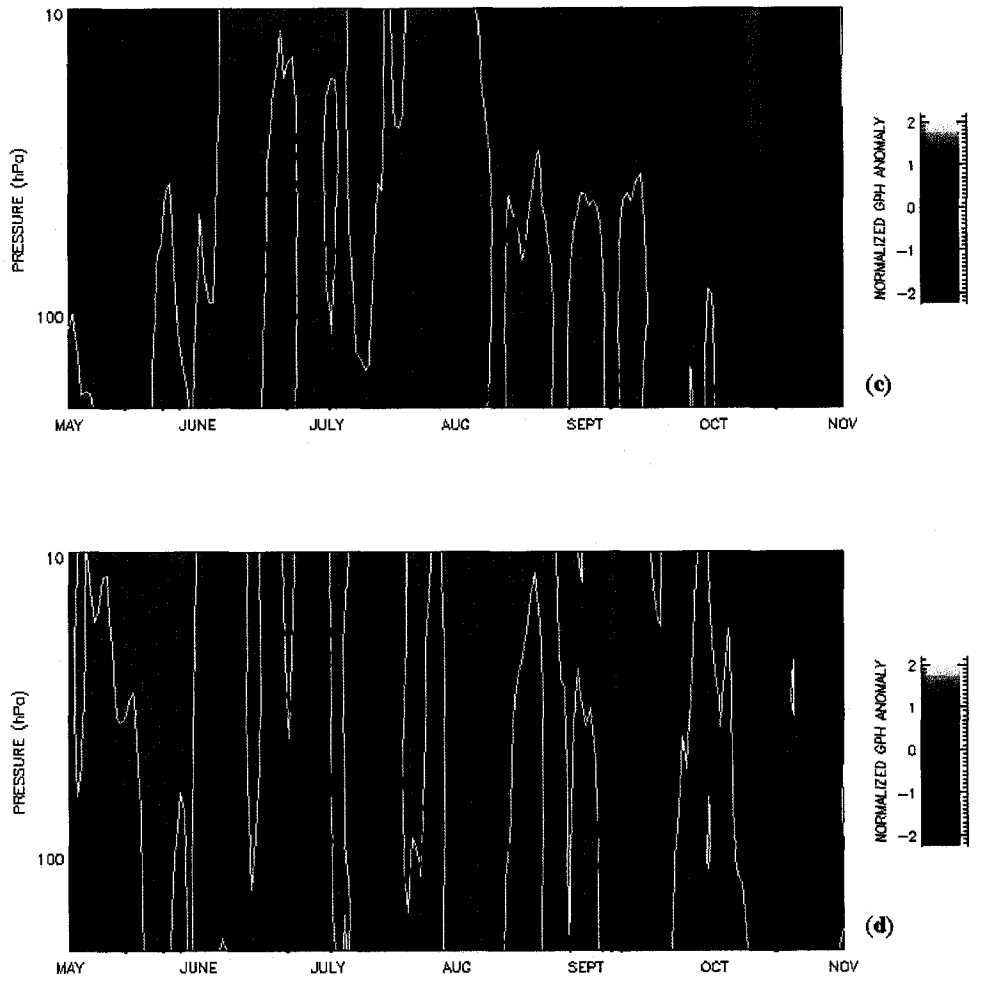

Figure 4.2 (cont.) Annual geopotential height anomalies and PSC structure. Averaged normalized geopotential height anomalies for 60.0° and 90.0° S from 200.0 – 10.0 mPa with attenuated scattering ratios (Fig. 3.5) superimposed at 1.5 and 3.0 isopleths for May – November 2004 (c) and 2005 (d). The white line represents the 0.0 isopleth.

S. Latitudinal averages were calculated as the mean for all data points available along a given band at 2.5° longitudinal resolution. Mean geopotential heights were then subtracted from daily 2000 and 2003 – 2005 data and normalized by the climatological

standard deviations. Daily averages both in longitude and latitude are shown in the figures for 60.0° S and 90.0° S. Data from Fig. 4.1 are redisplayed in Fig. 4.2, but only for the lower stratosphere (200.0 – 10.0 hPa, roughly corresponding to 10.0 to 28.0 km MSL; *Environmental Science Services Administration et al.*, 1967). Contoured ASR values (Fig. 3.5) are superimposed on these images using 1.5 and 3.0 isopleths. These values filter out periods of low ASR, and more distinctively delineate specific PSC episodes.

In the two colder years of the data sample, 2000 and 2003 (Figs. 4.1a and b; 4.2a and b), normalized GHA in early May in the lower stratosphere are negative, indicating lower than normal mean vortex heights. Normalized GHA in the warmer seasons, 2004 and 2005 (Figs. 4.1c and d), however, show positive values, or relatively high mean vortex heights around this time. It was shown in Fig. 3.8 that temperatures supporting NAT saturation at standard background concentrations of HNO_3 and water vapor occurred during 2003 – 2005 around 17 May each year. Cooling occurs in the lower-stratosphere at a rate approaching 1.0 K day^{-1} in May and June (Fig. 3.2). Although GHA episodes may be positive, that does not necessarily indicate warming. It does, however, indicate that a slower cooling rate was occurring than is observed on average. PSC in the colder years were observed in late-May, whereas, save for a very brief episode in 2005, PSC were not observed in 2004 and 2005 until mid-June. Onset dates for ice-saturation in the lower-stratosphere occurred later those years (Fig. 3.10). In all years, the onset of persistent MPL PSC measurements were first made during positive normalized GHA events, preceded by periods of prolonged (except for 2005) negative normalized.

GHA data are not necessarily proxies for thermal conditions at or near the South Pole. Since they are broad averages of geopotential heights with respect to mean conditions over the entire vortex, they may instead be interpreted to indicate periods of anomalous meridional transport. In the hypothetical limit of an infinitely deep vortex, circumpolar transport would approach geostrophic balance (e.g., *Wallace and Hobbs*, 1977), and broad-scale meridional transport would cease. Therefore, negative deviations from climatology indicate an abnormally deep vortex, and transport toward the South Pole will be minimized relative to mean flow. Positive deviations correlate with behavior in the opposite manner. There exists a broad but definitive correlation between more negative normalized GHA having occurred in the colder years, versus more positive normalized GHA having occurred in the warmer years. But, this is implicit from the data shown in Fig. 3.2, and needs no further corroboration.

Palm et al. (2005) describe PSC observed from the GLAS satellite, and investigate their occurrence in accordance with isentropic surfaces. They suggest broad-scale ascent and cooling along air trajectories as the primary mechanism driving their formation. From this view, PSC are clouds formed from moisture overrunning colder air, not so different from the frontal structure of mid-latitude cyclones (e.g., *Browning and Roberts*, 1994). *Teitelbaum et al.* (2001) discuss the role of synoptic-scale tropospheric disturbances, and anticyclonic potential vorticity anomalies near the tropopause inducing an upward displacement of isentropic disturbances in the lower stratosphere. Trajectories in these areas undergo quasi-adiabatic ascent and cooling, thereby inducing PSC nucleation and/or growth. *Tuck* (1989) showed similar structure in Antarctic PSC

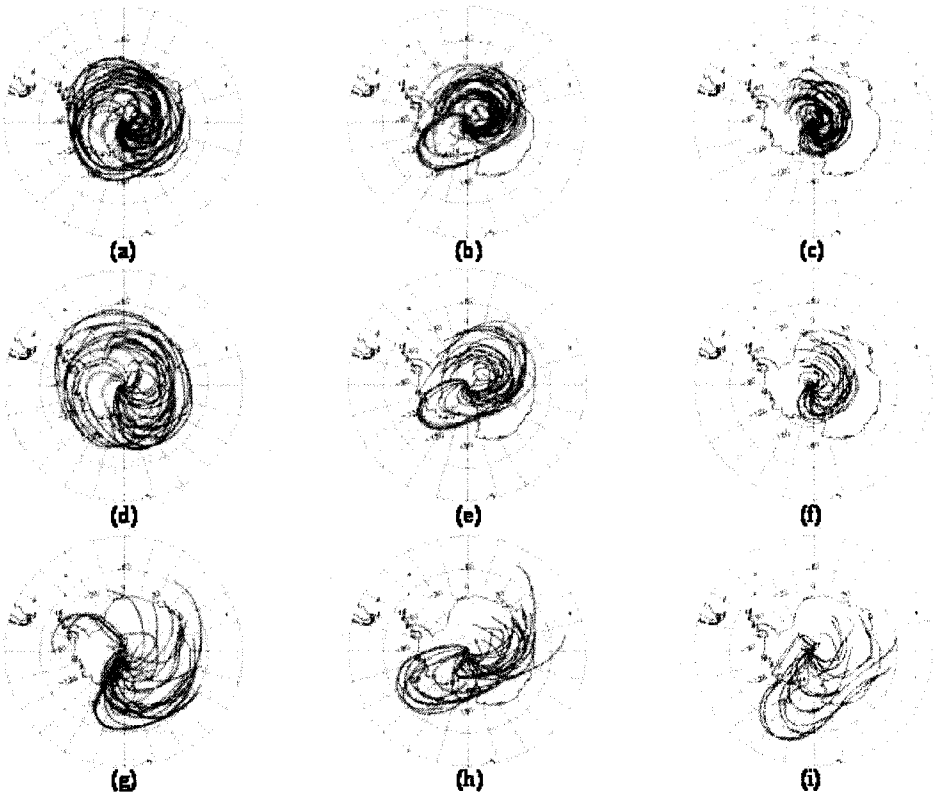

Figure 4.3 Daily five-day back-trajectories for 2000.
Daily five-day back-trajectories from 0000 UTC at South Pole in 2000 for June at 25.0 (a) 20.0 (d) and 15.0 km MSL (g); July at 25.0 (b), 20.0 (e) and 15.0 km MSL (h); August at 25.0 (c), 20.0 (f) and 15.0 km MSL (i). Non-saturated air is shaded blue, air saturated with respect to 10.0 ppbv HNO_3/4.0 ppmv water vapor is shaded green, and air saturated with respect to 4.0 ppmv water vapor is shaded red.

observations. *Fromm et al.* (1997) discuss observations of PSC inferred from passive radiometry and reconcile their occurrence with isentropic analysis. Trajectories approaching the South Pole are almost always rising and cooling quasi-adiabatically. Many of the observations in these papers occurred from points near the edges of the continent, where gravity wave influence was also considered a factor (*Wu and Jiang,*

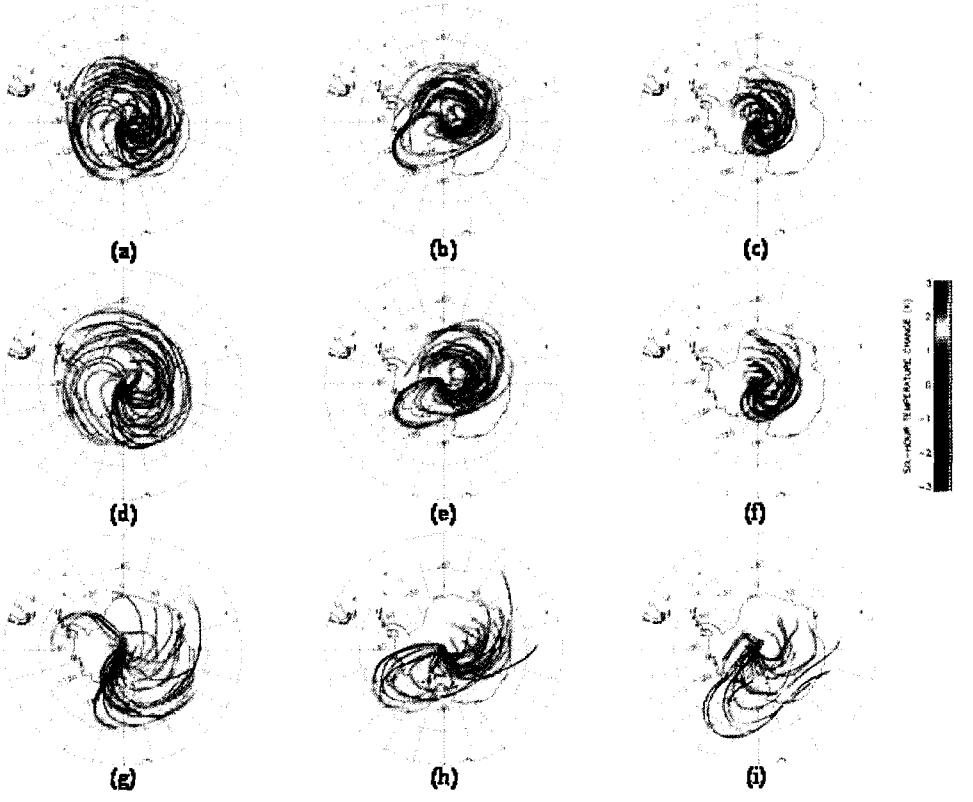

Figure 4.4 Six-hour temperature changes along trajectories in 2000. Six-hour temperature changes (see legend; K) along daily five-day back-trajectories from 0000 UTC at South Pole in 2000 for June at 25.0 (a) 20.0 (d) and 15.0 km MSL (g); July at 25.0 (b), 20.0 (e) and 15.0 km MSL (h); August at 25.0 (c), 20.0 (f) and 15.0 km MSL (i).

2002). Tropospheric enhancement of PSC below 15.0 km MSL was observed in brief episodes from August – September 2003. However, there is little evidence that tropospheric enhancement influences PSC at the South Pole above 15.0 km MSL.

Moisture overrunning appears to be a primary mechanism for PSC occurrence at the South Pole. Following the initial measurements of PSC observed at the South Pole each year, mostly in late May and June, observations from July through September correspond

with episodes of positive normalized GHA. In 2003, from mid-July forward, an extended period of negative normalized GHA was observed with no corresponding PSC. If the model for denitrification and dehumidification is to be believed, early season PSC (i.e., PSC occurring in unperturbed air) will result in removal of HNO_3 and water vapor at heights supporting particle nucleation and growth. For the MPL observations, it has been shown that this pertains almost exclusively to ice and Type II clouds. Subsequently, in the case of a strong vortex (negative normalized GHA), meridional transport will be minimized, and air over the South Pole will more likely reflect the influence of previous PSC sedimentation from air remaining in the vicinity. Clouds may be observed, as they are in below 15.0 km MSL late July 2003, but they will likely correspond (as they did that year) with periods of further cooling, nucleation and growth of background aerosols. However, should the vortex become weak, and transport increase, possibly unperturbed air from the edges of the vortex, and perhaps influenced by mixing across the vortex boundary, will be more likely to be transported poleward. In this case, overrunning will induce PSC, sedimentation, denitrification and dehumidification in these air masses. To test this hypothesis, and perhaps extend it to reconcile early-season observations of PSC, an analysis of air trajectories is required, and follows in the next section.

4.2 Transport Patterns and Thermodynamic Development of Air Observed at the South Pole

Five-day back-trajectories are discussed here to investigate transport and the thermodynamic evolution of air observed over the South Pole. Data are shown for 2000

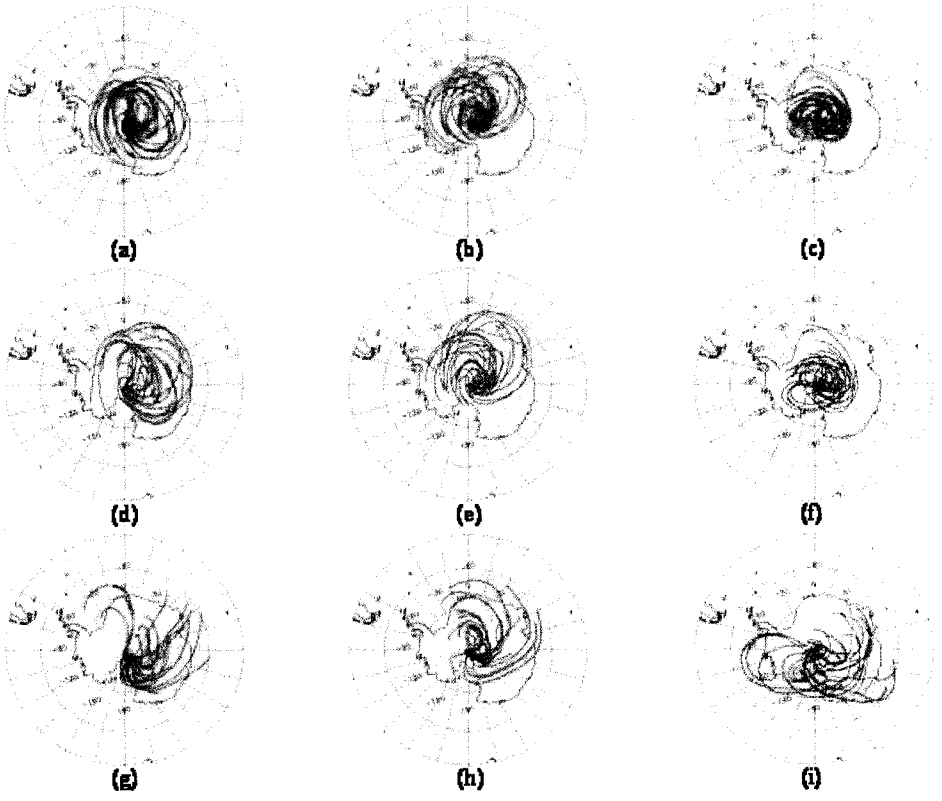

Figure 4.5 Daily five-day back-trajectories for 2003.
Daily five-day back-trajectories from 0000 UTC at South Pole in 2003 for June at 25.0 (a) 20.0 (d) and 15.0 km MSL (g); July at 25.0 (b), 20.0 (e) and 15.0 km MSL (h); August at 25.0 (c), 20.0 (f) and 15.0 km MSL (i). Non-saturated air is shaded blue, air saturated with respect to 10.0 ppbv HNO_3/4.0 ppmv water vapor is shaded green, and air saturated with respect to 4.0 ppmv water vapor is shaded red.

and 2003 – 2005, respectively, in Figs. 4.3, 4.5, 4.7 and 4.9. The daily five-day 0000 UTC back- trajectory is shown for June at 25.0 km (a), 20.0 km (d) and 15.0 km MSL (g), for July at 25.0 km (b), 20.0 km (e) and 15.0 km MSL (h) and for August at 25.0 km (c), 20.0 km (f) and 15.0 km MSL (i). Along each track, sub-saturated air is shown in blue, saturation with respect to NAT for 10.0 ppbv HNO_3/4.0 ppmv water vapor

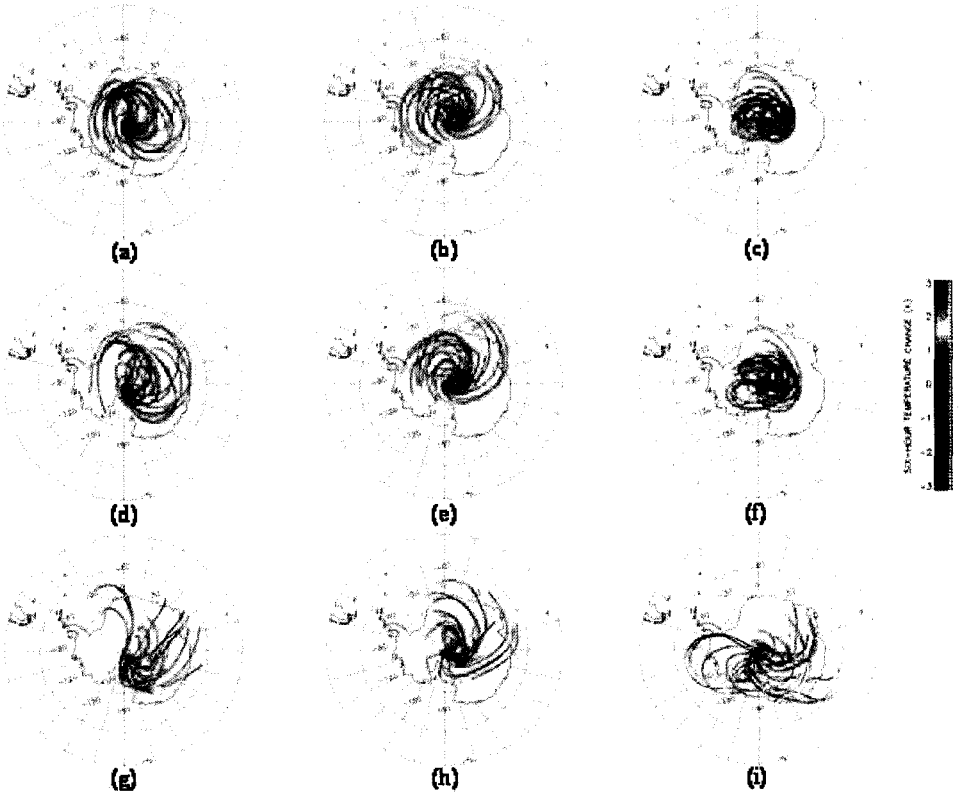

Figure 4.6 Six-hour temperature changes along trajectories in 2003. Six-hour temperature changes (see legend; K) along daily five-day back-trajectories from 0000 UTC at South Pole in 2003 for June at 25.0 (a) 20.0 (d) and 15.0 km MSL (g); July at 25.0 (b), 20.0 (e) and 15.0 km MSL (h); August at 25.0 (c), 20.0 (f) and 15.0 km MSL (i).

concentrations is shown in green, and for 4.0 ppmv water vapor with respect to ice is shown in red. In Figs. 4.4, 4.6, 4.8 and 4.10 are six-hour temperature changes along each track at one-hour resolution for each year, 2000 and 2003 – 2005, respectively, corresponding to the months and heights in the previously described figures.

Trajectories and cooling rates were derived using the NOAA Air Resources Laboratory HYbrid Single-Particle Lagrangian Integrated Trajectory (HYSPLIT) on-line

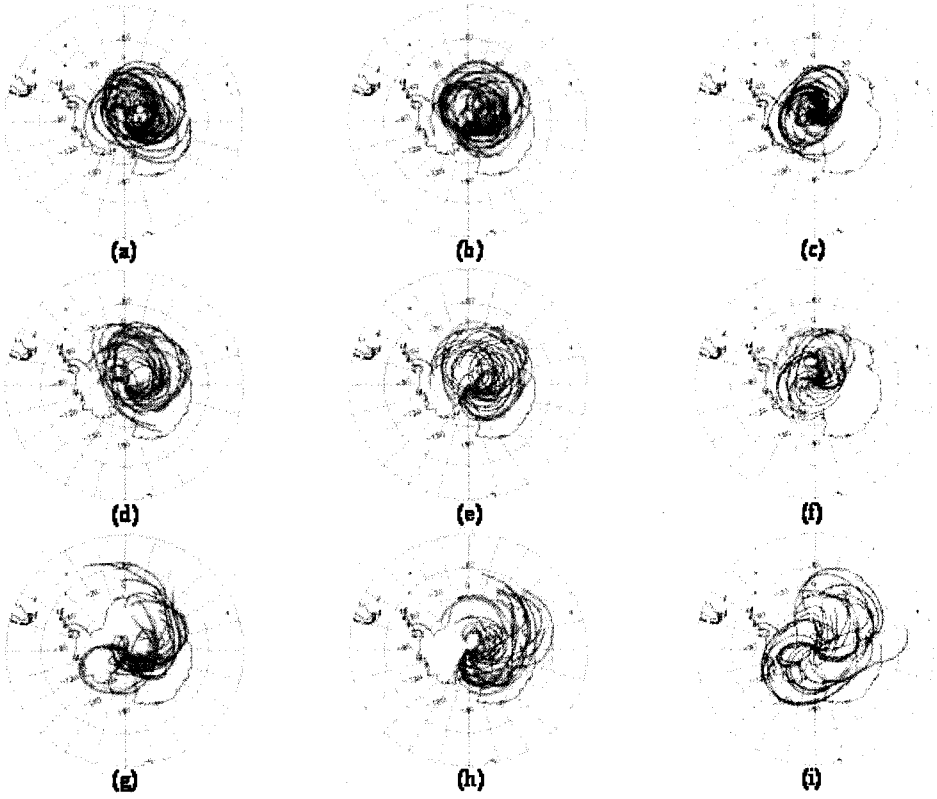

Figure 4.7 Daily five-day back-trajectories for 2004.
Daily five-day back-trajectories from 0000 UTC at South Pole in 2004 for June at 25.0 (a) 20.0 (d) and 15.0 km MSL (g); July at 25.0 (b), 20.0 (e) and 15.0 km MSL (h); August at 25.0 (c), 20.0 (f) and 15.0 km MSL (i). Non-saturated air is shaded blue, air saturated with respect to 10.0 ppbv HNO_3/4.0 ppmv water vapor is shaded green, and air saturated with respect to 4.0 ppmv water vapor is shaded red.

transport and dispersion model[2] (*Draxler and Rolph*, 2003) initiated with Final Global Data Assimilation System data. The model is based on isentropic trajectory analysis (*Draxler*, 1996). Table 4.1 details the mean distances traveled during each month, height and year, as well as the corresponding average farthest distances from the South Pole

[2] Model access via NOAA ARL READY Website, http://www.arl.noaa.gov/ready/hysplit4.html

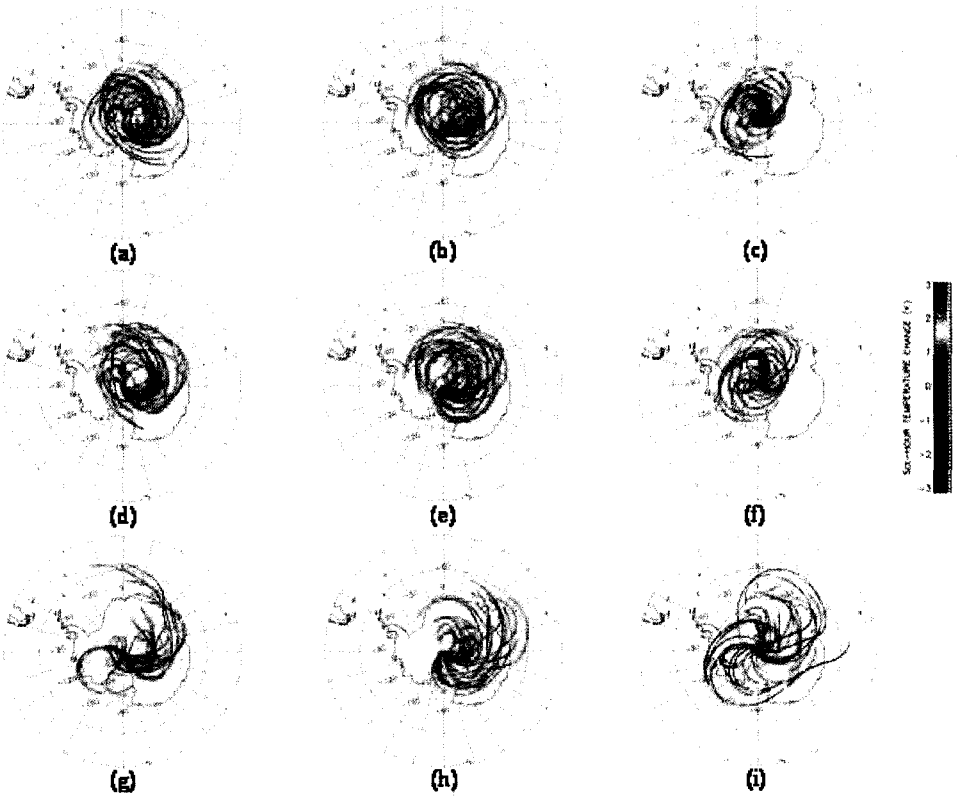

Figure 4.8 Six-hour temperature changes along trajectories in 2004. Six-hour temperature changes (see legend; K) along daily five-day back-trajectories from 0000 UTC at South Pole in 2004 for June at 25.0 (a) 20.0 (d) and 15.0 km MSL (g); July at 25.0 (b), 20.0 (e) and 15.0 km MSL (h); August at 25.0 (c), 20.0 (f) and 15.0 km MSL (i).

encountered along each trajectory. Tables 4.2, 4.3 and 4.4 display monthly-averaged six-hour cooling rates at each level, as a function of individual days working backward along each daily trajectory from the South Pole, as well as the total mean value. The data are shown for June, July and August in each table, respectively. Uncertainties exist in these retrievals, with error growing as a function of time (e.g., *Stohl*, 1998). Still, the analysis in this section is mostly qualitative.

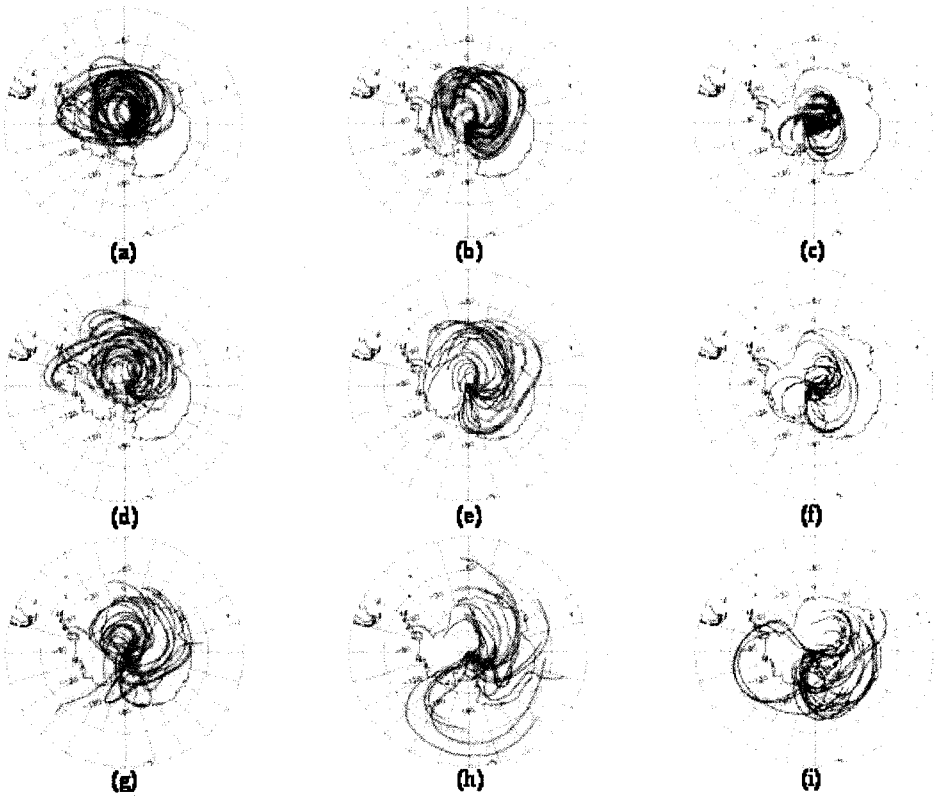

Figure 4.9 Daily five-day back-trajectories for 2005.
Daily five-day back-trajectories from 0000 UTC at South Pole in 2005 for June at 25.0 (a) 20.0 (d) and 15.0 km MSL (g); July at 25.0 (b), 20.0 (e) and 15.0 km MSL (h); August at 25.0 (c), 20.0 (f) and 15.0 km MSL (i). Non-saturated air is shaded blue, air saturated with respect to 10.0 ppbv HNO_3/4.0 ppmv water vapor is shaded green, and air saturated with respect to 4.0 ppmv water vapor is shaded red.

Immediately apparent from the distributions of trajectories is the evolving structure of the vortex as a function of height from June through August. As temperatures are understood to cool through at least mid-August (Fig. 3.2), the vortex strengthens accordingly. The winter polar jet-stream peaks in August, with mean wind speeds exceeding 60.0 m/s at heights as low as 30.0 km MSL (*Fleming et al.*, 1988).

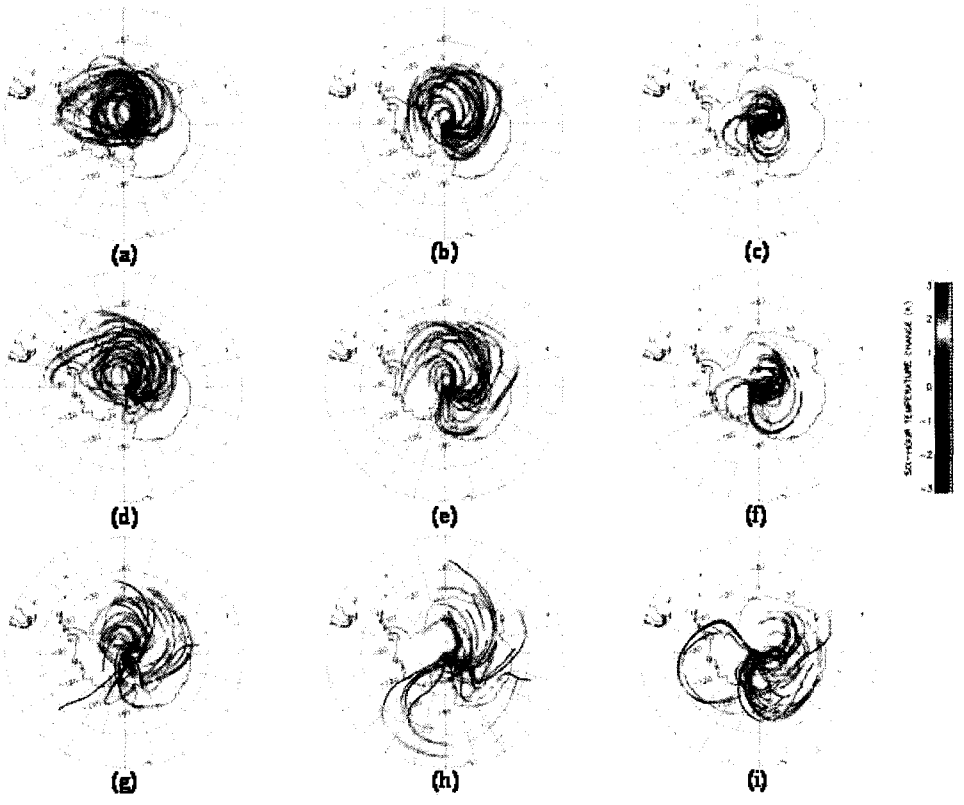

Figure 4.10 Six-hour temperature changes along trajectories in 2005. Six-hour temperature changes (see legend; K) along daily five-day back-trajectories from 0000 UTC at South Pole in 2005 for June at 25.0 (a) 20.0 (d) and 15.0 km MSL (g); July at 25.0 (b), 20.0 (e) and 15.0 km MSL (h); August at 25.0 (c), 20.0 (f) and 15.0 km MSL (i).

Trajectories in all years exhibit contraction through the period at 20.0 and 25.0 km MSL. Trajectories at 15.0 km MSL fluctuate greatly in relation, indicating a weaker vortex influence at this height.

Interpretation of the data in Table 4.1 leads to similar conclusions. Trajectory lengths increase with height during all years in June and July, indicating increasing wind speeds with height. However, the mean maximum distances from the South Pole along these

trajectories decreases with height at all levels. This indicates greater curvature in their circumpolar path lengths. In August, when the vortex is strongest, there are differences among the years. Disparity in these values relates to the vertical structure and strength of the vortex. In 2000, the mean trajectory length increases with height, and the mean maximum distance from the South Pole is highest of any year at all levels. In 2003, 2004 and 2005, mean path lengths are variable with height. A significant positive normalized GHA event in 2000 (Fig 4.1a) begin in late-August and lasted through September. Data relating to this event may be influencing these results. However, elevated PSC were persistent this year in August, in contrast to the other seasons. With respect to the conclusions from last section, these data are consistent with increased PSC occurrence at the South Pole occurring with greater advection of air from the edges of the vortex.

Results from 2003, 2004 and 2005 show mean path lengths increasing from 20.0 to 25.0 km MSL, though these values are lower than the 15.0 km MSL value. This is counterintuitive versus expected mean wind speeds, where the polar jet should, on average, be very close to these heights (*Fleming et al.*, 1988). Normalized GHA in August 2003 (Fig 4.1a) were anomalously negative in the early part of the month compared to other years at all heights in the lower-stratosphere. In 2005, normalized GHA at the highest levels were mostly negative as well during this month. Mean maximum distances from the South Pole were lowest at 25.0 km MSL during these years. Mean maximum distances from the South Pole, as a whole, are the lowest of any month, consistent with seasonal maximums of vortex influence.

Immediately apparent in the six-hour cooling rates, shown in Figs. 4.4, 4.6, 4.8 and 4.10, is that values from air reaching South Pole are almost exclusively positive. Averaged results for June, July and August, in Tables 4.2, 4.3 and 4.4, support this observations. On average, for each month and at each level sampled, cooling is always occurring for air traveling over five days to the South Pole. Given the lack of appreciable enthalpies of condensation and fusion at these altitudes, and assuming quasi-adiabatic ascent, estimates for the depth of ascent can be made relative to the dry adiabatic lapse rate, or 9.8 K/km (*Bohren and Albrecht*, 1998). On average, air rose from roughly 0.50 to 1.50 km along trajectories in June 2000 from 15.0 to 25.0 km MSL. Averages in 2003, 2004 and 2005 ranged from 0.30 to 0.75 km, with the lowest values occurring in 2004. Values from June 2000 were the highest of the entire sample, which corresponds to a high PSC occurrence rate that month (Fig. 3.5a).

In July, mean cooling rates drop, as the expansion of radiative cooling over the Antarctic continent with increasing darkness acts to dampen the slopes of isentropic surfaces. Notably, values in 2005 were highest of the four years from this month, which would compensate for low values in the previous month, and correlate with relatively high PSC occurrence that commenced in late June (Fig. 3.5d). In 2000, cooling was relatively high in July, maintaining persistence with the previous month, and again correlating with the high PSC occurrence observed (Fig. 3.5a). Minimums for all years occurred in August. Most notably, at 20.0 and 25.0 km MSL, only in 2000 did mean rates approach and exceed 1.0 K. In contrast, in 2003, which was from all other evidence a colder year, values were less than 0.3 K, and no PSC were observed during the period

Table 4.1 Five-day back-trajectory statistics.
From the five-day back-trajectories in Figs. 4.2, 4.4, 4.6 and 4.8, the monthly mean for distance traveled (km) in reaching South Pole and the average furthest distance away from South Pole along the length of the trajectory (km) for June, July and August 2000 and 2003-2005 at 15.0, 20.0 and 25.0 km MSL.

Year	Height (km MSL)	June Distance (km)	June Furthest (km)	July Distance (km)	July Furthest (km)	August Distance (km)	August Furthest (km)
2000	15.0	4424.57	2414.87	4896.87	2285.68	3882.68	1959.62
	20.0	7288.99	2066.14	4967.42	1678.56	4143.12	1518.95
	25.0	8252.17	1962.76	5093.97	1549.88	4314.45	1350.61
2003	15.0	2947.32	1903.53	2891.67	1472.97	3612.56	1746.24
	20.0	3798.57	1556.35	3761.88	1452.60	3154.42	1174.52
	25.0	4446.50	1410.16	3897.55	1311.46	3291.92	1073.23
2004	15.0	3980.63	1843.58	4192.10	1918.24	4597.17	1970.37
	20.0	5087.26	1731.32	5118.82	1653.16	3409.85	1261.71
	25.0	5641.65	1650.19	5413.56	1574.43	3461.01	1131.48
2005	15.0	4288.70	1932.44	3821.49	2098.32	4483.86	1903.68
	20.0	5478.18	1904.95	4481.83	1788.77	2727.31	1080.21
	25.0	6237.99	1772.84	4818.93	1611.54	2583.63	937.44

of extended positive normalized GHA. The likeliest explanation, under the guise of a very strong vortex, is that vortex was so strong so as to induce a dome of relatively stable cold air, with little amplitude to isentropic surfaces in the vicinity of the South Pole. As such, it appears that if the vortex is anomalously deep, isentropic transport occurs on relatively flat surfaces with little mixing from the vortex edges, and PSC occurrence (as measured with an MPL) is limited..

Table 4.2 Six-hour cooling rate statistics for June.
From the six-hour cooling rates (K) calculated along each daily five-day back-trajectory for June in Figs. 4.3, 4.5, 4.7 and 4.9, the mean values for each day and the total average cooling rate over the length of the trajectory for 2000 and 2003-2005 at 15.0, 20.0 and 25.0 km MSL.

Year	Height (km MSL)	Day 0	Day 1	Day 2	Day 3	Day 4	Total
2000	15.0	0.826	0.649	0.791	0.636	0.698	14.254
	20.0	0.515	0.506	0.383	0.329	-0.527	5.175
	25.0	0.617	0.438	0.109	-0.005	-0.040	4.663
2003	15.0	0.295	0.239	0.036	0.484	0.817	7.067
	20.0	0.158	0.211	0.231	0.038	0.019	2.650
	25.0	0.181	0.192	0.024	0.065	0.291	2.977
2004	15.0	0.410	0.088	0.299	0.587	0.074	5.740
	20.0	0.145	0.166	0.137	0.157	0.139	2.976
	25.0	0.172	0.123	0.046	0.154	-0.121	1.530
2005	15.0	0.516	0.296	0.255	0.278	0.646	7.580
	20.0	0.237	0.092	0.109	0.346	-0.073	2.867
	25.0	0.280	0.191	0.223	-0.317	0.152	2.377

Averages calculated for the individual days along these tracks show cooling occurring exclusively during the three days immediately preceding reaching the South Pole in June. Daily average maximum values for all months occur during this month at all heights. Again, this likely speaks to the slope of isentropic surfaces present at this time. However, this again supports the idea of moisture overrunning being a primary source for PSC observed during the initial pulse of cloud each season, which occurs in this month. In July, average rates drop from the two days before reaching the South Pole by as much 50%, except in 2005, which as noted above was marked by persistent cooling from late June and into mid-July. In August, daily averages reach minimum values. Although

Table 4.3 Six-hour cooling rate statistics for July.
From the six-hour cooling rates (K) calculated along each daily five-day back-trajectory for July in Figs. 4.3, 4.5, 4.7 and 4.9, the mean values for each day and the total average cooling rate over the length of the trajectory for 2000 and 2003-2005 at 15.0, 20.0 and 25.0 km MSL.

Year	Height (km MSL)	Day 0	Day 1	Day 2	Day 3	Day 4	Total
2000	15.0	0.662	0.596	0.410	0.394	-0.033	8.010
	20.0	0.232	0.207	0.091	-0.129	-0.077	1.420
	25.0	0.173	0.086	-0.051	-0.048	0.019	0.780
2003	15.0	0.315	0.184	0.091	0.542	0.432	5.967
	20.0	0.156	0.173	0.144	-0.163	-0.164	0.767
	25.0	0.159	0.175	-0.060	-0.209	0.089	0.690
2004	15.0	0.448	-0.178	0.072	0.392	0.360	4.335
	20.0	0.087	0.061	0.015	-0.059	0.015	0.623
	25.0	0.085	0.095	-0.099	-0.099	0.174	0.661
2005	15.0	0.263	0.458	0.496	0.512	0.588	9.006
	20.0	0.213	0.234	0.063	0.216	0.021	2.945
	25.0	0.220	0.191	0.164	-0.117	-0.129	1.532

interestingly, cooling in the two days immediately before reaching the South Pole is persistent relative to July. From Fig 3.2, the coldest air of the year typically occurs during this month between 15.0 and 25.0 km MSL. Most PSC are observed below this height in August, except for in 2000 and from cases of anomalously positive normalized GHA. Again, overrunning, here in the presence of sufficiently cold temperatures, appears likely to be the primary reason for PSC near this height. A more detailed analysis of PSC formation with respect to back-trajectories, particularly with respect to the nuances of Type I generations, is given by *Tabazadeh et al.* (1995).

Table 4.4 Six-hour cooling rate statistics for August.
From the six-hour cooling rates (K) calculated along each daily five-day back-trajectory from August in Figs. 4.3, 4.5, 4.7 and 4.9, the mean values for each day and the total average cooling rate over the length of the trajectory for 2000 and 2003-2005 at 15.0, 20.0 and 25.0 km MSL.

Year	Height (km MSL)	Day 0	Day 1	Day 2	Day 3	Day 4	Total
2000	15.0	0.574	0.308	0.328	0.160	0.201	6.403
	20.0	0.201	0.204	0.137	-0.071	-0.123	1.441
	25.0	0.209	0.259	0.046	-0.128	-0.187	0.874
2003	15.0	0.730	0.398	0.286	0.076	-0.116	5.642
	20.0	0.100	0.085	-0.117	-0.069	0.015	0.119
	25.0	0.104	-0.003	-0.154	0.011	-0.046	0.267
2004	15.0	0.323	-0.818	0.338	-0.308	0.109	5.187
	20.0	0.131	0.080	-0.090	-0.038	-0.066	0.161
	25.0	0.116	0.076	-0.099	-0.026	-0.074	0.058
2005	15.0	0.330	0.603	0.405	-0.044	-0.365	3.887
	20.0	0.052	0.125	0.065	0.009	-0.098	0.629
	25.0	0.024	0.075	0.015	-0.006	-0.055	0.232

4.3 Gravity Wave Characteristics at the South Pole

Gravity waves were recognized from early in-situ measurements for their potential influence on PSC nucleation and growth mechanisms (*Cariolle et al.*, 1989). Rapid cooling favors the nucleation and preferential growth of relatively low numbers of particles. Since surface area varies as the square of radius, a few large particles can increase chlorine activation relative to many small ones, particularly at temperatures were heterogeneous nucleation of hydrates and ice may further influence the efficiency of heterogeneous surface chemistry (e.g., *Solomon*, 1999). Additionally, appreciable fall velocities develop so as to enhance denitrification and dehumidification (e.g., *Kasten*,

1968; *Carslaw et al.*, 1998b; *Fahey et al.*, 2001). Orographic gravity waves are known to induce small-scale temperature fluctuations in the lower-stratosphere on the order of 10 K (*Gary*, 1989; *Volkert and Intes*, 1992; *Leutbecher and Volkert*, 1996). Non-orographic sources near the poles considered as first-order contributor to gravity wave energy densities include the geostrophic adjustment of the polar jet stream and propagation of low-latitude convective energy (*Wu and Waters*, 1996a, 1996b; *Sato*, 2000).

More complicated surface topography in the northern hemisphere leads to greater gravity wave activity there (*Yoshiki and Sato*, 2000). This yields a more disturbed Arctic polar vortex and warmer stratospheric temperatures in winter that exhibit greater interseasonal and interannual variability compared to the Antarctic (*Pawson and Naujokat*, 1999; *Newman et al.*, 2001). Underpredictions of wintertime ozone loss in numerical models over the boreal pole, in the absence of any thermal bias, have been hypothesized to be the result of a missing influence on PSC occurrence from a gravity wave component (*Becker et al.*, 1998; 1999; *Manney et al.*, 2003; *Eckerman et al.*, 2006). In the Antarctic, gravity waves are common along the edges of the vortex, both in response to coastal topography and polar jet dynamics (*Wu and Jiang*, 2002). *Cariolle et al.* (1989) describe PSC observed over the Palmer Peninsula and Weddel Sea driven by orographic gravity waves. They estimate that air between 14.0 and 18.0 km MSL within the polar vortex spent time 5% of its time inside these clouds from early August to late September 1987. *Shibata et al.* (2003) describe MPL observations of Type II PSC caused by nonorographic gravity waves at Syowa Station.

Two studies of gravity wave characteristics at the poles, built from operational radiosonde datasets, have been described by *Pfenninger et al.* (1999) and *Yoshiki and Sato* (2000). The latter paper is an exhaustive study of 33 stations over a period of ten years, including total, potential and kinetic gravity wave energies, vertical and horizontal directions of wave propagation and correlations between gravity wave energy in the lower stratosphere and the mean wind. They found that Arctic gravity waves were most commonly forced by topography, but that over Antarctica, mean wind directions shift in the lower-stratosphere, which leads to surface-generated wave-breaking. They identify the geostrophic adjustment in the polar night jet as a more likely source for wave presence in the stratosphere. The *Pfenninger et al.* (1999) study is focused on four-years (1993-1996) of radiosonde measurements specifically at the South Pole. This section is a reproduction of their work for 2000 and 2003-2005 to examine the relationship between PSC occurrence and gravity wave energy densities.

A brief summary of the *Pfenninger et al.* (1999) methodology is required, though limited to the most relevant steps. The fundamental assumption is that for any given radiosonde profile a background structure (Θ_o, T_o, u_o, v_o) exists upon which gravity wave structure (Θ', T', u' and v') is present. These profiles must be isolated. *Pfenninger et al.* (1999) includes all available radiosonde data files in their yearly samples. Their sample was collected during a period where two launches per day occurred at the South Pole. This is no longer the case for all days of the year. For example, in 2003, only one balloon launch per day occurred from mid-February through late-September. This coincides with regional air traffic schedules, and the need for increased radiosonde coverage to initiate

numerical models used for flight forecasts. Similar to Chapter 3, only those files where the balloon reached 18.0 km MSL were used here, limiting this sample to nearly 20% of the data available to *Pfenninger et al.* (1999).

Potential and actual temperatures (Θ and T) and vector wind components (u and v) were first smoothed to 1-day and 0.050 km resolution using the Hanning function (Appendix A) at 14-day and 2.0 km temporal and spatial half-widths. Next, each profile was gridded separately to 0.050 km resolution using the one-dimensional Hanning function at 0.250 km spatial half-width. For each gridded sounding profile the difference between it and the corresponding smoothed data points were derived, and low-order polynomials fit to these differences (second-order below 8.0 km MSL and third-order at all heights above). A background profile (Θ_o, T_o, u_o, v_o) was then defined as the sum of the smoothed profile and the polynomial fit. Accordingly, perturbations (Θ', T', u' and v') were then solved for by subtracting the background from the gridded profiles. Gravity wave component energy densities (J/kg) were solved for potential energy as

$$PE \equiv \frac{g^2 \overline{(T'/T_o)^2}}{2N_o^2} \tag{4.1}$$

where g is the acceleration from gravity. Kinetic energy densities are solved as

$$KE = \frac{1}{2}\left(\overline{u'^2} + \overline{v'^2}\right) \tag{4.2}$$

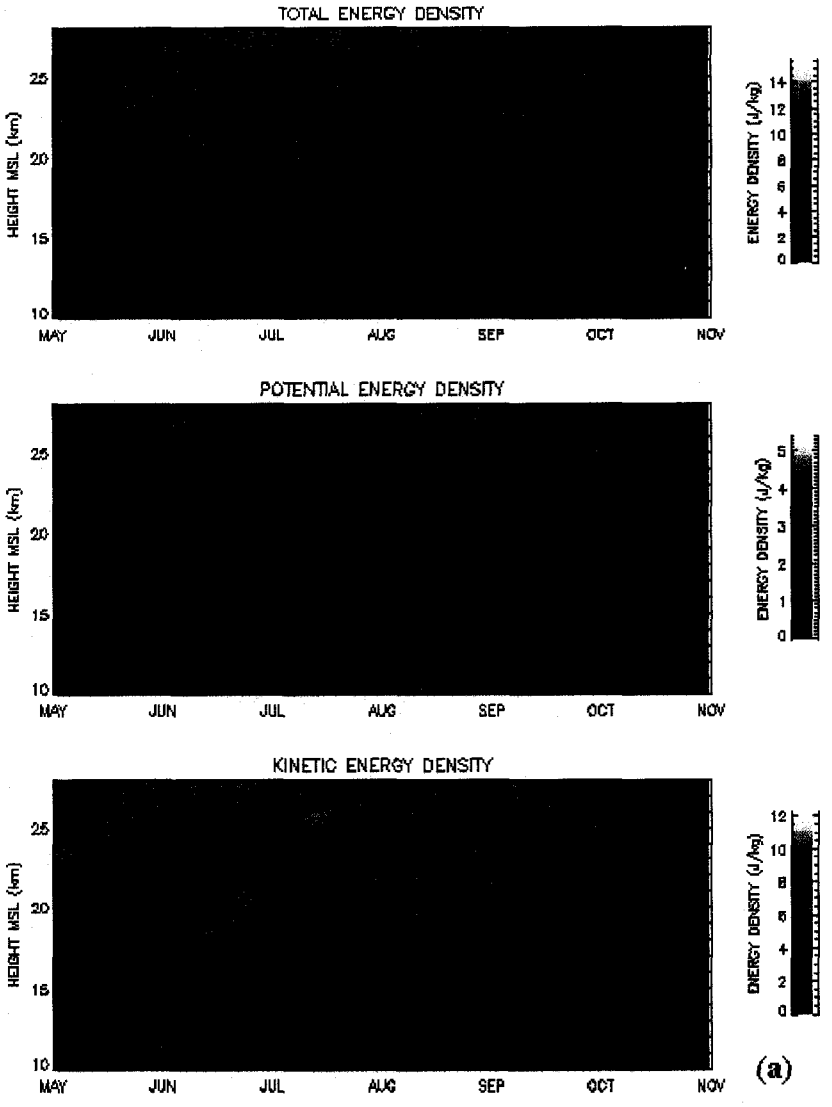

Figure 4.11 Gravity wave energy densities.
Total, potential and kinetic energy densities for gravity waves (J/kg) at South Pole from 10.0 – 28.0 km MSL at South Pole for May – October 2003 (a).

where

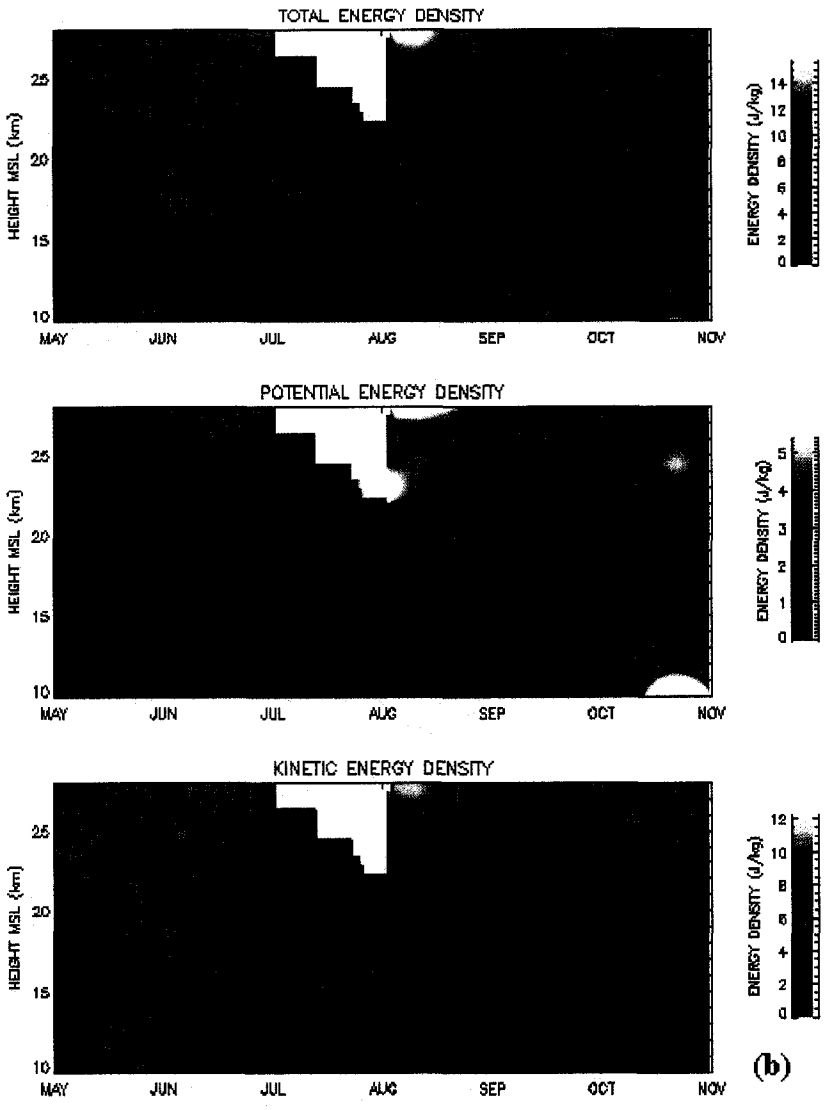

Figure 4.11 (cont.) Gravity wave energy densities.
Total, potential and kinetic energy densities for gravity waves (J/kg) at South Pole from 10.0 – 28.0 km MSL at South Pole for May – October 2004 (b). Missing data are in white, not to be confused with saturation of the color bar.

$$N_o^2 = g\frac{\partial \ln \bar{\theta}_o}{\partial z} \tag{4.3}$$

The total energy density the sum of Eqs. (4.1) and (4.2). To reduce the influence of noise, wind perturbations that exceeded 7.5 m/s were omitted in calculating Eq. (4.2).

Total, potential and kinetic energy densities for May through October from each season were then smoothed for imaging, again using the Hanning function (Appendix A) at 14-day and 2.0 km spatial half-widths. They are shown in Fig. 4.11 for 2003 (a), 2004 (b) and 2005 (c). Results from 2000 were excluded due to the effects of missing data in June and August that compromised the retrievals. Some contamination is possible in the results from 2004 and 2005 near periods of missing data. *Pfenninger et al.* (1999) display their results in composite form with all four years combined. Despite the possible caveats noted, the results here are mostly similar to their data in structure and magnitude. Kinetic energy densities generally exceed potential energy densities by as much as factor of 5. Cases of increased kinetic energy density do not necessarily coincide with increases in those for potential energy. High mean kinetic energy densities were reported by *Pfenninger et al.* (1999; Plate 3) throughout the winter stratosphere. They also found a consistent layer of high potential energy densities along the base of the winter thermal inversion of the mid-stratosphere. The latter signature is present in these data. However, kinetic energy maximums are more episodic here. Of course, these data are more representative of singular events rather than the bulk mean.

For the most part, definitive positive correlations are difficult to establish in comparing these data with specific events from the smoothed PSC ASR measurements in Figs. 3.5b-d. During May and June of both 2003 and 2005 (Figs. 4.11a and c), however,

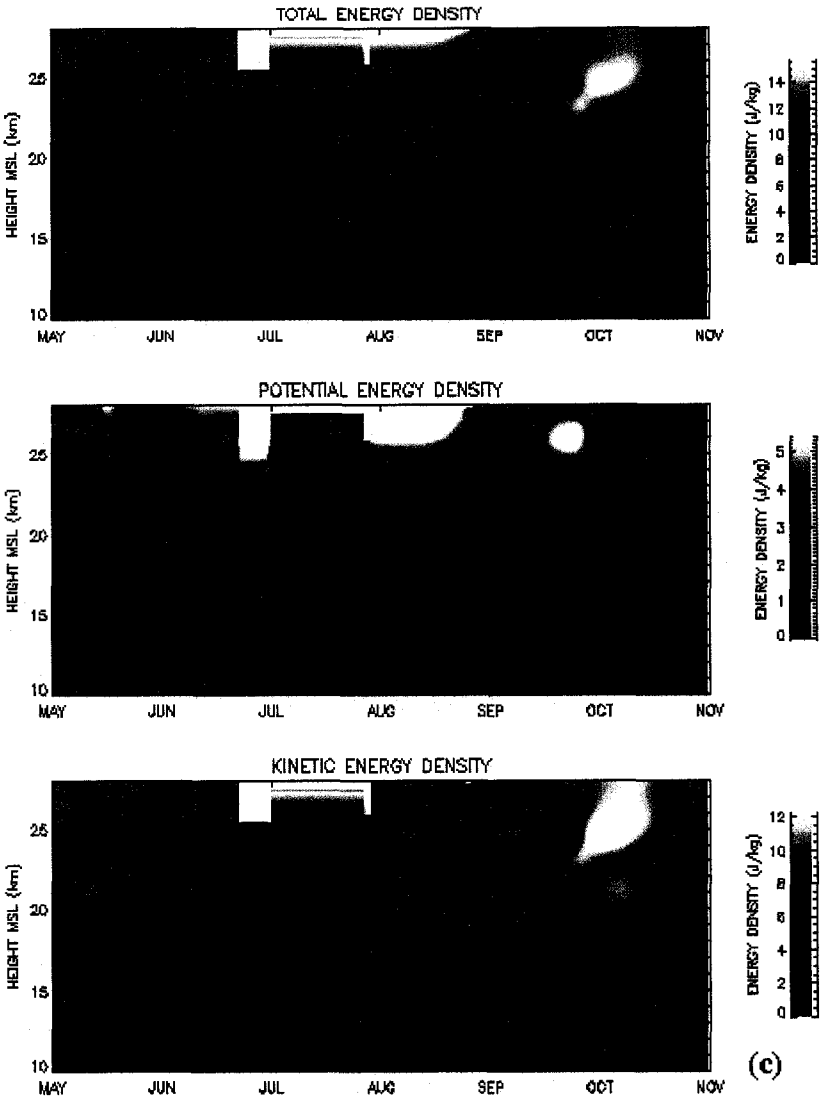

Figure 4.11 (cont.) Gravity wave energy densities.
Total, potential and kinetic energy densities for gravity waves (J/kg) at South Pole from 10.0 – 28.0 km MSL at South Pole for May – October 2005 (c). Missing data are in white, not to be confused with saturation of the color bar.

local maximums in kinetic energy density coincide with PSC episodes that occur in air unsaturated with respect to ice at the maximum estimated 6.0 ppmv water vapor

concentration (Figs. 3.6b and d). The onset of PSC in late May 2003 correlates with a maximum in kinetic energy density centered at 20.0 km MSL. ASR values seen outside of the upper-level bounds of the 6.0 ppmv isopleth similarly coincide with persistently high kinetic energy densities, including a nearly 10.0 J/kg maximum near the first of June at 25.0 km MSL. As seen in Fig. 3.8, temperatures cooled in 2005 more slowly relative to 2003. Ice-saturation was not observed that season until mid-June. But, a brief period of high ASR was measured during the first week of June that correlates with a local maximum in kinetic energy density centered at 20.0 km MSL, with a maximum value nearing 8.0 J/Kg. ASR were not detected for two weeks after this event.

From these limited data it is plausible that gravity waves are responsible for enhancing some PSC, such that their exhibited optical characteristics approach and exceed thresholds for MPL detection. However, these cases are likely limited to periods where temperatures are near the frost-point, and in early season when chemical concentrations are still mostly unperturbed (at the South Pole these periods are one in the same). Under these conditions, and consistent with earlier remarks, Type II PSC are most likely present from nucleation through rapid cooling experienced in gravity wave updrafts. Otherwise, if Type I are present, optically significant concentrations, so as to exceed algorithm detection levels, or anomalously large effective particle diameters are present as enhanced by local updrafts. This is most likely to occur, however, when HNO_3 concentrations are at maximum values. Over the course of the season, gravity waves would appear to be second-order mechanisms for PSC occurrence as measured with the

MPL. That is, they may be occurring and enhancing PSC growth, but it cannot be exclusively determined from these data that they are a primary cause for their presence.

CHAPTER 5

CONCLUSIONS

When the MPL was first deployed to the South Pole in 1999 the project was in the midst of an important restructuring. The instrument optical design had recently been upgraded to recede the field-stop (pinhole) position from the joint transmit/receive path to a position behind their intersection relative to incoming light. This introduced new difficulties to the standard preparatory tasks of collimating the transmitted beam and focusing the detector for ensuring optical clarity. For most lidar instruments, these are not terribly intensive assignments. However, for MPL, eye-safety requires an expanded beam to lower energy densities, followed by a narrow receiver field-of-view to limit ambient background signal relative to target backscatter (*Spinhirne*, 1993). The optical alignment is an extremely delicate procedure, and the instruments are focused using an elaborate 18-foot collimating bench with a dedicated 0.5 W laser source. Technicians at GSFC were going to great lengths to prepare instruments for field deployment for what wound up being an active 2000 field campaign season (the author logged over 1.0×10^5 km in air travel that year to support field experiments, including a visit to the South Pole). The South Pole experiment would be the first test, and they were faced with the prospect of not only deploying an instrument with what was basically an untested optical design with new components, but sending it to a site where the instrument could not be reached for a seven month period should something fail. In hindsight, it is too surprising that

instruments failed to survive the winter seasons of 2000 – 2002. Since then, however, with the benefit of experience and continued modification of the system design, data retrievals have occurred continuously there without major interruption.

The deployment to the South Pole was proposed to compliment the emerging science goals of the pending GLAS mission. Two questions, in particular, were to be addressed (*J. D. Spinhirne*, personal communication, 1999). First, there was concern on the GLAS Science Team for the ambiguities of multiple scattering that could arise in cases of blowing snow over the Polar Regions. For the satellite altimetry channel (the laser source wavelength at 1.064 μm, whereas atmospheric data was mostly collected at the doubled harmonic wavelength at 0.532 μm) multiple scattering could produce uncertainties in surface height retrievals outside of the specified bounds of the project mission statement. Second, there was concern for the safety of the GAPD detectors in the case of horizontally aligned ice crystals, and direct 180° backscatter off their basal faces. The installation of a turning mirror as part of the deployment, aside for aiding calibrations, was motivated by the desire to construct an experiment to study these effects by varying the viewing angle by a few degrees around zenith over brief periods. With three years before the eventual launch of GLAS, the South Pole MPL datasets offered a great opportunity to investigate these scenarios, and their results have been reported (e.g., *Mahesh et al.*, 2003; *Mahesh et al.*, 2005). Until an otherwise oblivious data technician, responsible for managing the South Pole data archive, brought a quick-look image to the MPL Principal Investigator and asked whether the instrument was failing or whether

there really signal being measured near 20.0 km on an otherwise ordinary June day, PSC were an afterthought.

The ozone hole remains a important social issue (*Weatherhead and Andersen*, 2006), though most of the science on the topic is settled, based on the bulk of research in the late 1980's through mid-1990's. The role of PSC in catalytic ozone destruction is well understood (e.g., *Solomon*, 1999). Cloud particles provide sites for heterogeneous reactions that free reactive chlorine and bromine molecules from inert forms. The uptake of nitric acid in intermediate stages of PSC growth, and subsequent sedimentation arising from the increase in particle fall velocity, remove nitrogen from nucleation heights (e.g., *Toon et al.*, 1990). Nitrogen otherwise reacts with and locks chlorine and bromine into relatively stable reservoir species that suppress catalytic ozone cycles (e.g., *Turco et al.*, 1989; *Solomon*, 1999). Still, models for ozone loss are not easily validated by current observations (e.g., *Douglass et al.*, 2006). Denitrification and dehumidification are not fully understood (e.g., *Tabazadeh et al.*, 2001). A primary reason these processes remain uncertain comes from a lack of continuous observations of PSC structure, type and phase over the entire austral pole, though chlorine and bromine concentration loading is also poorly resolved (e.g., *Douglass et al.*, 2006). While satellite techniques and coverage have improved understandably since the first observations of ozone loss in the early 1980's, limitations still exist, particularly with respect to coverage directly over the South Pole and vertical resolution.

Given the diversity and advances in most lidar technologies, MPL instruments would be an unlikely choice for a scientist wishing to collect PSC measurements. Over a decade

earlier, much higher-powered instruments were making robust observations of stratospheric clouds over Antarctica (e.g., *Fiocco et al.*, 1992, *Collins et al.*, 1993; *Gobbi et al.*, 1998). The advantages to the MPL technique, though, are eye-safety and the ability to make autonomous full-time measurements without otherwise inherent safety concerns (*Campbell et al.*, 2002). This is one characteristic that most lidar instruments have yet to match. Additionally, the MPL is easily deployed and maintained. Shipping to even the most remote field sites is possible with only minor modification to basic climate-controlled working spaces (*Campbell et al.*, 2003). Full-time operation yields datasets that satisfy the needs of long-term climate studies at high spatial and temporal resolutions. The PSC season at the South Pole lasts from between three and four months during winter. Sporadic or episodic observations lead to an incomplete perspective of seasonal cloud structure. MPL datasets can be used to answer the remaining questions of PSC occurrence and ozone loss that are not yet fully reconciled, including denitrification, dehumidification. Climatological cloud datasets using lidars have been demonstrated (e.g., *Sassen and Campbell*, 2001) This dissertation investigates these scenarios using data collected from 2000 and 2003-2005; a period important for it lacks any lingering stratospheric influence of the Mt. Pinatubo eruption of 1992 (e.g., *Cacciani et al.*, 1997b).

An algorithm is formulated and described for retrieving particulate layer boundaries from the MPL signal profile. In this integral first step, two goals are achieved. First, tropospheric and stratospheric cloud layers are found. Second, and equally important, the algorithm derives these layers as a function of attenuated scattering ratio relative to the uncertainties in the measured signal. This is premised on the photon-counting properties

of the GAPD detectors, and the use of Poisson statistical analysis. This works to relate the relative scattering intensity of detected cloud layers in a statistical manner that demonstrates the integrity of the retrievals. This work has applications outside of the just the MPLNET project (*Welton et al.*, 2001), and its nearly forty instruments. For low-powered instruments, this technique is a uniquely objective and sensitive method for determining layer boundaries in the presence of appreciable noise. For nadir-pointing lidars, where molecular scattering layers exist adjacent to the operating platform, and in between any particulate targets, the technique would be ideal. Such conditions are implicit for satellite experiments. Furthermore, the work may be expanded. Here, the processed datasets are shown for 0.01 fractional day iterations. This time may be increased, so as to improve the retrievals with respect to signal noise, though possibly at the expense of spatial and temporal structure. The base resolution (0.01 fractional day resolution, in this case) would serve as a means for profile-screening in longer averages so as to not bias them with attenuation-limiting effects that distort averaged profiles with respect to normalized molecular scattering profiles.

Upon examining the South Pole MPL PSC measurements relative to thermal and chemical properties, the primary finding is a linear correlation between total integrated MPL backscatter and integrated Dobson Unit days (relative to the 220 DU standard for ozone hole conditions; *Stolarski et al.*, 1986; *Geer*, 1996). The latter value relates the depth and temporal extent of seasonal ozone loss. This result is important since the MPL is not considered sensitive to all PSC likely present. Though the sample is thought to consist mostly of Type II PSC (i.e., ice), the possibility of Type I PSC measurements is

considered for periods early in the polar night, when background concentrations of nitric acid and water vapor are unperturbed by previous PSC events and gravity wave enhancement at upper-levels is occurring. Still, *Solomon* (1999) points out that while the microphysical mechanisms responsible for nucleation and denitrification are still in question, these processes are not necessarily critical. Heterogeneous chemistry occurs on all forms of PSC, whether they are ice, solid hydrate particles or solution droplets, albeit with varying efficiencies. This makes ozone depletion more a function of temperature and ambient concentrations of water vapor and nitric acid than it does specific thresholds for particle nucleation. *Tabazadeh et al.* (2001) points out an important nuance in this idea, but the overall premise is not changed. Ozone depletion is enabled in the presence of, and more dynamically, by the chemical preconditioning of air by PSC. Whereas traditional research lidars have been used in the past to record PSC macrophysical properties episodically, MPL instruments can be relied upon to serve this task in an autonomous full-time operating mode, with near real-time post-processing capability. In tandem with passive radiometric measurements of chemical concentrations, particularly those perturbed by heterogeneous activity (e.g., ClO, HCl, etc...), as well as chemical modeling, accurate forecasts for seasonal ozone losses and future trends may be accomplished.

Composite models for seasonal PSC occurrence, thermal evolution and ozone loss are described. Whereas traditional models for denitrification and dehumidification describe the irreversible removal of nitric acid and water vapor from PSC nucleating levels, they do not consider the effects of their redistribution (e.g., *Jensen et al.*, 2002). In late-May

and early June, when clouds are typically first observed, base heights are measured near and above 15.0 km MSL. Below these levels, evaporation of cloud particles is occurs from particles falling below. By mid-season, PSC are gradually observed with higher frequency at these lower heights. These data suggest a migration of nitric acid and water vapor downward through the lower stratosphere from May through July. Therefore, early season PSC at upper-levels (above 20.0 km MSL) may enhance the likelihood for PSC at lower levels (near 15.0 km MSL) in later months. Coincidentally or not, these heights are where maximum ozone losses are measured in spring.

Synoptic-scale overrunning in air along isentropic surfaces is found to be a primary mechanism for inducing PSC at the South Pole. Normalized geopotential height anomalies south of 60° S are investigated from 2000 and 2003 – 2005 relative to a 22-year climatology developed from NCEP reanalysis data (*Kalnay et al.*, 1996; *Kistler et al.*, 2001). Rather than a direct proxy for temperature, these data are considered as ones for anomalous meridional transport. In late May and early June, as temperatures approach the ice frost point, and PSC are first observed from the South Pole, particle growth and sedimentation dehumidify and denitrify air advecting over the region. In the absence of continuous mixing of unperturbed air within the vortex, perhaps even influenced by transport across this boundary, PSC observations should cease. In fact, this scenario was apparent from the July and August 2003 data sample. During 2000, however, when temperatures were sufficiently cold, episodes of strong positive geopotential height anomalies were observed. Elevated PSC were detected suggesting that mixing of unperturbed air was occurring, thereby inducing clouds at a late stage in

the season. Therefore, in spite of potentially cold temperatures, a vortex that is too stable and deep, so as to inhibit significant mixing, may actually suppress PSC occurrence and possibly the extent of ozone depletion in spring. Mixing of all vortex air toward the South Pole creates an overrunning scenario, whereby quasi-adiabatic lifting and cooling induce PSC nucleation, growth and sedimentation. Conversely, a vortex that is too weak to induce persistently low temperatures near the South Pole (i.e., 2004) would limit PSC occurrence in an opposite manner. Previous work has suggested the importance of isentropic surface enhancement from tropospheric disturbances and potential vorticity maximums (e.g, *Tuck*, 1989; *Fromm et al.*, 1997; *Teitelbaum et al.*, 2001; *Palm et al.*, 2005). At the South Pole, however, where temperatures on average are coldest, it is not clear that these mechanisms are anything but secondary processes since there is sufficient broad-scale isentropic lift for approaching air.

Recent studies have focused on the gradual recovery of the ozone layer in the southern hemisphere (e.g., *Weatherhead and Andersen*, 2006; *Newman et al.*, 2006). However, other studies have suggested that continued cooling of the lower-stratosphere in response to greenhouse warming near the planet surface could lead to ozone depletion in the northern hemisphere on similar magnitudes as in the south (e.g., *Ramaswammy et al.*, 2001; *Tabazadeh et al.*, 2001). Lidar instruments are unique tools for profiling relatively small atmospheric particles, and their application can be far-reaching. Long-term measurements of PSC, both from ground-based lidar experiments such as the South Pole MPL, and from satellites like GLAS and CALIPSO, will widen the perspective that scientists may view the PSC/ozone loss cycle. As more autonomous eye-safe instruments

are operated from an increasing number of ground sites, more datasets will be available to study this topic. Of course, technological advances will continue to improve the robust quality of all measurements. Designs for MPL instruments with polarization-diversity, for example, have been constructed, and prototypes are being tested. In advance of their deployment, this research and continuing objectives, will serve as a basis from which to consider future measurements.

REFERENCES

Akasofu, S.-I., B. Fogle and B. Haurwitz, eds., *Sydney Chapman, Eighty*, University of Alaska, 230 pp, 1967.

Anderson, J. G., W. H. Brune and M. H. Proffitt, Ozone destruction by chlorine radicals within the Antarctic vortex: The spatial and temporal evolution of ClO-O_3 anticorrelation based on in situ ER-2 data, *J. Geophys. Res.*, *94*, 11,465-11,479, 1989.

Andrews, D. G., J. R. Holton and C. B. Levy, *Middle Atmosphere Dynamics*, Academic, San Diego, 504 pp, 1987.

Ansmann, A, U. Wandinger, M. Riebesell, C. Weitkamp and W. Michaelis, Independent measurement of extinction and backscatter profiles in cirrus clouds using a combined Raman elastic-backscatter lidar, *Appl. Opt.*, *31*, 7113-7131, 1992.

Arnold, F., H. Schlager, J. Hoffmann, P. Metzinger and S. Spreng, Evidence for stratospheric nitric acid condensation from balloon and rocket measurements in the Arctic, *Nature*, *342*, 493-497, 1989.

Bates, D. R. and M. Nicolet, Atmospheric hydrogen, *Publ. Astron. Soc. Pac*, *62*, 106-110, 1950.

Becker, G., R. Müller, D. S. McKenna, M. Rex and K. S. Carslaw, Ozone loss rates in the Arctic stratosphere in the winter 1991/1992: Model calculations compard with match results, *Geophys. Res. Lett.*, *25*, 4325-4328, 1998; Correction, *26*, 327, 1999.

Bertram, A. K. and J. J. Sloan, Temperature-dependent nucleation rate constants and freezing behavior of submicron nitric acid dehydrate aerosol particles under stratospheric conditions, *J. Geophys. Res.*, *103*, 3553-3561, 1998a.

Bertram, A. K. and J. J. Sloan, The nucleation rate constants and freezing mechanism of nitric acid trihydrate aerosol under stratospheric conditions, *J. Geophys. Res.*, *103*, 13,261-13,265, 1998b.

Bevington, P. R., *Data Reduction and Error Analysis for the Physical Sciences*, McGraw-Hill Book Company, New York, 336 pp, 1969.

Blackman, R. B. and J. W. Tukey, *The Measurement of Power Spectra: From the Point of View of Communications Engineering*, Dover Publications, Inc., New York, 190 pp, 1959.

Bohren, C. F. and B. A. Albrecht, *Atmospheric Thermodynamics*, Oxford University Press, Oxford, 402 pp, 1998.

Bohren, C. F. and D. R. Huffman, *Absorption and Scattering of Light by Small Particles*. Wiley & Sons, 544 pp, 1998.

Browell, E. V., C. F. Butler, S. Ismail, P. A. Robinette, A. F. Carter, N. S. Higdon, O. B. Toon, M. R. Schoeberl and A. F. Tuck, Airborne lidar observations in the wintertime arctic stratosphere: Polar stratospheric clouds, *Geophys. Res. Lett.*, *17*, 385-388, 1990.

Browning, K. A. and N. M. Roberts, Structure of a frontal cyclone, *Q. J. R. Meteorol. Soc.*, *120*, 1535-1557, 1994.

Cacciani, M., G. Fiocco, P. Colagrande, P. Di Girolamo, A. di Sarra and D. Fuà, Lidar observations of polar stratospheric clouds at the South Pole 1. Stratospheric unperturbed conditions, 1990, *J. Geophys. Res.*, *102*, 12,937-12,943, 1997a.

Cacciani, M., P. Colagrande, A. di Sarra, D. Fuà, P. Di Girolamo and G. Fiocco, Lidar observations of polar stratospheric clouds at the South Pole 2. Stratospheric perturbed conditions, 1992 and 1993, *J. Geophys. Res.*, *102*, 12,945-12,955, 1997b.

Campbell, J. R., D. L. Hlavka, J. D. Spinhirne, D. D. Turner, C. J. Flynn, Operational cloud boundary detection and analysis from micropulse lidar data, In *Proc. 8th Atmospheric Radiation Measurement Science Team Meeting*, Tucson, AZ, DOE/ER-0738, pp. 119-122, 1998.

Campbell, J. R., D. L. Hlavka, J. D. Spinhirne, R. Ferrare and D. D. Turner, Automated aerosol retrieval algorithms for ARM micro pulse lidars, in *Preprints of Symposium on Lidar Atmospheric Monitoring*, pp. 71-74, American Meteorol. Soc., Boston, Mass, 2000.

Campbell, J. R., D. L. Hlavka, E. J. Welton, C. J. Flynn, D. D. Turner, J. D. Spinhirne, V. S. Scott and I. H . Hwang, Full-time eye-safe cloud and aerosol lidar observation at Atmospheric Radiation Measurement program sites: Instruments and data processing, *J. Atmos. Oceanic Technol.*, **19** (4), 431-442, 2002.

Campbell, J. R., E. J. Welton, J. D. Spinhirne, Q. Ji, S.-C. Tsay, S. J. Piketh, M. Barenbrug and B. N. Holben, Micropulse lidar observations of tropospheric

aerosols over northeastern South Africa during the ARREX and SAFARI 2000 dry season experiments, *J. Geophys. Res.*, *108*(D13), 8497, doi:10.1029/2002JD002563, 2003.

Cantrell, W. and A. Heymsfield, Production of ice in tropospheric clouds: A review, *Bull. Amer. Meteorol. Soc.*, **86,** 795-807, 2005.

Cariolle, D., S. Muller, F. Cayla and M. P. McCormick, Mountain waves, polar stratospheric clouds, and the ozone depletion over Antarctica, *J. Geophys. Res.*, *94*, 11,233-11,240, 1989.

Carslaw, K. S. and T. Peter, Uncertanties in reactive update coefficients for solid stratospheric particles, I, Surface chemistry, *Geophys. Res. Lett.*, *24*, 1743-1746, 1997.

Carslaw, K. S., B. P. Luo, S. L. Clegg, T. Peter, P. Brimblecombe and P. Crutzen, Stratospheric aerosol growth and HNO_3 gas phase depletion from coupled HNO_3 and water uptake by liquid particles, *Geophys. Res. Lett.*, *21*, 2479-2482, 1994.

Carslaw, K. S., T. Peter and S. L. Clegg, Modeling the composition of liquid stratospheric aerosols, *Rev. Geophys.*, *35*, 125-154, 1997a.

Carslaw, K. S., T. Peter and R. Müeller, Uncertainties in reactive uptake coefficients for solid stratospheric particles, 2, Effect on ozone depletion, *Geophys. Res. Lett.*, *24*, 1747-1750, 1997b.

Carslaw, K. S., M. Wirth, A. Tsias, B. P. Luo, A. Dornbrack, M. Leutbecher, J. Volkert, W. Renger, J. T. Bacmeister and T. Peter, Particle microphysics and chemistry in remotely observed mountain polar stratospheric clouds, *J. Geophys. Res.*, *103*, 5785-5796, 1998a.

Carslaw, K. S., M. Wirth, A. Tsias, B. P. Luo, A. Dörnbrack, M. Leutbecher, H. Volkert, W. Renger, J. T. Bacmeister, E. Reimer and Th. Peter, Increased stratospheric ozone depletion due to mountain-induced atmospheric waves, *Nature*, *391*, 657-678, 1998b.

Chapman, S., On ozone and atomic oxygen in the upper atmosphere, *Philos. Mag.*, *10*, 369-383, 1930.

Chipperfield, M. P. and J. A. Pyle, Model sensitivity studies of Arctic ozone depletion, *J. Geophys. Res.*, *103*, 28,389-28.403, 1998.

Chu, X., C. S. Gardner and G. Papen, Lidar observations of polar mesospheric clouds at South Pole: Seasonal variations, *Geophys. Res. Lett. 28*, 1203-1206, 2001.

Cicerone, R. J., R. S. Stolarski and S. Walters, Stratospheric ozone destruction by man-made chlorofluoromethanes, *Science*, *185*, 1165-1167, 1974.

Clothiaux, E. E., G. G. Mace, T. P. Ackerman, T. J. Kane, J. D. Spinhirne and V. S. Scott, An automated algorithm for detection of hydrometeor returns in micropulse lidar data, *J. Atmos. Oceanic Technol.*, **15**, 1035-1042, 1998.

Collins, R. L. K. P. Bowman and C. S. Gardner, Polar stratospheric clouds at South Pole in 1990: Lidar observations and analysis, *J. Geophys. Res.*, *98*, 1001-1010, 1993.

Cornu, A., Observation de la limite ultraviolette du spectre solaire á diverses altitudes, *C. R. Hebd. Seances Acad. Sci.*, *89*, 808, 1879.

Crutzen, P. J., The influence of nitrogen oxide on the atmospheric ozone content, *Q. J. R. Meteorol. Soc.*, *96*, 320-327, 1970.

Crutzen, P. J., Ozone production rates in an oxygen-hydrogen-nitrogen oxide atmosphere, *J. Geophys. Res.*, *76*, 7311-7327, 1971.

Crutzen, P. J., Estimates of possible future ozone reductions from continued use of fluoro-chloro-methanes/CF_2Cl_2, $CFCl_3$/, *Geophys. Res. Lett.*, *1*, 205-208, 1974.

Crutzen, P. J. and F. Arnold, Nitric acid cloud formation in the cold Antarctic stratosphere: A major cause for the springtime 'ozone hole', *Nature*, *324*, 651-655, 1986.

Crutzen, P. J., C. Bruhl, U. Schmailzl and F. Arnold, Nitric acid haze formation in the lower stratosphere: A major contributing factor to the development of the Antarctic "ozone hole", in *Aerosols and Climate*, edited by P. V. Hobbs and M. P. McCormick, pp. 287-204, A. Deepak, Hampton, VA, 1988.

de Zafra, R. L., M. Jaramillo, A. Parrish, P. Solomon, B. Connor and J. Barnett, High concentrations of chlorine monoxide at low altitudes in the Antarctic spring stratosphere : Diurnal variation, *Nature*, *328*, 408-411, 1987.

de Zafra, R. L., M. Jaramillo, J. Barrett, L. K. Emmons, P. M. Solomon and A. Parrish, new observations of low concentration of ClO in the springtime lower stratosphere over Antarctica and its implications for ozone-depleting chemistry, *J. Geophys. Res.*, *94*, 11,423-11428, 1989.

Douglass, A. R., R. S. Stolarski, S. E. Strahan and B. C. Polansky, Sensitivity of Arctic ozone loss to polar stratospheric cloud volume and chlorine and bromine loading

in a chemistry and transport model, *Geophys. Res. Lett.*, *33*, L17809, doi:10.1029/2006GL026492, 2006.

Draxler, R. R., Boundary layer isentropic and kinematic trajectories during the August 1993 North Atlantic Regional Experiment Intensive, J. Geophys. Res., *101*, 29,255-29,268, 1996

Draxler, R. R. and Rolph, G. D., HYSPLIT (HYbrid Single-Particle Lagrangian Integrated Trajectory) Model access via NOAA ARL READY Website (http://www.arl.noaa.gov/ready/hysplit4.html). NOAA Air Resources Laboratory, Silver Spring, MD, 2003.

Drdla, K. A. Tabazadeh, R. P. Turco, M. Z. Jacobson, J. E. Dye, C. Twohy and D. Baumgardner, Analysis of the physical state of one Arctic polar stratospheric cloud based on observations, *Geophys. Res. Lett.*, *21*, 2475-2478, 1994.

Dye, J. E., B. W. Gandrud, D. Baumgardner, K. R. Chan, G. V. Ferry, M. Lowenstein, K. K. Kelly and J. C. Wilson, Observed particle evolution in the polar stratospheric cloud of January 24, 1989, *Geophys. Res. Lett.*, *17*, 413-416, 1990.

Dye J. E., D. Baumgardner, B. W Gandrud, S. R. Kawa, K. K. Kelly, M. Loewenstein, G. V. Ferry, K. R. Chan and B. L. Gary, Particle size distributions in Arctic polar stratospheric clouds, growth and freezing of sulfuric acid droplets, and implications for cloud formation, *J. Geophys. Res.*, *97*, 8015-8034, 1992.

Eckermann, S. D., A. Dörnbrack, S. B. Vosper, H. Flentje, M. J. Mahoney, T. P. Bui and K. S. Carslaw, Mountain wave-induced polar stratospheric cloud forecasts for aircraft science flights during SOLVE/THESEO 2000, *Wea. Forecasting*, **21**, 42-68, 2006.

Egger, J., Topographic wave modification and the angular momentum balance of the Antarctic troposphere, *J. Atmos. Sci.*, **49**, 327-334, 1992.

Elkins, J. W., T. M. Thompson, T. J. Swanson, J. H. Butler, B. D. Hall, S. O. Cummings, D. A. Fisher and A. G. Raffo, Decrease in the growth rates of atmospheric chlorofluorocarbons 11 and 12, *Nature*, *364*, 780-783, 1993.

Eloranta, E. W., Practical model for the calculation of multiply scattered lidar returns, *Appl. Opt.*, **37**, 2464-2472, 1998.

Environmental Science Services Administration, National Aeronautics and Space Administration, and U. S. Air Force, *U. S. Standard Atmosphere Supplements, 1966*, Washington, D. C., 289 pp., 1967.

Fahey, D. W., K. K. Kelly, G. V. Ferry, L. R. Poole, J. C. Wilson, D. M. Murphy, M. Lowenstein and K. R. Chan, In situ measurements of total reactive nitrogen, total water, and aerosol in a polar stratospheric cloud in the Antarctic, *J. Geophys, Res.*, *94*, 11,299-11,316, 1989

Fahey, D. W., K. K. Kelly, S. R. Kawa, A. F. Tuck, M. Loewenstein, K. R. Chan and L. E. Heidt, Observations of denitrification and dehydration in the winter polar stratospheres, *Nature*, *344*, 321-324, 1990.

Fahey, D. W., et al., The detection of large HNO_3-containing particles in the winter arctic stratosphere, *Science*, *291*, 1026-1031, 2001.

Farman, J. C., B. G. Gardiner and J. D. Shanklin, Large losses of total ozone in Antarctica reveal seasonal ClO_x/NO_x interaction, *Nature*, *315*, 207-210, 1985

Ferry, G. V., E. Neish, M. Schultz and R. F. Pueschel, Concentrations and size distributions of Antarctic stratospheric aerosols, *J. Geophys. Res.*, *94*, 16,459-16,474, 1989.

Fiocco, G., D. Fuà, M. Cacciani, P. Di Girolamo, J. De Luisi, On the temperature dependence of polar stratospheric clouds, *Geophys. Res. Lett.*, *18*, 424-427, 1991.

Fiocco, G., M. Cacciani, P. D Girolamo and D. Fuà, Statospheric clouds at South Pole during 1988 1. Results of lidar observations and their relationship to temperature, *J. Geophys. Res.*, *97*, 5939-5946, 1992.

Fleming, E. L. S. Chandra, M. R. Shoeberl and J. J. Barnett, *Monthly Mean Global Climatology of Temperature, Wind, Geopotential Height and Pressure for 0-120 km*, NASA Technical Memorandum 100697, National Aeronautics and Space Administration, 88 pp, 1988.

Fox, L. E., D. R. Worsnop, M. S. Zahniser and S. C. Wofsy, Metastable phases in polar stratospheric aerosols, *Science*, *267*, 351-355, 1995.

Fromm, M. D., J. D. Lumpe, R. M. Bevilacqua, E. P. Shettle, J. Hornstein, S. T. Massie and K. H. Fricke, Observations of Antarctic polar stratospheric clouds by POAM II: 1994-1996, *J. Geophys. Res.*, *102*, 23,659-23,672, 1997.

Fuà, D., M. Cacciani, P. Di Girolamo, G. Fiocco and A. di Sarra, Stratospheric clouds at South Pole during 1988, 2, Their evolution in relation to atmospheric structure and composition, *J. Geophys. Res.*, *97*, 5947-5952, 1992.

Gable, C. M., H. F. Betz and S. H. Maron, Phase equilibria of the system sulfur trioxide water, *J. Am. Chem. Soc.*, *72*, 1445-1452, 1950.

Gaffen, D. J., M. A. Sargent, R. E. Habermann and J. R. Lanzante, Sensitivity of tropospheric and stratospheric temperature trends to radiosonde data quality, *J. Climate*, **13,** 1776-1796, 2000.

Gandrud, B. W., P. D. Sperry, L. Sanford, K. K. Kelly, G. V. Ferry and K. R. Chan, Filter measurement results from the Airborne Antarctic Ozone Experiment, *J. Geophys. Res.*, *94*, 11,285-11,297, 1989.

Gardner, C. S., G. C. Papen, X. Chu and W. Pan, First lidar observations of middle atmospheric temperatures, Fe densities, and polar mesospheric clouds over the north and south poles, *Geophys. Res. Lett.*, *28*, 1199-1201, 2001.

Gary , B. L., Observational results using the microwave temperature profiler during the Airborne Antarctic Ozone Experiment, *J. Geophys. Res.*, *94*, 11,223-11,231, 1989.

Geer, I. W., ed, *Glossary of Weather and Climate with Related Oceanic and Hydrologic Terms*, American Meteorological Society, Boston, 272 pp, 1996.

Gelbwachs, J. A., Iron Boltzmann factor LIDAR: proposed new remote-sensing technique for mesospheric temperature, *Appl. Opt.*, *33*, 7151-7156, 1994.

Gille, J. C, P. L. Bailey and C. A. Craig, Revised reference model for nitric acid, *Adv. Space Res.*, Vol. 13, No. 1, 59-72, 1993.

Gobbi, G. P., T. Deshler, A. Adriani and D. J. Hoffman, Evidence for denitrification in the 1990 Antarctic spring stratosphere: I, Lidar and temperature measurements, *Geophys. Res. Lett.*, *18*, 1995-1996, 1991.

Gobbi, G. P., Lidar estimation of stratospheric aerosol properties: Surface, volume, and extinction to backscatter ratio, *J. Geophys. Res.*, *100*, 11,219-11,235, 1995.

Gobbi, G. P., G. Di Donfrancesco and A. Adriani, Physical properties of stratospheric clouds during the Antarctic winter of 1995, *J. Geophys. Res.*, *103*, 10,859-10,873, 1998.

Hallett, J. and R. E. J. Lewis, Mother-of-pearl clouds, *Weather*, *22*, 56-65, 1967.

Hamill, P. and L. R. McMaster, eds., *Polar Stratospheric Clouds*, National Aeronautics and Space Administration, CP 2318, 1984.

Hamill, P., O. B. Toon and R. P. Turco, Characteristics of polar stratospheric clouds during the formation of the Antarctic ozone hole, *Geophys. Res. Lett.*, *13*, 1288-1291, 1986.

Hamill, P., O. B. Toon and R. P. Turco, On the growth of nitric and sulfuric acid hydrates under stratospheric conditions, *J. Atm. Chem.*, *7*, 287-315, 1988.

Hampson, J., Photochemical behavior of the ozone layer, *Tech. Note TH 1627/64,* Can. Armament Res. And Dev. Estab., Valcartier, Que., Canada, 1964.

Hanson, D. and K. Mauersberger, Laboratory studies of the nitric acid trihydrate: Implications for the south polar stratosphere, *Geophys. Res. Lett.*, *15*, 855-858, 1988.

Hanson, D. R. and A. R. Ravishankara, Reactive uptake of $ClONO_2$ onto sulfuric acid due to reaction with HCl and H_2O, *J. Phys. Chem.*, *98*, 5728-5735, 1994.

Hartley, W. N., On the probable absorption of solar radiation by atmospheric ozone, *Chem. News*, *42*, 268, 1880.

Heath, D. F., A. J. Krueger and P. J. Crutzen, Solar proton event: Influence on stratospheric ozone, *Science*, *197*, 886-889, 1977.

Hofmann, D. J. and T. Deshler, Stratospheric cloud observations during formation of the Antarctic ozone hole in 1989, *J. Geophys. Res.*, *96*, 2897-2912, 1991.

Hofmann, D. J. T. Deshler, F. Arnold and H. Schlager, Balloon observations of nitric acid aerosol formation in the Arctic stratosphere, II., Aerosol, *Geophys. Res. Lett.*, *17*, 1279-1282, 1990.

Holben, B. N., et al., AERONET – A federated instrument network and data archive for aerosol characterization. *Remote Sens. Environ.*, *66(1)*, 1-16, 1998.

Hoppel, K. W., R. Bevilacqua, D. Allen, G. Nedoluha and C. Randall, POAM III observations of the anomalous 2002 Antarctic ozone hole, *Geophys. Res. Lett.*, 10.1029/2003GL016938, 2003.

Iraci, L. T., T. J. Fortin and M. A. Tolbert, Dissolution of sulfuric acid tetrahydrate at low temperatures and subsequent growth of nitric acid trihydrate, *J. Geophys. Res.*, *103*, 8491-8498, 1998.

Iwasaka, Y., Lidar measurements on the Antarctic stratospheric aerosol layer, II, The changes of layer height and thickness in winter, *J. Geomagnet. Geoelectr.*, *38*, 99-109, 1986a.

Iwasaka, Y., Large depolarization ratio of the winter Antarctic stratospheric aerosol layer; Lidar measurement at Syowa station Antarctica, *J. Meteorol. Soc. Jpn.*, *64*, 303-309, 1986b.

Iwasaka, Y., T. Hirasawa and H. Fukunishi, Lidar measurement of the Antarctic stratospheric aerosol layer, I, Winter enhancement, *J. Geomagnet. Geoelectr.*, *37*, 1087-1095, 1985.

Jacob, D. J., *Introduction to Atmospheric Chemistry*, Princeton University Press, Princeton, 266 pp, 1999.

James, I. N., The Antarctic drainage flow: Implications for hemispheric flow on the southern hemisphere, *Antarctic Sci.*, *1*, 279-290, 1989.

Jensen, E. J., O. B. Toon, A. Tabazadeh and K. Drdla, Impact of polar stratospheric cloud particle composition, number density, and lifetime on denitrification, *J. Geophys. Res.*, *107*(D20), 8284, doi:10.1029/2001JD000440, 2002.

Jet Propulsion Laboratory (JPL), Chemical Kinetics and Photochemical Data for Use in Stratospheric Modeling, Evaluation number 12 of the NASA panel for data evaluation, *JPL Publ.* 97-4, 1997.

Johnston, H. S., Reduction of stratospheric ozone by nitrogen oxide catalysts from supersonic transport exhaust, *Science*, *173*, 517-522, 1971.

Jones, R. L., et al., Lagrangian photochemical modeling studies of the 1987 Antarctic spring vortex, 1, Comparison with AAOE observations, *J. Geophys. Res.*, *94*, 11,529-11,558, 1989.

Juckes, M. N., I. N. James and M. Blackburn, The influence of Antarctica on the momentum budget of the southern extratropics, *Quart. J. Roy. Met. Soc.*, **120,** 1017-1044, 1994.

Junge, C. E., Vertical profiles of condensation nuclei in the stratosphere, *J. Meteorol.*, *18*, 501-509, 1961

Junge, C. E. and J. E. Manson, Stratospheric aerosol studies, *J. Geophys. Res.*, *66*, 2163-2182, 1961.

Junge, C. E., C. W. Changnon and J. E. Manson, Stratospheric aerosols, *J. Meteorol.*, *18*, 81-108, 1961.

Kalnay, E., M. Kanamitsu, R. Kistler, W. Collins, D. Deaven, L. Gandin, M. Iredell, S. Saha, G. White, J. Woollen, Y. Zhy, A. Leetmaa, R. Reynolds, M. Chelliah, W. Ebuisuzaki, W. Higgins, J. Janowiak, K. C. Mo, C. Ropelewski, J. Wang, R. Jenne, D. Joseph, The NCEP/NCAR 40-year reanalysis project, *Bull. Amer. Meteor. Soc.*, **79**, 2753-2769, 1996.

Kasten, F., Falling speed of aerosol particles, *J. Appl. Meteorol.*, **7**, 944-947, 1968.

Kawa, S. R., D. W. Fahey, K. K. Kelly, J. E. Dye, D. Baumgardner, B. W. Gandrud, M. Lowenstein, G. V. Ferry and K. R. Chan, The Arctic polar stratospheric cloud aerosol: Aircraft measurements of reactive nitrogen, total water , and particles, *J. Geophys. Res.*, *97*, 7905-7923, 1992.

Kent, G. S., L. R. Poole and M. P. McCormick, Characteristics of Arctic polar stratospheric clouds as measured by airbone lidar, *J. Atmos. Sci.*, **43**, 2149-2161, 1986.

King, J. C. and J. Turner, *Antarctic Meteorology and Climatology*, Cambridge University Press, Cambridge, 409 pp, 1997.

Kinne, S., O. B. Toon, G. C. Toon, C. B. Farmer, E. V. Browell and M. P. McCormick, Measurements of size and composition of particles in polar stratospheric clouds from infrared solar absorption spectra, *J. Geophys. Res.*, *94*, 16,481-16,491, 1989.

Kistler, R., E. Kalnay, W. Collins, S. Saha, Glenn, White, J. Woollen, M. Chelliah, W. Ebisuzaki, M. Kanamitsu, W. Kousky, H. van den Dool, R. Jenne and M. Fiorino, The NCEP-NCAR 50-year reanalysis: Monthly means CD-ROM and documentation, *Bull. Amer. Meteor. Soc.*, **82**, 247-268, 2001.

Knopf, D. A., T. Koop, B. P. Luo, U. G. Weers and T. Peter, Homogeneous nucleation of NAD and NAT in liquid stratospheric aerosols insufficient to explain denitrification, *Atmos. Chem Phys. Discuss.*, 2, 669-687, 2002.

Ko, M. K. W. and N. D. Sze, Effect of recent rate data revisions on stratospheric modeling, *Geophys. Res. Lett.*, *10*, 341-344, 1983.

Ko, M. K. W., J. M. Rodrigues, N. D. Sze, M. H. Proffitt, W. L. Starr, A. Krueger, E. V. Browell and M. P. McCormick, Implications of AAOE observations for proposed chemical explanations of the seasonal and interannual behavior of Antarctic ozone, *J. Geophys. Res.*, *94*, 16,705-16,715, 1989.

Kondo, Y., H. Irie, M. Koike, G. E. Bodeker, Denitrification and nitrification in the Arctic stratosphere during the winter of 1996-1997, *Geophys. Res. Lett.*, *27*, 337-336, 2000.

Koop, T., H. P. Ng, L. T. Molina and M. J. Molina, A new optical technique to study aerosol phase transitions: The nucleation of ice from H_2SO_4 aerosols, *J. Phys. Chem. A*, *102*, 8924-8931, 1998.

Koop, T. B, P. Luo, A. Tsias and T. Peter, Water activity as a the determinant for homogeneous ice nucleation in aqueous solutions, *Nature*, *406*, 611-614, 2000.

Kröger, C., M. Hervig, B. Nardi, L. Oolman, T. Deshler, S. Wood and S. Nichol, Stratospheric ozone reaches new minima above Mc Murdo Station, Antarctica, between 1998 and 2001, *J. Geophys. Res.*, *108*(D17), 4555, doi:10.1029/2002JD002904, 2003.

Larsen, N., J. A. Rosen, N. T. Kjome and B. Knudsen, Deliquescence and freezing of stratospheric aerosol droplets observed by balloon-borne backscatter sondes, *Geophys. Re. Lett.*, *22*, 1233-1236, 1995.

Larsen, N., B. M. Knudsen, J. M. Rosen, N. T. Kjome and E. Kyro, Balloonborne backscatter observation of Type I PSC formation: Inference about physical state from trajectory analysis, *Geophys. Res. Lett.*, *23*, 1091-1094, 1996.

Leutbecher, M. and H. Volkert, Stratospheric temperature anomalies and mountain waves: A three dimensional simulation using a multi-scale weather prediction model. *Geophys. Res. Lett.*, *23*, 3329-3332, 1996.

Levelt, P. F., E. Hilsenrath, G. W. Leppelmeier, G. H. J. van den Oord, P. K. Bhartia, J. Tamminen, J. F. de Haan and J. P, Veefkind, Science objectives of the Ozone Monitoring Instrument, *IEEE Trans. Geosco. Remote Sens.*, vol 44, no 5, pp 1199-1208, May 2006.

Liou, K. N., *An Introduction to Atmospheric Radiation, Second Edition*, Elsevier, New York, 583 pp, 2002.

Lovelock, J. E., Atmospheric halocarbons and stratospheric ozone, *Nature*, *252*, 292-294, 1974.

MacKenzie, I. A., M. Kulmala, A. Laaksonen and T. Vesala, On the theories of type I polar stratospheric cloud formation, *J. Geophys. Res.*, *100*, 11,275-11,288, 1995.

Mahesh, A, R. Eager, J. R. Campbell, and J. D. Spinhirne, Blowing snow over the Antarctic plateau, *J. Geophys. Res.*, *108*(D22), 4707, doi:10.1029/2002JD003327, 2003.

Mahesh, A, J. R. Campbell, and J. D. Spinhirne, Multi-year measurements of cloud base heights at South Pole by lidar, *Geophys. Res. Lett.*, *32* (L09812), 2005.

Manney, G. L., J. L. Sabutis, S. Pawson, M. L. Santee, B. Naujokat, R. Swinbank, M. E. Gelman and W. Ebisuzaki, Lower stratospheric temperature differences between meteorological analyses in two cold Arctic winters and their impact on polar processing studies, *J. Geophys. Res.*, *108*, 8328, doi:10.1029/2001JD001149, 2003.

Marti, J. and K. Mauersberger, A survey and new measurements of ice vapor pressure at temperature between 170 and 250 K, *Geophys. Res. Lett.*, *20*, 363-366, 1993.

Massie, S. T., J. E. Dye, D. Baumgardner, W. J. Randel, F. Wu, X. X. Tie, L. Pan, F. Figarol, G. P. Brasseur, M. L. Santee, W. G. Read, R. G. Grainger, A. Lambert, J. L. Mergenthaler and A. Tabazadeh, Simultaneous observations of polar stratospheric clouds and HNO over Scandinavia in January 1992, *Geophys. Res. Lett.*, *24*, 595-598, 1997.

Masuda, K., Atmospheric heat and water budgets of Polar Regions: Analysis of FGGE data, In *Proceedings of the Third NIPR Symposium on Polar Meteorology and Glaciology*, National Institute of Polar Research, Tokyo, pp. 79-88, 1990.

McCormick, M. P., H. M. Steele, P. Hamill, W. P. Chu and T. J. Swissler, Polar stratospheric cloud sightings by SAM II, *J. Atmos. Sci.*, **39,** 1387-1397, 1982.

McElroy, M. B., R. J. Salawitch and S. C. Wofsy, Antarctic O_3: Chemical mechanisms for the spring decrease, *Geophys. Res. Lett.*, *13*, 1296-1299, 1986a.

McElroy, M. B., R. J. Salawitch, S. C. Wofsy and J. A. Logan, Reduction of Antarctic ozone due to synergistic interactions of chlorine and bromine, *Nature*, *321*, 759-762, 1986b.

McElroy, M. B. and R. J. Salawitch, Changing composition of the global stratosphere, *Science*, *243*, 763-770, 1989.

Measures, R. M., *Laser Remote Sensing: Fundamentals and Applications*, Wiley, 510 pp, 1984.

Molina, L. T. and M. J. Molina, Production of Cl_2O_2 from the self-reaction of the ClO radical, *J. Phys. Chem.*, *91*, 433-436, 1987.

Molina, M. J. and F. S. Rowland, Stratospheric sink for chlorofluoromethanes: Chlorine atomc-atalysed destruction of ozone, *Nature*, *249*, 810-812, 1974.

Montreal Protocol on Substances that Deplete the Ozone Layer, 15 pp, United Nations Environmental Programme (UNEP), New York, 1987.

Montzka, S. A., J. H. Butler, R. C. Myers, T. M. Thompson, T. H. Swanson, A. D. Clarke, L. T. Lock and J. W. Elkins, Decline in the tropospheric abundance of halogen from halocarbons: Implications for stratospheric ozone depletion, *Science*, *272*, 1318-1322, 1996.

Montzka, S. A., J. H. Butler, J. W. Elkins, T. M. Thompson, A. D. Clarke and L. T. Lock, Present and future trends in the atmospheric burden of ozone-depleting halogens, *Nature*, *398*, 690-694, 1999.

Murphy, D. M., D. S. Thomson and M. J. Mahoney, In situ measurements of organics, meteoritic material, mercury and other elements in aerosols at 5 to 19 kilometers, *Science*, *282*, 1664-1669, 1998

Nakamura, N. and A. H. Oort, Atmospheric heat budgets of the polar regions, *J. Geophys. Res.*, *93*, 9510-9524, 1988.

Newman, P. A., E. R. Nash and J. E. Rosenfield, What controls the temperature of the Arctic stratosphere during spring? *J. Geophys. Res.*, *106*, 19,999-20,010, 2001.

Newman, P. A., E. R. Nash, S. R. Kawa, S. A. Montzka and S. M. Schauffler, When will the Antarctic ozone hole reover? *Geophys. Res. Lett.*, *33*, L12814, doi:10.1029/2005GL025232, 2006

Palm, S. P., M. Fromm and J. Spinhirne, Observations of Antarctic polar stratospheric clouds by the Geoscience Laser Altimeter System (GLAS), *Geophys. Res. Lett.*, *32*, L22S04, doi:10.1029/2005GL023524, 2005.

Pawson, S. and B. Naujokat, The cold witners of the middle 1990s in the northern lower stratosphere, *J. Geophys. Res.*, *104*, 14,209-14,222, 1999.

Peter, T., Microphysics and heterogeneous chemistry of polar stratospheric clouds, *Annu. Rev. Phys. Chem.*, *48*, 785-822, 1997.

Pfenninger, M, A. Z. Liu, G. C. Papen, and C. S. Gardner, Gravity wave characteristics in the lower atmosphere at south pole, *J. Geophys. Res.*, *104*, 5963-5984, 1999.

Poole L. R. and M. P. McCormick, Airborne lidar observations of Arctic polar stratospheric clouds: Indication of two distinct growth stages, *Geophys. Res. Lett.*, *15*, 21-23, 1988.

Portmann, R. W., S. Solomon, R. R. Garcia, L. W. Tomason, L. R. Poole and M. P. McCormick, Role of aerosol variations in anthropogenic ozone depletion in the polar regions, *J. Geophys. Res.*, ,*101*, 22,991-23,006, 1996.

Prather, M. J. and R. T. Watson, Stratospheric ozone depletion and future levels of atmospheric chlorine and bromine, *Nature*, *344*, 729-734, 1990.

Prather, M. J., M. B. McElroy and S. C. Wofsy, Reductions in ozone at high concentrations of stratospheric halogens, *Nature*, *312*, 227-231, 1984.

Protecting the Ozone Layer, *Volume One*, 51 pp, United Nations Environmental Programme (UNEP), New York, 2001.

Pruppacher, H. R. and J. D. Klett, *Microphysics of Clouds and Precipitation, 2nd Edition*, Kluwer Academic Publishers, London, 954 pp, 1997.

Pyle, J. A., S. Solomon, D. Wuebbels and s. Zvenigorodsky, Ozone depletion and chlorine loading potentials, In *Scientific assessment of ozone depletion: 1991*, World Meteorological Organization Global Ozone Research and Monitoring Project, Report no. 25, World Meteorological Organization, Geneva, 1992.

Ramaswamy, V., M.-L. Chanin, J. Angell, J. Barnett, D. Gaffen, M. Gelman, P. Keckhut, Y. Koshelkov, K. Labitzke, J.-J. R. Lin, A. O'Neill, J. Nash, W. Randel, R. Rood, K. Shine, M. Shiotani and R. Swinbank, Stratospheric temperature trends: Observations and model simulations, *Rev. Geophys.*, *39*, 71-122, 2001.

Ravishankara, A. R. and D. R. Hanson, Differences in the reactivity of type I polar stratospheric clouds depending on their phase, *J. Geophys. Res.*, *101*, 3885-3890, 1996.

Renwick, J. A., Trends in the southern hemisphere polar vortex in NCEP and ECMWF reanalyses, *Geophys. Res. Lett.*, *31*, L07209, doi:10.1029/2003GL019302, 2004.

Rex, M., R. J. Salawitch, P. von der Gathen, N. R. P. Harris, M. P. Chipperfield and B. Naujokat, Arctic ozone loss and climate change, *Geophys. Res. Lett.*, *31*, L04116, doi:10.1029/2003GL018844, 2004.

Rosen, J. M, N. T. Kjome, and S. J. Oltmans, Simultaneous ozone and polar stratospheric cloud observations at South Pole Station during winter and spring 1991, *J. Geophys. Res.*, *98*, 12,741-12,751, 1993.

Rosenlof, K. H., S. J. Oltmans, D. Kley, J. M. Russell III, E-W. Chiou, W. P. Chu, D. G. Johnson, K. K. Kelly, H. A. Michelsen, G. E. Nedoluha, E. E. Remsberg, G. C.

Toon and M. P. McCormick, Stratospheric water vapor increases over the past half-century, *Geophys. Res. Lett.*, *28*, 1195-1198, 2001.

Rowland, F. S. and M. J. Molina, Chlorofluoromethanes in the environment, *Rev. Geophys.*, *13*, 1-35, 1975.

Rowland, F. S., J. E. Spencer and M. J. Molina, Stratospheric formation and photolysis of chlorine nitrate, *J. Phys. Chem.*, *80*, 2711-2713, 1976.

Salawitch, R.J., G. J. Gobbi, S. C. Wofsy and M. B. McElroy, Denitrification in the Antarctic stratosphere, *Nature*, *339*, 525-527, 1989.

Santacesaria, V., R. A. MacKenzie and L. Stefanutti, A climatological study of polar stratospheric clouds (1989-1997) from LIDAR measurements over Dumont d'Urville, *Tellus B*, *53*, 306-321, 2001.

Santee, M. L., W. G. Read, J. W. Waters, L. Froidevaux, G. L. Manney, D. A. Flwoer, R. F. Jarnot, R. S. Harwood, G. E. Peckham, Interhemispheric differences in polar stratospheric HNO_3, ClO and O_3, *Science*, *267*, 849-852, 1995.

Santee, M. L., G. L. Manney, N. J. Livesey, L. Froidevaux, I. A. macKenzie, H. C. Pumphery, W. G. Read, M. J. Schwartz, J. W. Waters and R. S. Harwood, Polar processing and development of the 2004 Antarctic ozone hole: First results from MLS on Aura, *Geophys. Res. Lett.*, *32*, L12817, doi:10.1029/2005GL022582, 2005.

Sassen, K., Backscattering cross sections for hydrometeors: Measurements at 6328 Å, *Appl. Opt.*, **17**, 804-806, 1978.

Sassen, K., The polarization lidar technique for cloud research: A review and current assessment, *Bull. Amer. Meteor. Soc.*, **72**, 1848-1866, 1991.

Sassen, K., Lidar cloud research, *Rev. Laser Engin.*, **23**, 148-153, 1995.

Sassen, K. and B. S. Cho, Subvisual-thin cirrus lidar dataset for satellite verification and climatological research, *J. Appl. Meteor.*, **31**, 1275-1285, 1992.

Sassen, K. and J. R. Campbell, A remote sensing midlatitude cirrus cloud climatology from the Facility for Atmospheric Remote Sensing. Part I: Macrophysical and synoptic properties, *J. Atmos. Sci.*, **58**, 481-496, 2001.

Sato, K, Sources of gravity waves in the polar middle atmosphere, *Adv. Polar Upper Atmos. Res.*, *14*, 233-240, 2000.

Schauffler, S. M., L. E. Heidt, W. H. Pollock, T. M. Gilpin, J. F. Vedder, S. Solomon, R. A. Lueb, E. L. Atlas, Measurements of halogenated organic compounds near the tropical tropopause, *Geophys. Res. Lett., 20,* 2567-2570, 1993.

Schoeberl, M. R., et al., Earth Observing System missions benefit atmospheric research, *Eos Trans. AGU, 85,* 177-197, 2004.

Shibata, T., K. Sato, H. Kobayashi, M. Yabuki and M. Shiobara, Antarctic polar stratospheric clouds under temperature perturbation by nonorographic inertia gravity waves observed by micropulse lidar at Syowa Station, *J. Geophys. Res., 108,* 4105, doi:10.1029/2002JD002713, 2003.

Shindell, D. T., D. Rind and P. Lonergan, Increased polar stratospheric ozone losses and delayed eventual recovery owing to increased greenhouse-gas concentrations, *Nature, 392,* 589-592, 1998.

Simmonds, I. and R. Law, Associations between Antarctic katabatic flow and the upper level winter vortex, *Int. J. Climatol., 15,* 403-421, 1995.

Solomon, S., Progress towards a quantitative understanding of Antarctic ozone delpeltion, *Nature, 347,* 347-353, 1990.

Solomon, S., R. R. Garcia, F. S. Rowland and D. J. Weubbles, On the depletion of Antarctic ozone, *Nature, 321,* 755-758, 1986.

Solomon, S., Stratospheric ozone depletion: A review of concepts and history, *Rev. Geophys., 37,* 275-316, 1999.

Spinhirne, J. D., J. A. Reagan and B. M. Herman, Vertical distribution of aerosol extinction cross section and inference of aerosol imaginary index in the troposphere by lidar technique, *J. Appl. Meteorol.*, **19,** 426-438, 1980.

Spinhirne, J. D., Micro pulse lidar, *IEEE Trans. Geosci. Remote Sens.*, 31, 48-55, 1993.

Spinhirne, J. D., J. A. R. Rall and V. S. Scott, Compact eye safe lidar systems, *Rev. Laser Eng.*, **23,** 112-118, 1995.

Spinhirne, J. D., S. P. Palm, W. D. Hart, D. L. Hlavka and E. J. Welton, Cloud and aerosol measurements from GLAS: Overview and initial results, *Geophys. Res. Lett., 32,* L22S03, doi:10.1029/2005GL023507, 2005.

Stanford, J. L., Possible sink for stratospheric water vapor at the winter Antarctic pole, *J. Atmos. Sci.*, **30,** 1431-1436, 1973.

Stanford, J. L. and J. S. Davis, A century of stratospheric cloud reports: 1870-1972, *Bull. Am. Meteorol. Soc.*, **55,** 213-219, 1974

Steele, H. M., P. Hamill, M. P. McCormick and T. J. Swissler, The formation of polar stratospheric clouds, *J. Atmos. Sci.*, **40,** 2055-2068, 1983.

Steffanutti, L., M. Morandi, M. Del Guasta, S. Godin, G. Megie, J. Brechet and J. Piquard, Polar stratosphierc cloud observations over the Antarctic continent at Dumont D'Urville, *J. Geophys. Res.*, *96*, 12,975-12,987, 1991.

Stohl, A., Computation, accuracy and applications of trajectories – A review and bibliography, *Atmos. Environ.*, *32*, 947-966, 1998.

Stolarski, R. S. and R. J. Cicerone, Stratospheric chlorine: A possible sink for ozone, *Can. J. Chem.*, *52(8)*, 1610-1615, 1974.

Stolarski, R. S., A. J. Kruger, M. R. Schoeberl, R. D. McPeters, P. A. Newman and J. C. Alpert, Nimbus 7 satellite measurements of the springtime Antarctic ozone decrease, *Nature*, *322*, 808-811, 1986.

Tabazadeh, A. and O. B. Toon, The presence of metastable HNO_3/H_2O solid phases in the stratosphere inferred from ER-2 data, *J. Geophys. Res.*, *101*, 9071-9078, 1996.

Tabazadeh, A., R. P. Turco, K. Drdla and M. Z. Jacobson, A study of Type I polar stratospheric cloud formation, *Geophys. Res. Lett.*, *21*, 1619-1622, 1994.

Tabazadeh, A., O. B. Toon and P. Hamill, Freezing behavior of stratospheric sulfate aerosols inferred from trajectory studies, *Geophys. Res. Lett.*, *22*, 1725-1728, 1995.

Tabazadeh, A., O. B. Toon, B. L. Gary, J. T. Bacmeister and M. R. Schoeberl, Observational constraints on the formation of Type Ia polar stratospheric clouds, *Geophys. Res. Lett.*, *16*, 2109-2112, 1996.

Tabazadeh, A., M. L. Santee, M. Y. Danilin, H. C. Pumphrey, P. A. Newman, P. J. Hamill and J. L. Mergenthaler, Quantifying dentrification and its effect on ozone recovery, *Science*, *288*, 1407-1411, 2000.

Tabazadeh, A., E. J. Jensen, O. B. Toon, K. Drdla, M. R. Schoeberl, Role of the stratospheric freezing belt in denitrification, *Science*, *291*, 2591-2594, 2001.

Teitelbaum, H., M. Moustaoui and M. Fromm, Exploring polar stratsospheric cloud and ozone minihole formation: The primary importance of synoptic-scale flow perturbations, *J. Geophys. Res.*, *106*, 28,173-28,188, 2001.

Tolbert, M. A., M. J. Rossi and D. M. Golden, Heterogeneous interactions of chlorine nitrate hydrogen chloride and nitric acid with sulfuric acid surfaces at stratospheric temperatures, *Geophys. Res. Lett.*, *15*, 847-850, 1988.

Toon, O. B. and M. A. Tobert, Spectroscopic evidence against nitric acid trihydrate in polar stratospheric clouds, *Nature*, *375*, 218-221, 1995.

Toon, O. B., P. Hamill, R. P. Turco and J. Pinto, Condensation of HNO_3 and HCl in the winter polar stratospheres, *Geophys. Res. Lett.*, *13*, 1284-1287, 1986.

Toon, O. B., R. P. Turco, J. Jordan, J. Goodman and G. Ferry, Physical processes in polar stratospheric ice clouds, *J. Geophys. Res.*, *94*, 11,359-11,380, 1989.

Toon, O. B., R. P. Turco, P. Hamill, Denitrification mechanisms in the polar stratosphere, *Geophys. Res. Lett.*, *17*, 445-448, 1990.

Toon, O. B., A. Tabazadeh, E. V. Browell and J. Jordan, Analysis of lidar observations of Arctic polar stratospheric clouds during January 1989, *J. Geophys. Res.*, *105*, 20,589-20,615, 2000.

Tuck, A. F., Synoptic and chemical evolution of the Antarctic vortex in late winter and early spring, *J. Geophys. Res.*, *94*, 11,687-11,737, 1989.

Turco, R. P., O. B. Toon and P. Hamill, Heterogeneous physicochemistry of the polar ozone hole, *J. Geophys. Res.*, *94*, 16,493-16,510, 1989.

van der Leun, J. C., Y., Y. Takiyawa and J. D. Longstreth, Human Health, Chapter 2 in *Environmental Effects of Ozone Depletion*; J. C. van der Leun, M. Trevini and R. C. Worress (Eds.), 11-24, United Nations Environment Programme, Nairobi, Kenya, 1989.

van der Leun, J. C. and F. R. de Gruijl, *Influences of ozone depletion on human and animal health, in UV-B Radiation and Ozone Depletion*, M. Tevini (ed.), Lewis Publishers, Boca Raton, pp. 95-123, 1993.

Volkert, H. and D. Intes, Orographically forced stratospheric waves over northern Scandinavia, *Geophys. Res. Lett.*, *19*, 1205-1208, 1992.

Waibel, A. E., Th. Peter, K. S. Carslaw, H. Oelhaf, G. Wetzel, P. J. Crutzen, U. Pöschl, A. Tsias, E. Reimer and H. Fischer, Arctic ozone loss due to denitrification, *Science*, *283*, 2064-2069, 1999.

Wallace, J. M. and Hobbs, P. V., *Atmospheric Science: An Introduction Survey*, Academic Press, Inc. Harcourt Brace Jovanovich Publishers, 467 p, 1977.

Waters, J. W., et al., The Earth Observing System microwave limb sounder on the Aura satellite, *IEEE Trans. Geosci. Remote Sens.*, *44*, 1075-1092, 2006.

Waugh, D. W. and W. J. Randel, Climatology of Arctic and Antarctic polar vortices using elliptical diagnostics, *J. Atmos. Sci.*, **56,** 1594-1613, 1999.

Wayne, R. P., *Chemistry of Atmospheres*, Oxford University Press, Oxford, 464 pp, 1991.

Weatherhead, E. C. and S. B. Andersen, The search for signs of recovery of the ozone layer, *Nature*, *441*, 39-45, 2006.

Welton, E. J., J. R. Campbell, J. D. Spinhirne, and V. S. Scott, Global monitoring of clouds and aerosols using a network of micro-pulse lidar systems, *Proc. Int. Soc. Opt. Eng.*, *4153*, 151-158, 2001.

Welton, E. J. and J. R. Campbell, Micropulse lidar signals: Uncertainty analysis, *J. Atmos. and Oceanic Technol.*, **19** (12), 2089-2094, 2002.

Wilson, J. C., M. Loewenstein, D. W. Fahey, B. Gary, S. D. Smith, K. K. Kelly, G. V. Ferry and K. R. Chan, Observations of condensation nuclei in the Airborne Antarctic Ozone Experiment: Implications for new particle formation and polar stratospheric cloud formation, *J. Geophys. Res.*, *94*, 16,437-16.448, 1989.

Wofsy, S. C., M. B. McElroy and Y. L. Yung, The chemistry of atmospheric bromine, *Geophys. Res. Lett.*, *2*, 215-218, 1975.

World Meteorological Organization, *Scientific Assessment of Ozone Depletion: 1998, Global Ozone Res. Monit. Proj. Rep.*, vol. 44, Geneva, Switzerland, 1998.

Worsnop, D. R., L. E. Fox, M. S. Zahniser and S. C. Wofsy, Vapor pressures of solid hydrates of nitric acid: Implications for polar stratospheric clouds, *Science*, *259*, 71-74, 1993.

Wu, D. L. and J. W. Waters, Gravity-wave scale temperature fluctuations seen by the UARS MLS, *Geophys. Res. Lett.*, *23*, 3289-3292, 1996a.

Wu, D. L. and J. W. Waters, Satellite observations of atmospheric variances – a possible indication of gravity waves, *Geophys. Res. Lett.*, *24*, 3631-3634, 1996b.

Wu, D. L. and J. H. Jiang, MLS observation of atmospheric gravity waves over Antarctica, *J. Geophys. Res.*, *107*, 4773, 10.1029/2002JD002390, 2002.

Yoshiki, M. and K. Sato, A statistical study of gravity waves in the polar regions based on operational radiosonde data, *J. Geophys. Res.*, *105*, 17,995-18,011, 2000.

Zhang, R., P. J. Wooldridge and M. J. Molina, Vapor pressure measurements for the $H_2SO_4/HNO_3/H_2O$ and $H_2SO_4/HCL/H_2O$ systems: Incorporation of stratospheric acids into background sulfate aerosols, *J. Phys. Chem.*, *97*, 8541-8548, 1993.

APPENDIX A

TWO-DIMENSIONAL HANNING FUNCTION FOR DATA SMOOTHING

At various points in this research datasets were smoothed, either as a means for reducing noise or for interpolating data points to increase temporal and/or spatial resolutions. This was done using a two-dimensional Hanning function (*Blackman and Tukey*, 1959; also referred to as the "Von Hann" window). The formula is easy to implement and minimizes spectral energy leakage from high frequencies (*Pfenninger et al*, 1999). The solution to the equation is a weighting function

$$w(z,t) = \left\{\frac{1}{4}\left[1+\cos\left(\frac{\pi z}{\alpha}\right)\right]\left[1+\cos\left(\frac{\pi t}{\beta}\right)\right]\right\} \qquad \textbf{(A.1)}$$

where $-\alpha \le z \le \alpha$

$-\beta \le t \le \beta$

$$w(z,t) = 0 \qquad \text{elsewhere} \qquad \textbf{(A.2)}$$

where z and t are spatial and temporal variables. α is the temporal half-width and β is the spatial half-width. The filter is solved for any given point (z,t) acting as the center of the spatial and temporal domain as

$$\chi(z,t) = \frac{\sum_{i,j} w(z - z_i, t - t_j)\chi(z_i, t_j)}{\sum_{i,j} w(z - z_i, t - t_j)} \qquad \textbf{(A.3)}$$

where $\chi(z,t)$ is the dependent variable. α and β are chosen on a case-by-case basis so as to optimize the smoothing routine for a given scenario. Maximizing the two is advantageous for cases where there are significant data gaps. However, this reduces the signal of small scale structures that may or may not be relevant. When addressing use of the Hanning function in the text the chosen values for α and β are noted as well as the rationale behind their selection.

APPENDIX B

LIDAR INTERCOMPARISON TO INVESTIGATE THE SENSITIVITY OF MICROPULSE LIDAR POLAR STRATOSPHERIC CLOUD DETECTION AND ALGORITHM RETRIEVALS AT THE SOUTH POLE

During the 2000 winter season, a Fe-Boltzmann lidar (0.372, 0.374 μm) was operated episodically at the South Pole Atmospheric Research Observatory building by the University of Illinois, Urbana-Champaign (UIUC). The focus of their work was the detection of polar mesospheric clouds (PMC; *Chu et al.*, 2001). However, in profiling to heights approaching 80.0 km MSL, their measurements include cases where polar stratospheric clouds (PSC) were present. The MPL instrument was run autonomously in a full-time data collection mode. Therefore, overlap between the two datasets occurred and intercomparisons are possible. Notably, since the UIUC instrument was designed for upper-atmospheric study, the instrument emits higher laser pulse energies relative to MPL. The sensitivity to PSC scattering is higher (with caveats, discussed below), and therefore, these data can serve as a validation source for MPL algorithm output and help to further understand the sensitivity of algorithm retrievals and of the instrument to PSC detection.

The UIUC lidar is designed to measure temperatures from 30.0 – 80.0 km MSL using the Rayleigh technique, and at heights above this in the mesopause region using the Fe-Boltzmann technique (*Gelbwachs*, 1994). Volume backscattering cross-sections and

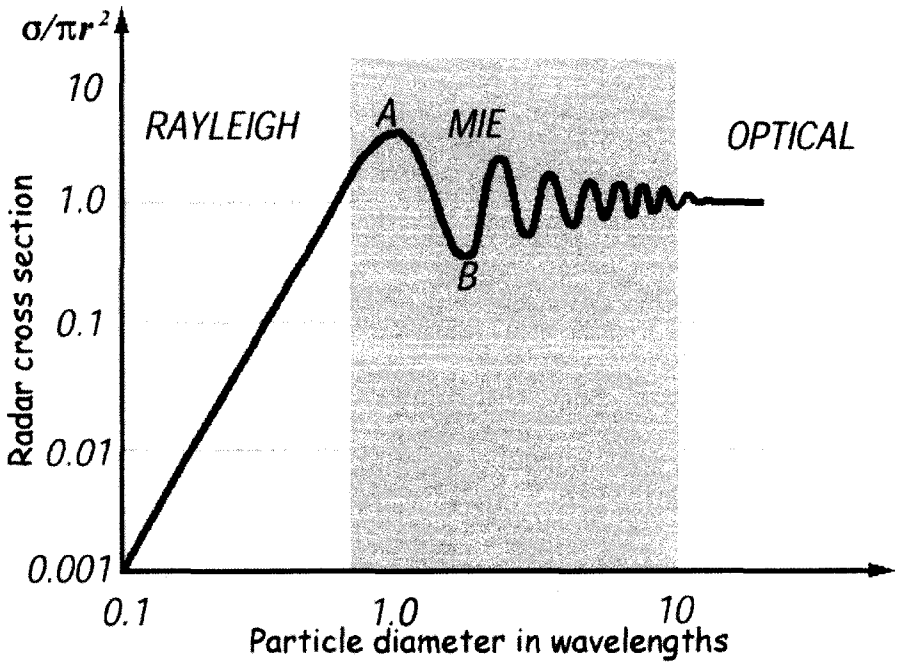

Figure B.1 Rayleigh, transitional and Mie scattering domains.
Scattering cross-section versus particle dimension parameter (d/λ). Three scattering domains are highlighted; Rayleigh, transitional and Mie/optical (*Xinzhao Chu*, personal communication, 1996).

scattering ratios are also derived for PMC and PSC (*Chu et al.*, 2001). The system includes two 0.4 m diameter telescopes and two injection-seeded pulsed Alexandrite lasers. Both are frequency-doubled to be in tune with Fe resonance lines at 0.372 and 0.374 μm, with an average output power of approximately 3 W (*Gardner et al.*, 2001). The system is operable during both day and night. To minimize solar background noise, the divergence of each laser beam and the field-of-view for each telescope are limited to 0.5 mrad full-width, and narrowband interference filters and Fabry-Perot etalons are used along the receive path in conjunction with 30 GHz optical bandwidth detectors.

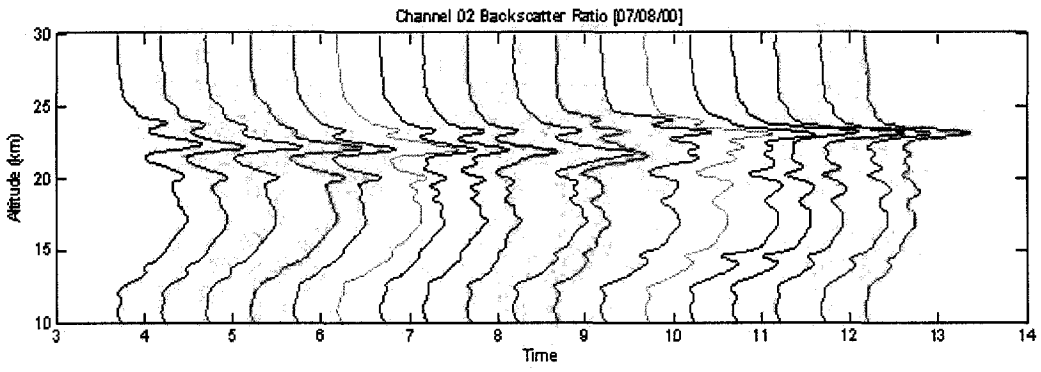

Figure B.2 UIUC lidar attenuated scattering ratios from 8 July 2000. UIUC Fe-Boltzmann lidar (0.372, 0.374 μm) attenuated scattering ratio data (laterally offset for values of 1.0 and 2.2) in thirty-minute averages from 8 July 2000 at the South Pole from 0300 – 1200 UTC and 10.0 – 30.0 km MSL (*Xinzhao Chu*, personal communication, 1996).

Additionally, to limit saturation effects of scattering from lower-atmospheric targets, including to heights common for PSC occurrence, energy "choppers" are used (*Xinzhao Chu*, personal communication, 2006).

A common range for PSC particle diameter is 0.1 to 10.0 μm (e.g., *Dye et al.*, 1992; *Toon et al.*, 2000). At ultraviolet and visible wavelengths, the particle dimension parameter, defined here as diameter versus wavelength (or a factor of π less than they typically referenced size parameter; e.g., *Measures*, 1984), ranges between approximately 0.5 and 20. Figure B.1 is a plot of the natural logarithm of scattering cross-section relative to the particle size dimension (*Xinzhao Chu*, personal communication, 2006). Three scattering domains are apparent. For values less than about 1.0, the scattering cross-section per particle varies according to the Rayleigh-Ganz approximation, or proportional to diameter raised to the fourth power. Between values of 1.0 to 10.0 a

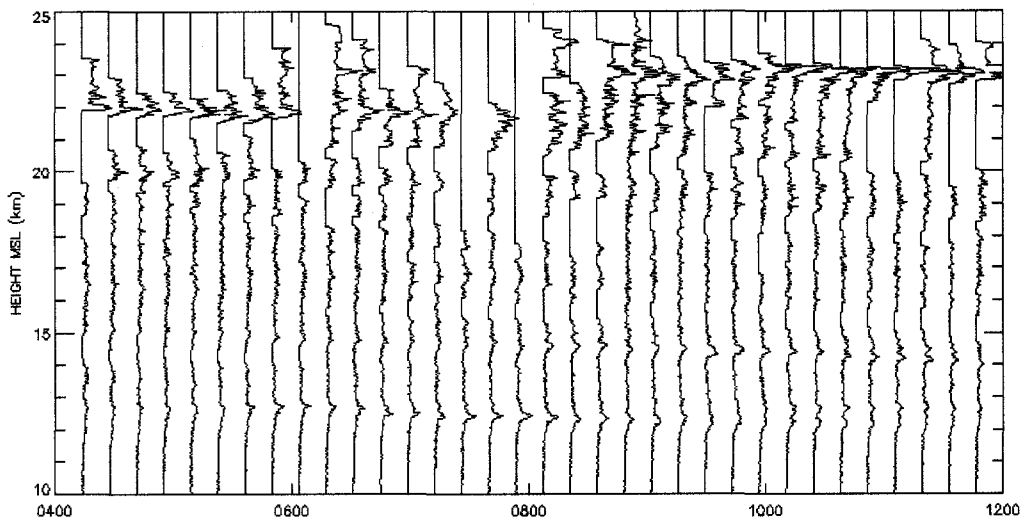

Figure B.3 MPL algorithm output at base resolution for 8 July 2000. MPL (0.523 μm) attenuated scattering ratio data (laterally offset for values between 1.0 and 5.0) at 0.01 fractional day resolution from 8 July 2000 at the South Pole from 0400 – 1200 UTC and 10.0 – 25.0 km MSL.

transition region occurs, where the Rayleigh-Ganz approximation and Mie solution are both prominent. Above 10.0, the Mie solution mostly dominates, and scattering cross-section varies linearly with the particle size dimension. Therefore, for all but the sub-micron PSC particles, scattering detected by both the MPL and UIUC Fe-Boltzmann lidar would be considered as Mie scatterers. In this case, the molecular scattering response difference between the UIUC and MPL wavelengths would cause corresponding ASR values to be offset by a factor of approximately 4.0.

Figure B.2 displays attenuated scattering ratio (ASR) profiles (offset laterally for values between 1.0 and 2.2) derived from thirty-minute averages of UIUC Fe-Boltzmann lidar data for 0300 – 1200 UTC from 10.0 – 30.0 km MSL on 8 July 2000 at the South

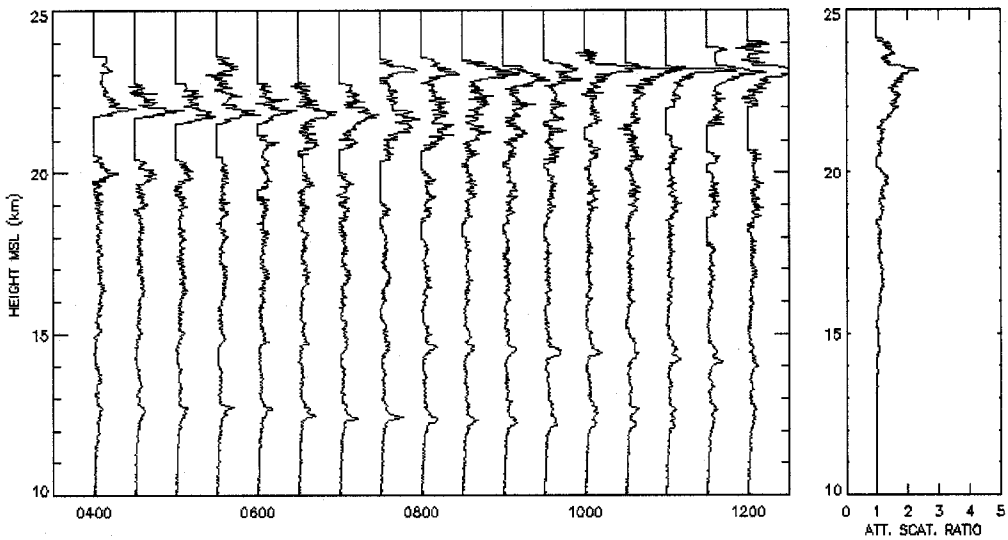

Figure B.4 MPL algorithm output at 0.02 and full-day resolutions. MPL (0.523 μm) attenuated scattering ratio data (laterally offset for values between 1.0 and 5.0) at 0.02 fractional day resolution from 8 July 2000 at the South Pole from 0400 – 1200 UTC and 10.0 – 25.0 km (left), followed by the attenuated scattering ratio derived from an

Pole. Figure B.3 displays ASR profiles (similarly offset for values between 1.0 and 5.0) calculated from MPL data at 0.01 fractional day resolution for 0400 – 1200 UTC from 10.0 – 28.0 km MSL on the same day. Figure B.4 shows MPL ASR profiles calculated at 0.02 fractional day resolution for the same time period, accompanied by a plot of the ASR profile derived from the average signal for the entire day. Figure B.5 displays thermal parameters valid at 0000 UTC from 10.0 – 28.0 km MSL, including temperature (a) and thermal depressions relative to the NAT condensation-point for 10.0 ppbv HNO_3/4.0 ppmv water vapor (b) and the ice frost-point for 4.0 ppmv water vapor. From these approximated concentrations, NAT-saturated conditions were present throughout

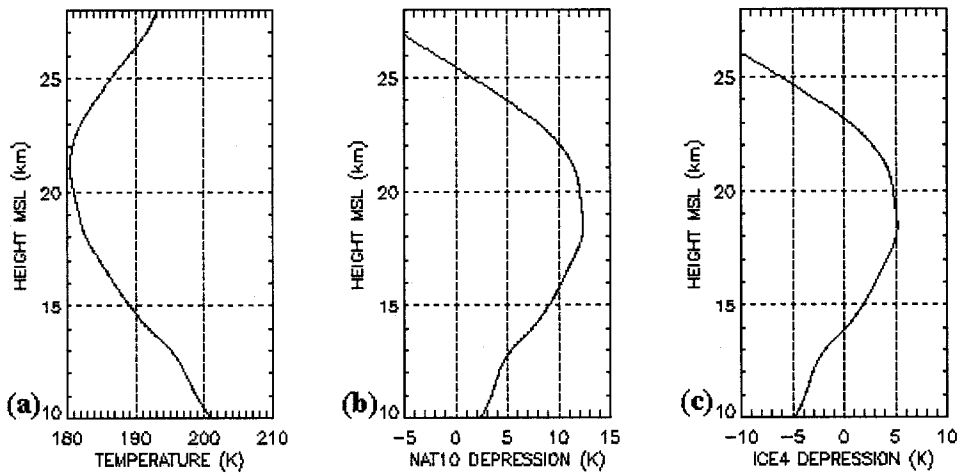

Figure B.5 Thermal profiles at the South Pole for 0000 UTC 8 July 2000. From 10.0 – 28.0 km MSL, air temperature (K; a), thermal depression relative to NAT condensation point for 10.0 ppbv HNO_3/4.0 ppmv water vapor (K; b) and relative to ice frost point for 4.0 ppmv water vapor (K; c)

the lower-stratosphere up to 26.0 km MSL, and ice-saturated conditions were present between 14.0 and 23.0 km MSL.

PSC structure depicted in these images is consistent. Both lidars measure mostly continuous cloud above 10.0 km MSL to near 24.0 km MSL. The UIUC data depict a gradual lessening of ASR above that height to near 26.0 km MSL, whereas the MPL data depict a fairly contiguous cloud top. At 0.01 fractional day resolution, the MPL retrievals are relatively noisy, gaps are present throughout the profiles, and the upper regions of the cloud are not well-resolved. This is consistent with high minimum scattering ratio thresholds required to resolve cloud structure at that resolution setting. These gaps and inconsistencies are improved by decreasing temporal resolution in profiles shown at 0.02

fractional day processing (Fig. B.4). A narrow gap persists in these data, near 21.0 km MSL. The UIUC measurements depict this gap, but do not shown ASR dropping to that of clear-air.

Differences in ASR scaling reflect the difference in molecular scattering cross-section in the UV versus green wavelengths. ASR values scale to agreement, consistent with Mie scattering, above 20.0 km MSL. Below this height, differences are apparent. Normalization of the UIUC profiles is derived above the PSC layer, near and above 30.0 km MSL. Some differences would arise through transmission loss caused by these clouds below this region (not shown). Another possible cause may be due to relatively low effective size diameters at these lower heights. The presence of sub-micron particles would lead to enhanced scattering in the UV, and ASR offsets would no longer reflect that of Mie theory.

MPL ASR is capped along the top height corresponding to ice-saturation, whereas the UIUC values are capped by the top height corresponding to NAT-saturation. Below 15.0 km MSL, both instruments detect ASR below the apparent ice-saturation level. For the MPL, these are similar results to those from Fig. 3.8. Sub-micron particles near and below the ice-saturation boundary are more likely consistent with concentrated solution droplets, and therefore Type I PSC than pure ice. Recall, this boundary reflects that for the latter scenario, which is not necessarily reflective of conditions common to Type II nucleation in the atmosphere (e.g., *Tabazadeh et al.*, 1994; *Koop et al.*, 1998; *Koop et al.*, 2000). Still, this comparison reinforces two conclusions drawn from the main body of this thesis. First, the MPL at 0.01 fractional day resolution is not detecting all types of

PSC, particularly Type I above 15.0 km MSL. Second, those PSC detected with the MPL are most likely ice, or Type II PSC, where optical depths and scattering cross-sections are typically large so as to overcome higher minimum thresholds for ASR. However, there are likely some Type II PSC present below detection thresholds. The seasonal MPL datasets (Chapter 3), therefore, cannot be considered representative of all ice occurring during any season. The detection of Type I PSC is still plausible, particularly at lower levels, and in the presence of gravity wave activity (Chapter 4). However, with respect to total seasonal integrated attenuated backscatter, the value used in correlating PSC with ozone loss in Figs. 3.10 and 3.11, the contribution of Type I clouds to the overall sample is still likely to be low.

Decreasing the resolution of the MPL retrievals should implicitly improve them. However, there are two caveats to consider when comparing and considering the merits of Figs. B.3 and B.4. First, by increasing averaging intervals, there must be a method for eliminating single profiles where attenuation or cloud scattering exhibit strong influences. Their inclusion in long aggregate averages biases the shape of the profile when normalized to a molecular scattering profile. In these cases, the algorithm technique designed for this research is limited. Second, the longer the average the less structure is retained. For example, in Fig. B.4, the ASR profile derived for the entire day reflects averaging of cloud and clear-air measured intermittently with height. ASR values are relatively low, peaking below 2.5, compared to the structure shown adjacent to that plot from 0.02 fractional day retrievals, where ASR exceeds 5.0 in some cases. It turns out that even otherwise ubiquitous PSC are not so temporally persistent so as to overcome the

potential weakness in over-averaging. In advance of a secondary smoothing step, as was done in Chapter 3 with the Hanning window, retention of structure and variability will play an undeterminable role in the final product.

In this dissertation, 0.01 fractional day retrievals were used because the period was sufficient to produce meaningful results without high amounts of data loss from signal biasing, while retaining a high measure of signal structure. However, for this case study, it is clear that the lower resolution retrieval produces more meaningful results. Though not a factor in this subject case, higher resolution processing can still be useful for deriving lower resolution results. At higher resolution (for example, 0.01 fractional day), successful calibration of the profile can act as an independent and objective means for testing for attenuation-limited profiles. Running the algorithm at the higher setting first then acts as a screen for data to be included in longer averages. Tuning the resolution setting to maximize the efficiency of the retrieval is also important. Too long of an averaging interval weakens the process. At any rate, signal averaging is a process that introduces caveats into resulting datasets. These factors must be qualified and discussed within the context of any conclusions drawn from the results.